8-2011

BIOLOGICAL AND ECOLOGICAL RESPONSES TO CARBON-BASED NANOMATERIALS

Tatsiana Ratnikova
Clemson University, tratnik@clemson.edu

BIOLOGICAL AND ECOLOGICAL RESPONSES TO
CARBON-BASED NANOMATERIALS

A Dissertation
Presented to
the Graduate School of
Clemson University

In Partial Fulfillment
of the Requirements for the Degree
Doctor of Philosophy
Physics

---

by
Tatsiana A. Ratnikova
August 2011

Accepted by:
Dr. Pu-Chun Ke, Committee Chair
Dr. Lyndon Larcom
Dr. Apparao Rao
Dr. Hong Luo

ABSTRACT

Nanotechnology has been undergoing tremendous development in recent decades, driven by realized perceived applications of nanomaterials in electronics, therapeutics, imaging, sensing, environmental remediation, and consumer products. Along with these developments there have been increased evidences that engineered nanomaterials are often associated with hazardous effects they invoke in biological and ecosystems through intentional designs or unintentional discharge. Consequently there is a crucial need for documenting and understanding the interactions between nanoparticles and biological and ecosystems. This dissertation is aimed at bridging such a knowledge gap by examining the biological and ecological responses to carbon nanoparticles, a major class of nanomaterials which have been mass produced and extensively studied for their rich physical properties and commercial values.

Chapter I of this dissertation offers a comprehensive review on the structures, properties, applications, and implications of carbon nanomaterials, especially related to the perspectives of biological and ecosystems. Given that there are many types of carbon nanomaterials available, this chapter is focused on three major types of carbon-based nanomaterials only, namely, fullerenes, single walled and multi-walled carbon nanotubes.

Based on the literature review in Chapter I, Chapters II-VI present step-by-step my PhD research on elucidating the biological and ecological responses to carbon nanoparticle exposure, from the whole organism level down to the cellular and molecular level.

On the whole organism level, specifically, Chapter II presents a first study on the fate of fullerenes and multiwalled carbon nanotubes in rice plants, which was facilitated by the self assembly of these nanomaterials with NOM. The aspects of fullerene uptake, translocation, biodistribution, and generational transfer in the plants were examined and quantified using bright field and electron microscopy, FT-Raman, and FTIR spectroscopy. The uptake and transport of fullerene in the plant vascular system were attributed to water transpiration, convection, capillary force, and the fullerene concentration gradient from the roots to the leaves of the plants.

On the cellular level, Chapter III documents the differential uptake of hydrophilic $C_{60}(OH)_{20}$ vs. amphiphilic C_{70}-NOM complex in *Allium cepa* plant cells and HT-29 colon carcinoma cells. This study was conducted using a plant cell viability assay, and complemented by bright field, fluorescence and electron microscopy imaging. In particular, $C_{60}(OH)_{20}$ and C_{70}-NOM showed contrasting uptake in both the plant and mammalian cells, due to their significant differences in physicochemistry and the presence of an extra hydrophobic plant cell wall in the plant cells. Consequently, $C_{60}(OH)_{20}$ was found to induce toxicity in *Allium cepa* cells but not in HT-29 cells, while C_{70}-NOM was toxic to HT-29 cells but not to the plant cells.

Along with the biophysical study presented in Chapter III, Chapter IV further delineates the toxicological consequences of cell exposure to $C_{60}(OH)_{20}$. The cytoprotective properties of $C_{60}(OH)_{20}$ against copper were demonstrated using a double-exposure system: HT-29 cells were first exposed to $C_{60}(OH)_{20}$ and then to copper, a physiologically essential element and a major toxin. Using cell viability, proliferation,

and intracellular reactive oxygen species (ROS) production assays, I demonstrated the inhibition of copper-induced cell damage and ROS production by $C_{60}(OH)_{20}$. Neutralization of copper ions by $C_{60}(OH)_{20}$ in the extracellular space, as well as adsorption and uptake of the nanoparticles surface-modified by the cell medium were identified as plausible mechanisms for the cytoprotective activities of $C_{60}(OH)_{20}$ against copper.

Extended from the cellular studies in Chapters III and IV, Chapter V and VI show molecular-level inhibitions of two major cellular processes -- DNA amplification and MT polymerization -- by $C_{60}(OH)_{20}$. Such inhibitions were mainly attributed to the formation of hydrogen bonding between the nanoparticles and the hydrogens of the triphosphate tail of the nucleotide/DNA or the tubulin heterodimers, the building blocks of microtubules. Specifically, in Chapter V, the effect of $C_{60}(OH)_{20}$ on the amplification of an HSTF gene was examined using PCR and real-time PCR, whereas in Chapter VI circular dichroism spectroscopy, GTP hydrolysis assay, and ITC measurements were utilized to examine the effect of $C_{60}(OH)_{20}$ on MT polymerization. In both cases, the experimental results were confirmed and substantiated by molecular dynamics simulations.

Based on the studies documented in Chapters II-VI, Chapter VII summarizes and rationalizes the results obtained from the dissertation research and projects future work which may be beneficial to our understanding of nanoparticles at large.

In short, this dissertation is composed of the following chapters:

- o Chapter I: Literature review

- o Chapter II: Uptake, translocation and transmission of carbon-based nanomaterials in rice plants

- o Chapter III: Differential uptake of carbon nanomaterials by plant and mammalian cells

- o Chapter IV: Cytoprotective properties of a fullerene derivative against copper

- o Chapter V: Experimental and simulations studies of a real-time PCR in the presence of a fullerene derivative

- o Chapter VI: *In vitro* polymerization of microtubules with a fullerene derivative

- o Chapter VII: Conclusions and future work

DEDICATION

This dissertation is dedicated to my family and my loved ones.

ACKNOWLEDGMENTS

I would like to thank all the people who have helped and supported me over the last four years at Clemson.

I owe my deepest gratitude to my research advisor, Dr. Pu-Chun Ke, for his guidance, help, and unlimited kindness and support. He brought me to Clemson from a northern corner of the world, and exposed me to these fascinating fields of biophysics and nanotechnology. He helped me make this tremendous cultural transition and trained me into an experimentalist who understands languages of multidisciplines. His passion about science, his intelligence and his deep understanding of the principles and methodologies of biophysics, supramolecular assembly, plant and cell biology, and nanotechnology inspired me to be a better researcher. This dissertation would not be possible without him.

My gratitude also goes to the members of my PhD committee, Dr. Lyndon Larcom, Dr. Apparao Rao and Dr. Hong Luo for their scientific suggestions, technical editions, and valuable time, which all contributed to the success of my PhD study.

I wish to thank the people I have collaborated with over the past four years. I especially wish to thank Dr. Emppu Salonen and Praveen Govindan for their computer simulations which enriched and complemented my study. I wish to thank Dr. George Huang for teaching me cell culture and Drs. Junjun Shang and Halina Knap for teaching me PCR.

I would like to give my special thanks to my fellow students in the lab: Sijie Lin, Priyanka Bhattacharya, Ran Chen, Pengyu Chen, Poonam Choudhary, Karthikeyan

Pasypathy, Marcus Allegood, Andrew Baker, and Mark Bebber, for their help and unreserved friendships. This lab was my home away from home.

I also wish to express my love and gratitude to my family, for their understanding, tolerance, support, and endless love through the course of this journey.

TABLE OF CONTENTS

Table of Contents (Continued)

LIST OF TABLES

LIST OF FIGURES

List of Figures (Continued)

xiv

List of Figures (Continued)

List of Figures (Continued)

Figure   Page

List of Figures (Continued)

List of Figures (Continued)

Figure   Page

CHAPTER ONE

LITERATURE REVIEW

1.1 Introduction

"Nanotechnology is the principle of manipulation of the structure of matter at the

molecular level" - K. E. Drexler, 1980.

Nanotechnology encompasses particles in the range from 1 to 100 nm in two or three dimensions. The word itself is derived from the words *nano* and *technology* the prefix of which (*nano*) defines a quantity of one-billionth or mathematically as 1×10^{-9} and the suffix of which (*technology*) provides society with items needed or desired. The term *nanotechnology* combines these two terms and describes the process that offers goods and services which are achieved from matter at the nanometer level.

The concept of nanotechnology for the first time was announced by physicist R. Feynman in his talk "There is plenty of room at the bottom" at an American Physical Society meeting in 1959 and later explored in much more depth by K. E. Drexler in 1980. Afterwards, two major expansions, the beginning of cluster science and the invention of scanning tunneling microscope, yielded the science of nanotechnology in the early 1980s.

Science laws behave differently at the nanoscale; gravity is less important, whereas statistical and mechanical effects, such as "quantum size effect" – the alteration of electronic properties with great reduction in particle size, are more significant. In other

words, in the nano-scale range, the "quantum realm" is the arbiter. Nanoparticles possess large surface areas and essentially no inner mass, providing extremely a high surface-to-mass ratio. This phenomenon, in turn, yields particles with a much higher surface density and reactivity. Thus, within the nano-range, the physical, chemical, electrical, biological, mechanical and other properties can differ drastically from the properties of bulk materials [1].

The acceptance of nanotechnology by the public has led to research on the applications and implications of nanomaterials, and the development of nanoscale devices now impacts every aspect of human society [2]. For example, zinc oxide, zinc and silver nanoparticle have been employed as an anti-microbial, anti-bacterial, anti-biotic and anti-fungal agents when incorporated in coatings, fibers, polymers, first aid bandages, plastics, soap and textiles; carbon nanotubes, silicon oxide, silicon, copper, copper oxide, indium nanoparticles have been exploited as superconductors, conductors or semiconductors; and quantum dots have demonstrated vast potential in electronics, high speed computing, telecommunication, and space travel [3].
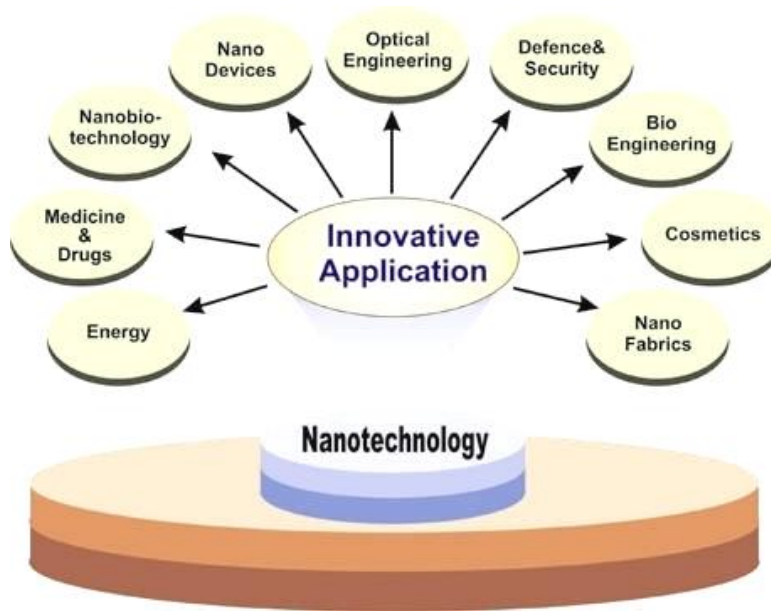
Figure 1-1. Diverse applications of nanotechnology in modern society [2].

According to the first publicly available on-line inventory, it is estimated that 1,317 nanotechnology products or product lines are now available as of March 10, 2011 [4]. Figure 1-2 represents the industrial fields in which nanotechnology consumer products and major nanomaterials have been applied over the last 5 years.

Obviously, the presence of nanoparticles in commercially available products is now commonplace (Figure 1-2 (a)). Moreover, the production of nanoparticles is projected to increase from the estimated 2,300 tons produced today to 58,000 tons by 2020 [5]. Thus, it is of great importance to assess the potential risks and benefits of nanotechnology, which is the overall goal of this particular dissertation.

Total Products Listed

y = 243.29x - 164
R² = 0.9963

54, 256, 580, 803, 1015, 1317

Major Materials

Mar 8, 2006
Mar 10, 2011

Silver 313, Carbon 91, Titanium 59, Silicon/Silica 43, Zinc 31, Gold 28
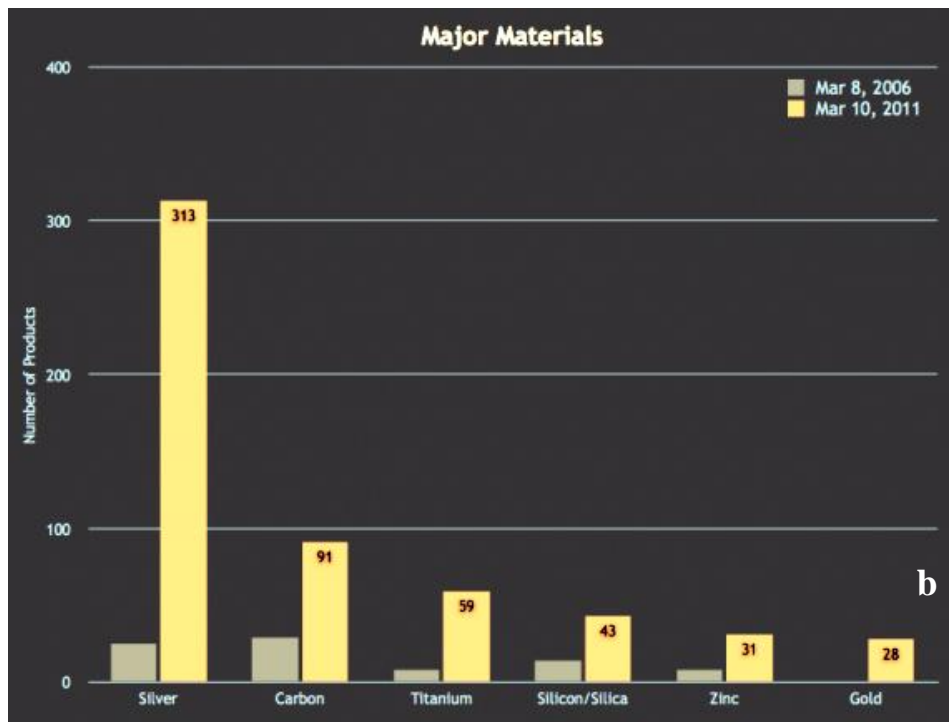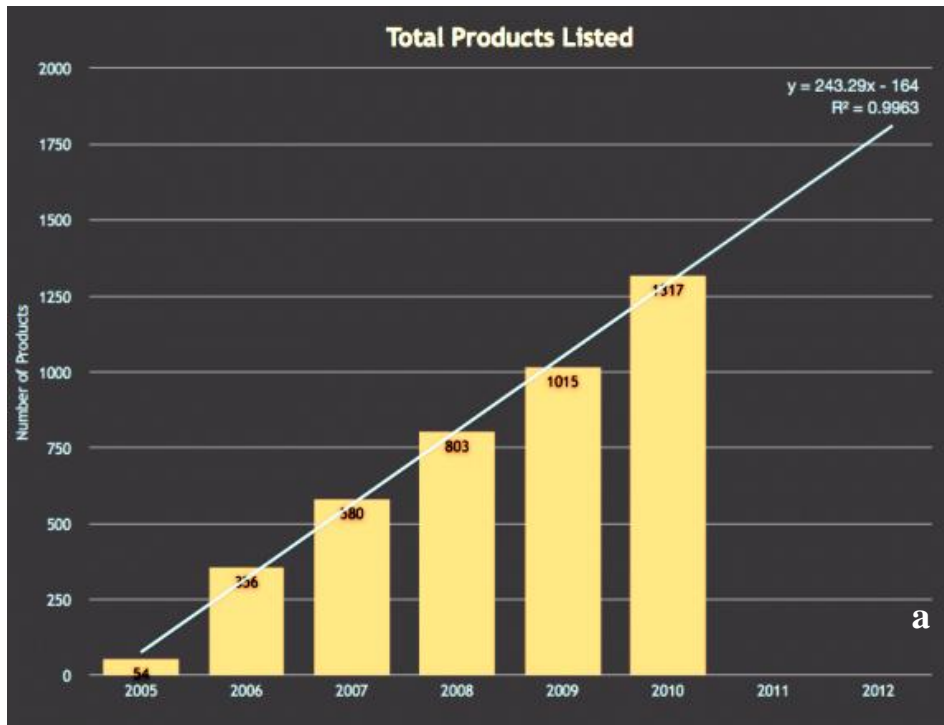
Figure 1-2. The number of products (a) listed by date of inventory update, with regression analysis; (b) associated with a specific material [4].

Nanoparticles may include liposomes, emulsions, polymers, ceramic nanoparticles, metallic nanoparticles, gold shell nanopaticles, quantum dots, carbon nanomaterials, and others [1]. It is known [1, 4] that carbon-based nanomaterials are the most established and most widely used type of nanomaterials. The rapid production and the great economical potential of carbon-based nanomaterials warrant the necessity and importance of examining these nanoparticles with respect to their health, environmental, and biological effects and implications. Naturally, understanding the biological and ecological responses to carbon nanomaterials has become the focus of this PhD research.

1.2 Carbon-based nanomaterials

The first engineered carbon nanomaterial, fullerene C_{60}, was discovered by Kroto in 1985. the schematic structure of which is illustrated in Figure 1-3 [6]. It is a polygon with 60 carbon atoms which form 12 pentagons (5-member ring) and 20 hexagons (6-member ring). The aromatic properties of the molecule give rise to the π electrons present on both the inner and outer surfaces of the molecule [6].

| Nanodiamond | Fullerene C60 | Fullerene C540 | Carbon Onion | SWNT | MWNT | Graphene |

sp^3 $sp^2 + \pi$
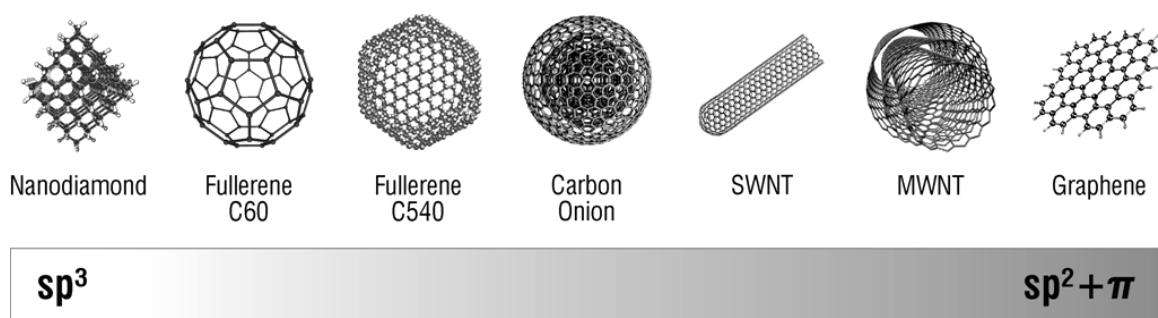
Figure 1-3. Hybridization states of carbon allotropes [7].

The physical, chemical and electronic properties of carbon nanomaterials are directly related to the carbon hybridization state. The orbital configurations of six carbon electrons assume $1s^2$, $2s^2$, and $2p^2$. Depending upon the neighboring carbon atoms, it can hybridize into sp, sp^2 and sp^3 configurations due to the small energy gap between the 2s and 2p electron shells. The various hybridizations of carbon lead to the different bulk organizations of each carbon (Figure 1-3). For example, planar graphite carbon atoms assume the form of sp^2 hybridization, with the carbon bonds bent to form a closed sphere or tube. This step is associated with the change of sp^2-hybridized carbon bonds into sp^3-hybridized bonds, resulting in a decrease in the bond angles from 120º to 109.5º accordingly. Therefore, the carbon molecule becomes more stable, due to the decrease in bond angle, which would bend less when closed into the sphere or tube structure.

Structures with a smaller number of hexagons exhibit a greater sp^3 bonding character, higher strain energies, and more reactive carbon sites [7]. Therefore, the thermodynamically favorable configuration of carbon is the sp^3 diamond configuration.

Although C_{60} is a tiny particle consisting of a cage of 60 carbon atoms with a van der Waals diameter of 1 nm [6], fullerene molecules in practice crystallize into larger structures. Due to their hydrophobicity, C_{60} is not soluble in polar solvents, but becomes soluble in selected organic solvents [7]. In order to enhance dispersion, and thus minimize the degree of aggregation, surface modifications are commonly used to enable dispersion of the nanoparticles in aqueous solutions. Water-soluble fullerene derivatives can be obtained by attaching various functional groups ($-OH$, $-COOH$, $-NH_2$, etc.), and amphiphilic amoities can be easily adsorbed onto the fullerene cage. Fullerenes can also

be solubilized by the adsorption of biomolecules, forming molecular self-assembly through noncovalent van der Waals, electrostatic, and hydrophobic interactions [7]. Moreover, if sonicated for an extended time in water, fullerene can yield a water suspension of fullerenes - nC_{60}.

Since the discovery of fullerenes, many more types of carbon nanomaterials have been synthesized for use in commercially available products. These nanoparticles include fullerene [6, 8], carbon nanorods [9], nanofoams [10], carbon dots [11], nanohorns [12], nano-onions [13], and nanodiamonds [14]. Fullerenes - C_{60}, single-walled carbon nanotubes (SWNTs) and multi-walled carbon nanotubes (MWNTs) are the most widely used types of carbon nanomaterials [15]. Therefore, the literature review in this analysis of the biological and ecological responses to carbon nanomaterials will be focused on these three types of nanomaterials.

1.3 Biological applications of carbon nanomaterials

Currently, nanotechnology plays a central role in human existence (Figure 1-1). Regarding nanomaterials, considerable efforts have been devoted to their use in biological applications as well as for improving human health. Examples of such applications include the design of tissue-implantable or subcellular sensors [16, 17], drug delivery systems, including the gene delivery [18-20], deoxyribonucleic acid (DNA) and ribonucleic acid (RNA), oligopeptides [21, 22], lipids and antibiotics [23], and disease diagnosis and therapy [24-26]. Carbon nanotubes can be modified by biomolecules

through covalent binding, non-covalent binding, and through a hybrid approach, in which a small molecule 'anchor' is adsorbed on carbon surface, followed by a chemical reaction between the anchor and a biomolecule of interest (Figure 1-4) [27]. Indeed, because carbon nanotubes can be taken up by a variety of mammalian and plant cells, they can be utilized for the delivery of drug and prodrug molecules to living systems.
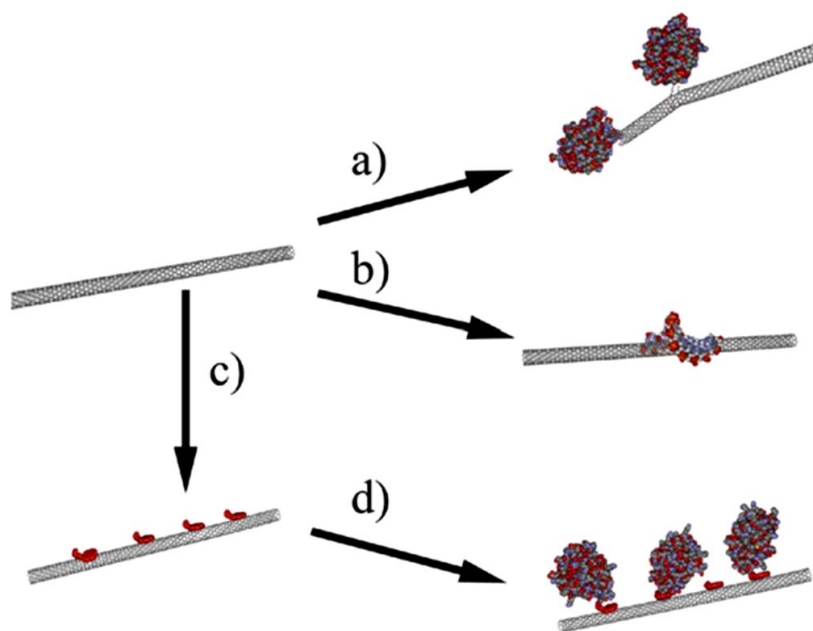
Figure 1-4. Three major approaches to modify carbon nanotubes with biomolecules [27].

Regarding the process of gene delivery, Pantarotto et al. [21] reported the first attempt of utilizing carbon nanotubes for engineering a novel gene delivery system. In their scheme, supramolecular complexes of ammonium-functionalized MWNT and plasmid DNA, formed through electrostatic interaction, were taken by HeLa cells and delivered into cell nuclei with low toxicity (Figure 1-5). This novel research was but a prelude of that which was to follow. Recently, Al-Jamal et al. [18] improved the delivery

of double-stranded siRNA and gene silencing in vitro by using newly synthesized series of polycationic dendron-MWNT constructs; each of a precisely tailored number of amino functions (dendron generations). Here, minimal toxicity was reported during MWNT-siRNA transporting into the cells under study.
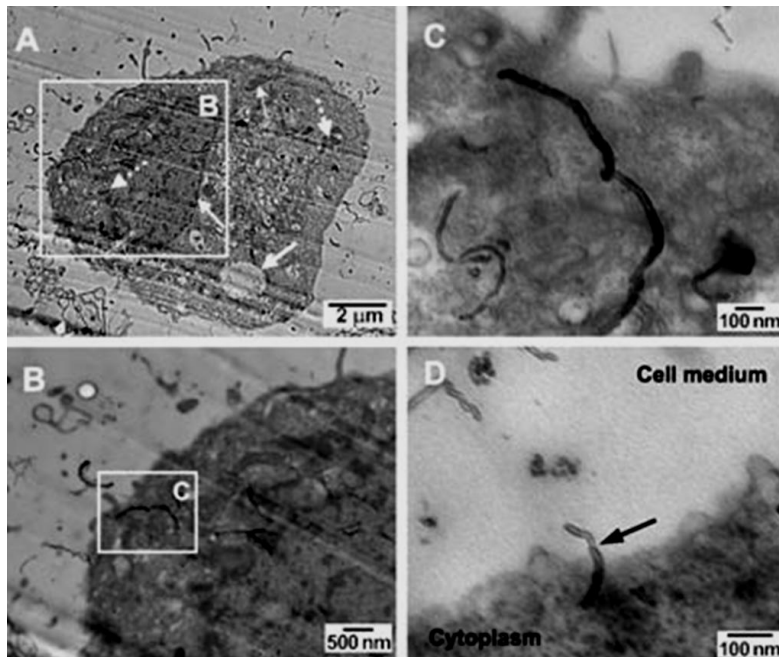
Figure 1-5. TEM images of ultrathin section of HeLa cells treated with ammonium functionalized-MWNTs [21]: (a) the entire cell, (b) and (c) two subsequent magnifications, and (d) MWNT crossing the cell membrane.

The ability of SWNTs to deliver oligonucleotides for the first time was reported by Pantarotto et al. [28] (Figure 1-6). In this study, SWNTs – oligonucleotides complexes were shown to penetrate both cellular and nuclear membranes without inducing toxicity for concentrations of less than 10 µM. This uptake was achieved by both passive diffusion as well as the endocytotic pathway. In addition, the researchers in this study

demonstrated the potential application of SWNTs in vaccine delivery; specifically, peptides from virus were employed and their integrity and recognizition were confirmed by monoclonal and polyclonal antibodies [22].
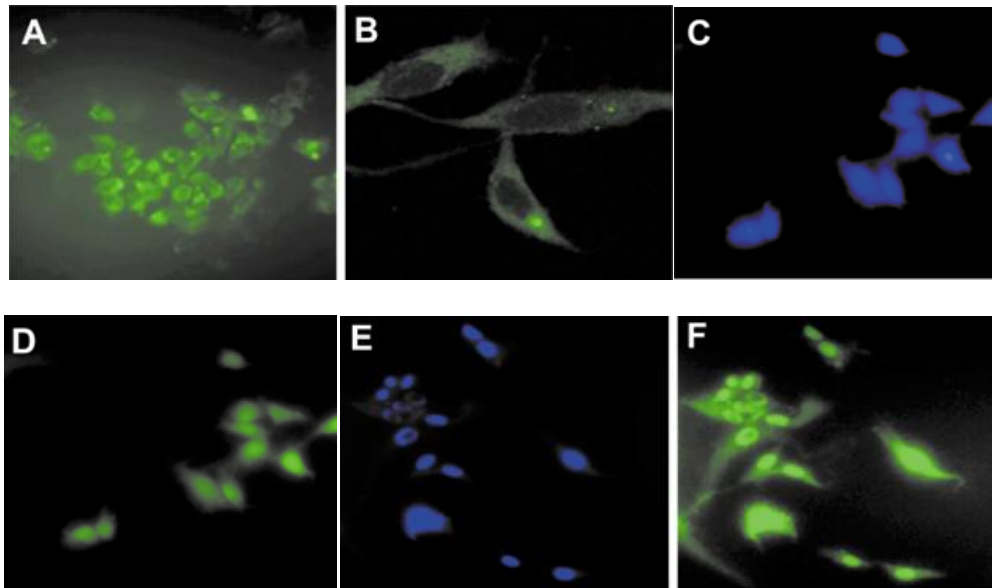
Figure 1-6. The delivery of oligonucleotides by SWNTs into mouse fibroblasts: Epifluorescence (a) and confocal microscopy (b) images of 3T3 cells incubated at 37°C with 1 and 5 mM concentration of SWNT, respectively; Epifluorescence microscopy images (c, d, e and f) of fibroblasts incubated at 37 °C with 1 and 5 mM concentration of SWNT. The nucleus was stained with 4',6-diamidino-2-phenylindole (blue) and SWNT was stained with FITC dye (green) [28].

Regarding the delivery of DNA, Kam et al. [29] demonstrated the transport, release, and nuclear penetration of DNA oligonucleotides carried by SWNTs in mammalian cells. The biological significance of this study was the attachment of DNA to phospholipid functionalized SWNT via a cleavable disulfide linkage (Figure 1-7). It was

shown that SWNT transported various types of biomolecules inside the cells through endocytosis.
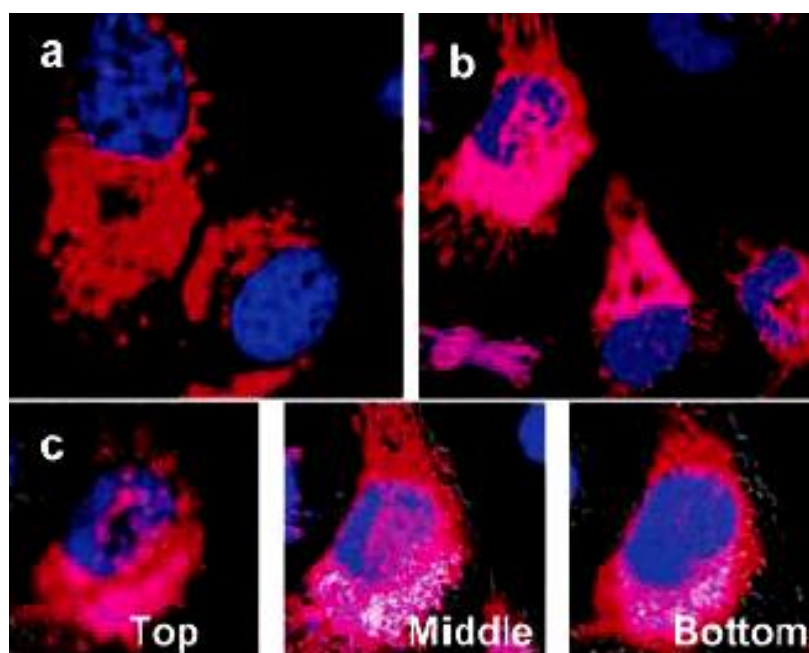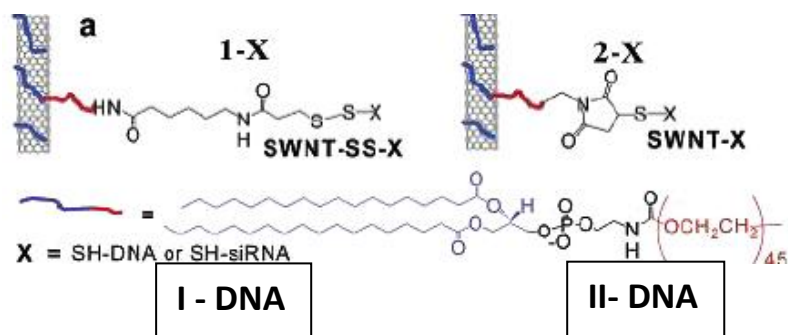
Figure 1-7. Confocal fluorescence images of HeLa cells, incubated with functionalized SWNTs (a) II-DNA and (b) I-DNA (c) Three confocal images recorded with different focal planes (top, middle, and bottom of cells) along the viewing direction for a cell shown in (b) [29].

Herein, wrapped inside endosomes, DNA-SWNT complexes were then delivered into lysosomes, in which their disulfide linkage bond was cleaved by thiol reducing enzymes aided by the acidic pH in the lysosomes. The biomolecules, which were finally released from SWNT, eventually reached the cytosol.

Two complexes were used to prove this hypothesis: I-DNA, in which DNA is attached to phospholipid functionalized SWNT through a disulfide bond; and II-DNA, with no disulfide linkage. Figure 1-7 illustrates the direct evidence of such molecular behavior: short oligonucleotides, while released from SWNT, are readily internalized into the cell nuclear (the fluorescence of DNA (pink) can be seen inside the nuclei), where nonreleased DNA do not penetrate through the cell nucleus).

Correspondingly, Pantarotto et al. [21] demonstrated that, by covalently attaching pyrrolidine rings, each bearing a free amno-terminal oligoethylene glycol moiety attached to the nitrogen to SWNT and MWNT, negatively charged phosphate groups of plasmid DNA were bound to positively charged ammonium functionalized nanotubes, thus enabling the delivery of DNA into HeLa cells without cytotoxicity.

Though the delivery of RNA using carbon nanotubes as transporters has already been reported by different groups, ours [30] was the first to report the delivery of RNA using SWNT. In our study, RNA polymer polyadenylic-uridylic acid (poly(rU)) was bound through nitrogenous bases to the hydrophobic surface of SWNR through hydrophobic interaction and pi-stacking. The transport of RNA through the cellular membrane and nuclear membrane was monitored by confocal microscopy (Figure 1-8).
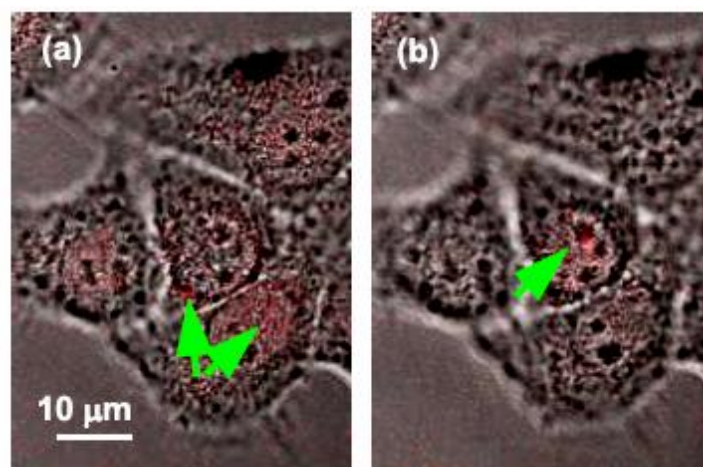
Figure 1-8. Confocal fluorescence images of human breast adenocarcinoma cells (MCF7) incubated with propidium iodide (PI)-labelled SWNT–poly(rU) for 3 h [30]. The arrows point to large fluorescent SWNT–poly(rU) hybrids (a) on the cell membrane, in the cell cytoplasm and (b) in the cell nucleus. The concentration of PI-labelled SWNT-poly(rU) was 0.05 ml/mL.

In addition to RNA delivery, we also demonstrated the ability of SWNT to deliver phospholipids into cancer cells [31]. Here, the phosphlipid loads were labeled with Rhodamine (Rd) through hydrophobic interaction (Figure 1-9). Our group [32] has also developed what is known as the assembly mechanism: single-tailed phospholipids that assemble into a highly organized striation on SWNT, offering biocompatibility and high solubility to SWNTs in aqueous solutions. Here, we used fluorescence resonance energy transfer (FRET) to monitor the behavior and translocation of labeled lipids across the cell membrane. The absorption spectrum of the acceptor–SWNT overlapped with the

13

fluorescence emission spectrum of the donor–Rd dye, thus enabling the energy transfer between the Rd-phospholipid complex and the SWNT. After incubation with cells, the fluorescent signal of this complex was observed within the cell (Figure 1-9), signifying the release of phospholipids from SWNTs due to the relatively weak binding strength between the two species.
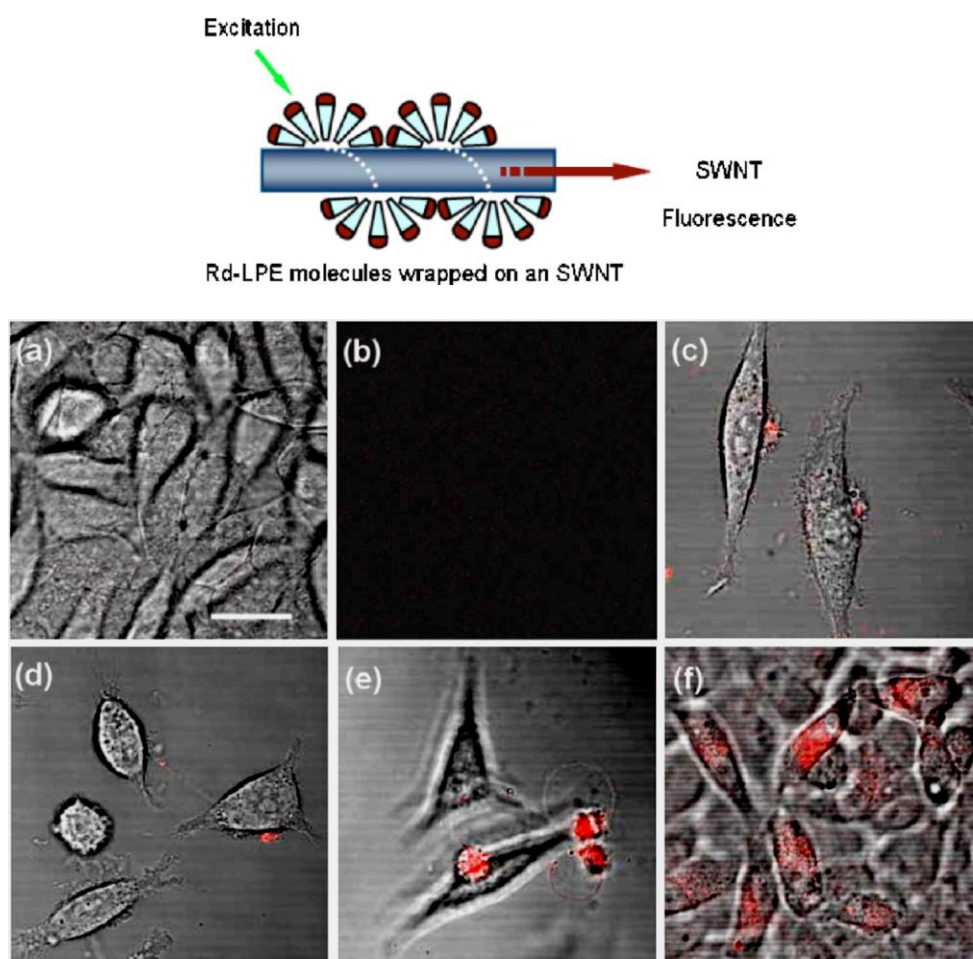
Figure 1-9. Uptake of SWNT coated with Rd-labeled phospholipids by MCF7. Top: Illustration of an SWNT coating with Rd-labeled phospholipids [32]; Bottom: Confocal images of MCF7 incubated with SWNT [31]. (a) Control MCF7 cells, (b) SWNT, (c-f) increased translocation of Rd-labeled phosholipids across MCF7 cells with incubation

times of 0.5, 1, 2, and 3 h. The red spots in the images suggest the dissociation of Rd-labeled phospholipids from SWNTs. Scale bar: 10 μm.

Regarding protein delivery, Kam et al. reported the transport of three proteins (i.e. bovine serum albumin, cytochrome C, and human immunoglobulin) that were noncovalently bound to SWNT into cells through endocytosis. Once released from the endosomes, the protein-SWNT complexes entered the cytoplasm of the cells and performed biological functions, as evidenced by the apoptosis induction by the transported cytochrome c [33].
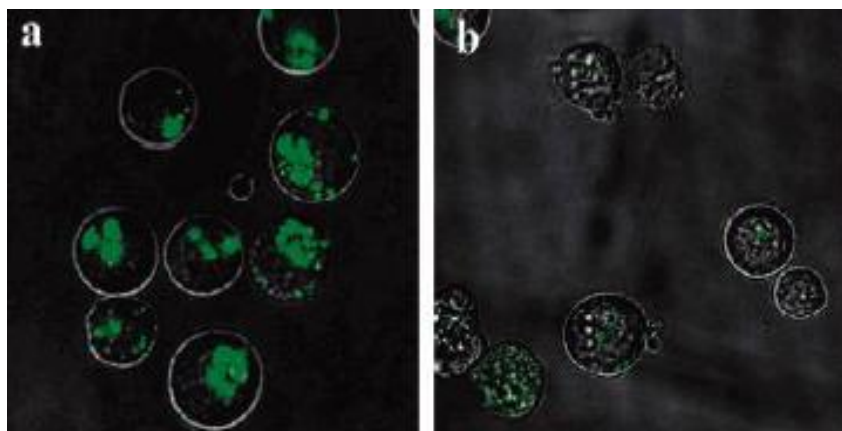
Figure 1-10. Endocytotic pathway of protein–SWNTs [33]. Confocal images of human promyelocytic leukemia cells after incubation in cytochrome c-SWNTs for 2 h. at (a) 37 °C and (b) 4 °C.

The inherent electronic, thermal and optical properties of carbon nanotubes make them uniquely applicable for use in both disease and diagnostic therapies. Specifically these properties, in combination with transporter capability, make SWNTs most useful in

the development of novel cancer therapies. Cancer cells, that grow and divide at a rapid, uncontrolled, and infinitely exponential rate, have different structures, energy usage, and functions compared to their normal cell counterparts. One of the distinctive traits of cancer cells is the quantity of folate receptor tumor markers on their cell membranes. Using folate moiety functionalized SWNTs, Kam et al. [34] reported a selective delivery of functionalized SWNTs into cancer cells. When exposed to near-infrared light, which is useful in enhancing the transparency of biological objects, SWNT was observed to produce excessive local heat *in vitro*, killing cancer cells without harming normal cells.
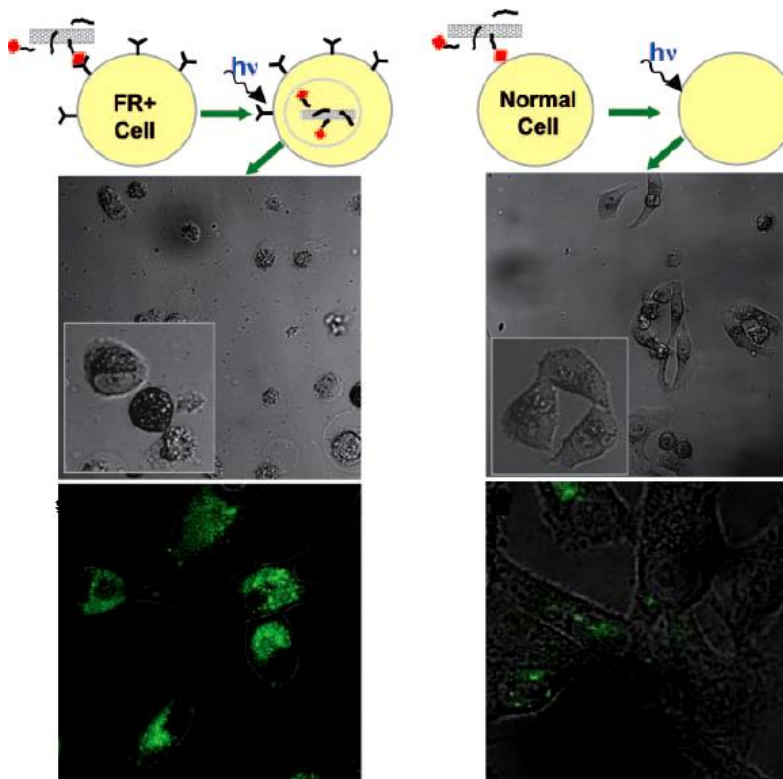
Figure 1-11. Selective targeting and killing of cancer cells [34]: Left, cancer cells; Right, normal cells. Bright field microscopy images (upper), fluorescence microscopy images (lower) SWNTs were labeled with green FITC dye.

16

Similarly, Chen at al. developed a novel SWNT - based tumor-targeted drug delivery system, which consisted of a both functionalized SWNT linked to tumor-targeting modules and prodrug modules. Figure 1-12 illustrates the three key steps involved in their proposed nanotube-based drug delivery system. First, the biotin-SWNT-linker-taxoid conjugate was internalized into tumor cells through receptor mediated endocytosis. The choice of biotin as a tumor-targeting module was determined by the earlier finding of Russel-Jones [35, 36]. Biotin moieties, covalently attached to SWNT, could recognize biotin receptors, which were overexpressed on the tumor surfaces. Secondly, the released drug migrated through the cleavage of the disulfide bond in the linker moiety, connecting the taxoid to the SWNT. Finally, the released taxoid bound to tubulins/microtubules and inhibited cell mitosis by stabilizing the microtubules, which then triggered the apoptosis signaling pathway.
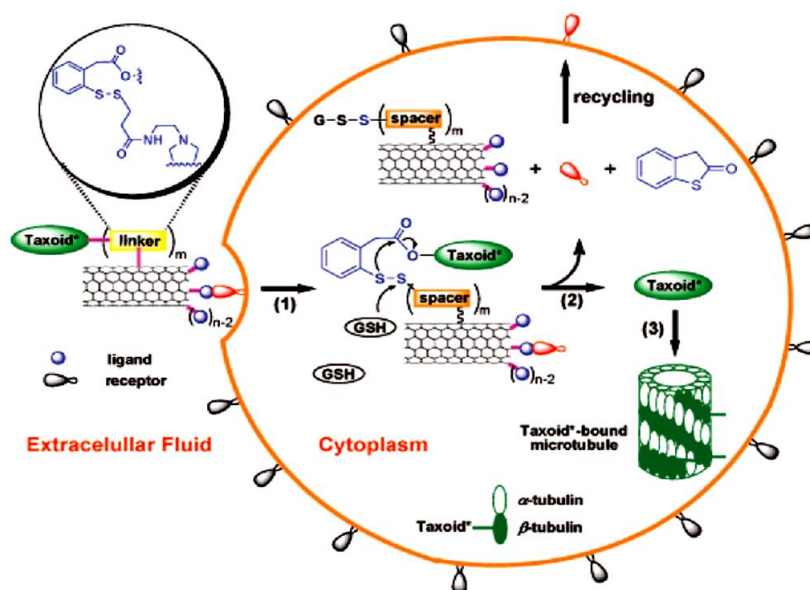
Figure 1-12. Schematic illustration of an SWNT-based tumor-targeted drug delivery system [25].

In one of the latest disease-prevention measures, a dime-sized carbon nanotube forest was created to trap cancer cells when blood passed through [26]. Dr. Mehmet Toner, a professor of biomedical engineering at the Harvard and Massachusetts Institute of Technology Division of Health Sciences and Technology improved the device by using carbon nanotubes instead of silicon. In this seminal work, antibodies were attached to carbon nanotubes, which would trap cancer cells upon passing. This same mechanism is projected for use in human immunodeficiency virus (HIV) detection.

Similarly, Raman scattering and infrared fluorescence signals of carbon nanotubes is useful in tracking nanotubes within biological samples, since SWNTs have distinguished peaks in the near-infrared region at 985, 1060, 1150 and 1280 nm, respectively. Thus, near-infrared fluorescence microscopy at wavelengths above 1100 nm provides high contrast images, indicating the locations of SWNTs within the cell.

Based upon these principles described above, Heller et al. [16] proposed the use of SWNT as a long term optical sensor in live cells. In this study, DNA-SWNTs exhibited resistance to photobleaching and remained functional in live cells for three months, thus enabling long-term live cell imaging. The Raman scattering and fluorescence spectra of DNA-SWNTs were measured from within live as well as hematoxylin- and eosin-stained cells; upon uptake no changes occurred to the emission spectra of the nanotubes. The nanotubes, which were observed to remain within cells even after multiple cell divisions, were incorporated into the cytoplasmic vesicles and did not enter the nuclear envelope. Transmission electron microscopy (TEM) images and

light-microscopy images confirmed the uptake of these nanotube complexes by endocytosis and their perinuclear endosomal localization within the cells.
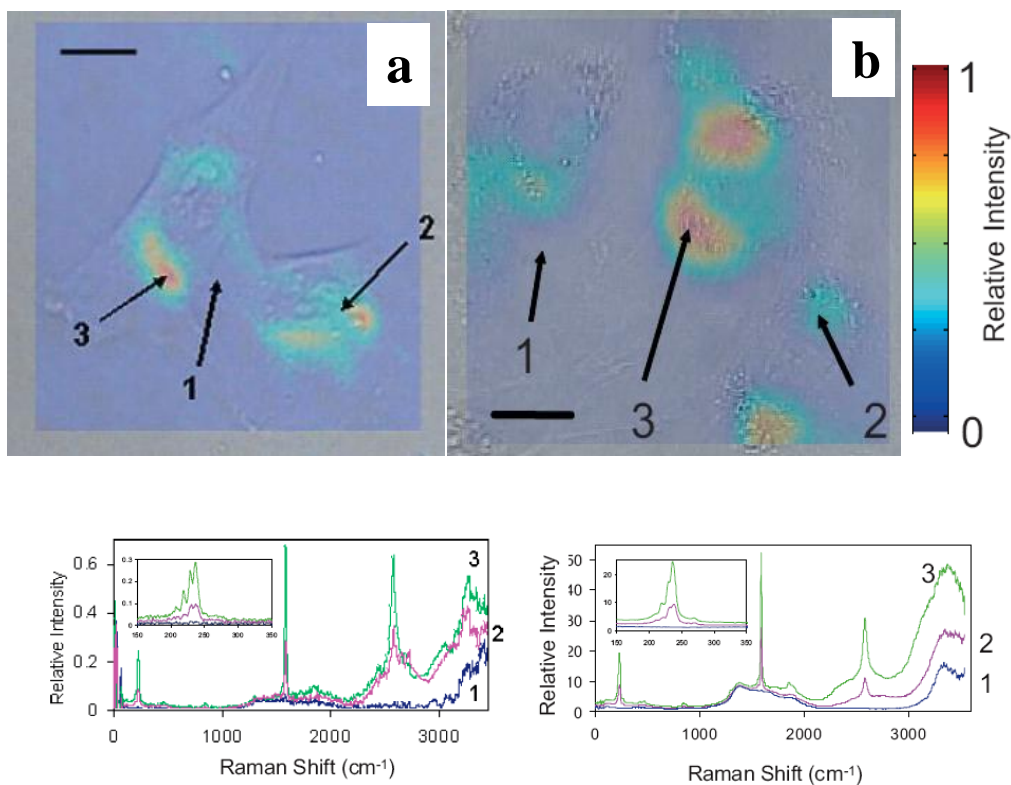
Figure 1-13. Raman intensity area maps of live fibroblast and myoblast stem cells and corresponding spectra [16]: (a) Top: area map of Raman radial breathing modes intensity of SWNTs in live fibroblasts cells after 48 h. in culture overlaid onto an optical micrograph of the same region; Bottom: combined Raman and fluorescence spectra of live murine mouse embryonic fibroblast cells incubated with DNA-suspended SWNTs. The three spectra correspond to locations on the area map: (b) Top: area map of RBM intensity of mouse embryonic fibroblast cells in culture for 8 days; Bottom: Raman and fluorescence spectra of nanotubes in live mouse embryonic fibroblast cells after 8 days. The scale bars represent 20 μm. Color legend is valid for all images.

Using a similar approach, Cherukuri et al. [37] and Jin et al. [38] have studied the uptake of SWNTs into macrophage-like systems for both the endocytosis and exocytosis of SWNTs in human embryonic stem cells and mouse embryonic fibroblast cells, respectively.

<u>1.4 Biological responses to carbon nanomaterials</u>

The understanding that nanotechnology can provide many benefits to society, including economic gains, has prompted a rapid growth in the production of an array of nanomaterials. Fullerenes and their derivatives are the most studied class of nanoparticles within the context of biological systems [39]. Although many research groups have reported various biological responses of fullerenes and their derivatives *in vivo* and *in vitro*, the knowledge on the health effects of fullerene nanoparticles remains limited. According to Johnston et al. [40] the physicochemical properties of nanomaterials should be considered with a high priority in toxicological assessments, as outlined in Figure 1-14. For example, the behaviors of nanoparticles in biological systems depend upon the shape, size, surface charge, and chemical composition of the nanoparticles [40, 41]. The National Institute for Environmental and Health Sciences has reported that, "generally, the smaller the nanoparticles, the more reactive and toxic are these new nanomaterials" [42]. Indeed, smaller nanoparticles possess greater surface areas and surface functional groups per unit mass [43], which may induce a greater impact on biological activities

than larger sized particles [44, 45]. The author's purpose in this section is therefore to examine the literature on the biological responses to carbon nanoparticles.
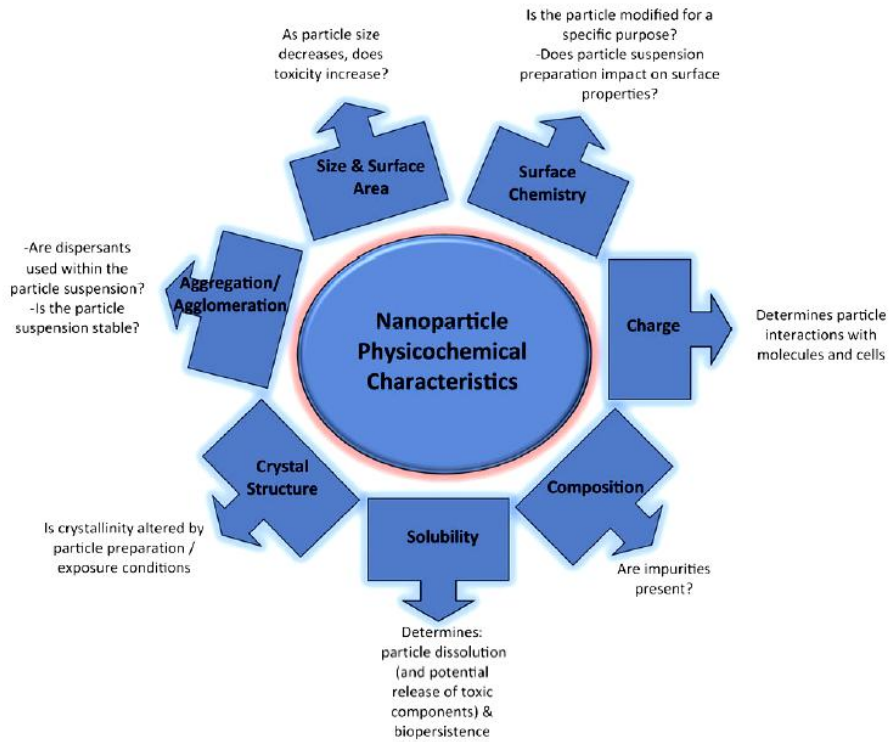
Figure 1-14. Physicochemical characterization of nanomaterials [40].

1.4.1 Whole organism response

As human exposure to nanoparticles is a legitimate concern due to their large-scale production and ever increasing varieties [42], much work and time is required to generate a comprehensive database for risk assessment. Human exposure to nanomaterials can occur via oral, dermal, pulmonary and injection routes; the first three can occur accidentally, whereas the last path assumes their injection in the body for

further diagnostic evaluation. Naturally, rats and mice are used to elucidate their responses to carbon nanoparticles *in vivo*.

According to Brown et al. humans have been exposed to large numbers of ambient nanoparticles through environmental air pollution [46]. In addition, fullerenes can occur naturally, such as those released from combustion processes of forest fires [47]. As such, the combustion-derived nanoparticles have become the focus of many researchers as a likely source of health hazards [48]. However, many studies have demonstrated that C_{60} induced no acute toxicity or minimal toxicity in rats [49-51] when inhaled. For instance, research by Baker et al., in which [49] rats were exposed to 55 nm and 0.93 μm forms of C_{60} via nasal inhalation, did not elicit any inflammation or toxicity for C_{60}, for both nano- and microparticles. Similarly, Fujita et al. [50] showed that C_{60} induced no significant inflammation or tissue injury over one month period of inhalation exposure.

While small differences were found in highly up-regulated genes associated with the inflammatory response, oxidative stress, apoptosis, and metalloendopeptidase activity one month post- nanoparticle exposure, no severe pulmonary toxicity was measured under the experimental conditions. According to Sayes et al. [51], when compared to controls, exposures to both fullerene derivatives, such as nano-C_{60} or water-soluble $C_{60}(OH)_{24}$ (fullerols), produced little or no difference in the lungs. It should be noted that although the researchers observed minor transient inflammatory and cell injury on the first day after exposure to the fullerene derivative, no such effects were observed with longer exposures. Interestingly, these results were inconsistent with their previous *in vitro*

22

studies, in which exposures to nano-C_{60} water suspensions induced significant cytotoxic effects on three different human cell lines [52, 53].

Donaldson et al. demonstrated the ability of carbon nanotubes to induce proinflamatory effects in the lungs of rats [43]. Though water soluble fullerene derivatives were reported to have an anti-inflammatory effect at lower doses [54], at higher concentrations, the pro-inflammatory effect was shown *in vivo* [54, 55]. A similar phenomenon is known for other antioxidants, such as vitamin E and carotenoids [56]. According to [54] mice treatment with fullerols led to attenuation of the inflammatory response to quartz, an effect due to reduction of reactive oxygen species (ROS) mediated inflammation by the fullerols. Specifically, chemically-reactive ROS exhibit highly reactive responses due to the presence of unpaired valence shell electrons molecules. Consequently, in response to different types of stress (e.g. ultraviolet heat, exposure) a rapid increase of ROS is the result [57]. The authors [54] specified that such a protective behavior of fullerols could be seen only at low concentrations, whereas at high concentrations, fullerols exhibited a pro-inflammatory response instead.

Resorting to a large existing database of particles which induced lung toxicity [58], Donaldson et al. determined that the same material in the nano size form is more toxic than in the form of larger, still respirable particles. Hazard studies in rats indicating that inhaled carbon nanoparticles could induce significant lung toxicity in rats support this position, which is inversely proportional to the size of nanoparticles; smaller nanoparticles produce greater toxicity in rats compared to large particles [59]. These results closely agree with the studies by Brown et al. [60], Stoeger et al. [61] and Duffin

23

et al. [45]. In short, the findings from these studies demonstrated that fullerene and their derivatives could be either inflammatory toxic or not at all toxic depending upon the method of exposure method and the doses applied. Further studies are necessary for evaluating the toxicity of nanoparticles *in vivo*.

The drug delivery potential of carbon nanoparticles often leads to their injection into the body. According to Chen et al., water soluble C_{60}, when injected either intraperitoneally or intravenously, showed acute toxicity in rats [55]. Fullerenes induced a distinct lysosome-overload nephrosis, also known as a phagolysosomal nephropathy. A preliminary study of microsomal enzyme activity analysis exposed a suppression effect of liver cytochrome P-450–dependent monooxygenase activities, including cytochrome P-450, cytochrome b5, and benzopyrene hydroxylase, but an increased level of kidney cytochrome P-450–dependent monooxygenase activities, including nicotinamide adenine dinucleotide phosphate cytochrome P-450 reductase. Chen et al. [62] and Erlanger et al. [63] showed the ability of fullerene derivatives to act as a sensitizing agent and their potential use for modulating subsequent immune responses. Overall, limited studies have been conducted which involved the injection of fullerenes *in vivo*, in which most of the researchers claimed that the kidney, liver and spleen were the targets for the fullerenes [64].

Gharbi et al. [64] showed that aqueous C_{60} suspensions prepared without using any polar organic solvent not only had no acute or subacute toxicity in rodents but also protected their livers in a dose-dependent manner against free-radical damage. Figure 1-15 represents the liver colors of the individual rats depending upon the amount of C_{60}

injected, and the processing times. After injection with large amounts of C_{60} (2 g/kg of body weight), most of the livers of treated rats were a dark brown color after 7 days of exposure and a pale brown color after 14 days of exposure. Between the 14 days to 21 f exposure range, all of the animals exhibited livers with a normal color, indicating that fullerene can be eliminated and/or transformed by the rat livers.

Further microscopic examinations of the liver sections of rats treated with C_{60} showed a normal parenchymal architecture without either inflammation or fibrosis (Figure 1-15 (E)). The authors chose carbon tetrachloride CCl_4, a well-known *in vivo* free radical initiator, to be oxidative stress-related product. As is evident, though treated cells with CCl_4 were either mostly dead or damaged (Figure 1-15 (G)), once treated with C_{60}, the recovery of the cells was observed.
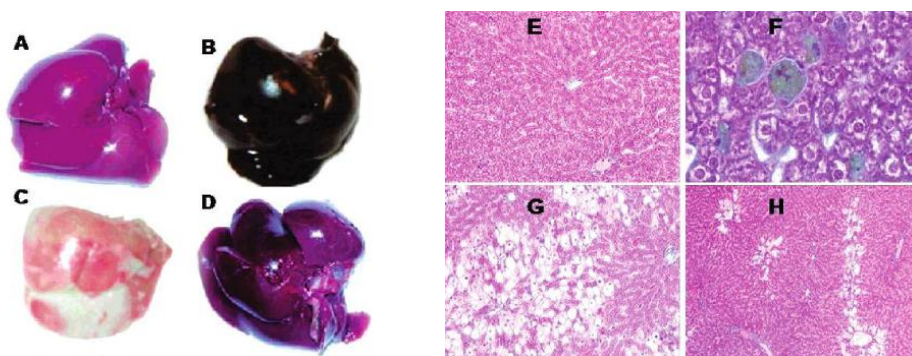
Figure 1-15. Macroscopic and microscopic effects of fullerene on rat livers [64]: (A) control liver; (B) liver after 7 days of pretreatment with C_{60} (2.0 g/kg of body weight); (C) liver of a rat intoxicated with CCl_4 (1 mL/kg of body weight); (D) liver after 14 days of pretreatment with C_{60} before CCl_4-treatment. Plates E-F were imaged at magnification

levels of 100x from: (E) C_{60} treated rat; (F) magnification of E; (G) CCl_4 treated rat; (H) an example of fullerene pretreated rat before CCl_4 treatment showing a few necrotic areas limited to some cords of hepatocytes.

Magnification of the liver tissues, treated with fullerene, showed an abundance of C_{60}-containing macrophages and a slight hypertrophy without strong macrophagic activity. All macrophages had a mottled ochre color with black spots and were localized mostly in the periportal areas (Figure 1-15(F)). Similarly, using doxorubicin-induced cardio- and hepatotoxicity in rats with colorectal cancer model Injac et al. [65] demonstrated that the protective effect of $C_{60}(OH)_{20}$ against doxorubicin toxicity was better than that exhibited by powerful antioxidant, vitamin C.

Regarding the dermal exposure to carbon nanomaterials, most of the studies were performed with dermal cell lines [66, 67], with the effects of fullerols on the dermal present in only a single *in vivo* study [68]. To assess whether fullerene could induce any significant skin hazards, two methods were chosen: thirty volunteers were subjected to a patch test (filter paper Whatman 3 saturated with water suspension of fullerene soot) and controlled during 96 h with four albino rabbits eyes instilled with water suspension of fullerene soot. Both of the studies showed that it is unlikely that working with fullerene soot is associated with any risk of skin irritation and allergy.

The industrial scale production of fullerenes and their derivatives should eventually lead to their entrance into the environment, wherein the nanoparticles may interact with plants and aquatic systems and impact on the food chain. Using a major

food crop, rice plants, our group reported that once fullerenes and their derivatives were taken in by the plants, they could be transported to the second-generation plant through the progeny, thus remaining in the food crops [69]. This study emphasized the necessity of investigating the *in vivo* effect of fullerenes and their derivatives through oral exposure. Overall, there is a lack of literature regarding the oral administration of fullerenes. Though a majority of the studies available suggested that fullerenes and their derivatives would be eliminated within feces [70, 71], there exists a possibility that some of the nanoparticles would pass through the gut wall and thereby enter the circulatory system.

According to Chen et al., rats exposed to water soluble fullerenes via oral administration did not exhibit any toxicities [55]. Similarly, using a mixture of C_{60} and C_{70} Mori et al. reported no lethality or other signs of toxicity in terms of animal behavior or body weight [70]. Specifically, the administration of fullerenes at the dose of 2000 mg/kg did not induce abnormalities in the necropsy, thus confirming the nontoxic effect of fullerenes. Assessing the behaviors of fullerene and their derivatives is necessary for understanding both the biological responses to carbon nanoparticles and for identifying the potential mechanisms of fullerene toxicity. Further research in this area is essential to converge and rationalize the data available.

1.4.2 Cellular level response

Though *in vivo* studies of nanomaterials are essential, they are difficult to control and expensive to reproduce. In comparison, *in vitro* studies offer important clues on how nanomaterials may behave in biological systems, allowing researchers to better control experimental conditions and obtain reproducible data with less time and effort.

The first toxicity study of pristine C_{60} was conducted in 1993 by Nelson et al. [67], in which the authors used a C_{60}, solubilized in benzene, to determine its cytotoxicity. This study did not show any acute toxic effects on mouse skin cells. In subsequent work, Scrivens et al. [72] observed no acute toxicity of C_{60} in human keratinocytes with Zakharenko et al. [73] confirming these results via the somatic mosaicism model. In their early stages of cytotoxicity studies of pristine C_{60}, they observed no acute toxicity induced by C_{60} in human leucocytes [74], human phagocytes [74], human keratinocytes [72], and bovine alveolar macrophages [75].

Later studies revealed the toxicity of fullerenes and their derivatives in different cell lines. Sayes et al. [52] demonstrated the differential toxicity of water soluble fullerene derivatives in human dermal fibroblasts and human liver carcinoma cells (Figure1-16). Here, the different cytotoxicities of the nanoparticles were closely related to their surface derivatization; C_{60} was cytotoxic to both human cell lines at the 20 ppb level, while water-soluble fullerene species, such as C_3 (three carboxyl groups attached to one C_{60} molecule) and $Na^+{}_{2-3}[C_{60}O_{7-9}(OH)_{12-15}]^{(2-3)-}$, were much less cytotoxic, and

$C_{60}(OH)_{24}$ showed no cytotoxicity up to its limits of solubility. The cytotoxicity of the pristine C_{60} was attributed to its high electron affinity and ability to generate free radicals to oxidize lipid molecules, which would thusly disrupt the membrane [53, 76].
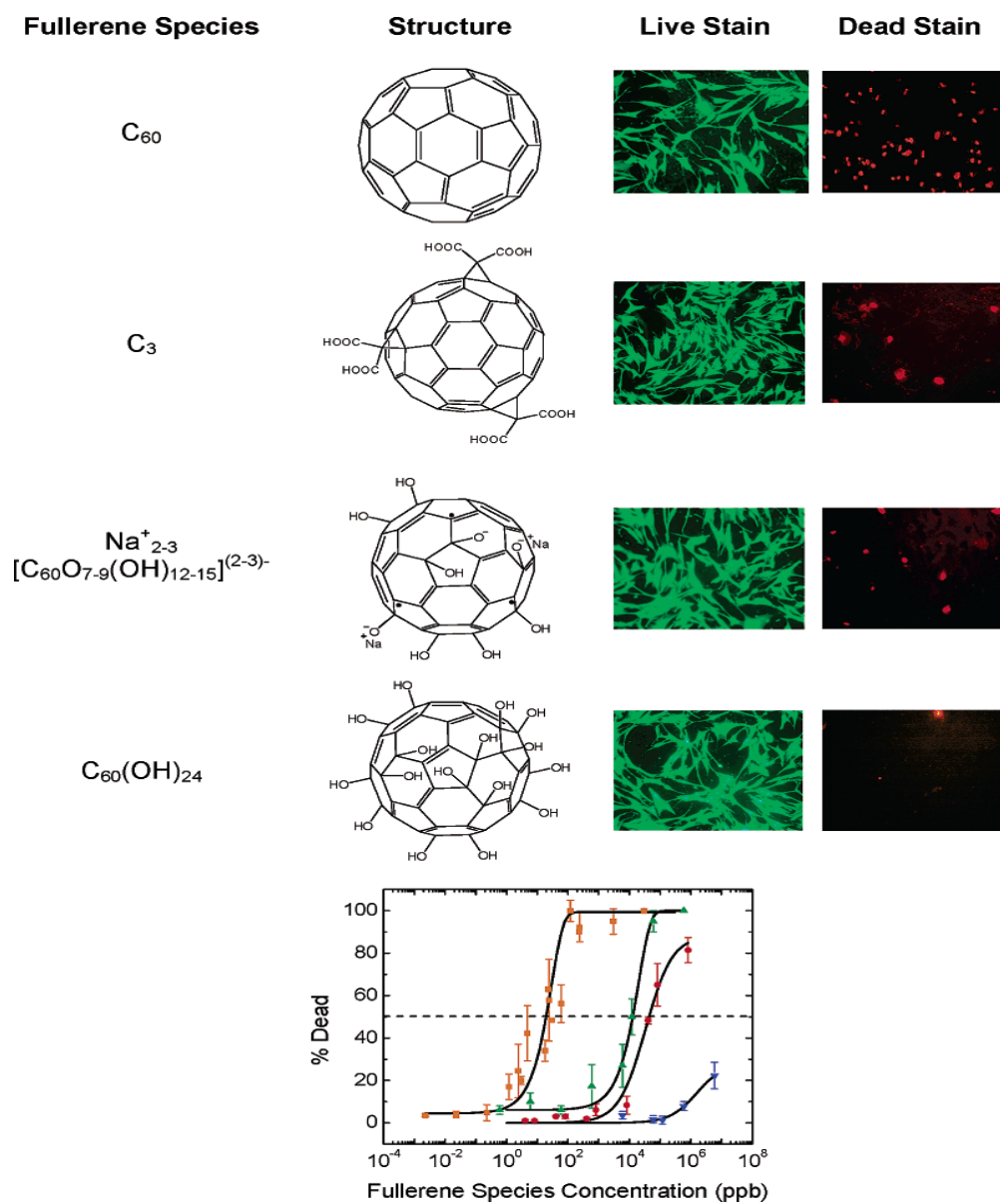
Figure 1-16. Different cytotoxicity based on different functionalization of C_{60} [52].

Sayes et al. using three different human cell lines showed that the cytotoxicity of C_{60} was mainly due to lipid peroxidation of the cell membrane. Interestingly, in one cell line - human dermal fibroblast cells, lipid peroxidation due to the presence of C_{60} was prevented by the addition of L-ascorbic acid, resulting in normal cell viability, compared to the control. Oberdoster [76] reported similar consistencies in lipid peroxidation in juvenile largemouth bass in response to C_{60}, and C_{60} transport along the central nervous system neurons, thusly confirming that a common method for evaluating the cytotoxicity of nanoparticles involves examining the intracellular ROS production. Since photosensitization occurs commonly in biological systems, Kamat et al. [77, 78] examined the ability of fullerene and its derivative to generate ROS in rat liver microsomes upon photo-excitation. They found that C_{60} generated predominantly $_1O^2$ to induce significant lipid peroxidation, while $C_{60}(OH)_{18}$ produced mainly radical species that caused significant lipid peroxidation and protein oxidation in membranes. However, endogenous natural antioxidants were observed to prevent such damage.

Isacovic et al. compared the capacity of C_{60} and its derivative for preferential induction of both apoptosis and necrosis. Apoptosis is a cell death type characterized by chromatin condensation, activation of caspases, and fragmentation of DNA without plasma membrane breakdown. Conversely, necrosis is typified by vacuolation of the cytoplasm, breakdown of the plasma membrane and release of cellular contents and pro-inflammatory molecules. In apoptosis, cells are removed by phagocytic cells in the absence of inflammation, and in the case of necrosis, the induction of inflammation around the dead cell is the result. The authors reported that $C_{60}(OH)_{20}$ exerted mainly

antioxidant/cytoprotective and only mild ROS-independent pro-apoptotic activity, clearly showing C_{60} to be endowed with strong pro-oxidant capacity responsible for the rapid necrotic cell death [79].

Some studies have reported that, in the case of fullerenes, the most significant factor which influences the cytototoxicity of nanoparticles is the cell type. For example, most of the studies on macrophages revealed minimal or no toxicity of fullerenes [52, 53, 80-82].
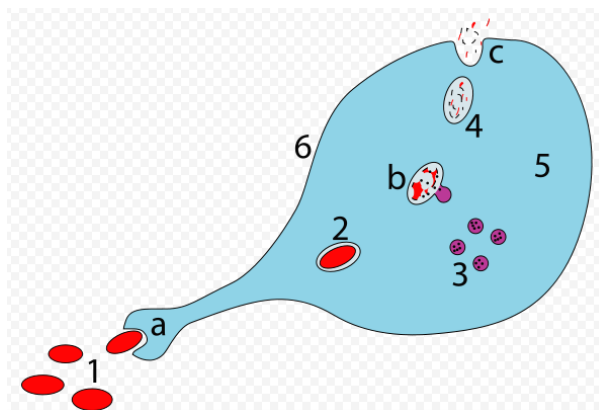
Figure 1-17. Steps of a macrophage ingesting a pathogen [83]. (a) Ingestion through phagocytosis forms a phagosome, (b) The fusion of lysosomes with the phagosome creates a phagolysosome; the pathogen is broken down by enzymes, (c) Waste material is expelled. Parts: (1) Pathogens, (2) Phagosome, (3) Lysosomes, (4) Waste material, (5) Cytoplasm, (6) Cell membrane.

The role of macrophages is to engulf and digest cellular pathogens, or in this instance, carbon nanoparticles. Jia et al. [82] investigated the phagocytic ability of alveolar macrophages to uptake 2 µm colloid gold latex beads in the presence of different

31

types of carbon nanomaterials: C_{60}, SWNTs and MWNTs (Figure 1-18). They observed

that SWNTs inhibited the ability of macrophages to engulf latex beads at very low doses

of 0.38 µg/cm^2, while C_{60} and MWNTs achieved this effect at 3.06 µg/cm^2 more

significantly than other nanomaterials. Moreover, at all doses SWNTs caused a larger

number of macrophages to be nonphagocytic compared to both MWNTs and C_{60}. The

researchers attributed this effect to the differences in geometric structures, number, and

surface area of the particles.
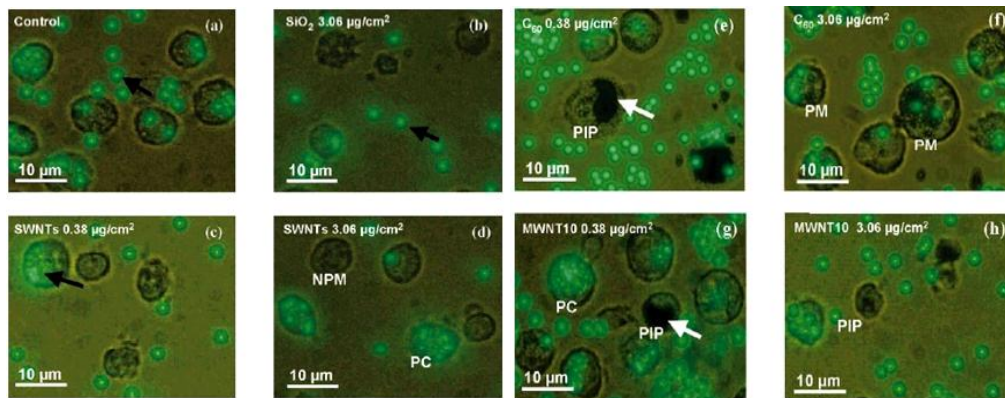
Figure 1-18. The overlay of bright field microscopy and fluorescence microscopy

pictures of alveolar macrophages exposed to MWNTs [82]. The white arrows indicate

carbon nanotubes and black arrows indicate latex beads. PC represents macrophages

phagocytose-only beads; PIP indicates inhibition of macrophages phagocytosis by

nanotubes, PM phagocytic macrophage, and NPM non phagocytic macrophage.

TEM images were provided to illustrate cell responses in the presence of different

nanomaterials. The condensed folds and the formation of plywood body with further

swelling of the endoplasmic reticulum, vacuolar changes and phagosomes were observed

in the cells, in which the concentration of SWNTs was increased from 0.76 $\mu g/cm^2$ to 3.06 $\mu g/cm^2$. In the case of MWNTs, at low concentrations only a large phagosome was observed, while at higher doses the nucleus experienced degeneration, enlargement, and a rarefaction of the nuclear matrix. Moreover, in the presence of both SWNT and MWNT, chromatin condensation at the nuclear envelope and some condensed organelles was observed.

Using human epidermal keranocytes, Rouse et al. [66] determined the threshold concentration of fullerene based amino nanoparticles to be 0.04 mg/mL. The smaller concentration of nanoparticles did not affect cell viability, whereas the higher concentration of nanoparticles at the range of 0.4 and 0.04 mg/mL induced cytotoxicity and initiated a proinflammatory response.

Despite a number of reports on the cytotoxicity and pro-oxidant behavior of fullerenes and their derivatives, some fullerene derivatives possess cytoprotective activities. For example, water soluble fullerene derivatives have been shown to exhibit antioxidant, antiviral and anticancerous effects on mammalian cells [79, 84-89].

Fullerene molecules exhibit high reactivity towards various organic radicals [90, 91]. Since investigations of the biological activity and potential uses of fullerenes have been hampered by the poor water solubility of C_{60} [90], many research groups have devoted their efforts to synthesize water soluble derivatives and examine their biomedical and therapeutic applications as either free radical scavengers or antioxidants in biological systems. The first water soluble fullerene derivative - polyhydroxylated C_{60} - was synthesized in 1993 and consisted of a C_{60} cage along with 18-OH moieties. Later,

33

fullerol was shown to be a potent free radical scavenger because the hydroxyl groups are susceptible to attacks by high reactive radicals [92].

The review by Dordevic et al. highlighted the antioxidant properties of $C_{60}(OH)_{24}$ in different *in vivo* and *in vitro* systems [93]. Specifically, $C_{60}(OH)_{24}$ reacted with superoxide anion radicals, hydroxyl radicals and nitrous oxide radicals in both chemical and biological systems did not inhibit human breast cancer cell growth at concentrations from 0.8 to 3.45 μM, but strongly modulated the cytotoxic effects of doxorubicin and cis-platinum after 24 and 48 hours of treatment. The radioprotective effects of fullerenol $C_{60}(OH)_{24}$ were also found to be of significance. In a study by Wang et al. [88], C_{60} and its three derivatives and vitamin E were examined for their antioxidant effects on prevention of lipid peroxidation by superoxide and hydroxyl radical. All samples, including polar soluble and water soluble fullerene derivatives, were able to prevent lipid peroxidation and breakdown of membrane integrity. Surprisingly, the liposoluble C_{60} demonstrated a stronger effect on the prevention of lipid peroxidation than did vitamin C.

Yin et al. [89] reported the ability of three water soluble fullerene derivatives in their protection against oxidant-induced cytotoxicity and mitochondrial damage *in vitro* (Figure 1-19), in agreement with our results presented in chapter IV. Here, they employed the electron spin resonance technique to provide direct evidence that water soluble fullerene derivative can scavenge different ROS. The inhibition of lipid peroxidation and the protection of cell against H_2O_2-induced cytotoxicity were observed in the presence of the fullerene derivative.
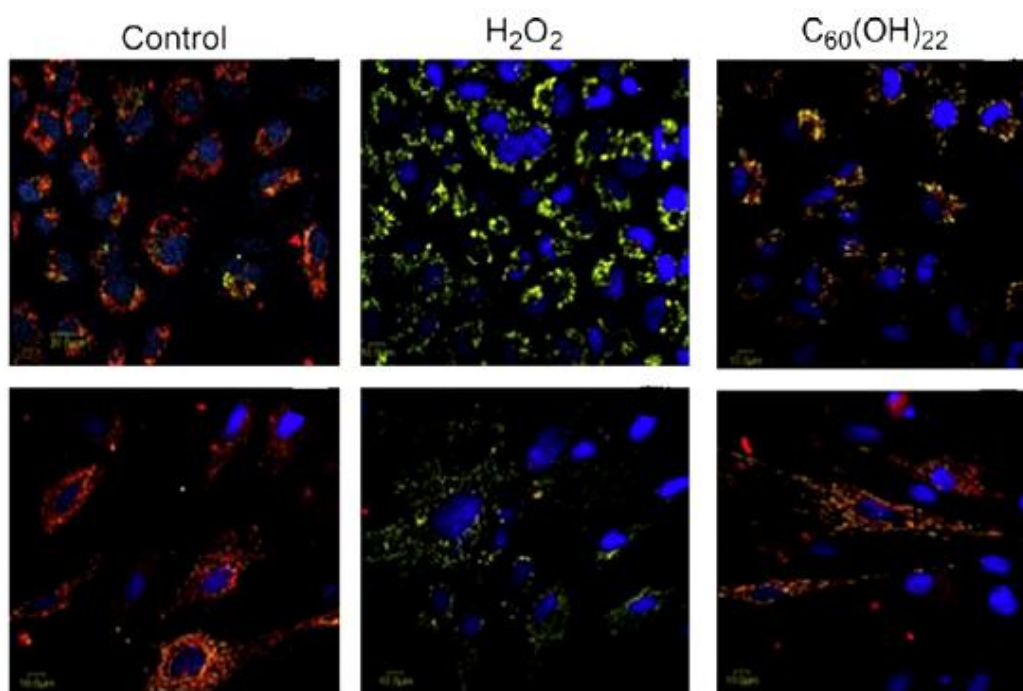
Figure 1-19. The protective effects of $C_{60}(OH)_{20}$ against H_2O_2-induced mitochondrial damage in human cells; adenocarcinomic human alveolar basal epithelial cells (top), and in rat brain capillary endothelial cells (bottom) [89]. The cells were treated with 100 mM $C_{60}(OH)_{20}$ before incubation with 50 mM H_2O_2. Aggregation of the dye, seen as red fluorescence, indicates integrity of the mitochondrial membrane.

In addition, Trakcovich et al. [87] reported the radio protective and tissue protective effects of fullerenes in rats, at a dosage of 100 mg/kg.

Attempts to use SWNTs and MWNTs as delivery agents in both therapeutic and diagnostic applications have also resulted in investigations to determine any cytotoxicity of these carbon nanotubes. The toxicity of SWNTs/MWNTs has been found to depend upon the length of the nanostructures (more detailed discussion is provided below).

35

Pantoroto et al. [28] using FITC surface coating of SWNTs (1 nm is in diameter and 0.3-1.0 μm in length) demonstrated SWNT cytotoxicity in the range of 20 μM on mouse embryonic fibroblast cells. Here, SWNTs were shown to accumulate in cytoplasm and could even reach the nuclei. Shvedova et al. [94] reported that the cytotoxicity of SWNTs in human epidermal keranocytes occurred through accelerated oxidative stress and cellular toxicity; specifically, the formation of free radicals, accumulation of peroxidative products, antioxidant depletions and loss of cell viability were observed in cells exposed to SWNTs. Similarly, Manna et al. [95] found that SWNTs induced an oxidative mechanism leading to the activation of nuclear factor-kappa B, suggesting cell involvement in both immune and inflammatory reactions (Figure 1-19).
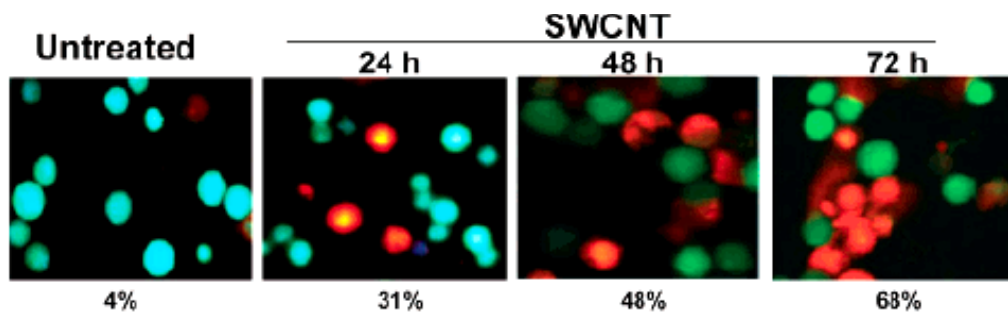
Figure 1-19. Effect of SWNT on human kerotinocytes cells viability [95]. Cell viability was assayed by MTT dye uptake. Cells were treated with 10 μg/mL SWNTs for different time intervals, and the number of dead cells (red color) was counted. The percentage of dead cells is indicated below each photograph.

Wick et al. [96] reported that the cytotoxicity of carbon nanotubes depended upon their degree of agglomeration, in which surprisingly, suspended nanotubes induced less

cytotoxicity than rope-like agglomerates. This cytotoxicity discrepancy was explained by the structural characteristics of carbon nanotubes: as aggregates are larger, stiffer and more solid, they induce stronger cytotoxic response on cells. The adverse effects of functionalized and non-functionalized SWNTs were reported in human keratinocytes [94, 95], human epidermal keranocytes [97], human embryonic kidney cells [37], HeLa cells [95], human fibroblasts [97], and mesothelioma cells [96], which depended upon the surface functionalization, diameter, length and SWNT concentration and properties of the host cells.

A large number of studies are available in the literature regarding the cytotoxicity of MWNTs. Some studies reported MWNT cytotoxicity in different cell lines, such as human epidermal keratinocytes [98], human skin fibroblasts [99], guinea pig alveolars [82], human lung-tumor cell lines [100], and human umbilical vein endothelial cells [101], etc., whereas in others, MWNTs were reported as non-toxic and suitable for use as drug delivery transporters [18, 21, 30].

For example, Magrez et al. [100] demonstrated that MWNTs, at a dose of 0.2 µg/mL, decreased the viability of human lung-tumor cells by 30%, and the toxicity of carbon nanotubes increased significantly when carbonyl, carboxyl or hydroxyl groups were present on the nanotube surfaces. Similarly, Jia et al. [82] reported adverse effects of MWNTs on guinea pig alveolar macrophages: MWNTs at a dose of 3.06 µg/cm^2 led to cell necrosis. Conversely, Flahaut et al. [101] reported no cytotoxic effect of three samples of MWNTs on human umbilical vein endothelial cells.

The interactions of fullerene and their derivatives with cell membranes are of central importance for the biomedical applications of these nanoparticles. A number of reports reported the interactions between fullerenes and the lipids in membranes [53, 76-78, 88, 102, 103]. It should be emphasized that localization of the nanoparticles and their storage inside cells depends upon their pathway of cellular uptake. For example, if a nanoparticle is taken by the cell via endocytosis, it will be internalized by macrophages and localized inside endocytotic vesicles. On the other hand, if the nanoparticle enters the cell through passive diffusion, it will be located in the cytosol. In other words, if the therapeutic agents are delivered to either the cytosol or cell nuclei, one should choose the nanoparticle transporters which would penetrate the cellular membrane with minimal cytotoxicity.

Because nanomaterials are typically integrated by cells through endocytosis [29, 33, 104], they are internalized by the cells into membrane-bounded endosomes, preventing their possible access to the cytosolic components. This phenomena is in contrast to certain biomacromolecules [105, 106], very small metal clusters [107], and carbon nanotubes [108], which have been reported to pass through cell membranes and, in some cases, even avoid lipid disruption [105, 106].

A recent study by Verma et al. highlighted the importance of structure in the interactions of nanoparticles with cellular membranes [104]. Here, the size, shape, chemical composition and ratio of hydrophobic to hydrophilic molecules were kept the same; only the location of functionalized group were in striated (structured nanoparticles) and non-striated (unstructured nanoparticles) ligand organizations respectively. Confocal

microscopy showed an endosomal uptake for unstructured nanoparticles, whereas the structured counterparts were taken up by cells through diffusion (nanoparticles were in cytosol). Under endocytosis blockage conditions (4°C), structured nanoparticles diffused through cell membranes, whereas unstructured nanoparticles were almost completely excluded from cell entry.

Kostarelos et al., however, reported that the cellular uptake of functionalized carbon nanotubes is independent of both the functional groups of the nanotubes and cell type [108]. In this study a variety of cell types, including HeLa, Fibroblasts, Chinese hamster ovary cells, human embryonic kidney cells, keratinocytes, human alveolar basal epithelial cells (A549), mouse intestinal epithelial cell lines, Jurkat, C. neoformans, E. coli, and S. cerevisiae, and differently functionalized SWNTs and MWNTs were chosen for examining the uptake of carbon nanomaterials. The green signal from functionalized carbon nanotubes was detected in all cell types. The researchers also determined that intracellular localization of functionalized carbon nanotubes within A549 was equally distributed throughout the cell, reaching the cell nuclei in some cases. Carbon nanotubes were taken up by cells even under conditions commonly used to prevent uptake of extracellular material by energy-dependent mechanisms, including endocytosis.

The contradictory results reported by Kostarelos et al. [108], Kam et al. [29, 33] and Verma et al. [104] could be due to the substantial differences in the characteristics of functionalized nanoparticles used in their studies. Carbon nanomaterials with different geometric structures and dimensions exhibit remarkably different cytotoxicity. Indeed, Grabinsky et al. [109] reported the different cellular effects of carbon-based materials,

such as carbon fibers of 10 μm, carbon nanofibers of 100 nm, MWNTs of 10 nm, and SWNTs of 1 nm in diameter on mouse keratinocytes. Carbon fibers and nanofibers did not influence the viability of the cells, while MWNTs and SWNTs reduced cell viability after 48 h of exposure.

Using lung tumor cells Magrez et al. [100] demonstrated that MWNTs were less toxic than carbon fibers and nanoparticles, although the cytotoxicity of MWNTs was enhanced when their surfaces were treated with acid. Figure 1-20 clearly demonstrates that MWNTs exhibited a high toxicity on this type of cell: after one day treatment with 0.02 μg/mL, MWNT cells lost their mutual attachments, the cytoplasm of the cells were retracted, and the cell nuclei became smaller and more condensed.
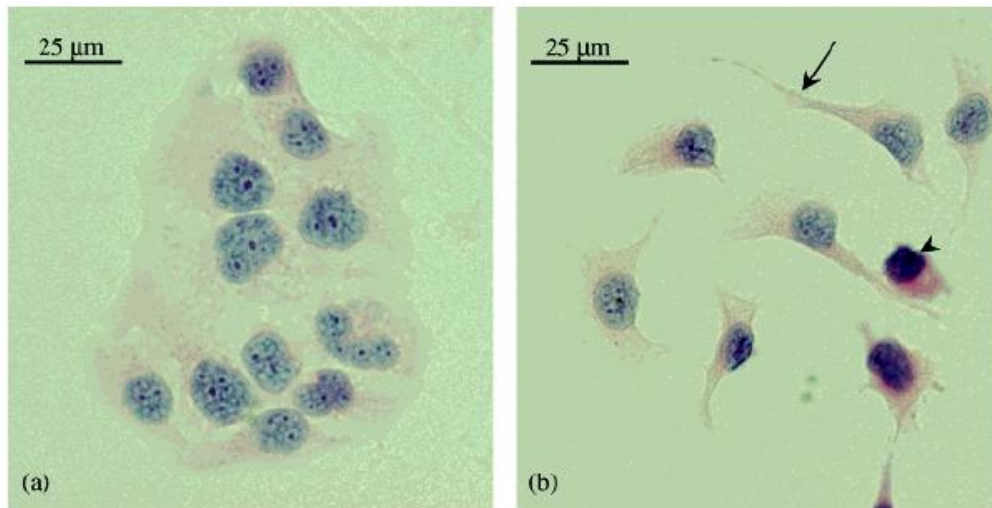
Figure 1-20. Cytopathological analyses of H596 cells [100]: (a) Control image of human lung adenosquamous carcinoma (H596) cells, cells were stained with hematoxylineeosine, the nuclei appear purple and patchy, the cytoplasm was weakly stained (pink); (b) H596 cells after 1 day treatment with 0.02 μg/mL of MWNTs.

Similarly, Jia et al. used relatively low doses to observe the difference in cytotoxicity in the alveolar macrophages of studied nanoparticles [82]. They observed that cytotoxicity induced by the nanoparticles apparently followed a sequential order on a mass basis: SWNTs > MWNTs > quartz > C_{60}. Since the researchers employed macrophages, these toxicities could be explained by the different sizes of the nanoparticles. As C_{60} is smaller than SWNT, MWNT and quartz, it induced less toxicity on this type of cell. For other cell types, larger sized nanoparticles often showed less toxicity, due to their inability to penetrate the membranes or be taken through endocytosis.

Indeed, the cellular uptake of carbon nanoparticles depends upon their dimensions. For example, Jin et al. [110] developed a quantitative model to correlate the endocytosis rate by considering the nanoparticle geometry. The total uptake of both SWNT and Au nanoparticles was found to be maximal at a common radius of 25 nm. These results are in a good agreement with that reported by Chan et al., in which a maximal uptake of gold nanoparticles incurred by HeLa cells with the use of nanoparticles of 50 nm in diameter [111, 112]. The length-dependent uptake of SWNT was reported by Becker et al. [113]. As seen in the Figure 1-21, the sample fraction I (367 ± 61) nm is excluded from the interior of the cell, while the sample fraction III (138 ± 60) nm is clearly present in the cytoplasm. A mixture of samples I and III confirmed that only sample III was present in the cytoplasm, suggesting that shorter tubes could be more toxic to cells than longer tubes. Specifically, the researchers determined an approximate uptake threshold to be of 189 ± 17 nm, and hypothesized that nanotubes any shorter could

induce toxicity, while nanotubes any longer would be excluded by the cell membrane and would therefore be non-cytotoxic.
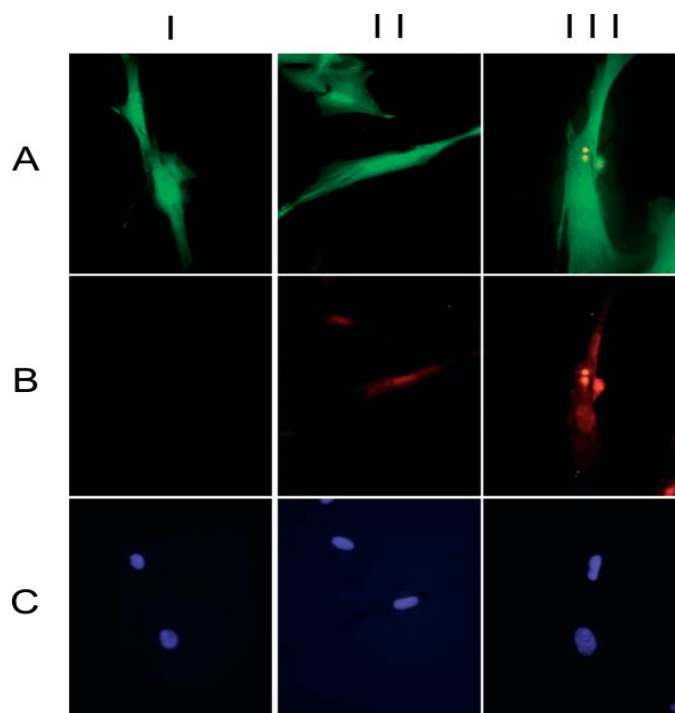
Figure 1-21. Size dependence of carbon nanotubes on the degree of inflammation in the macrophage [113]: Fraction I represents an SWNT (367 ± 61) nm in length, sample fraction III (138 ± 60) nm; Sample fraction II represents a 50:50 mix of sample fractions I and III. An Alexa-488 C2-maliimide labels the cytoskeleton (A), (B) indicates either the absence or presence of the DNA-wrapped SWNTs, and (C) is a DAPI nuclear stain.

Sato et al. [114] investigated the degree of inflammatory response in subcutaneous tissue of rats induced by MWNTs of different lengths. Specifically, MWNTs of 220 nm induced little inflammatory response in rat tissue as compared with the MWNTs of 825 nm in length. These results are in agreement with the results of

Becker et al. in which smaller nanotubes taken by macrophages did not induce inflammation, whereas the larger nanotubes, not taken by macrophages, did indeed do so [113].

To summarize, the cellular uptake of nanoparticles depends upon the size, shape, surface modification, hydrophobicity/hydrophilicity, charge, and other physicochemcial characteristics of the nanoparticles, as well as the properties of their host systems.

1.4.3 Molecular level response

Despite the plethora of papers published over the last 20 years on the biomedical potential of fullerene derivatives, little is known regarding their toxicity on the molecular level.

For nanoparticles to interact with any intracellular organelle or biomolecule, they must first cross the cell membrane. Serving as a selective barrier, this membrane consists of a lipid bilayer with a variety of transmembrane proteins embedded within. To study the interaction of the biological membrane and nanoparticles at the molecular level, researchers often use synthesized model membranes, such as vesicles and lipid mono-and bilayers. Even so, assessing the interactions between nanoparticles and simplified model systems are nontrivial, since they involve knowledge of biochemistry, biophysics, as well as the soft matter of biological systems and the soft condensed matter of nanoparticles.

Computer simulation studies regarding the effect of carbon nanomaterials on lipid bilayers have been reported in the last four years [115-123]. The amphiphilic character of

the membrane (hydrophilic heads and hydrophobic tails) promotes the penetration and partitioning of hydrophobic carbon nanomaterials into the hydrophobic core of the membrane. Predictably, our group [120] and Li et al. [119] found that hydrophobic nanoparticles would penetrate into the hydrophobic interior of the lipid bilayer, while hydrophilic would adsorb onto the membrane. Their findings are in good agreement with the experimental data presented in chapter IV. The differences in the translocation of C_{60} versus $C_{60}(OH)_{20}$ would lead to the different cytotoxicities of these nanoparticles since it is energetically favorable for C_{60} to remain within the lipid bilayer pristine fullerenes and exert more toxicity than $C_{60}(OH)_{20}$, which is mostly excluded by the lipid bilayer. This hypothesis is also in good agreement with the experimental study by Sayes et al. [52].

Due to the hydrophobic nature of C_{60}, it is more relevant to simulate the interactions between fullerene aggregates and the lipid bilayer. One of the representative studies by Wong Ekkabut et al. [121] (Figure 1-22) showed that fullerene aggregates up to 10 nanoparticles penetrated into the dioleoylphosphatidylcholine bilayer and could be dissembled to single fullerenes within microseconds, suggesting that the toxicity attributed to the fullerenes is not likely due to their induced mechanical damage. This too is in good agreement with the results of Li et al. [115], in which the formation of fullerene aggregates in lipid bilayer was not observed to influence the free energy of the system.
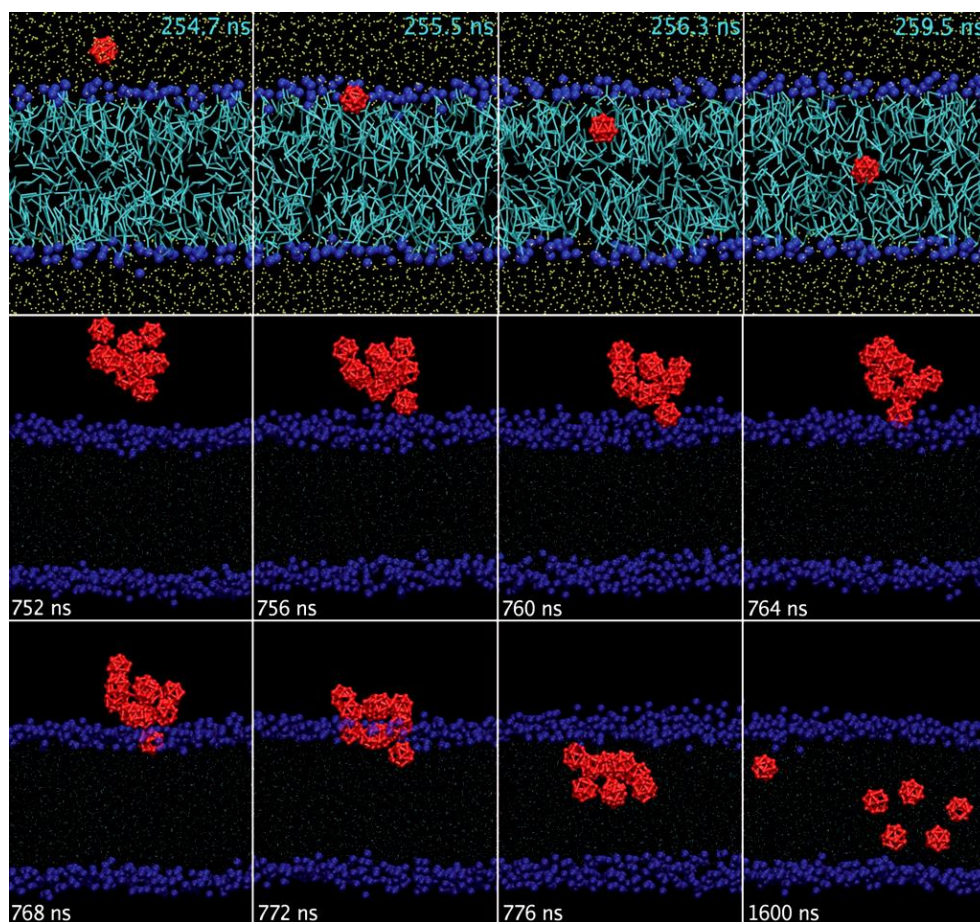
Figure 1-22. Mechanism of permeation of fullerene through a lipid membrane [121]. Top row: monomeric fullerene permeation occurs on nanosecond time scale. Fullerene is shown in red, the lipids in cyan with blue head groups (phosphodiester groups), and water is shown in yellow. Second and third rows: Penetration of a cluster of ten fullerenes into the bilayer, occurring on a time scale that is approximately one order of magnitude slower compared to single fullerene permeation. Lipid phosphodiester groups are shown as blue spheres, lipid tails in cyan; water is not shown for clarity.

According to Chang et al. [117] the shape and structure of carbon nanoparticles plays a major role in their mobility, adsorption and permeation behavior. Round shaped particles were found to remain within the membrane near the dimyristoylphosphatidylcholine bilayer center, whereas precursors with other shapes were found within the hydrocarbon tail region of the membrane.

Regarding the use of nanocarbons for drug delivery, a molecular dynamic (MD) simulation by Wallace et al. [122] showed that it would be more suitable to attach cargo outside of a SWNT, since the lipids of the cell membrane tend to block the tube, thus preventing the delivery of internally located cargoes.
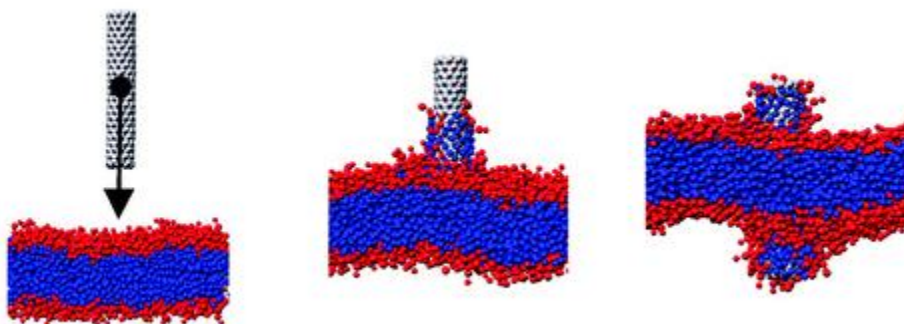
Figure 1-23. The penetration of a SWNT into a dipalmitoylphosphatidylcholine bilayer [122].

The molecular-level impact of carbon nanomaterials has been reported in the literature. For example, fullerene-oligonucleotides conjugates was shown to bind to DNA and cleave the double strands of the DNA [92]. Moreover, fullerene modified with an

acridine moiety exhibited stronger DNA-cleaving activity than C_{60} [124]. Pinteala et al. [125] reported a method of determining the binding of $C_{60}(OH)_{20}$ and double stranded DNA (dsDNA) based upon the fluorescence enhancement induced by the nanoparticle. The increase of fullerol intensity was proportional to the concentration of the DNA. Due to the negative charge of both the DNA phosphate backbone and the fullerol, electrostatic interaction was deemed as a nonfactor for their binding. Rather, the interaction between nucleic acids and fullerols was believed to be realized through hydrogen bonding [126]. The researchers [126] predicted the formation of hydrogen bonding between the hydroxyl groups of the fullerol and the free or bridged amino groups in the major grooves of the DNA base pairs. Since the interactions between phenols and phosphates have been documented previously, it is plausible to assume that fullerols also bind to DNA through hydrogen bonding [127]. Two possible mechanisms of fullerol binding with dsDNA were proposed and are illustrated in Figure 1-24; the second mechanism (Figure B) is conjectured to play a major role in $C_{60}(OH)_{20}$-DNA binding.
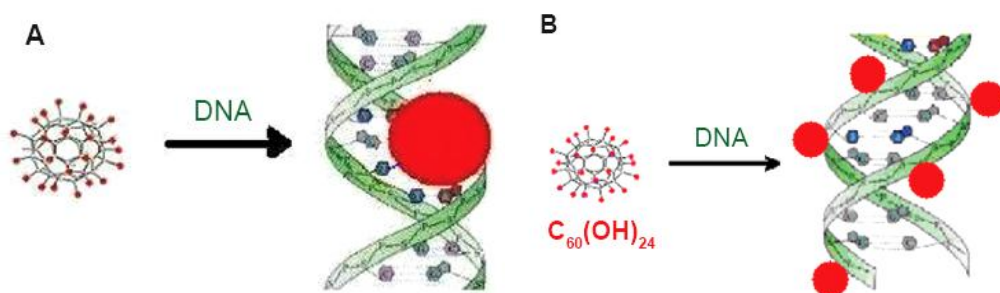
Figure 1-24. Binding of fullerol $C_{60}(OH)_{24}$ to dsDNA [125]: A) Binding fullerol to the major groove of the sodium salt of dsDNA; B) Binding fullerol to the outside of the dsDNA.

The genotoxicity of MWNTs was reported for mouse embryonic stem cells [128]. Accumulation of MWNTs in mouse cells led to the activation of tumor suppressor protein p53 within 2 h of exposure. Moreover, further study showed that MWNTs could increase the mutation frequency by two-fold, with increased expressions observed for the base excision repair protein 8-oxoguanine-DNA glycosylase 1, the double strand break repair protein Rad 51, and other molecular changes. Additional research conducted by other groups [129, 130] as well as our own [131] showed that fullerene derivatives could inhibit DNA amplification *in vitro*, and that the polymerase chain reaction (PCR) could be inhibited in the presence of fullerol, mainly due to the hydrogen bonding formed between the nanoparticle and Taq DNA polymerase.

Bingshe et al. [126] used a fluorescence method to examine the interaction of fullerols with bovine serum albumin in a physiological environment. Non-covalent hydrogen bonds were formed between the oxygen of the fullerol hydroxyl groups and the acceptor chemical elements of the protein. Yang et al. reported that the number of malonic acid molecules added to C_{60} played an important role in the induced phototoxicity, and that the blockage of the cell cycle might be a mechanism of this activity [132].

Computer modeling is often used to provide additional insight on the interaction of biomolecules and fullerenes and their derivatives. Using theoretical modeling, the interactions between carbon nanoparticles and nucleotides [133], single stranded DNA (ssDNA) [133-135], dsDNA [133], different proteins such as HIV protease [136, 137], and other biomolecular species have been investigated.
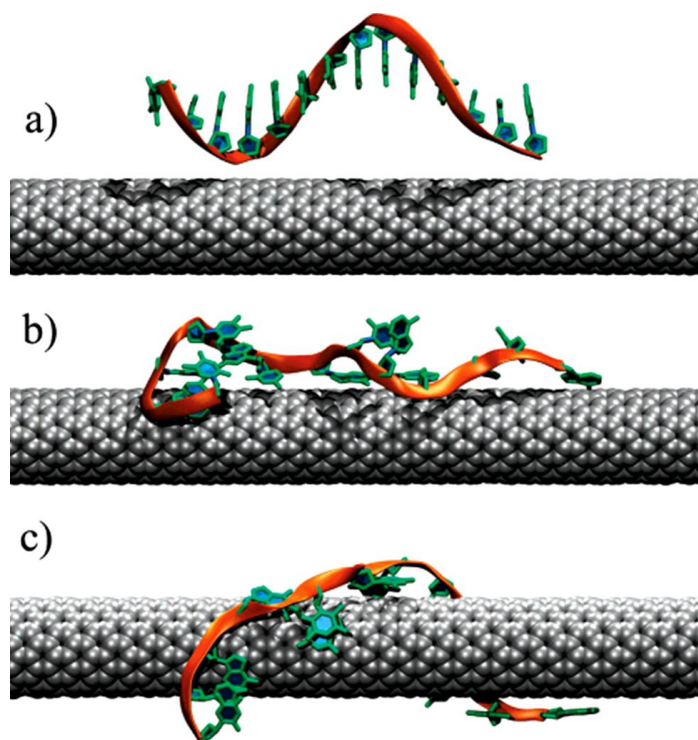
Figure 1-25. Self-assembly of a ssDNA-SWNT hybrid in aqueous solution [135]: (a) Initial configuration; (b) Configuration after 5.5 ns; (c) Final configuration after 21 ns.

Figure 1-25 represents ssDNA – SMNT self-assembly via the pi-pi stacking interaction between the ssDNA bases and the SWNT sidewall [135]. Within a few nanoseconds the ssDNA was helically wrapped from 3' to 5' ends around the SWNT, driven by electrostatic and torsional interactions within the sugar-phosphate backbone.

Additionally, Zhao et al. [133] simulated the interaction of DNA with fullerene. DNA-C_{60} complexes were formed with the preferred locations of fullerenes occurring at either the hydrophobic ends or at the minor grooves of the nucleotides. The binding of C_{60} to ssDNA deformed nucleotides significantly, thus impacting the stability, structure,

and biological functions of the ssDNA. The same research team later further examined the interactions of fullerene and its three derivatives with ssDNA [134].
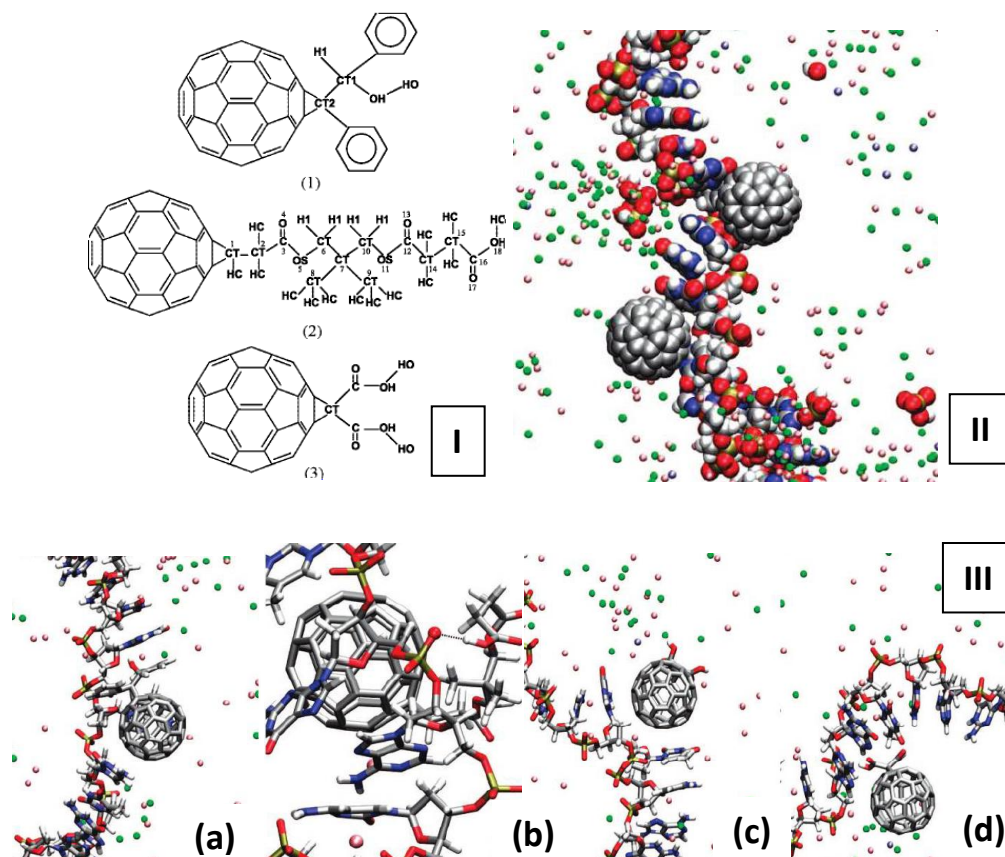
Figure 1-26. MD simulation of fullerene derivatives with ssDNA [134]. I: C_{60} derivatives, denoted as compounds 1, 2, and 3 from top to bottom; II: Snapshot of buckyballs interacting with an ssDNA, consisting of 32 bases in phosphate buffered saline (PBS) solution at 300 K and 1 bar. The atoms in DNA and C_{60}, and the phosphate ions are in space-fill, the salt ions are in small spheres, and water molecules are not shown for clarity. Color scheme: gray, C; red, O; blue, N; yellow, P; white, H; green, Cl$^-$; pink, Na$^+$; ice blue, K$^+$; III: (a)   interaction between compound 1 and ssDNA, (b)

hydrogen bonding between the functional chain of compound 2 and ssDNA backbone, and (c-d) two binding patterns between compound 3 and ssDNA.

They determined that the binding (Figure 1-26 (I)) was related to the structure of the functionalized fullerene groups: the benzene rings of component 1 were bound to ssDNA base rings through pi-pi stacking, the hydrophilic chain of component 2 was bound to ssDNA backbone through hydrophilic interaction, and both mechanisms were employed for the binding of component 3 with ssDNA. This component 3 binding was accomplished through the hydrophobic interaction of the C_{60} and the ssDNA bases (preferred), as well as the weak hydrogen bonding between the carboxylic groups on the nanoparticles and the ssDNA.

In their research elucidating the genotoxicity of nC_{60} in human lymphocytes, Dhawan et al. hypothesized that the response was due to either one or a combination of three mechanisms (Figure 1-27). The first postulate is that nC_{60} produced oxygen radicals and caused lipid peroxidation and membrane leakage in three human cell lines [53]. The second postulate is that nC_{60} can partition into DNA. Using computer modeling, Zhao et al. calculated the binding energy between two C_{60} molecules in the aqueous solution to be -7.5 kcal/mol, and that between a 20-base oligonucleotide and a C_{60} -27 to be -42 kcal/mol (which is the same range as the binding energy required for the oligonucleotide to hybridize with its target sequences [138]). Therefore, "partitioning" of C_{60} from the aqueous solution into DNA matrix or other organic matrices (if present) is probable. The

third postulate is that pristine and modified C_{60} may cause DNA damage. Using an oligonucleotide attached to C_{60} carboxylic acid, Tokuyama et al. showed that upon photo activation, the C_{60} carboxylic acid cut at the guanine sites in a DNA sequence [139]. Boutourine et al. later confirmed that the guanine sites in the vicinity of C_{60} were preferentially cut and hypothesized that this cutting was due to the damage induced by the oxygen radicals on the DNA [92]. This characteristic of fullerene has also been implicated in virus inactivation [140] and in the nonenzymatic cleavage of DNA [141], among other applications.
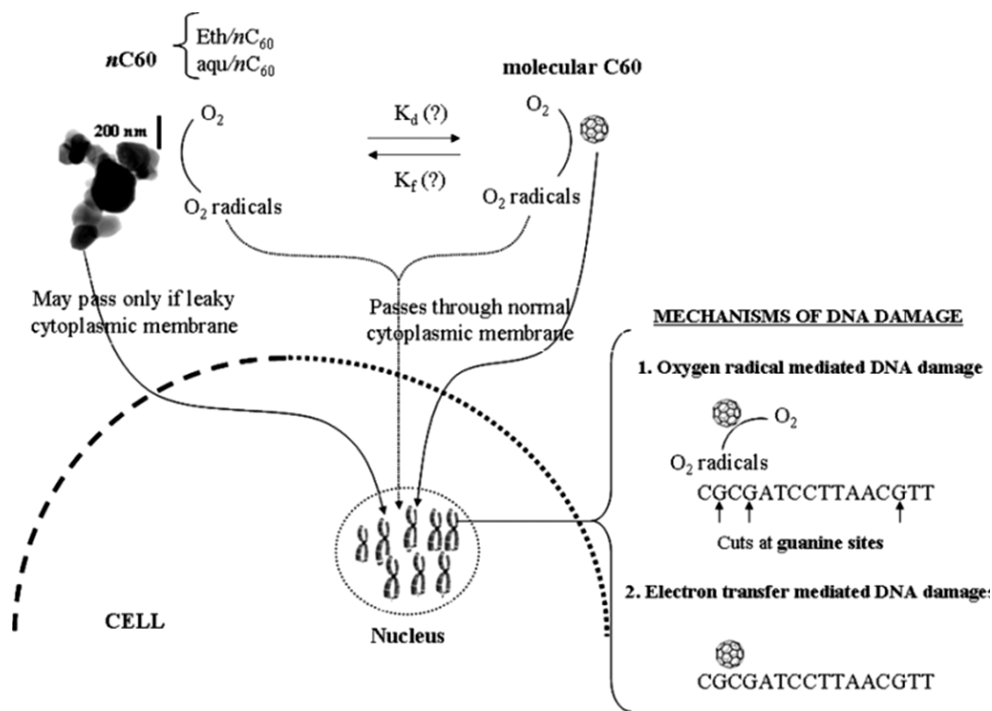
Figure 1-27. Possible mechanisms of genotoxicity induced by nC_{60}.

Despite these research efforts, however it is apparent that a molecular level understanding of the nanoparticle-cell organelle interaction is critically lacking.

1.5 Ecological applications of carbon nanomaterials

Carbon nanomaterials have been proposed for a variety of applications, including electronics, fuel cells, optical devices, and medicine. However, the environmental impact of such nanomaterials has yet to be fully explored, being limited presently to but a few examples of carbon nanomaterials used as environmental sensors, antimicrobial agents, filters, high-flux membranes, and in pollution prevention devices [7].

The electron transport properties of carbon nanotubes are sensitive to their surface modifications, such as local structural defects, and the presence of adsorbed species on the surface, making them an ideal nanomaterial for environmental sensing. Indeed, carbon based nanowire sensors were reported for sensing of microbial pathogens and different gases (NO_2, NH_3, CO_2, CO, N_2, O_2, and CH_4) [142-145]. Experiments showed a reduction in the electrical resistance of single SWNT, in the presence of NO_2 of pico-molar concentrations, and an enhancement in electrical resistance in the presence of NH_3 [145]. Therefore, adsorption of charged species could change the electrical properties of carbon nanotubes, which can be exploited for the analysis of either the composition or concentration of the adsorbed materials. In addition, MWNTs have been used to sense water vapor, NH_3, CO and CO_2 [144]. The adsorption of gases onto the MWNTs could be reversible, like a water vapor, or irreversible, such as in the case of NH_3. Other studies have focused on the potential use of carbon nanomaterials for the adsorption and removal of toxic metal and inorganic materials from water [146-148].

Detection sensitivities of attomolor (10^{-18} M) and zeptomolar (10^{-21} M) concentrations have been reported with carbon nanotubes [7]. This high sensitivity could be utilized for developing rapid response to microbial outbreaks in drinking water systems, thus preventing the spread of a range of diseases.

The antimicrobial and antiviral properties of carbon nanoparticles have attracted focused attention. To date carbon nanomaterials have been reported to be effective for water disinfection, antimicrobial surface coating, and in microbiology lab protocols [7]. The first direct evidence of the antibacterial properties of SWNT was reported by Kang et al. [149], in which the incubation of E. coli with SWNTs led to cell death, most probably due to the membrane damage caused by SWNT aggregation. Brady-Estevez et al. [150] explored the use of carbon nanomaterials for the removal of bacterial and viral pathogens from water. Srivastara et al. [151] reported the removal of bacteria from drinking water, filtration of heavier hydrocarcon species form hydrocarboneus oil (a crucial step in post-distillation of the crude oil), and filtration of nanomatre sized polioviruses. Figure 1-28 illustrates the visual removal of E. coli from water.
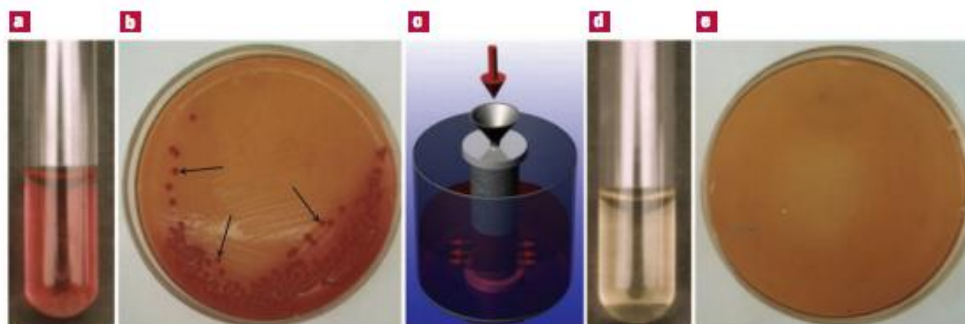
Figure 1-28. Removal of bacteria using nanotube filtration [151]: (a) Unfiltered water containing E. coli phenol red as an indicator; (b) colonies of E. coli (marked by arrows) grown by the culture of the polluted water; (c) assembly for the filtration experiment with horizontal arrows showing the flow direction of the filtered liquid; (d) water filtered through a nanotube macrofilter; (e) the filtrate after culture showing the absence of bacterial colonies.

A number of studies have exploited the use of carbon nanomaterials for filtration and separation applications using carbon based filters. Particularly, MWNTs filters were reported to remove bacteria pathogens and viral pathogens from water [150, 151], as well as nicotine and tar from cigarette smoke [152]. More sensitive filtration could be achieved by using nanotube-based membranes, which includes aligned carbon nanotubes embedded in an impermeable support matrix. Additional experimental studies demonstrated the great promise of aligned carbon nanotubes membranes for high-flux water treatment [153, 154]. For example, MWNTs with an inner diameter of approximately 4 nm embedded in a polymer film were shown to be highly efficient for

water ultrafiltration [154]. Aligned carbon nanomaterial membranes could deliver a water flux five orders of magnitude higher than that predicted by conventional fluid-flow theories [155]. Moreover, separation of materials of different composition, size, and surface structure could be achieved by these membranes with different modifications and depths [156].

In addition to water treatment, carbon nanomaterials may also be used as sorbents [157, 158], potential renewable energy systems [159, 160] and agents for preventing environmental pollution [161]. Along with their expanding list of applications, the health risks associated with these materials must be understood.

1.6 Ecological responses to carbon nanomaterials

Because nanotechnologies are now widely used at all levels of society (Figure 1-1), there is a growing concern regarding the environmental implications these materials. Though Colvin [162] in 2003 predicted that nanomaterial exposures were unlikely to pose any substantial risk to the public health, the production of nanomaterials has increased by ~30 times over the past ten years [5], with the potential environmental impact also rising in proportion. To date, a number of studies have been conducted examining the potential hazardous effects of carbon nanomaterials, particularly focusing on the motility, bioavailability, and exotoxicity of these materials in the environment.

Figure 1-29 presents a summary of the major transmission motilities of these engineered nanoparticles in the environment.
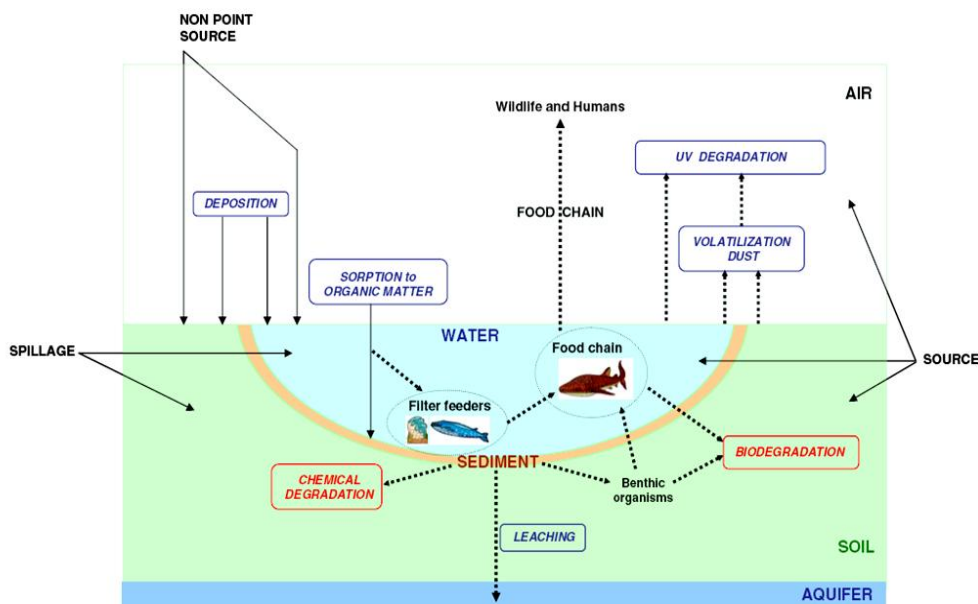
Figure 1-29. Major pathways involving engineered nanoparticles transmitted environmentally [163].

Owing to their mutual interaction, the ready aggregation of carbon-based nanomaterials precludes them as potential contaminants in the liquid phase [164]. When discharged into the environment, however, the interaction of nanomaterials with natural organic matter (NOM) (the natural heterogeneous mixture of decomposed plant and animals) mitigates their hydrophobicity (NOM) [165] (Figure 1-30), Consequently, mobile NOM-modified nanomaterials may pose unknown threats to ecological terrestrial species through naturally occurring physical, chemical, and biological processes.
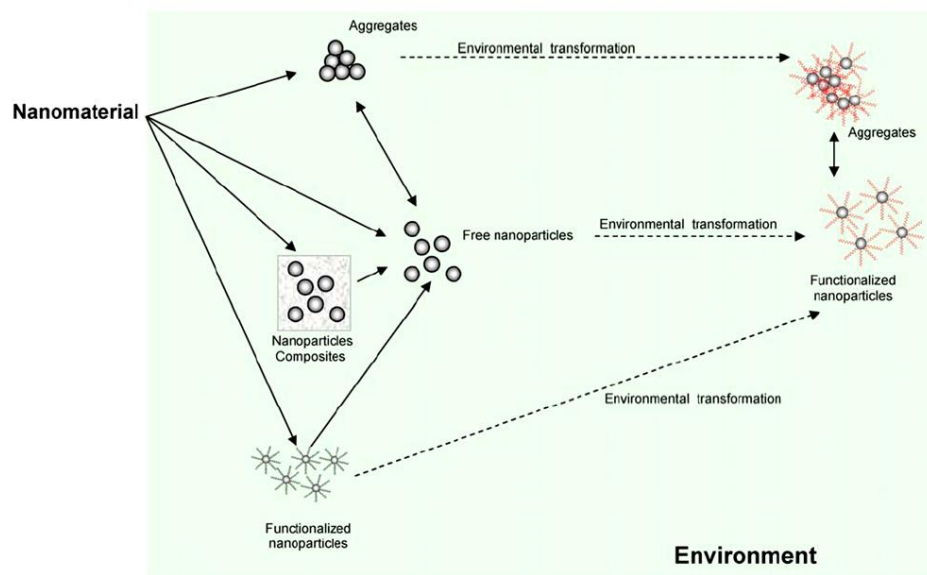
Figure 1-30. Modifications of the nanoparticles released to the environment [163].

1.6.1 Whole organism response

While the behaviors of carbon nanomaterials in the environment and their effects on living organisms are not well understood, as a major class of nanomaterials, their release into the environment is expected to increase rapidly [166]. The impact of carbon nanomaterials on ecosystems, including algae, plant and fungi, is of great concern, particularly because the water cycle runoff receives the wastewater from domestic and industrial sources. The effects of carbon nanomaterials on aquatic systems, such as bacteria [167, 168], daphnia [169-171], and various fish species, specifically the Zebra fish [172-174] [76, 170], have also been reported. As the foundation of the aquatic

ecosystems, microorganisms are considered as the first and key step for both mimicking and elucidating the ecotoxicity of carbon nanomaterials. The rapid growth and ease of culture make microorganisms particularly convenient ecosystems for this research. In addition, as with biological systems, it is easier strategically to assess the effects of nanoparticles on a single biochemical reaction in bacteria and then expand the focus to complex ecosystems, such as Daphnia *magna*, Zebra fish, and fish.

The uptake and further distribution and redistribution of MWNTs during cell division in protozoan *Stylonychia mytilus* was observed by Zhu et al. via optical microscopy [168]. The toxicity of MWNTs was reported for doses higher than 1 mg/L, with their cellular distribution mainly in mitochondria. In addition, Fang et al. [175] demonstrated bacterial adaption to fullerenes, whereas membrane lipid composition, membrane phase transition, and membrane fluidity depended upon nanoparticle concentration as well as cell morphology. In addition nC_{60} was shown to exhibit an antibacterial effect on a broad range of bacteria, while carbon nanotubes were reported to be cytotoxic to microbes caused by cell membrane damage.

Most of the studies on the ecological responses to carbon nanomaterials were performed on Daphnia *magna*. For example, the biomodification of carbon nanotubes by Daphnia *magna* was reported by our group and our collaborators [176], in which we fed SWNTs coated with lysophophatidylholine to the organism (Figure 1-31). Subsequent to Daphnia *magna* digesting the lipid coating and altering the nanotube structure, accumulations of carbon nanotubes were observed in the gut track of Daphnia 45 min and 1 h after ingestion. The precipitated carbon nanotubes can be seen 20 h after exposure in

the figure below, with the toxic effect of lipid-coated SWNT observed at concentrations of 5 mg/L.
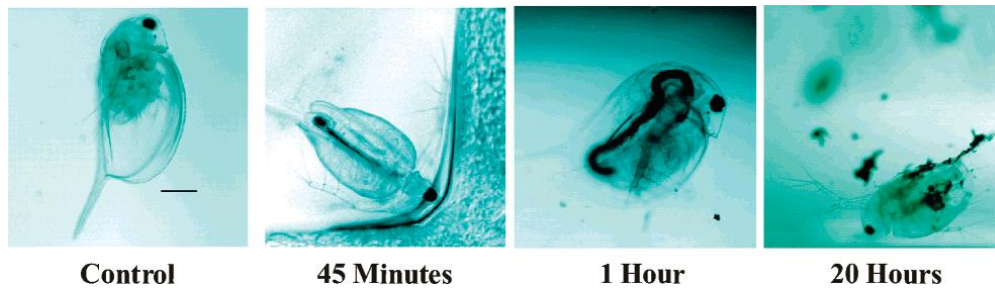
Figure 1-31. Time course micrographs of Daphnia *magna* exposed to 5 mg/L of lysophosphatidylcholine coated SWNTs. Scale bar: 20 µm [176].

This above study suggested that carbon nanomaterials coated with organic molecules may become soluble in the aquatic phase and could subsequently exhibit toxicity to biological or ecological systems, while digested by aquatic organisms the carbon nanomaterials may aggregate in large clumps and lose solubility, thus reducing the toxicity. Our group and Kim et al. [177] also discovered that SWNTs could serve as a carrier for copper to enter Daphnia *magna* and trigger this acute toxicity.

According to Cheng et al. [174] SWNTs and carbon black did not influence embryonic development of zebra fish due to the nanosized dimensions of the embryo chorion pores (in which the size of the SWNT agglomerates was in the micrometer range), which served as a filter for SWNTs to form agglomerates. A significant hatching effect was observed in zebra fish embryos in response to SWNTs, however.

Similarly to carbon nanotubes, water soluble fullerene derivative $C_{60}(OH)_{20}$ at a concentration of 50 mg/L did not exert any toxicity to zebra fish embryos, while nC_{60} at a concentration of 1.5 mg/L caused developmental toxicity (exhibited by decreased heart rate, pericardial ederma and even death), most probably due to the free radical induced mechanism or other forms of oxidative stress [173].

Templeton et al. [178] reported the size-dependent toxicity of SWNTs on the nauplius copepod, in which smaller carbon nanotubes exhibited increased mortality and delayed copepod development. The mechanism of SWNT toxicity in this aquatic organism could be the mechanical disruption of the feeding appendages, caused by penetration of the gut wall, followed by oxidative stress (Figure 1-32).
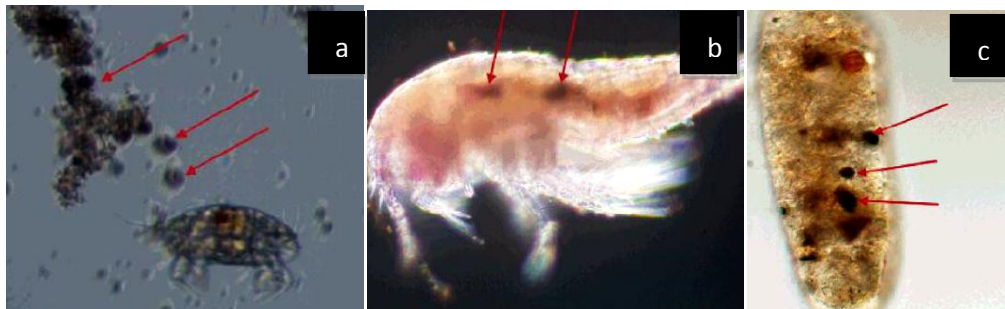
Figure 1-32. Illustration of SWNTs in the gut of the nauplius copepod [178]: (a) Inverted light microscope image of pure SWNT aggregates following feeding - red arrows show a strand of SWNTs and compacted SWNT spherical bundles following feeding by nauplii; (b) confocal microscopy image of an adult copepod with multiple ingested pure SWNT aggregates dispersed through its gut; (c) confocal microscopy image of adult copepod fecal pellets with compacted pure SWNT bundles.

The uptake of different types of nanoparticles in high plant species, a major component of the ecosystems, is illustrated in Figure 1-33 [179]. The comprehensive mechanisms of nanoparticle transport into plant cells are not well known, however. It has been shown that C_{70}, when solubilized in NOM, can be taken up by the plant root hair and transported to the xylem along with water and other nutrients [69]. In contrast, SWNTs [180] and MWNTs [181, 182] were mostly adsorbed on plant root surfaces, and rarely penetrated to the plant cortex. Moreover, the uptake of nanoparticles by plant cells depends upon endocytosis, in which the nanoparticles could first bind to carrier proteins or organic chemicals in the environment, and then enter the plant cells through either ion channels or aquaporins [179].
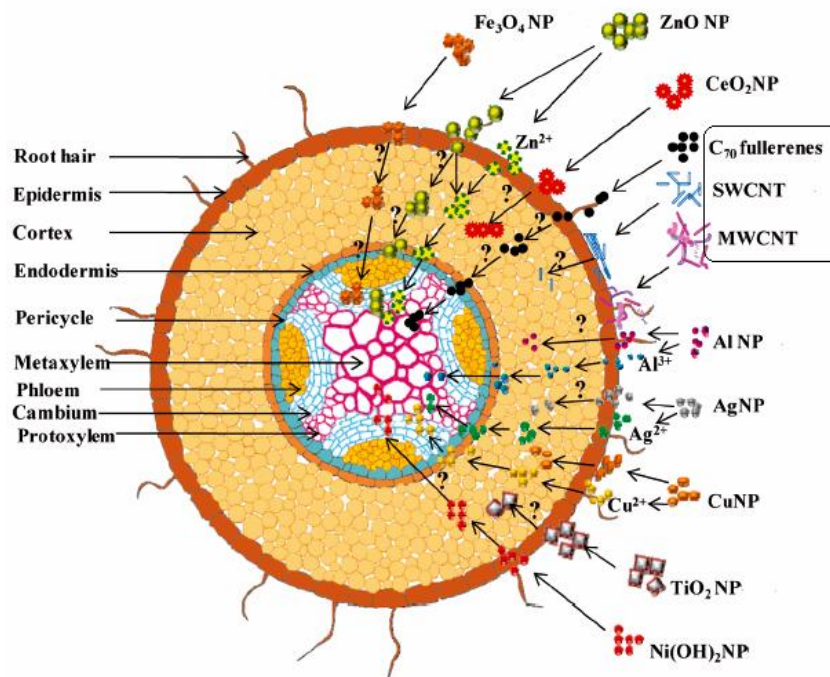
Figure 1-33. The uptake, translocation, and biotransformation pathways of various nanoparticle species in high flora. The transverse cross section of the root absorption

zone illustrates differential tissue penetration upon exposure of the plant to the nanoparticles [179].

Both enhanced [181, 183] and inhibited [69, 183, 184] growth have been reported for various plant taxa exposed to carbon nanomaterials at various developmental stages. For example, Khodakovskaya et al. reported the potential use of SWNTs in agriculture as a plant fertilizer [181] (Figure 1-34). Due to the existence of a thick seed coat [185], the possibility of carbon nanoparticles penetrating through plant seed is perhaps minimal, compared to their biodistributions in either plant cell walls or plant plasma membranes.

Control   40 μg/mL   Control   10 μg/mL   40 μg/mL   Control   10 μg/mL   40 μg/mL
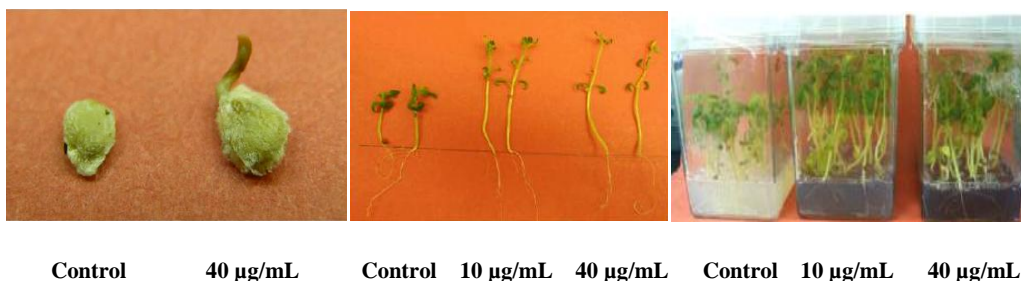
Figure 1-34. Phenotypes of tomato seeds incubated in medium both with and without SWNTs; for 3 days (left); of 27-day-old tomato seedlings (center); and of 25-day-old tomato seedlings [181].

SWNTs were found to penetrate tomato seeds to enhance plant germination. Though seed germination and the biomass and length of the plants accelerated in the presence of the SWNTs in the medium, root growth and elongation remained unaffected. This phenomenon can be explained by the ability of SWNTs to penetrate the seed coat, thus supporting water and nutrient uptake by the plants (Figure 1-34). In a similar study

Stampoulis et al. [184] compared the effects of five different nanomaterial types−including MWNTs−on seed germination, root elongation, and biomass of Cucurbita *pepo* (zucchini). The seed germination of the plants remained unaffected by the presence of MWNTs in the growth medium. After exposure to 1000 mg/L of MWNTs, the plant biomass was reduced by 60%, however, possibly due to blockage of the pores in the seed coat, thus preventing the uptake of water and nutrients. Note that the MWNTs used in this study were 5-20 nm in diameter and 1-10 μm in length, whereas Khodakovskaya et al. used SWNTs with an outer diameter of 3-5 nm.

Lin et al. [186] also investigated the effects of five different nanomaterials−also including MWNTs−on seed germination and root growth of radish, rape, ryegrass, lettuce, corn, and cucumber. It was observed that MWNTs at a concentration of 2000 mg/L after 5 days of treatment exhibited no effect on all six plant types, most probably due to their exclusion by the seed coat. Similarly, Wild et al. observed no significant physiological responses in wheat in the presence of MWNTs [182].

Canas et al. [183] examined the effects of nonfunctionalized SWNTs and SWNTs functionalized with poly-3-aminobenzenesulfonic acid on the root elongation of carrot, cabbage, cucumber, lettuce, onion, and tomato. Depending on the functional groups present on the SWNTs, different effects were observed on the plants. In most of the cases the nonfunctionalized SWNTs altered root length more significantly than the functionalized nanotubes. Specifically, functionalized SWNTs inhibited root elongation in lettuce, and nonfunctionalized nanotubes inhibited root elongation in tomato while promoting root elongation in both onion and cucumber.

Using scanning electron microscopy, the researchers identified the presence of SWNTs on the plant root surfaces (Figure 1-35). Although the adsorption of SWNTs on the plant roots might not affect root elongation, it could affect the ability of the root surface chemistry to influence the interaction of the root with its environment. The hydrophobic nature of carbon nanotubes promotes their interaction with organic substances, whereas their low surface friction facilitates the flow of organic substances into cytoplasm [187]. This study is consistent with our recent report on the uptake, translocation, and transmission of carbon nanoparticles in rice plants [69].
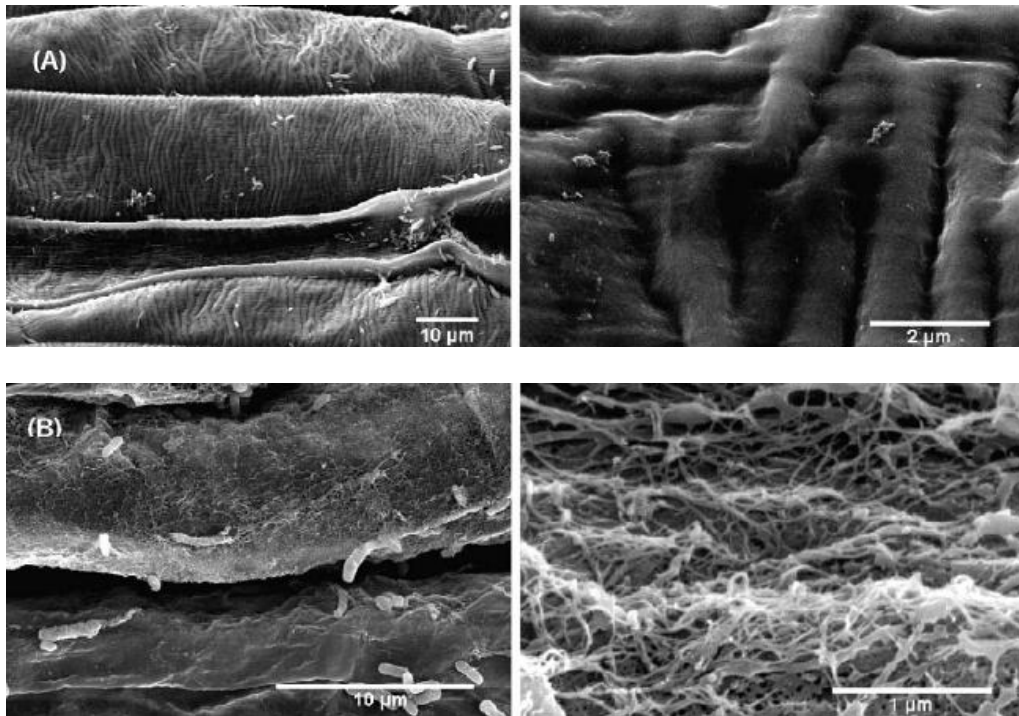
Figure 1-35. Scanning electron microscopy images of cucumber roots [183]: (a) Control, (b) Roots exposed to SWNTs. The left and right panels represent low and high magnifications, respectively, concerning the selected areas.

1.6.2 Cellular level response

Although the focus of most nanotoxicity studies has involved elucidating the impact of nanoparticles upon human health, research into their ecotoxicity (i.e. the impact of nanoparticles upon entire ecological systems) has been steadily growing in recent years. On the cellular level, both plants and bacteria resist the uptake of many types of nanoparticles owing to the additional barrier–the plant cell wall, a thick, hydrophobic, and porous media located outside of the cell plasma membrane. This wall provides the plant cell with both structural support and protection, and may serve as a filtration membrane for the exclusion of nanoparticles and other external substances (Figure 1-36).
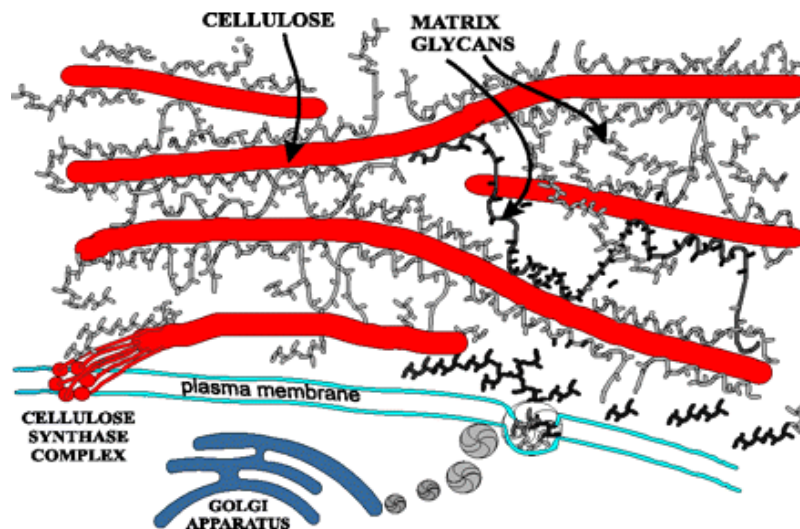
Figure 1-36. The structure of the plant cell wall [188].

Eukaryotes, however, those organisms containing complex cell structures within membranes lack this additional fibrous barrier. Consequently, the porous nature of such structures may facilitate the integration of nanoparticles through either endocytosis or direct penetration through the cell membrane. Plant cells with removed plant cell walls, or protoplasts [180, 189], have been used in two discrete analyses to assess the phytotoxicity of carbon nanoparticles; here, it was discovered that SWNTs caused adverse cellular responses in protoplasts through oxidative stress. The cell aggregation and plasma membrane deposition of protoplasts induced by SWNTs is illustrated in Figure 1-37. It should be emphasized, however, that the omission of the plant cell wall prevents a precise representation of protoplasts as artificial models for accurately representing whole plants in ecosystems.
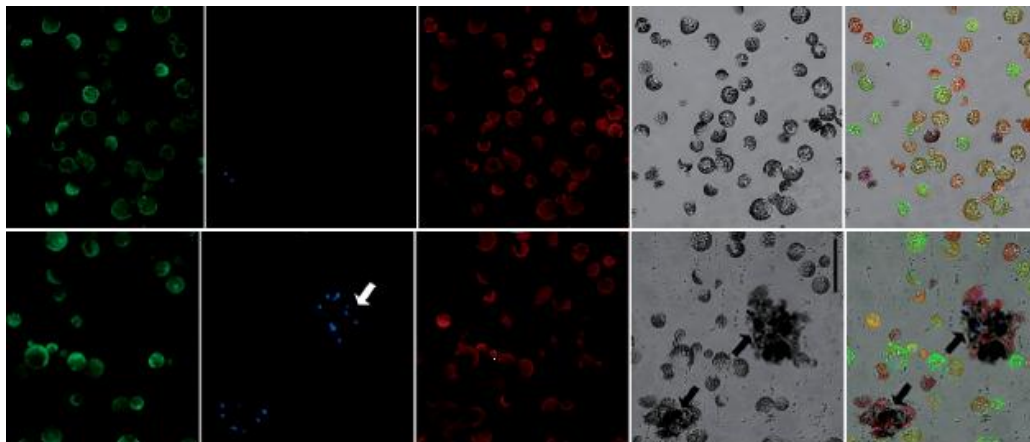
Figure 1-37. Induction of cell death in clusters of *Arabidopsis* protoplasts after culturing with SWNT; for 12 h in W5 medium with (bottom panel) and without (top panel) 25 μg of SWNTs per mL of cells. The cells were doubly stained with FDA (green color) and DAPI (blue color) to distinguish the viable from the nonviable cells. The micrographs

were obtained with multichannel microscopy. The red areas in the images represent the autofluorescence of the protoplasts. The arrows indicate clusters of nonviable cells. Scale bar: 100 μm [180].

The uptake of nanoparticles by plant cells has recently been reported [168, 190-193]. Additionally, the penetration of SWNTs through both the cell wall and the cell membrane in an intact plant cell were observed by Liu et al. [190]. In this study, confocal fluorescence microscopy was used to monitor the uptake of fluorescein isothiocyanate-labeled SWNTs by *Nicotiana tobacum* cells. Using SWNT–DNA conjugates, the researchers demonstrated the ability of SWNTs to deliver DNA to plant cells (Figure 1-38).
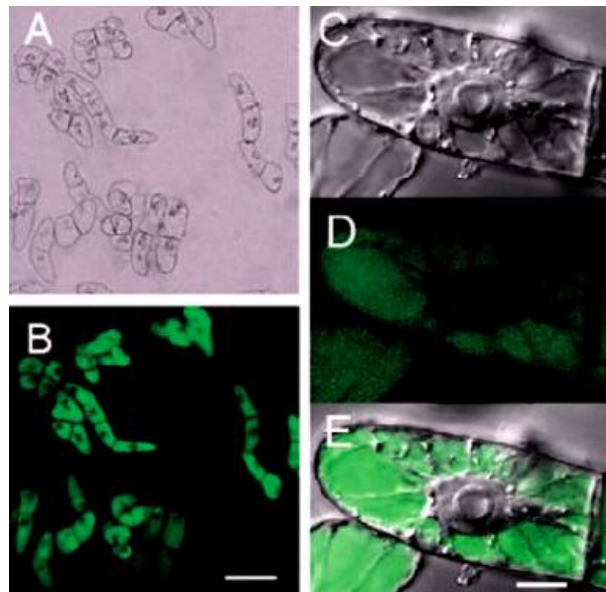
Figure 1-38. Confocal microscopy images of *Nicotiana tobacum* cells incubated with SWNT labeled with fluorescein isothiocyanate: (A) bright field image; (B) fluorescence

image; (C) image under high magnification; (D) fluorescence image under high magnification; (E) overlay of C and D. Scale bars are 100 μm for (A) and (B) and 10 μm for (C-E) [190].

The uptake of MWNTs by unicellular protozoans was reported by Zhu et al. [168], in which most of the MWNTs were localized within the mitochondria of the cells. The inhibition of *Stylonychia mytilus* and cell damage were observed in the presence of MWNTs, at concentrations higher than 1 µg/mL.

Our group [191] was the first to compare the uptake of $C_{60}(OH)_{20}$ molecule and C_{70}-NOM complex by *Allium cepa* plant and mammalian cells. The hydrophilic fullerol was found to easily penetrate the plant cell wall that was mostly excluded by the amphiphilic cellular membrane, while the more hydrophobic C_{70}-NOM complexes were mostly retained in the hydrophobic plant cell wall. As a result, C_{70}-NOM did not exhibit any toxicity on the plant cell, while fullerols induced increased cell damage with increased concentration. At high concentrations, fullerols caused this damaged by accumulating between the plant cell wall and the plasma cell membrane, and were finally pushed through the fluidic cell membrane due to the concentration gradient across the plant cell. For more detailed information please refer to chapter III.

According to Tan et al. [193] MWNTs exhibited toxic effects (reduction of cell viability and ROS production) on rice cells. Specifically, relatively low concentrations of

MWNTs induced apoptosis, while high concentrations of the nanotubes triggered necrosis. In addition, rice cells invoked self-defense when exposed to MWNTs [192].

1.6.3 Molecular level response

The impact of carbon nanomaterials on plants has been the subject of infrequent examination in the current literature. In addition, most of these rare studies focused on the effect of carbon nanomaterials on plant growth, seed germination, root elongation and the alteration of biomass, while fundamental questions regarding the impact of carbon nanomaterial in ecosystems on molecular level remain unanswered. Indeed, to date only a single study has reported on the genetic analysis of plants exposed to carbon nanoparticles [194]. Here, tomato plants were exposed to cell growth medium containing 50 µg/mL of MWNTs (10-35 nm in diameter, 6 µm in average length). The uptake of MWNTs by the tomato plants and their presence in roots, leaves, and fruits (Figure 1-39) were detected using photoacoustic and photothermal spectroscopy. The enhancement of biomass was observed for both MWNTs and SWNTs, which were introduced from the cell growth medium (right bottom part of the Figure 1-39).
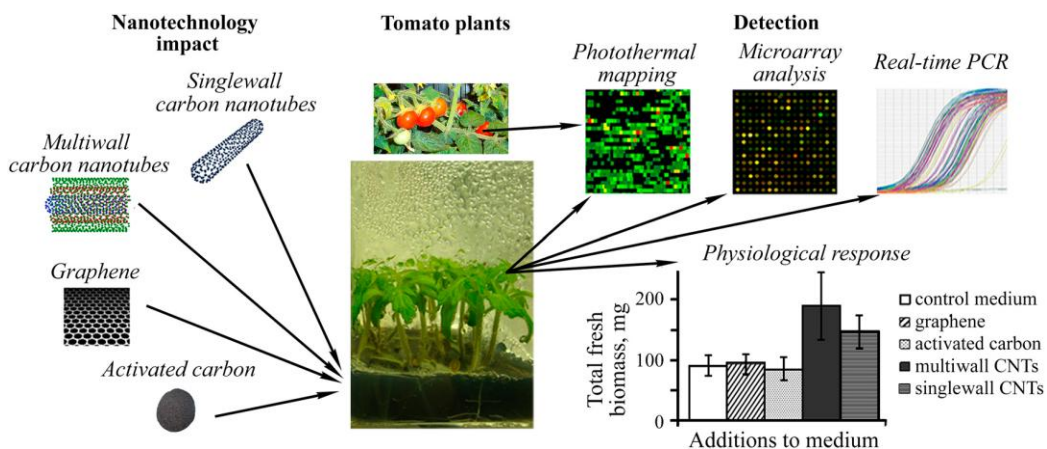
Figure 1-39. Schematics of integrated genomic and photothermal-based analysis of nanoparticle-plant interaction [194]. The pseudocolor in example of photothermal leaf map on right top indicates signals from small carbon nanotubes clusters (red- maximum signal, green low signals).

The direct injection of MWNTs into the tomato leaves verified that the source of these photothermal signals were carbon nanotubes, the majority of which were distributed far away from the vascular system, possibly due to their large sizes. Genomic analysis performed in tomato plants treated with and without carbon nanotubes suggested that penetration of MWNTs into plant cell tissue could be sensed by plants as a stress (Figure 1-40). Indeed, many stress-related genes, such as LeAgp2 protein, TDR3 protein, Heat shock protein 90, were activated in the presence of carbon nanotubes. The enhanced growth and generation of the tomato plant in the presence of carbon nanotubes in the cultured medium was attributed to the up-regulation of the expression of the water-s channel's gene in roots and leaves exposed to MWNT.
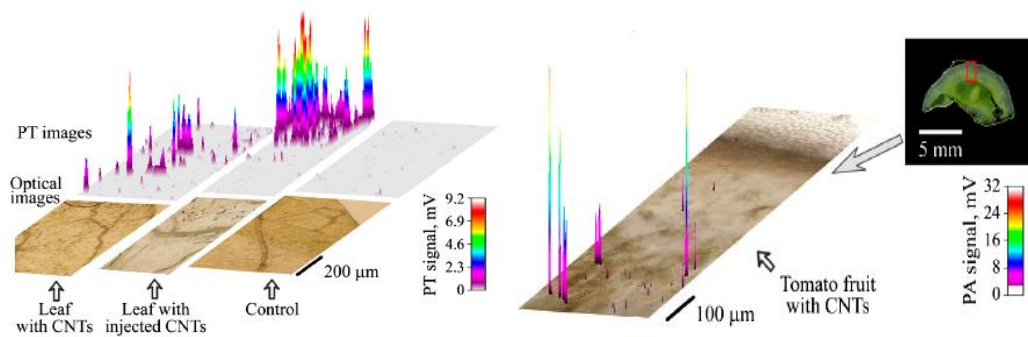
Figure 1-40. Photothermal detection of MWNTs in tomato leaves (left) and tomato fruits (right) [194]. A calibration model was constructed by injection of CNTs into the leaf.

In our recent study, we examined the molecular effect of fullerols on the plant gene−heat shock transcription factor [131]. The amplification of the gene was monitored through a real-time polymerase chain reaction, which was fully inhibited in the presence of fullerols of 0.16 μM in concentration, mainly due to the binding of the nanoparticles to Taq DNA polymerase, the molecular machine which assembles free nucleotides into dsDNA. More detailed discussion on this study is presented in chapter VI.

CHAPTER TWO

UPTAKE, TRANSLOCATION, AND TRANSMISSION OF CARBON NANOMATERIALS IN RICE PLANTS

The purpose of this chapter is to understand the ecological responses to carbon nanomaterials on the whole organism level. The development of nanotechnology - large scale production and commercialization of nanomaterials - has raised concerns about the adverse effects of nanomaterials on biological systems and the environment. Discharged into the environment carbon nanomaterials could be suspended by a major pollutant carrier in nature, natural organic matter (NOM), a heterogeneous mixture of decomposed animals and plants, and thus, may pose a threat to ecological and terrestrial species through further physical, chemical, and biological processes. The solubility and mobility of carbon nanomaterials is facilitated by the hydrophobic-hydrophobic interaction, π-π stacking, electrostatic forces, as well as van der Waals interaction between the hydrophobic carbon nanomaterials and the amphiphilic NOM. In this current study, rice plants -- a major food crop for over half the world's population -- were exposed to NOM-suspended C_{70} (i.e., C_{70}-NOM) and MWNTs (i.e., MWNT-NOM) to examine the whole plant response to carbon nanomaterials.

The uptake, accumulation, and generational transmission of C_{70}-NOM and MWNT-NOM in rice plants was examined using bright field, fluorescence and electron microscopy, Fourier transform infrared spectroscopy (FTIR) and Fourier transform (FT)

Raman spectroscopy techniques to yield comprehensive information on the biodistribution of the nanoparticles in the plants.

2.1 Introduction

Due to their hydrophobicity, carbon nanomaterials readily aggregate and are not considered potential contaminants in the liquid phase [164]. Nevertheless, when released into the environment, the hydrophobicity of nanomaterials can be averted through their interaction with NOM [165], a broken down matter that comes from dead plants and animals. As a result, mobile NOM-modified nanomaterials could interact with plants, a major component of the food chain.

The impact of nanomaterials on high plants has scantly been examined in the current literature. Among the studies available, none have used major food crops or carbon nanoparticles (a major class of nanomaterials) for their evaluations. Although both enhanced and inhibited growth have been reported for vegetations exposed to nanomaterials at various developmental stages, including seed germination, root growth, and photosynthesis, fundamental questions remain regarding the uptake, accumulation, translocation, and transmission of nanomaterials in plant cells and tissues, and the impact of these processes on plant reproduction. Here, we provide the first evidence on the uptake, accumulation, and generational transmission of NOM-suspended carbon nanoparticles in rice plants, the staple food crops of over half the world's population. The data presented in this study suggests the potential impact of nanomaterial exposure on

plant development and the food chain, and prompts further investigation into the genetic consequences through plant-nanomaterial interactions.

2.2 Experimental section

2.2.1 Nanomaterial suspensions preparation and characterization

Carbon nanoparticles C_{70} (SES Research, purity: 99%) and MWNTs (Sigma, OD: 40-70 nm, ID: 5-40 nm, and 0.5-2 µm in length, purity: 95%) were added separately to Nordic NOM suspensions (IHSS, MN), the concentration of each being 1.0 mg/mL. NOM in freshwater ecosystems ususally has a concentration between 1-100 mg/L[14]. To mimic the natural ecosystems we formed an NOM solution of 100 mg/L in Milli-Q water and suspended fullerene C_{70} and MWNT in the NOM. After probe sonication at 8W for 30 min (VC130 PB, Sonics & Materials), the nanoparticle suspensions were diluted into nominal concentrations of 2.5~800 mg/L using the same NOM solution. Each sample was vortexed, and its absorbance was measured immediately (Biomate 3, λ=400 nm).

The absorbance vs. nominal concentration obeyed the Beer-Lambert law (column 2, Tables 2-1 and 2-2), suggesting negligible sample precipitation on day 0. After one day of incubation all suspensions were stablized with slight to medium level precipitations. The absorbance of each sample on day one was measured using its supernatant (column 3, Tables 2-1 and 2-2) and the amount of C_{70} or MWNTs in each suspension was estimated (column 5, Tables 2-1 and 2-2).

Nominal C_{70} concentration: C_1 (mg/L)	Absorbance on day 0: a_1	Absorbance on day 1: a_2	a_2/a_1	Estimated C_{70} concentration $C_2=C_1*a_2/a_1$ (mg/L)
2.5	0.012	0.006	50.0%	1.3
5	0.020	0.013	65.0%	3.3
10	0.043	0.029	67.4%	6.7
20	0.092	0.056	60.9%	12.2
40	0.186	0.104	55.9%	22.4
80	0.365	0.192	52.6%	42.1
400	1.818	0.907	49.9%	199.6
800	3.640	1.770	48.6%	388.8

Table 2-1. Characterization of C_{70} concentration by UV-vis spectrophotometer.

Nominal MWNT concentration: C_1 (mg/L)	Absorbance on day 0: a_1	Absorbance on day 1: a_2	a_2/a_1	Estimated MWNT concentration $C_2=C_1*a_2/a_1$ (mg/L)
2.5	0.087	0.077	88.5%	2.2
5	0.171	0.160	93.6%	4.7
10	0.347	0.320	92.2%	9.2
20	0.680	0.632	92.9%	18.6
40	1.382	1.224	88.6%	35.4
80	2.738	2.363	86.3%	69.0

Table 2-2. Characterization of MWNT concentration by UV-vis spectrophotometer.

The size distributions of the nanoparticle suspension were measured by Zetasizer S90. Here "size" refers to the hydrodynamic diameter of a Rayleigh particle. According to Rayleigh's approximation, the intensity of scattering of a particle is proportional to the sixth power of its diameter. The sample of NOM in Milli-Q water (100 mg/L) displayed size peaks at 1.11 nm (area percentage: 38.9%), 4.89 nm (17.7%), and 31.21 nm (21.1%)

(Figure 2-1(a)). The registered larger particle sizes were possibly due to dusts in the suspension.

The size distribution of the sample of C_{70}-NOM (nominal concentration: 20 mg/L) in Milli-Q water, or "without buffer" displayed size peaks at 1.19 nm (area percentage: 55.5%), 17.99 nm (28.5%), and 722.10 nm (16%). The sample of C_{70}-NOM in rice germination buffer, or "with buffer", had size peaks at 2.36 nm (42.8%), 45.24 nm (34.3%), and 1212.00 nm (22.9%). The peaks at 1.19 nm ("without buffer") and 2.36 nm ("with buffer") may be attributed to free NOM or small C_{70}-NOM (Figure 2-1 (b)). The relatively large peaks "with buffer" could be mediated by salts.

MWNT-NOM in Milli-Q water ("without buffer", nominal concentration: 20 mg/L) had one size peak at 239.70 nm (area percentage: 100%). MWNT-NOM in germination buffer ("with buffer") had one peak at 252.40 nm (98.2%) (Figure 2-1 (c)).

The nonspecific assembly of NOM with C_{70} or MWNTs is believed to be a dynamic equilibrium process [165], with the hydrophobic moieties of the NOM interacting and π-stacking with the hydrophobic carbon nanoparticle surfaces.
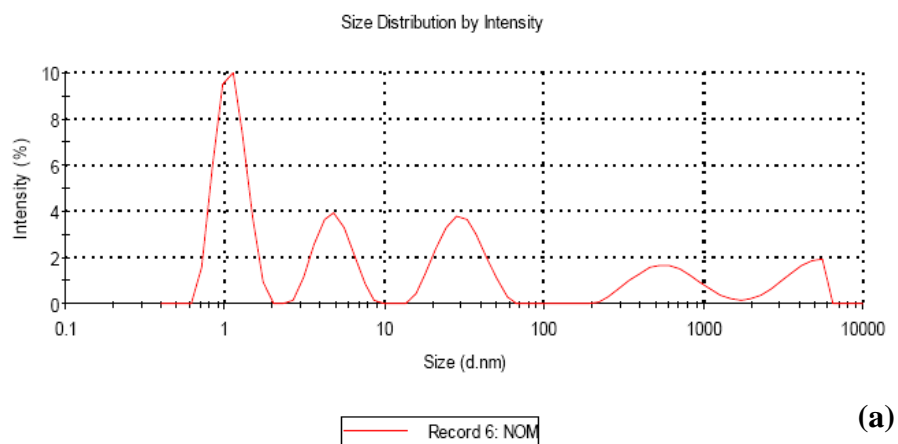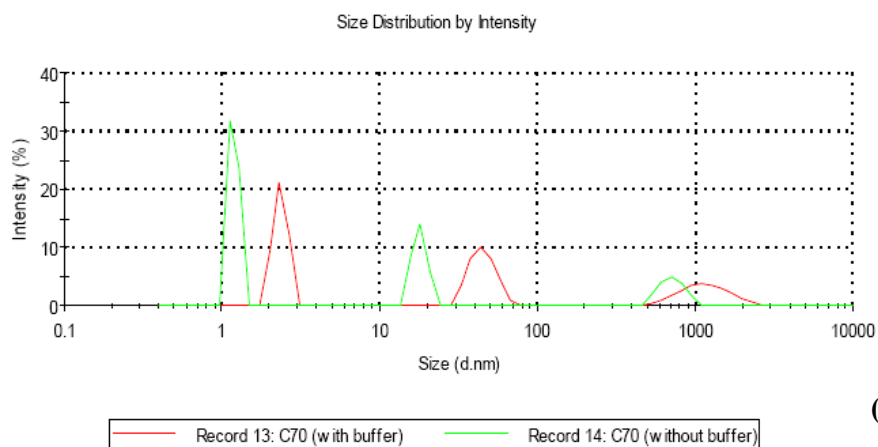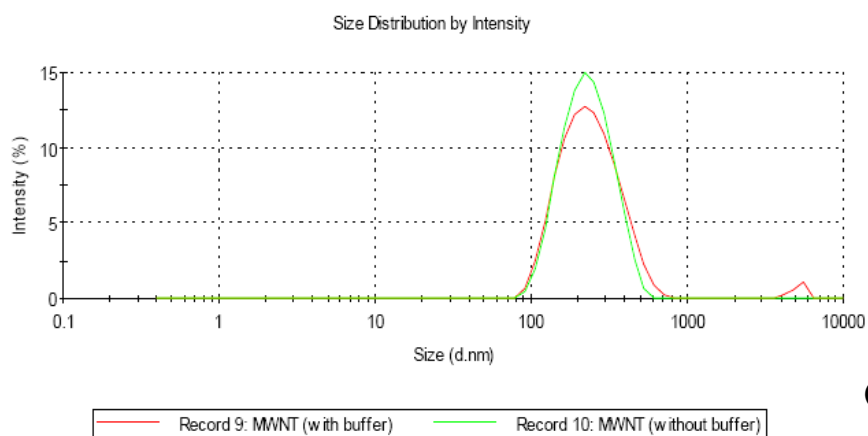
Figure 2-1. Size distribution measured by Zetasizer S90 of (a) NOM, (b) C_{70}-NOM and (c) MWNT-NOM.

2.2.2 Plants preparation and exposure to carbon nanomaterials

Newly harvested rice seeds (*Oryza sativa* L. ssp. *japonica*, cv Taipei 309) were soaked in 70% ethanol for 30 sec, surface sterilized twice in 10% (v/v) Clorox® bleach plus two drops of Tween-20™ (Polysorbate 20), and stirred for 30 min. Rice germination buffer (half-strength MS basal salts and vitamins and 7.5g/L sucrose, pH=5.7) was mixed with C_{70}-NOM and MWNT-NOM and autoclaved at 120°C for 20 min. These samples were used for the uptake experiments (Figure 2-2). For easy description hereafter we refer to the samples based on their nominal concentrations.
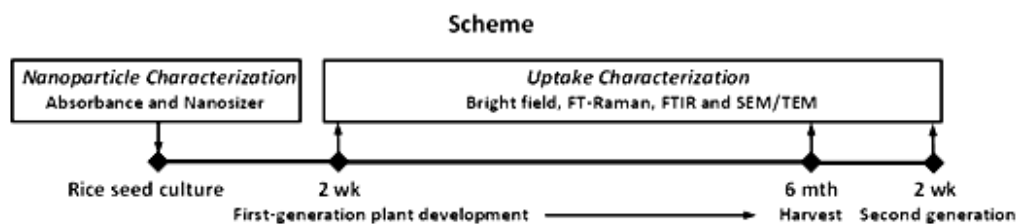
Figure 2-2. Experimental scheme of rice plant exposure to carbon nanoparticles.

Newly harvested rice seeds were incubated in Petri dishes that contained 15 mL of different concentrations of C_{70}-NOM and MWNT-NOM in rice germination buffer. After germination at 25±1°C for 2 weeks the seedlings were transplanted to soil in big pots and grown in a green house to maturity without addition of nanoparticles. For each sample concentration, 5 pots of plants were maintained for analysis. These plants are referred to as the *first generation*. The plants grown in the germination buffer are known as the *control*. Identical amounts of NOM were used for C_{70}-NOM and MWNT-NOM for

each concentration. For example, the NOM concentration in "NOM400" was identical to that in C_{70}-NOM or MWNT-NOM of 400 mg/L. To investigate generational transmission of nanomaterials, mature seeds from the control plants and C_{70}-treated plants were harvested 6 months after germination, and 60 seeds of similar size for each plant were chosen and sterilized using the same method as described above. Ten seeds were planted in each Petri dish filled with rice germination buffer and kept at $25\pm1°C$ for 2 weeks. These germinated plants without the addition of nanomaterials are known as the *second generation*.

2.2.3 FTIR and FT-Raman spectroscopy

For FT-Raman spectroscopy (IFS 66v/s Bruker FT-Raman spectrometer) measurement, a 1064 nm laser beam was focused to a 1 mm spot size, and the Raman-scattered signal was detected using a liquid nitrogen-cooled germanium detector. A Bruker Fourier transform infrared spectrometer (model IFS 66v/s) equipped with a deuterated triglycine sulfate detector was used to collect the infrared absorption spectrum of the selected samples in the range of 400–4000 cm^{-1}. The FTIR absorption measurements used ~3 mg of the root, leaf, or stem mixed with ~50 mg of KtBr powder and pressed into a ~5 mm diameter. The sample chamber was evacuated down to 0.002 mbar to eliminate interfering IR absorption by water vapor and CO_2 present in the ambient atmosphere.

2.2.4 Electron microscopy

Ten samples of the plant roots and leaves were evenly coated with a thin film of platinum (~5 nm) using a Hummer® 6.2 sputtering system. SEM imaging was performed using an FESEM, Hitachi 4800, microscope operating at 5 kV. For TEM imaging, ten samples of the roots and leaves of rice plants were placed in 3.5% Glutaraldehyde, post fixed in osmium tetroxide, dehydrated in a graded series of ethanol, and embedded in LR White embedding media. Samples were polymerized overnight and sectioned using an Ultracut E microtome. Tissues of plant roots and leaves were cut at 60-90 nm. TEM images were acquired using a Hitachi H7600 microscope operated at 80 and 100 kV. The lattice spacing of C_{70} particles was analyzed by performing Fast Fourier Transform of the TEM images, using software "Diffractogram".

2.3 Results and disscussions

2.3.1 Uptake of carbon nanoparticles by rice plant

Tissues of exposed to nanoparticles rice plants at various developmental stages were sampled, thoroughly washed using distilled water, cut, sectioned to make thin layers, and imaged on glass slides using a bright field microscope (Imager A1, Zeiss). Figure 2-3 (lower panel) shows bright field images of the plant tissues acquired ~one week after incubating in C_{70} of 20 mg/L. Black aggregates were frequently found in the

seeds and roots, and less frequently in stems and leaves, indicating that the sequence of nanoparticle uptake was from the plant seeds and roots to the stems and leaves. The appearance of black aggregates mostly in and near the stem's vascular system (Figure 2-3, lower panel, top panel, and Figure 2-4 (a)), suggests the transport of C_{70} occurred simultaneously with the uptake of water and nutrients in the xylem.
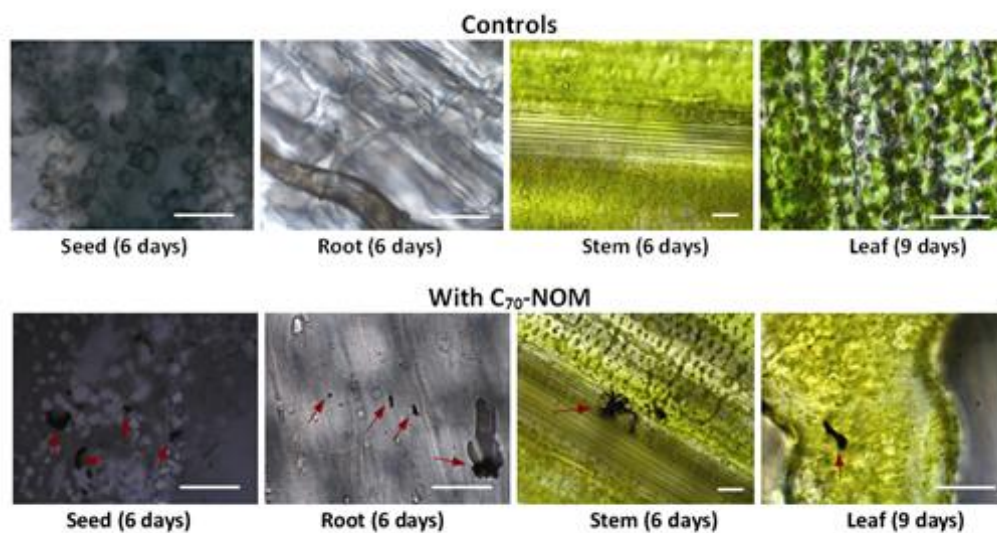
Figure 2-3. Bright field imaging of C_{70} uptake by one week-old rice plants. Top panel: bright field images of the controls. Lower panel: aggregates of nanoparticles (indicated by arrows) observed for corresponding plant tissues treated with C_{70}-NOM. The scale bars are 20 μm for all images.

To zoom in the picture for further examination of nanoparticles uptake and localization in plant cell, TEM image were acquired in a plant leaf. Figure 2-4 illustrates the significant uptake of C_{70} particles by a plant leaf cell; the C_{70} particles appear as numerous small

aggregates in the vacuole and the cell walls of the leaf cell are shown as dark layered structures in the image.
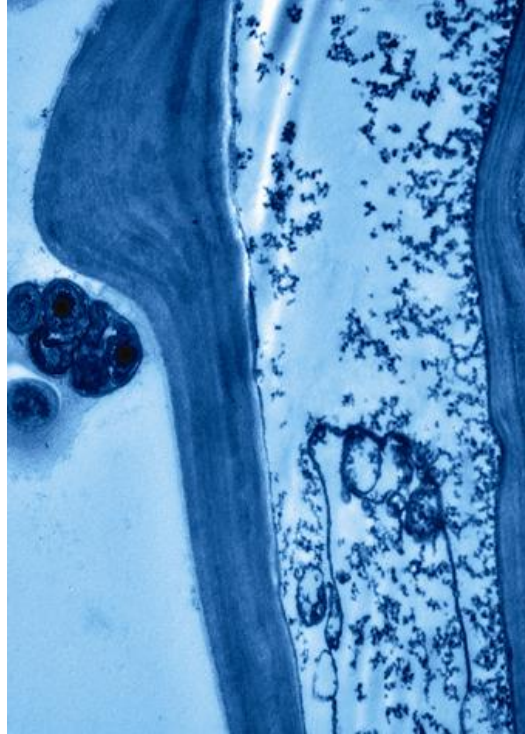
Figure 2-4. TEM image of a significant uptake of C_{70} particles by a plant leaf cell. Scale of image: 5×6 μm.

2.3.2 The transmission of carbon nanoparticles to the second generation rice plant

Remarkably, black aggregates were also spotted in the leaf tissues of the second-generation plants, though much less frequently (Figure 2-5(a)).
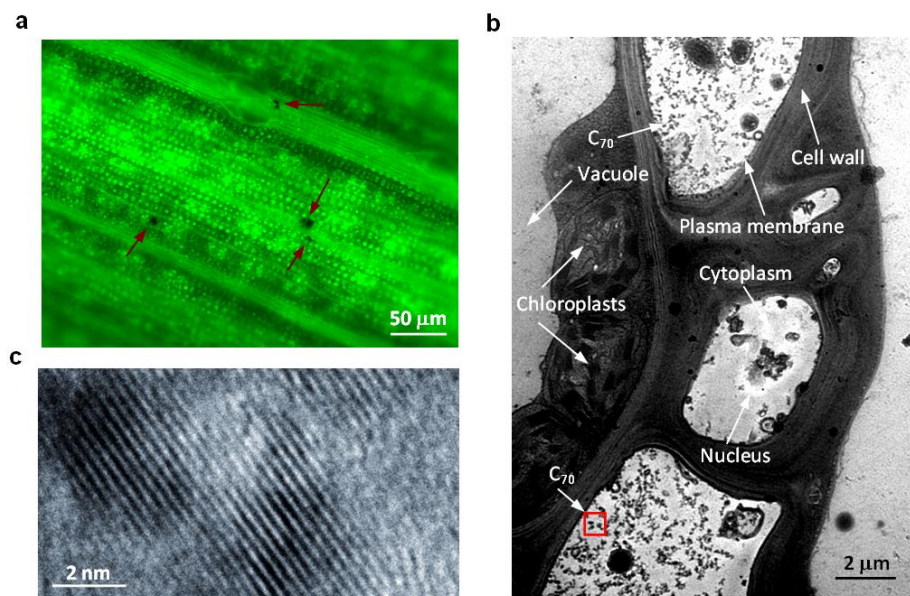
Figure 2-5. The transmission of carbon nanoparticles to the second generation rice plant. (a) Bright field image of a second-generation plant leaf, where C_{70} aggregates (indicated by arrows) appeared mostly in or near the vascular system of the leaf. (b) TEM image of C_{70} particles in the leaf cells of a 2 week-old rice plant (C_{70}: 20 mg/L). Also indicated are plant cell walls and other organelles. (c) Higher magnification TEM image of the C_{70} particles in (b) (red square). The lattice spacing of the C_{70} particles was determined to be 0.257 nm from Fast-Fourier Transform (FFT) analysis of the TEM image.

2.3.3 FTIR and FT-Raman studies of the uptake of carbon nanoparticles by rice plant

To confirm that the aggregates were composed of C_{70} or C_{70} derivatives, FT-Raman and FTIR spectra were acquired at room temperature for both the first- and second-generation rice plants. Typical FT-Raman (red traces) and FTIR-spectral (blue traces) finger prints are presented in Figure 2-6 for C_{70}, control, first-generation seeds and

leaves, and second-generation leaves. Clearly, the dominant FT-Raman (indicated by "+") and FTIR (indicated by "diamonds") features [195] of C_{70} were observed in the first-generation seeds and leaves and in the second-generation leaves, thus confirming the uptake and transmission of C_{70}. After collecting of the absorption spectrum, each of the C_{70} peaks was fit to a Lorentzian line shape and the area under the peak (integrated intensity) was calculated via equation: $I \bullet A\pi / \Gamma$, where A is the amplitude, and Γ is the FWHM. This area was then converted into a percent uptake of C_{70} by dividing it by the total area of all the combined samples.
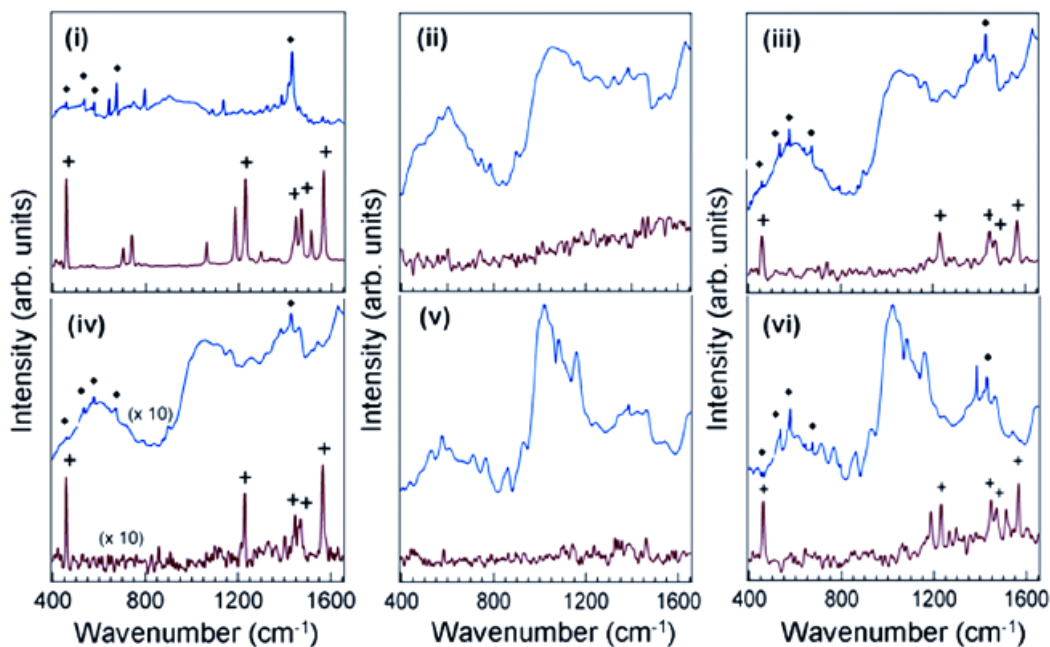
Figure 2-6. FTIR and FT-Raman studies of the uptake of carbon nanoparticles by rice plant. FT-Raman (red traces) and FTIR (blue traces) of (i) C_{70}, (ii) control leaf, (iii) first-generation leaf, (iv) second-generation leaf with uptake of C_{70}, (v) control seed, and (vi) first-generation seed with uptake of C_{70}.

2.3.4 Dynamics of C_{70} uptake by rice plant

To quantify the dynamics of C_{70} uptake, a detailed FTIR study was carried out for the roots, stems, and seeds of the first-generation rice plants when the concentration of C_{70} was increased from 20 to 800 mg/L. As shown in Figure 2-7 (c), C_{70} particles were prevalent in the roots as well as in the stems and leaves of the 2 week-old plants, while the distribution of C_{70} in these plants showed no significant concentration dependence.
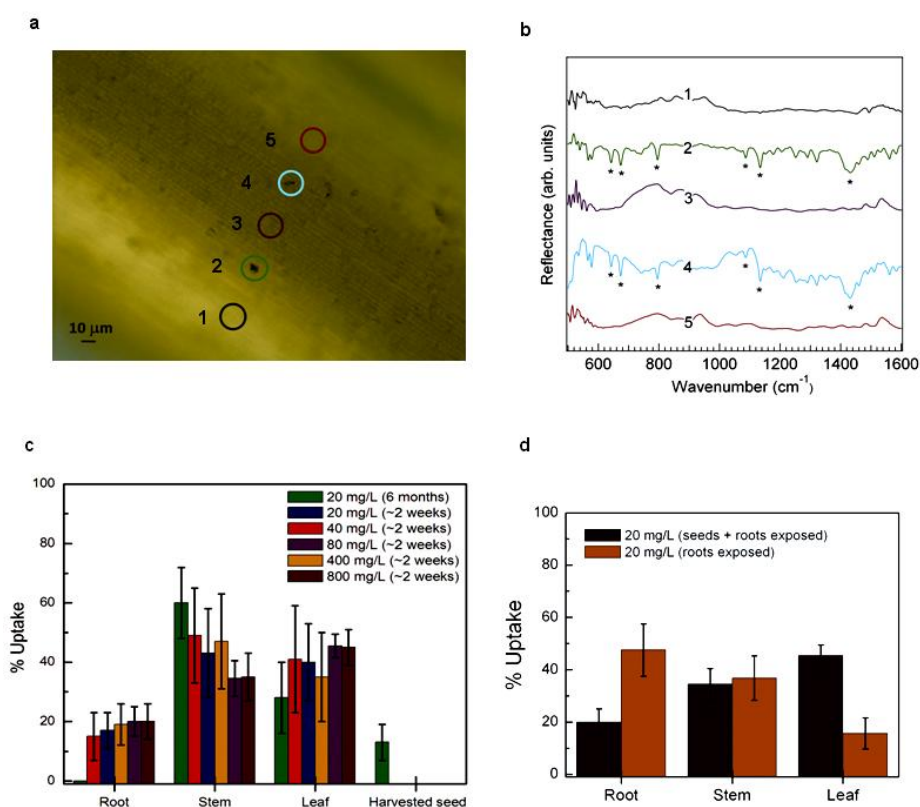
Figure 2-7. Dynamics of C_{70} uptake by rice plant. (a) Bright field image of a sectioned leaf tissue. The circles indicate the positions of a line-scan across the tissue from which FTIR spectra (panel b) were obtained. (b) Infrared features corresponding to C_{70} are seen in spectra labeled 2 and 4. (c) Uptake dynamics for rice plants of ~2 weeks and 6 months

after germination. All samples were initially exposed to C_{70} for 2 weeks through their seeds. Only the 6 month-old plants had harvested seeds. (d) Comparison of uptake dynamics for rice plants exposed through "seeds+roots exposed" (dark red bars) and "roots exposed" (brown bars) to C_{70} of 20 mg/L.

The prevalence of C_{70} in plant leaves and roots is also evident in Figures 2-5(b) and 2-8(a). For the mature (six-month-old) plants, however, C_{70} was predominantly present in or near the stems' vascular systems, less in the leaves, and understandably even less in the seeds due to the multiplied uptake rates (green bars). Furthermore, no C_{70} was left in the roots of the mature plants, suggesting robust transport of nanomaterials from the plant roots to the leaves.
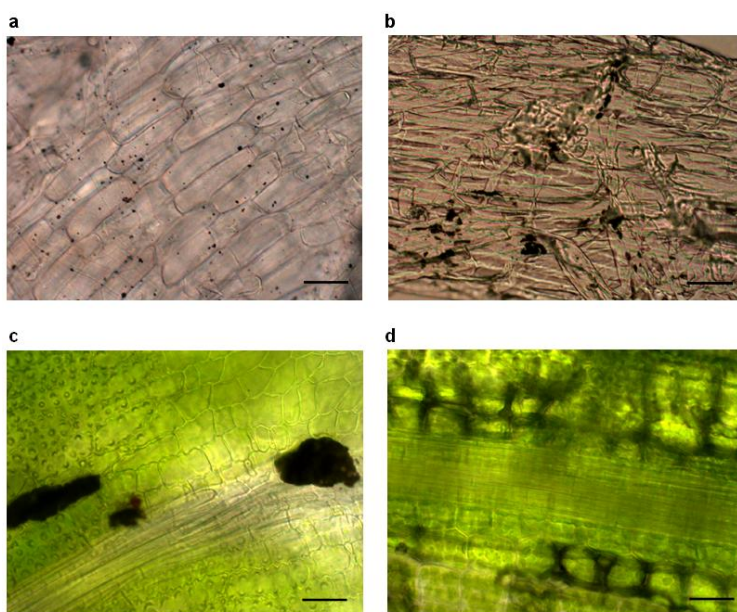
Figure 2-8. Uptake of carbon nanomaterials by roots of the plant. (a) Significant uptake of C_{70} by plant roots (C_{70}: nominal 400 mg/L). (b) Aggregation of MWNTs in plant roots

(MWNT: nominal 400 mg/L). Little MWNTs is seen inside the root cells. (c) Aggregation of C_{70} in the vascular system and nearby tissues of a leaf tissue (C_{70}: nominal 400 mg/L). The vascular system is partially blocked by the aggregation. (d) Leakage of C_{70} (darker areas) from the vascular system to nearby leaf tissue (C_{70}: nominal 400 mg/L). All scale bars: 20 µm.

To compare the uptake capacity of plant seeds vs. roots, we germinated two sets of rice seeds in rice germination buffer and in C_{70}-NOM mixed rice germination buffer (20 mg/L), respectively. Within 3 days these seeds started germination to first produce shoots and then roots. One week after shooting at three-leaf stage, the seeds, no longer able to provide sufficient nutrients for the newly germinated plants, detached from the seedlings. At this point we transferred the seedlings in rice germination buffer to be in contact for 1 week with C_{70} suspensions (20 mg/L), prior to FTIR study of the roots, stems and leaves of these plants. This set of sample is termed as "roots exposed". The other set of sample which had been exposed to nanoparticles from the beginning of germination is termed as "seeds+roots exposed" and FTIR study was conducted for the roots, stems, and leaves of these plants at the end of the second week. Since shoots usually come out 1-2 days earlier than roots during seed germination, C_{70} taken up by the seeds could first be transported to the shoots (stems and leaves) and then to the roots. This may have led to more accumulation of nanoparticles in the leaves than in the roots (Figure 2-7(d), "seeds+roots exposed", dark red bars). The "roots exposed" samples showed a different trend of nanoparticle translocation possibly because C_{70} first entered

88

the roots and then was transported to the stems and leaves (Figure 2-7(d), "roots exposed", brown bars).

In contrast to C_{70}, the uptake of MWNTs at concentrations of 20 to 800 mg/L was found to be insignificant, with few black aggregates appearing in the vascular system and almost none in the plant tissues (Figure 2-8(b)). In our study the minimal uptake of MWNTs was not characterized also due to the relatively weak Raman and non-existent IR signatures for the MWNTs.

The accumulation and transformation of nanoparticles in plant tissues and cells suggests a plausible mechanism for nanoparticle uptake: a dynamic competition between nanotransport driven by water and nanoparticle convections and the physical hindrances of plant tissues and nanoparticle aggregation. Individual C_{70} nanoparticles may enter plant roots through osmotic pressure, capillary forces, pores on cell walls (3.5~5 nm) [196], and intercellular plasmodesmata (50~60 nm at midpoint) [197], or via the highly-regulated symplastic route. Once in the plant roots and stems, individual C_{70} nanoparticles may share the vascular system with water and nutrients and may be transported via transpiration [198], the evaporation of water from the plant leaves. Individual C_{70} nanoparticles may also form aggregates or even clog the vascular system (Figure 2-8(c)) due to hydrophobic interaction, or may leak into nearby tissues and cells (especially cytoplasm and vacuoles) (Figure 2-8(d) and Figure 2-5(b)) via the mechanisms that are discussed above for plant roots. Indeed, we observed a permeation of C_{70} from the vascular system to form aggregates in the cortex (Figure 2-9).
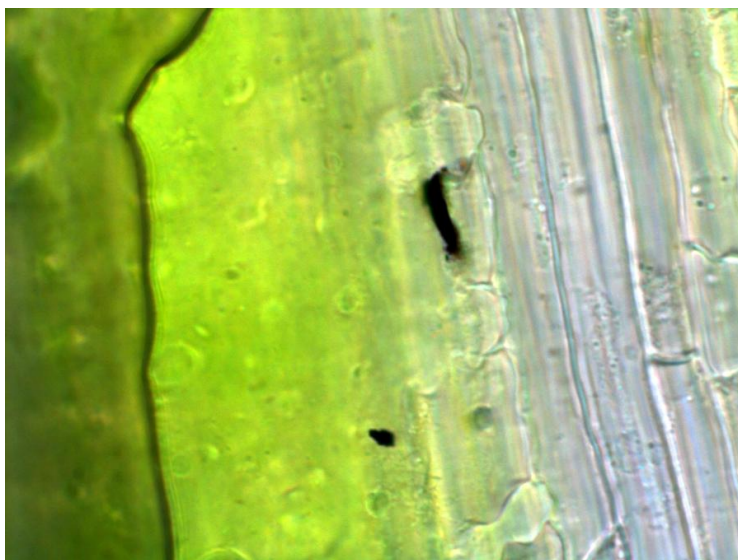
Figure 2-9. Aggregation of C_{70} near the vascular system (top arrow) and in cortex; (lower arrow) of a rice plant stem (C_{70}: nominal 20 mg/L). Scale bar: 20 µm.

However, no C_{70} aggregates were found in the epidermis, possibly due to increased distance from the vascular system, therefore reducing the amount of translocated nanoparticles. At high concentrations, C_{70} aggregation within the vascular system and in plant tissues and cells is expected to interfere with nutrients and water uptake, and hinder plant development (Figure 2-10(a)).
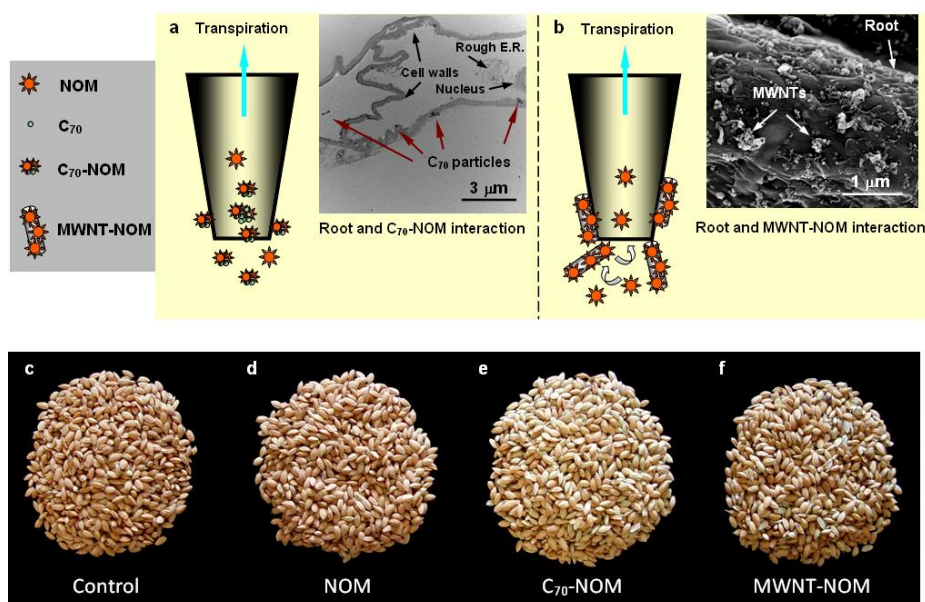
Figure 2-10. (Top row) Hypothesized uptake of (a) C_{70}-NOM and (b) MWNT-NOM by plant roots. The binding and dissociation of NOM with respect to the MWNTs are illustrated in (b). Inset of (a): TEM image of C_{70} particles translocating across root cells. Inset of (b): SEM image of MWNTs adsorbed on a plant root. (Lower row) Photo of 1,500 rice seeds each harvested from (c) control plants, (d) plants incubated with NOM400, (e) plants incubated with C_{70}-NOM (400 mg/L), and (f) plants incubated with MWNT-NOM (400 mg/L). The seeds in (c) and (d) were harvested 6 months after germination. In comparison, the seeds in (e) and (f), shown here as less mature from their slightly greenish coloring and lower seed setting rates, were harvested 7 months after germination. The seed setting rate was 98.6% (2,758 seeds counted), 98.6% (2,366 seeds counted), 94.0% (2,891 seeds counted), and 88.1% (2,900 seeds counted) for the control, NOM400, C_{70}-NOM, and MWNT-NOM incubated plants, respectively.

It is also very likely that plant cell-nanoparticle interaction could lead to the modification of plant gene expression and related biological pathways, and consequently impacting plant development. Indeed, flowering of the rice plants incubated with C_{70}-NOM (400 mg/L) was delayed by at least one month and their seed setting rate reduced by 4.6% (Figure 2-10(e)), compared to the controls or the NOM-fed plants. MWNTs, meanwhile, are larger one–dimensional nanostructures and, unless oriented approximately perpendicular to plant tissues, are less likely to enter plants (Figure 2-10(b)). Our bright field (not shown) and scanning electron microscopy imaging (Figure 5b inset) showed that MWNTs adsorbed to the plant root surfaces, possibly because of the high affinity of the tubes for the epidermis and the waxy casparian strips of the roots. At high MWNT concentrations, uptake of water, nutrients, and NOM as well as plant development could be impeded due to increased blockage of the plant roots and root hairs by surface-adsorbed nanotubes. In our experiment, flowering of the rice plants incubated with MWNT-NOM (400 mg/L) was delayed by at least one month and their seed setting rate reduced by 10.5% (Figure 2-10(f)), compared to the controls (Figure 2-10(c)) or the NOM-fed plants (Figure 2-10(d)). Accordingly, the weight per 100 seeds was reduced by 8.59% ($p<0.05$) and 11.2% ($p<0.05$) for the plants incubated with C_{70}-NOM (400 mg/L) and MWNT-NOM (400 mg/L) respectively, while no statistically significant change was found for the plants treated with NOM400, as compared with the controls.

In summary, we have characterized the dynamic uptake, compartment distribution, and transformation of fullerene C_{70} in rice plants and have detected the transmission of C_{70} to the progeny through seeds. The mobility of the hydrophobic C_{70}

was elicited by NOM, a collection of organic substances abundant in nature. The integration of nanoparticles by plant species may result from the nanoparticles' small dimension and self assembly and from the nanoparticles' interactions with plant organelles and the NOM. The potential impacts of these processes on both food safety and the environment are important subjects to understand.

CHAPTER THREE

DIFFERENTIAL UPTAKE OF CARBON NANOPARTICLES BY PLANT AND MAMMALIAN CELLS

Chapter two investigated the interaction between carbon nanomaterials and plants on the whole organism level, whereby fullerenes were mobilized by NOM and taken by rice plants along with water and other nutrients and further transmitted into the plant tissues and cells. The integration of nanoparticles in rice plants resulted from the nanoparticles' small dimension and self assembly, as well as interactions between the nanoparticles and plant organelles and the NOM. Once translocated through the hydrophilic cell wall and amphiphilic cell membrane, carbon nanoparticles became stored in the cell vacuoles; moreover, some of the fullerenes were transmitted through seeds to the second generation rice plants. Since this finding is directly related to the safety of the environment especially the food chain, further investigation into the cellular and molecular level impacts of carbon nanomaterials on biological and ecological systems are deemed necessary. In comparison with plant cells, mammalian cells do not possess the cell wall, which acts as an additional barrier for the uptake of extracellular materials and chemical species. Furthermore, according to Johnston et al. [40], the dimension, surface charge, and hydrophilicity of nanoparticles may invoke different cell responses. Consequently, this chapter examines how carbon nanomaterials may interact differently

with plant and mammalian cells and, furthermore, how the physicochemistry of carbon nanomaterials may influence cell response upon exposure.

3.1 Introduction

Carbon nanomaterials are a most commonly used and studied class of nanomaterials. To enable their broad applications, carbon nanomaterials have been purposely reacted, or coated with surfactants, proteins, DNA, and other organic molecules for the purpose of targeting desired cell with increased biocompatibility [27]. On the other hand, when discharged into the environment, carbon nanomaterials may alter their mobility through physical, biochemical, and biological transformations, and consequently posing a threat to ecological species [69].

It has been realized recently that understanding the fate of nanomaterials from cradle to grave is essential to the sustainability of nanotechnology [199]. Consequently, a body of literature over the past decade has been centered on cytotoxicity, genotoxicity, and ecotoxicity of nanomaterials, pointing to the general understanding that nanotoxicity is often derived from the physiochemical properties of the nanomaterials and their interplay with the host environment [69, 76, 94, 108, 131, 164]. However, while biological and ecological systems constantly interact and are integrated in the network of nature, it remains a new challenge to evaluate and correlate the biological and

environmental impacts of nanoparticles within the same context [164, 199]. The fundamental units for both biological and ecological systems are mammalian and plant cells, which share numerous common traits in their cell organelles and properties. On the other hand, major differences do exist between these two types of cells, such as existence of the cell wall, chloroplasts and vacuoles in plant cell, and cell, which tends to be more round for mammalian cells and elongated for plant cells.

This chapter presents a first parallel study of carbon nanoparticle uptake by plant and mammalian cells. Specifically, *Allium cepa* and HT-29 human colonic adenocarcinoma cell lines were used as model plant and mammalian systems and were exposed to different doses of fullerene C_{70} suspended in NOM and fullerol $C_{60}(OH)_{20}$, a water-soluble fullerene derivative (Figure 3-1).
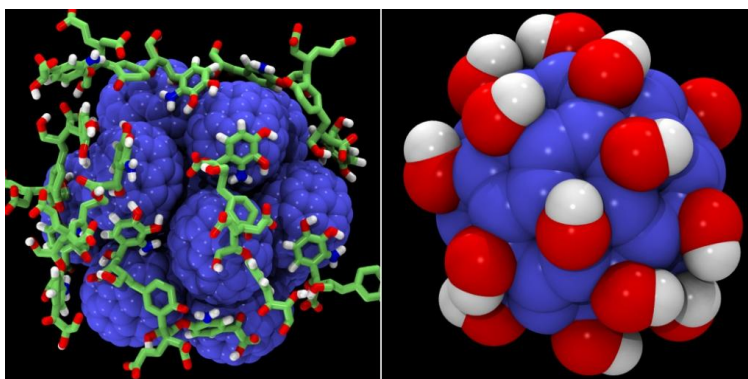
Figure 3-1 Atomistic illustrations of a C_{70}-NOM supramolecular assembly and a single $C_{60}(OH)_{20}$ molecule. In the left panel, the C_{70} molecules are shown in blue, while the heterogeneous NOM molecules are shown in green, red and white. In the right panel, the C_{60} molecule is shown in blue while the OH groups are illustrated in red and white.

3.2 Experimental Section

3.2.1 Carbon nanoparticle suspension preparation and characterization

Fullerenes C_{70} (SES Research, purity: 99%) (Figure 5.1 (left)) were dissolved in aqueous NOM (IHSS) solution to self assemble into C_{70}-NOM as described in chapter two. Different concentrations of C_{70}-NOM (from 10 to 110 mg/L) were prepared by diluting the stock of C_{70}-NOM suspension (1 mg/mL) using MilliQ water. The solubilities of the C70-NOM suspensions were characterized using UV-vis absorbance reader and were monitored during first 9 hours. Physical adsorption of NOM on fullerene surface does not alter the structure and properties of C_{70}. However, physical adsorption is less stable, and nanoparticles tend to aggregate overtime. The absorbance value of C_{70}-NOM was measured at 400 nm right after sonication (blue dots) and after 9 hours of keeping the sample at the room temperature after probe sonication (green dots) (Figure 3-2). Carbon nanoparticle samples incubated at room temperature for 9 h were used in all plant and mammalian cell experiments. The decrease in absorbance (green vs. blue) at the same wavelength indicates C_{70} precipitation; particularly, at high concentrations 110 mg/L the precipitation of C_{70}-NOM reached 30%.
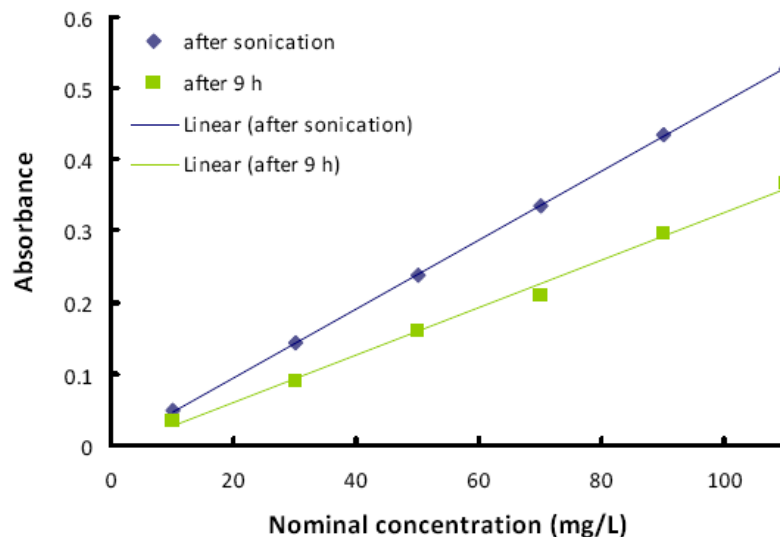
Figure 3-2. Absorbance of C_{70}-NOM vs. nominal C_{70} concentration. (Blue curve) Fresh samples measured immediately after probe sonication. (Green curve) Samples measured 9 hours after probe sonication.

The size distribution of nanoparticles was measured using dynamic light scattering techniques (Nanosizer S90). Here "size" refers to the hydrodynamic diameter of a Rayleigh particle. To remove dust particles from the ambient air and further to suppress scattering from large particles, which masks presence of the small nanoparticles, the suspension was filtered through a 20 nm pore size Anotop 10 (Whatman) filter and 0.45 μm pore size Nalgene filter in case of 10 mg/L and 110 mg/L if nominal C_{70}-NOM concentrations accordingly.

Figure 3-3 illustrates the continuous aggregation of C_{70}-NOM with increase of nanoparticles concentration; at lower concentrations of 10 mg/L, the hydrodynamic size

of C_{70}-NOM complexes was ranging from 18 to 44 nm (average 20 nm) (Figure 3-3 (top panel)), while with the increase of concentrations (110 mg/L), the hydrodynamic size of C70-NOM increases, ranging from 27 to 100 nm (average 35 nm) (Figure 3-3 (lower panel)).
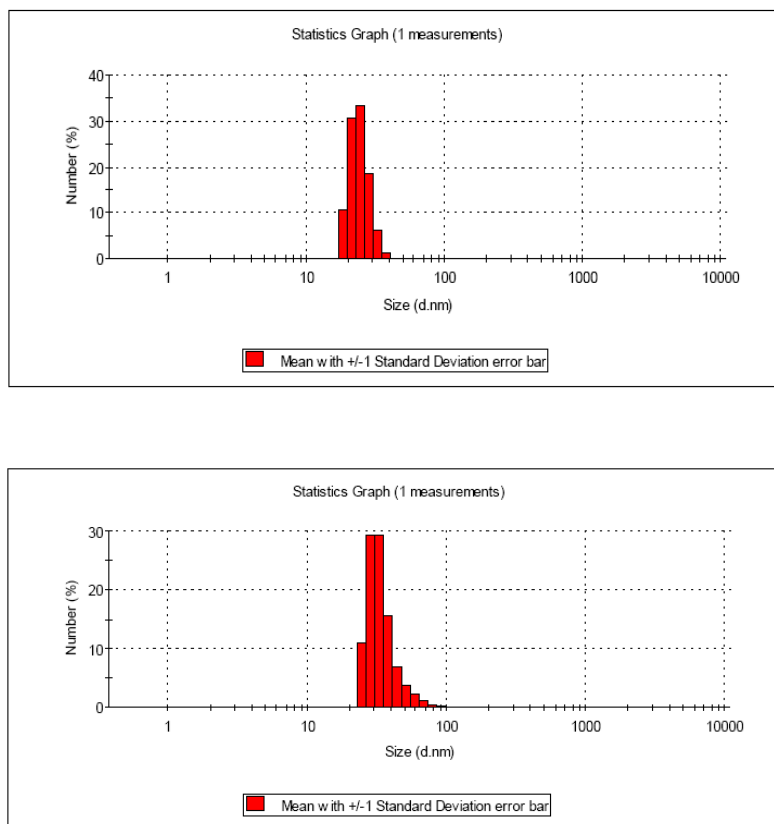
Figure 3-3. Hydrodynamic size of C_{70}-NOM at 10 mg/L (top panel) and 110 mg/L (lower panel), with Polydispersity Index (PDI) of 0.296 and 0.528 accordingly.

The large sizes and broad size distributions of C_{70}-NOM was attributed to the non-covalent binding between the C_{70} aggregates and the inhomogeneous, amphiphilic,

and aromatic-rich NOM. Consequently, C_{70}-NOM complexes were heterogeneous and more hydrophobic than the covalent structure of $C_{60}(OH)_{20}$.

Fullerol $C_{60}(OH)_{20}$ (Figure 3.1 (right)) was purchased from BuckyUSA and directly dissolved in Milli-Q water to obtain a stock of 1 mg/mL. The nanoparticle suspensions were diluted in Milli-Q at concentrations of 10-110 mg/L and their UV-vis absorbance was measured using a Biomate 3 spectrophotometer. The absorbance values of $C_{60}(OH)_{20}$ at 252 nm right after sonication and 9 h of keeping the sample at room temperature after sonication showed no precipitation, for all fullerols concentrations. Chemical modification of fullerene with OH groups requires the breakage of the sp2 bonds on the fullerenes surface, resulting in the alteration of the structure and optical, electrical and mechanical properties of fullerenes. Once covalently modified with hydrophilic hydroxyl groups, fullerols become hydrophilic and show stability overtime. To test the stability of such suspension, centrifugation at high velocity (10,000 g RCF) was applied to fullerol sample for 5 mins.

In Figure 3-4 the red dots stand for the absorbance values at 252 nm of each concentration before centrifugation (10,000 g RCF, 5 min), and the blue dots represent the absorbance values at the same wavelength after centrifugation. Thus, the differences in the absorbance values denote the amount of $C_{60}(OH)_{20}$ settled down or precipitated out of the suspensions.
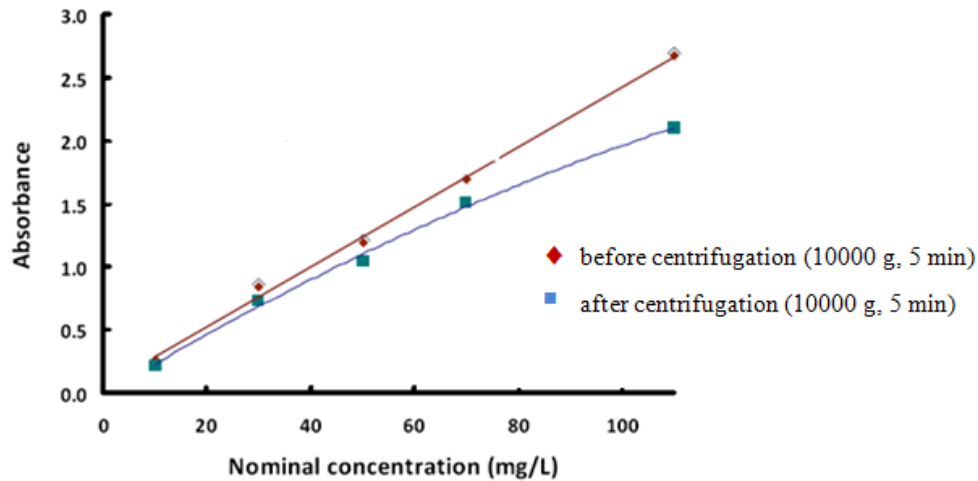
Figure 3-4. Absorbance of $C_{60}(OH)_{20}$ vs. nominal $C_{60}(OH)_{20}$ concentrations. Fresh samples measured immediately after probe sonication and samples measured 9 hours after probe sonication (red curve), samples measured after 10,000 g RCF centrifugation (5 min) (blue curve).

The hydrophilicity of fullerols was illustrated by their small size in the MilliQ water. For diluted solution of 10 mg/L in concentration, the presence of individual nanoparticles was detected. As illustrated in Figure 3-5 the hydrodynamic size ranges from 1.12-1.74 nm with an average value of 1.5 nm (van der Waals diameter of an individual C_{60} is 1 nm [6]). At higher concentrations (110 mg/L) fullerols formed larger size complexes through hydrogen bonding between their hydroxyl groups and water, and the hydrodynamic size ranges from 15.69-24.36 nm with an average value of 20 nm. In

comparison with C_{70}-NOM no filtration was applied to the $C_{60}(OH)_{20}$ suspension, due to the high solubilization of fullerenes in MilliQ water.
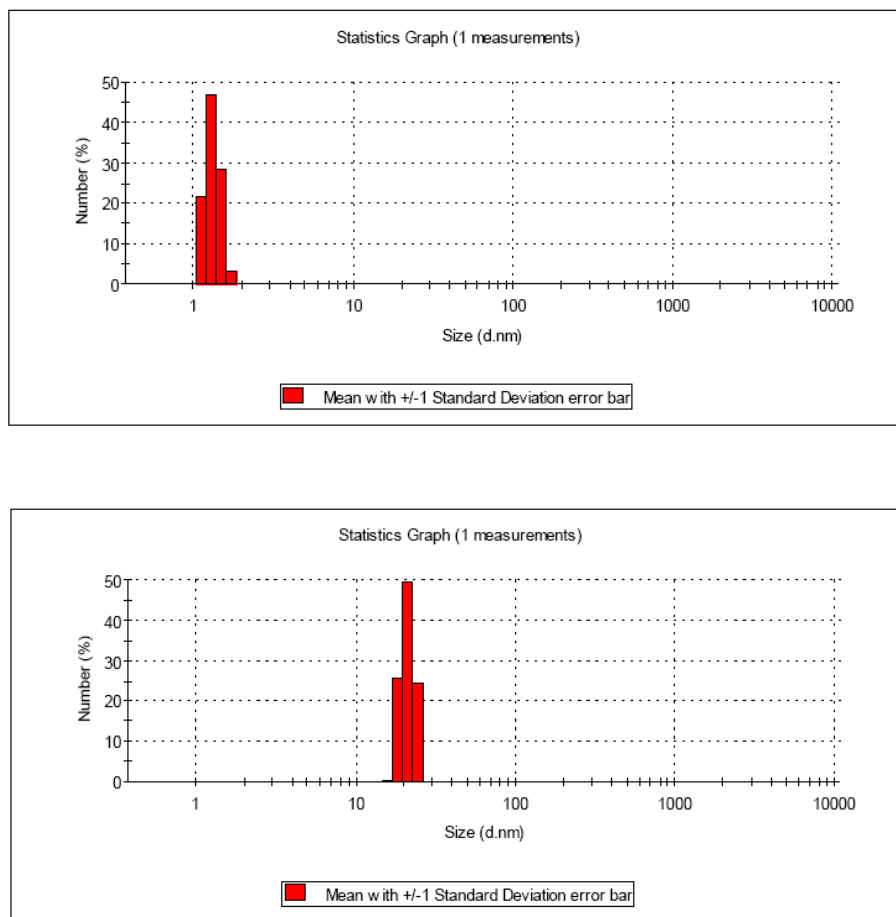
Figure 3-5. Hydrodynamic size of $C_{60}(OH)_{20}$ at 10 mg/L (top panel) and 110 mg/L (lower panel) with PDI of 0.725 and 0.843 accordingly.

TEM imaging was performed for dehydrated carbon nanoparticles. Figure 3-6 further confirms the better suspension of $C_{60}(OH)_{20}$ over C_{70}-NOM.

The surface charges of the nanoparticles were measured using a ZetaSizer Nano ZS, with a zeta potential of -34.3 mV recorded for C_{70}-NOM and a comparable but more stable -42.6 mV for $C_{60}(OH)_{20}$ (pH = 6.3).
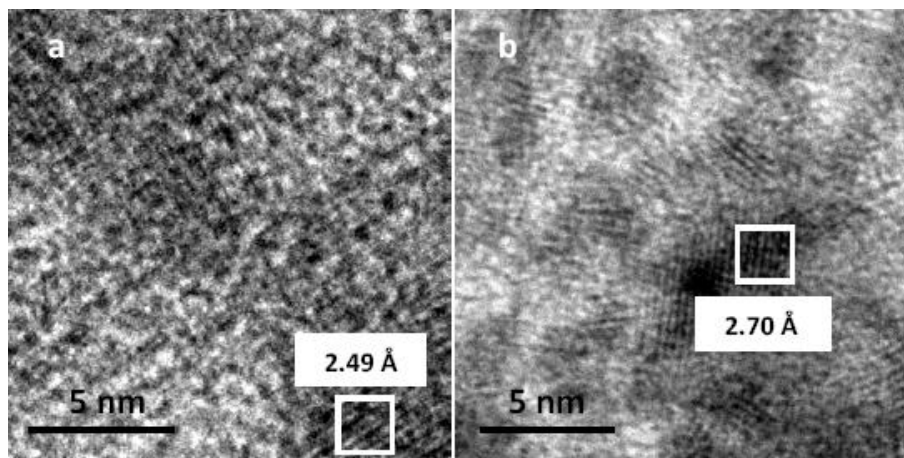
Figure 3-6. High resolution TEM images of C_{70}-NOM and $C_{60}(OH)_{20}$, showing (a) a C_{70}-NOM lattice spacing of 2.49 Å and (b) a $C_{60}(OH)_{20}$ lattice spacing of 2.70 Å

3.2.2 Plant and mammalian cell preparations

Allium cepa samples were obtained from produce quality onion bulbs. Storage leaves of area 1 cm^2 were removed, and laminar cells were collected from the inner layers of the plant tissue. Samples were immersed in $C_{60}(OH)_{20}$ and C_{70}-NOM suspensions to obtain final concentrations of 10-110 mg/L in MS buffer (pH = 6) [69] (Higher concentrations introduced significant aggregation, especially for C_{70}-NOM, and therefore were not included for the current study).

HT-29 human colonic adenocarcinoma cell lines were cultured in DMEM with 1% penicillin streptomycin, 1% sodium pyruvate, and 10% fetal bovine serum. Approximately 5,000 HT-29 cells were seeded in each well (200 µL) of an eight-chamber glass plate and allowed to attach overnight at 37°C with 5% CO_2. After the cells reached a 60% confluence C_{70}-NOM and $C_{60}(OH)_{20}$ were added in each chamber glass well to obtain final concentrations of 10, 30, 50, 70, 90 and 110 mg/L. After 9 h incubation, the cells were thoroughly rinsed three times using PBS buffer to remove dead cells and un-bound nanoparticles.

3.2.3 Viability assay and data analysis

After 9 h incubation and gentle shaking the plant cells samples were washed in MS buffer prior to the addition of a plant cell viability assay (Sigma). A stock solution of the viability assay contained 1% of PI and an equal amount of fluorescein diacetate (FD) in MS buffer. Each sample was incubated with 14.29% of the stock solution (total volume 400 µL) for 5 min before imaging with a Zeiss A1 microscope. Each data point was sampled from an area of approximately 8 mm^2, which contained an average of 303 onion cells. Twenty data points, corresponding to approximately 6,000 cells, were collected for each concentration used. Fluorescence images were taken from the FITC (for FD emission) and Rhod (for PI emission) channels. Damaged cells showed orange fluorescence (peak at 620 nm) in the nuclear region when viewed under the Rhod

channel. Data points were taken only for areas on the interior of the sample to exclude artificial damage due to handling. Significant difference from the control was examined using student *t*-test. Statistical significance was accepted when the probability of the result assuming the null hypothesis (p) is less than 0.01.

3.2.4 Transmission electron microscopy

For TEM imaging, thin layers of *Allium cepa* cells were fixed in 3.5% glutaraldehyde overnight and dehydrated in a graded series of ethanol. The dehydrated samples were then embedded in LR white resin overnight at 40°C and sectioned into thin films approximately 200 nm thick using an Ultracut E Microtome. No osmium tetroxide was added in order to eliminate the introduction of artifacts. TEM images were acquired using a Hitachi H7600 microscope operated at 80 and 100 kV. The lattice structures of C_{70}-NOM and $C_{60}(OH)_{20}$ were captured using a Hitachi H9500 microscope operated at 150 kV. The lattice spacings of the nanoparticles in *Allium cepa* were analyzed by performing Fast Fourier Transform of the TEM images, using "Diffractogram" software.

3.2.5 Confocal microscopy

An Argon laser of 488 nm was used as an excitation source for confocal imaging (LSM510, Zeiss), and 10 images (900×900 µm) were acquired for each sample condition using a 10× objective. The images were then analysed and the cells of each sample were counted using LSM Image Browser.

3.3 Results and discussions

3.3.1 Plant cell responses to carbon nanoparticles

Laminar *Allium cepa* cells were incubated separately with C_{70}-NOM and $C_{60}(OH)_{20}$ of 10~110 mg/L, for 9 h. Figure 3-7 shows optical images of *Allium cepa* cell morphology (bright field) and loss of membrane integrity (propidium iodide or PI, emission in orange) in the presence of $C_{60}(OH)_{20}$ (Figures 3-7 (a-f)) and C_{70}-NOM (Figures 3-7 (g-i)). Specifically, more orange fluorescent spots can be seen in Figure 3-7 (e) than Figure 3-7 (b), indicating increased cell damage with $C_{60}(OH)_{20}$ concentration of 30 mg/L to 70 mg/L. The bright green fluorescence regions in Figures 3-7 (c), (f), and (i) signify hydrolysis of FD by intracellular esterases, which were indicative of viable cells.
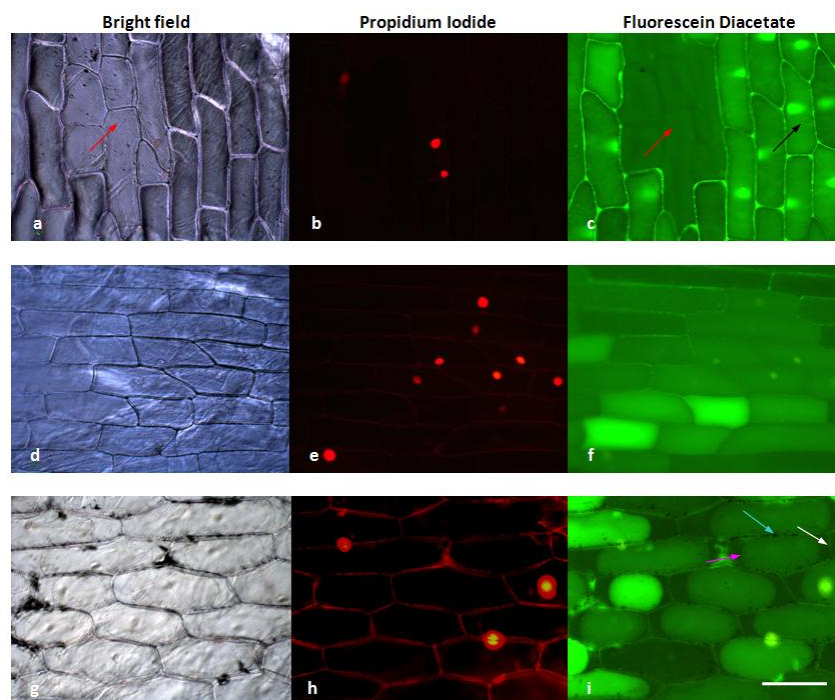
Figure 3-7. Optical imaging of *Allium cepa* plant cell damage in the presence of C_{70}-NOM and $C_{60}(OH)_{20}$. (a-c) Plant cells incubated with $C_{60}(OH)_{20}$ of 30 mg/L for 9 h. (d-f) Plant cells incubated with $C_{60}(OH)_{20}$ of 70 mg/L for 9 h. (g-i) Plant cells incubated with C_{70}-NOM of 50 mg/L for 9 h. Images were acquired using the bright field, Rhodamine (propidium iodide), and FITC (fluorescein diacetate) modes. (b, e, h) The orange fluorescence indicates staining of nucleic acids by propidium iodide due to loss of cell viability. (c, f, i) The bright green fluorescence indicates hydrolysis of fluorescein diacetate by intracellular esterases of viable cells. (a, c) Examples of non-viable (red arrows) and viable cells (black arrow). (g-i) Osmosis procedures were applied to split plasma cell membranes (pink arrow in (i)) from plant cell walls (white arrow in (i)). Aggregation of C_{70} particles is exemplified by the blue arrow in (i). All images are of the same scale (scale bar: 50 μm).

The cells shown in Figures 3-7 (g-i) were further treated with mannitol (0.8 M) for 15 min, after their incubation with C_{70}-NOM of 50 mg/L for 9 h. The mannitol gradient across the cell surfaces induced an osmotic pressure, which in turn split plant cell walls from their underlining plasma membranes. C_{70} aggregates were revealed by the osmosis assay as mostly adsorbed on or trapped within the hydrophobic cellulose matrices of the plant cell walls (Figure 3-7 (i)). A comparison between the bright field and fluorescence images shows a good correlation between damaged membranes (orange spots in Figures 3-7 (b) and (e)), cells of impaired viability (dim green regions in Figures 3-7 (c) and (f)), and cells of altered morphology (rough cell surfaces in Figures 3-7 (a) and (d)). The appearances of contagious nonviable cells (regions denoted by red arrow in Figure 3-7 (c) and orange spots in (e)) further suggest that upon $C_{60}(OH)_{20}$ uptake cells underwent necrosis, which is typically invoked by abnormal environmental conditions and viruses.

A summary of plant cell damage in the presence of C_{70}-NOM and $C_{60}(OH)_{20}$, each of 10-110 mg/L is shown in Figure 3-8.
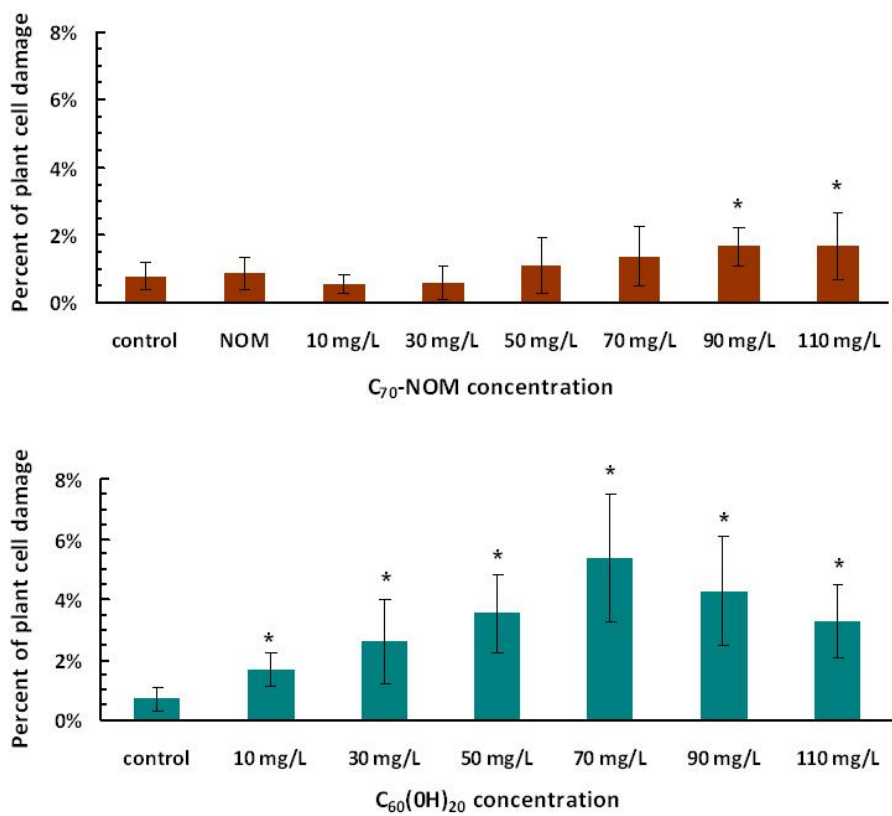
Figure 3-8. Percent of *Allium cepa* plant cell damage in the presence of C_{70}-NOM and $C_{60}(OH)_{20}$ of various concentrations. Incubation time: 9 h. The asterisks indicate data which are statistically different from the control ($p<0.01$). NOM: positive control.

The damage was calculated by counting percent of nonviable cells in the PI channel, while the FD channel was used as a reference due to its susceptibility to crosstalk from the PI channel and cell autofluorescence. As shown in the top panel of Figure 3-8, C_{70}-NOM caused a mere 0.8% more plant cell damage than the control at 90 mg/L and 110 mg/L, and no damage at lower concentrations. This phenomenon is

attributed to the large size and hydrophobicity of the C_{70}-NOM, which tended to block the porous plant cell wall and form clusters therein through hydrophobic interactions (Figures 3-9 (b) and (c), Figure 3-2).
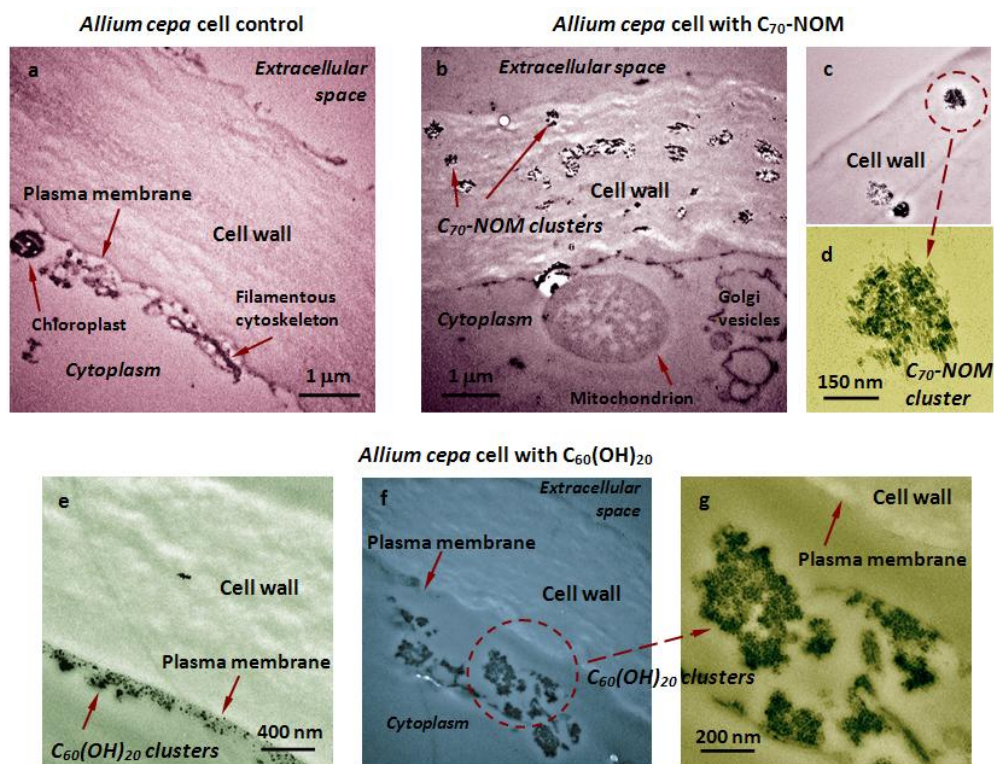
Figure 3-9. TEM imaging of carbon nanoparticle uptake by *Allium cepa* plant cells. (a) Control showing plant cell wall and plasma membrane. The cell wall typically bends towards its intracellular space. (b-d) Plant cell walls entrapped with C_{70}-NOM clusters of 50-400 nm. C_{70}-NOM concentration: 50 mg/L. (d) Magnified view of a C_{70}-NOM cluster in (c). (e-g) Translocation of $C_{60}(OH)_{20}$ across plant cell walls. $C_{60}(OH)_{20}$ clusters can be seen (e) near the interface between the plant cell wall and the plasma membrane and (f, g) in intracellular space. $C_{60}(OH)_{20}$ concentration: 50 mg/L. (g) Magnified view of the $C_{60}(OH)_{20}$ clusters in (f).

The lattice structures of C_{70}-NOM and $C_{60}(OH)_{20}$ in *Allium cepa* cells are confirmed in Figure 3-10.
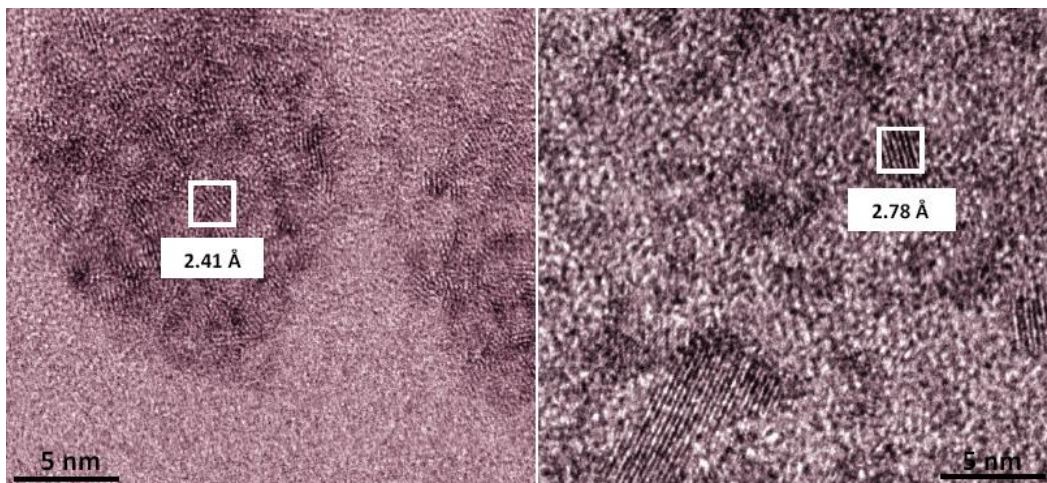
Figure 3-10. High resolution TEM images of C_{70}-NOM $C_{60}(OH)_{20}$ in *Allium cepa*, showing (left) a C_{70}-NOM lattice spacing of 2.41 Å, and (right) a $C_{60}(OH)_{20}$ lattice spacing of 2.78 Å. Images were obtained for the nanoparticles in *Allium cepa*.

$C_{60}(OH)_{20}$, in comparison, triggered a steady rise in cell damage, causing a maximum 4.7% more damage than the control at 70 mg/L. Due to their small size and good solubility, $C_{60}(OH)_{20}$ readily permeated through the plant cell wall driven by a concentration gradient, and were mostly excluded by the plasma membrane due to their hydrophilicity, mutual electrostatic repulsion, and hydrogen-bonding with water [120]. Under capillary and *van der Waals* forces these nanoparticles were confined between the cell wall and the plasma membrane (Figure 3-11), and accumulated under the concentration gradient to protrude the plasma membrane (Figure 3-9 (e)).
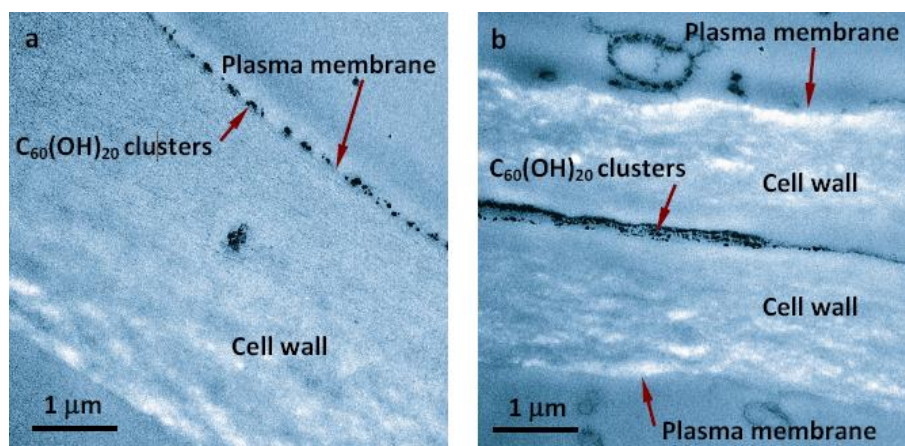
Figure 3-11. TEM images of $C_{60}(OH)_{20}$ fate in plant cells. (a) Presence of $C_{60}(OH)_{20}$ clusters at the interface between plant cell wall and plasma membrane. (b) Presence of $C_{60}(OH)_{20}$ clusters in the apoplastic pathway between two plant cell walls.

Since fullerols—unlike pristine fullerenes—have been shown as relatively inactive in creating ROS [52], the loss of membrane integrity (Figures 3-7 (b), (e)) is therefore inferred as a result of mechanical damage exerted by $C_{60}(OH)_{20}$ aggregation. Such damage would impinge on membrane fluidity and the transport of nutrients and ions between the plant cell and its extracellular space, further stressing the physiological state of the cell and its neighboring cells. $C_{60}(OH)_{20}$ clusters occasionally appeared near the plasma membrane within the cytoplasm (Figures 3-9 (f) and (g)), likely due to membrane damage and a low-level steady state endocytosis [200]. Although not intended to be a focus in this study, accumulation of $C_{60}(OH)_{20}$ between adjacent epidermal cell walls (Figure 3-11 (b)) further implies that transport of $C_{60}(OH)_{20}$ in the plant tissue was partially conveyed through the apoplastic pathway [201], whose blockage could also

impact on cell viability. The ease of cell damage at 90 mg/L and 110 mg/L (Figure 3-8 (lower panel)) is attributed to the gradual aggregation of $C_{60}(OH)_{20}$ at these concentrations, which would have hindered nanoparticle uptake.

3.3.2 Mammalian cell responses to carbon nanoparticles

HT-29 cell lines were cultured to 60% confluence, which were then incubated separately with C_{70}-NOM and $C_{60}(OH)_{20}$ of 10~110 mg/L, for 9 h. In contrast to the observations made above for plant cells, mammalian cells showed distinctly different responses to the two types of carbon nanoparticles. After 9 h incubation and thorough washing to remove dead cells and unbound nanoparticles, the number/density of viable HT-29 cells decreased continuously with increased C_{70}-NOM concentration up to 70 mg/L, and then leveled off at higher concentrations due to nanoparticle aggregation (Figure 3-12 (lower panel)). The cell morphology also changed from the healthy elongated form to the less viable more spherical shapes at higher C_{70}-NOM concentrations, showing abundant nanoparticle aggregates bound to/imbedded in the cell membranes (Figure 3-12 (top panel)). Cell lysis was visible, likely due to exhaustive endocytosis (Figure 3-12 (d)) and occurrence of necrosis in the damaged cells. By comparison, no cell damage was found for HT-29 cells exposed to $C_{60}(OH)_{20}$ of all concentrations used (Figure 3-13), thus confirming the low affinity of $C_{60}(OH)_{20}$ for mammalian cell membranes. These contrasting damages induced by the noncovalent

assembly of C_{70}-NOM and covalent $C_{60}(OH)_{20}$ to HT-29 cells are in good agreement with the *in vitro* study by Sayes et al. [52] and the simulations by Qiao et al. [120], on the cytotoxicities of pristine fullerene C_{60} and fullerol $C_{60}(0H)_{24}/C_{60}(OH)_{20}$.
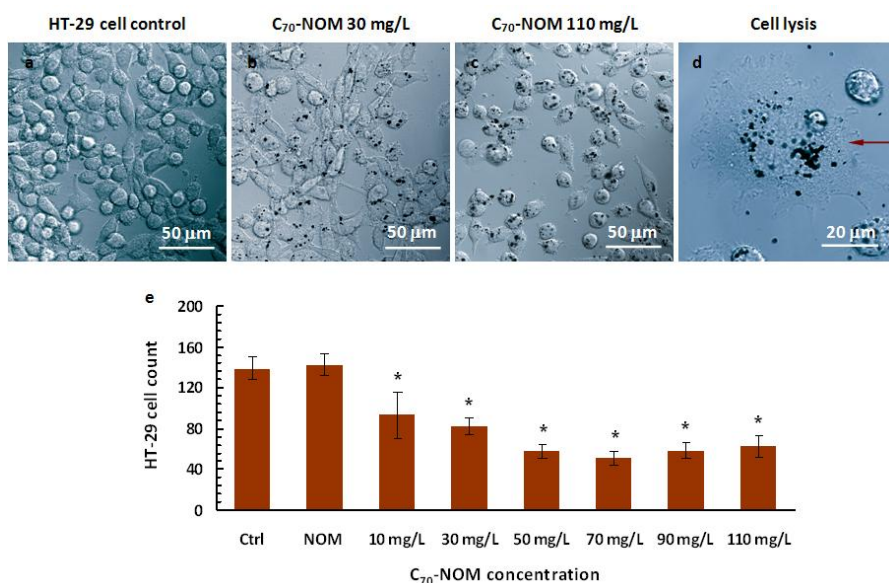
Figure 3-12. Mammalian cell damage in the presence of C_{70}-NOM of various concentrations. Incubation time: 9 h. (a) HT-29 cell control. (b) HT-29 cells in the presence of C_{70}-NOM of 30 mg/L. (c) HT-29 cells in the presence of C_{70}-NOM of 110 mg/L. (d) Cell lysis (indicated by red arrow) observed after incubating with C_{70}-NOM at 110 mg/L and washing. The aggregation of C_{70} particles is evident in (b-d). (e) HT-29 cell count in the presence of C_{70}-NOM of various concentrations. The asterisks indicate data which are statistically different from the control ($p<0.01$). NOM: positive control.

This suggests that C_{70}-NOM impacts mammalian cells similarly to C_{60}, possibly due to the hydrophobicity and dissociation of C_{70}-NOM to facilitate C_{70} interacting with the fatty acyl chains in the lipid bilayer. Such hydrophobic interaction, when coupled with the ROS production by C_{70}, could result in cytotoxicity and cell lysis, especially at high nanoparticle concentrations [202]. Unlike C_{70}-NOM, $C_{60}(OH)_{20}$ is more hydrophilic and, therefore, is largely excluded by mammalian cells due to the same reasons discussed above for plant cell membranes.
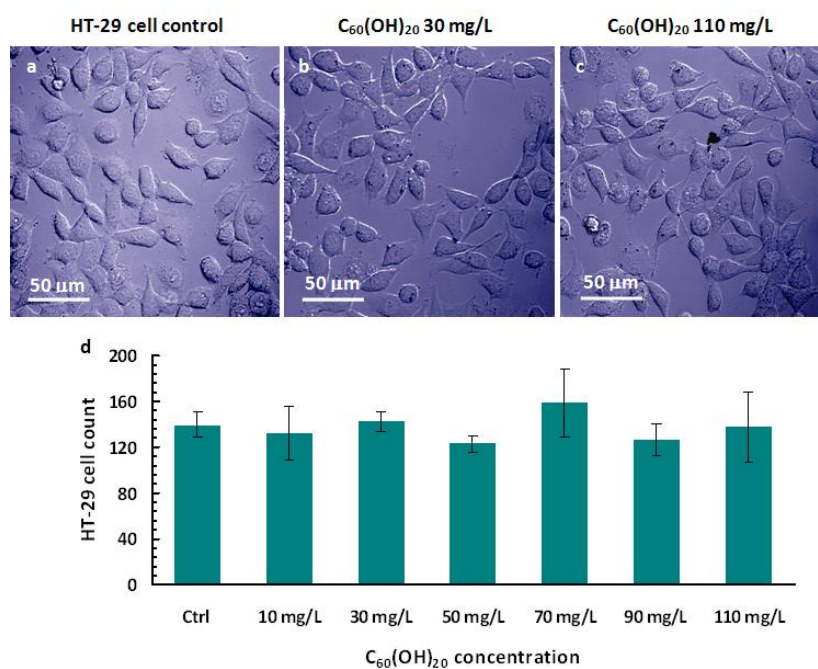
Figure 3-13. Mammalian cell damage in the presence of $C_{60}(OH)_{20}$ of various concentrations. Incubation time: 9 h. (a) HT-29 cell control. (b) HT-29 cells in the presence of $C_{60}(OH)_{20}$ of 30 mg/L. (c) HT-29 cells in the presence of $C_{60}(OH)_{20}$ of 110 mg/L. (d) HT-29 cell count in the presence of $C_{60}(OH)_{20}$ of various concentrations.

3.3.3 Comparison of plant and mammalian cell responses to carbon nanoparticles

The differential plant and mammalian cell responses to nanoparticles (Figure 2-8 (top panels) vs. Figure 3-12 (e); Figure 2-8 (lower panel) vs. Figure 3-13 (d)) can be understood as a combined result of nanoparticle filtration by the porous plant cell wall, confinement on nanoparticle mobility by the hydrophobic, thick (a few to tens of micrometers), and rigid plant cell wall and the amphiphilic, thin (~7 nm), and fluidic plasma membrane [201], as well as the physiochemical properties of the nanoparticles. The filtration by the plant cell wall favors uptake of smaller and more hydrophilic nanoparticles. Post-translocation these small and hydrophilic nanoparticles are confined at the interface between the plant cell wall and the plasma membrane, and self assemble to initiate a mechanical damage to the plasma membrane. Larger and more hydrophobic nanoparticles of low concentrations exert little damage on the plant cell. However, at high concentrations adsorption of hydrophobic nanoparticles onto the plant cell wall and their retention within the plant cell wall would still impact on the physiological state of the plant cell, as implied by the emergence of cell damage with C_{70}-NOM of 90 mg/L and 110 mg/L (Figure 3-8 (top panel)). Absence of a cell wall in mammalian cells is favorable for minimizing the adverse effect of hydrophilic nanoparticles, but encourages membrane partitioning [203] by hydrophobic and/or noncovalently-functionalized nanoparticles to induce cell damage. Such differentiality on nanoparticle uptake may help shed light on the intensive debate on nanotoxicity, and shall prove beneficial for guiding the design of nanomedicine and environmentally sustainable nanotechnologies.

CHAPTER FOUR

CYTOPROTECTIVE PROPERTIES OF A FULLERENE DERIVATIVE AGAINST

COPPER

Chapter three examined the differential uptake of carbon nanoparticles by plant and mammalian cells. It was revealed that the interaction between fullerenes and the cell depends on both the surface properties of the nanoparticles and the properties of the cell. Conceivably, the presence of a thick, rigid, and porous cell wall acts as a barrier for large and hydrophobic nanoparticles and their aggregates while imposing little hindrance to the translocation of hydrophilic nanoparticles to induce increased toxicity. In contract to plant cells, more hydrophobic carbon nanomaterials induced more pronounced damage in mammalian cells [69]. In addition to these biophysical observations, the antioxidant, antiviral, and anti-cancerous activities of fullerene derivatives have been reported in the literature [64, 85, 86], and such phenomena were attributed to suppressed accumulation of superoxide- and hydroxyl radical-initiated lipid peroxidation as well as initiation of free radical-scavenging activities of the nanoparticles. Despite these findings, few investigations so far have considered how the occurrence of nanoparticle exposure may impact cell uptake and exchange of physiological ions and toxins, an aspect essential for describing cell response to nanoparticles and relevant to the field studies of nanotoxicology and nanomedicine.

The goal of chapter four is to assess a complex scenario of cell exposure first to fullerol and then to copper. The latter is an essential element for continuous cell growth and development, but in excess is toxic and can catalyze the formation of radical species such as ROS, which are capable of cell destruction [204, 205].

4.1 Introduction

Both cytotoxic and cytoprotective properties of fullerene derivatives have been documented for mammalian and plant systems [40, 52, 64, 69, 72, 74, 75, 79, 85, 86, 206]. For example, it was reported that fullerenes were capable of increasing toxicity through stimulation of inflammatory response and involvement of oxidative stress [40, 52], while other data suggested that fullerenes and their derivatives imposed no acute or sub-acute toxicity on mammalian cell lines and organisms [72, 74, 75, 79]. Furthermore, the some of the studies claimed the cytoprotective properties of fullerene derivatives in mammalian cells [64, 85, 86]. It is known that the fate of nanoparticles in living systems is derived from both the physicochemical properties of the nanoparticles [206] as well as the regulated activities of the host system [39].

Compared with pristine fullerenes, the water-soluble fullerene derivative $C_{60}(OH)_{20}$, or fullerol, has been found far more compatible with mammalian systems. Fullerol has been studied both experimentally and through computer simulations

concerning their interactions with nucleic acids, Taq DNA polymerase, microtubules, and plant and mammalian cells [125, 131, 133, 134, 191]. Regardless of many potential biological and biomedical applications of fullerols, little is understood how the nanoparticle may impact cell uptake and cell responses.

In the present study we expose human colon carcinoma HT-29 cells first to $C_{60}(OH)_{20}$ nanoparticles and then to copper ions. The selection of copper as a model toxin is based on the consideration that its cytotoxic mechanisms have been well documented [207-209]. Furthermore, copper is one of the most abundant physiological elements and is required for important cellular processes such as respiration, ion transport, pigmentation, peptide hormone production, and oxidative stress production. Copper is also an element which is required by cells, and could be toxic when in excess. A recent study [210] showed that copper-mediated amyloid cytotoxicity was not due to ROS production but copper binding to the human islet amyloid polypeptide, which changed the conformation of the protein and induced the formation of cytotoxic granular oligomers. On the other hand, ROS inhibition by copper has also been reported as a result of cytosolic antioxidant defense [211], suggesting that copper ions may be involved in both the generation of and defense against ROS in the cell.

In the following we present an *in vitro* study on HT-29 cells doubly exposed to both $C_{60}(OH)_{20}$ nanoparticles and copper ions. We perform cell count and lactate dehydrogenase (LDH) and intracellular ROS production assays to quantify the cytotoxic effects induced by fullerol and copper in combination. Based on these protocols we draw

119

the conclusion that fullerene derivative $C_{60}(OH)_{20}$ is a cytoprotective agent against the adverse effects of copper.

4.2 Experimental section

4.2.1 Nanoparticle suspension characterization

$C_{60}(OH)_{20}$ was purchased from BuckyUSA. The nanoparticles were suspended directly in Milli-Q and sonicated for 10 min to prevent agglomeration. The size distribution of the nanoparticles was determined using dynamic light scattering (Malvern, nanosizer S90, range: 0.3 nm-5 μm, resolution: 1 nm) at room temperature. A single peak value at ~1 nm was identified for the suspension. The good solubility of $C_{60}(OH)_{20}$ in water was confirmed by its zeta potential, which was measured at -57.9 mV using a Zetasizer (Nano ZS). Such negative charge of $C_{60}(OH)_{20}$ is attributed to the bond strenching or deprotonation of the hydroxyl groups of the nanoparticle in the polar solvent of water [16, 30]. The key physical parameters of the nanoparticle suspension are summarized in the supporting information (Table 4-1).

Hydrodynamic diameter (nm)	Zeta potential (mV)	Polydispersity index
1.11±0.34	-57.9±1.1	0.141

Table 4-1. Characterization of $C_{60}(OH)_{20}$ in MilliQ water.

4.2.2 HT-29 cell exposure to $C_{60}(OH)_{20}$ and copper

HT-29 human colon carcinoma cells were obtained from ATCC (HTB-38, American Type Culture Collection, Manassas, VA) and grown to 90-95% confluency. The cells were cultured in McCoy's 5a medium supplement with a final concentration of 10% fetal bovine serum (FBS), 100 U/mL penicillin, and 100 µg/mL streptomycin at 37°C and with 5% CO_2. The cultured cells were washed once with phosphate buffered saline (PBS, pH 7.4) and trypsinated for 5 min at 37°C and with 5% CO_2. Newborn calf serum was added to the RPMI-1640 medium to halt the action of the enzyme. Tubes containing removed cell medium and trypsinated cells were centrifuged for 5 min at 5,418 g RCF to spin the cells down. The supernatant was removed and the cells were resuspended in cell medium. For cytotoxicity analysis, 1×10^6 cells were seeded with 3 mL of total medium volume in a 6-well plate, to obtain a confluent layer of approximately 90-100% after 33 h. For cell viability, proliferation analysis, and intracellular ROS production analysis, 2×10^4 cells were seeded with 100 µL of total cell medium in a 96-well plate to acquire a confluent layer of approximately 90-100% after 33 h. The copper ion solution was made by solubilising $Cu(NO_3)_2$ in Milli-Q. The cells were exposed to selected fullerol concentrations in a humidified atmosphere at 37°C and with 5% CO_2.

4.2.3 Analysis of cytotoxicity

The HT-29 cells were exposed to 20 mg/L of fullerols for 9 h. After exposure the cells were washed thrice with PBS and then treated with 35 µM of copper in cell medium, corresponding to 20% of cell death (Lethal Dose, or LD20), and 85 µM of copper, corresponding to 50% of cell death (LD50) measured for the metal ions (figure 4-1(b)). After 24 h of exposure to copper the medium was discarded and cells were washed thrice with PBS. Approximately 2 mL of trypsin was added and incubated with the cells for 5 min at 37°C and with 5% CO_2, and 0.5 mL of newborn calf serum was added to the trypsinised cells. Cell count was performed in a glass chamber, by mixing 0.1 mL of the cell suspension with 0.9 mL of 0.4% Trypan Blue Solution (Sigma). The cell count was performed in triplicate for each sample.

4.2.4 Cell viability and proliferation assay

A DHL cell viability and proliferation assay kit (AnaSpec) was used to monitor cell damage and reproduction. This fluorescence method detects the number of viable cells based on their active mitochondrial dehydrogenase activity. Cell proliferation is continuously measured over 12 h, with resaurin used as a sensitive redox indicator. Resaurin is reduced to the strongly fluorescent resorudin by accepting electrons from

mitochondrial respiratory chain in live cells. In our assay the cells were exposed to 20 mg/L and 50 mg/L of $C_{60}(OH)_{20}$ for 9 h. After exposure, the cells were washed thrice with PBS and treated with copper of 85 µM (LD50) in the cell medium. After an additional 6 h and 12 h of exposure to copper (37°C, 5% CO_2) the medium was discarded and the cells were washed thrice with PBS. After this step 20 µL of the assay solution was added to 80 µL of the medium and incubated with the cells for 3 h at 37°C. The cell fluorescence was finally measured on a plate reader (FLx800, BioTek Instruments), for Ex/Em = 530/590 nm.

4.2.5 Intracellular ROS production

The hydroxyl, peroxyl, or other ROS activities were measured within living cells using an OxiSelect ROS Assay Kit (Cell Biolabs, Inc.), based on the fluorescence intensity of 2',7'-dichlorodihydrofluoresceine. The oxidation-sensitive fluoroprobe 2',7'-dichlorofluorescein diacetate (DCFH–DA) diffuses into the cells and is deacetylated by cellular esterases to non-fluorescent 2',7'-dichlorodihydrofluorescein, which is rapidly oxidized to highly fluorescent 2',7'-dichlorodihydrofluoresceine by the ROS. In our experiment the HT-29 cells were seeded in a 96-well plate overnight. The medium was removed from all wells and discarded. The cells were gently washed thrice with PBS. Approximately 100 µL of 1X DCFH–DA/media solution was added to the cells and incubated for 60 min at 37°C. The dye was removed and the cells were washed thrice

again with PBS. Afterwards the DCFH-DA-loaded cells were treated with 20 mg/L of fullerols for 9 h. The fluorescence of the cells was measured on the plate reader (FLx800, BioTek Instruments) at Ex/Em = 480/530 nm during the incubation. To monitor the ROS accumulation induced by copper, the cells were washed with PBS thrice after treatment with $C_{60}(OH)_{20}$, and copper of LD50 concentration was then added to the cell medium. As a positive control, 10 µM of oxidant H_2O_2 was added to the cells, with and without being supplemented with $C_{60}(OH)_{20}$. The fluorescence of 2',7'-dichlorodihydrofluoresceine was measured 9 h later.

4.2.6 Analysis of $C_{60}(OH)_{20}$ interaction with HT-29 cells

UV-vis absorbance measurement was performed (BioMate 3) to infer the adsorption and/or uptake of fullerols by the HT-29 cells. The absorbance spectra of the samples were scanned for the wavelength range of 240-390 nm. $C_{60}(OH)_{20}$ in the concentrations of 20 mg/L and 100 mg/L were mixed respectively with RPMI-1640 cell medium and PBS. The relative blanks for these measurements were RPMI-1640 medium and PBS accordingly. Approximately 1×10^6 cells were seeded with 1 mL medium in a 12-well plate overnight. The medium was then discarded and the cells were treated with new medium and PBS, with and without $C_{60}(OH)_{20}$. After 9 h of incubation, the total liquid volumes from all samples were collected and the cells were washed thrice with the medium or PBS, respectively. This step was done to match the experimental conditions,

where the cells were washed with PBS thrice to remove free nanoparticles. The absorbance of the collected samples was measured for the blanks, the medium and PBS, and precise dilutions were taken into account. The RPMI-1640 cell medium is known to contain a variety of vitamins, amino acids, and proteins, which aid cells for their development, growth, and reproduction. To eliminate the differences in absorbance spectra due to the cell uptake of biomolecules, relative controls -- such as the medium and PBS -- were also added to the cells for 9 h, collected and used as blanks. The difference between the absorbance of $C_{60}(OH)_{20}$ before and after incubation with the cells provided quantitative data on the adsorption and uptake of the nanoparticles by the HT-29 cells.

4.3 Results and discussions

4.3.1 Cytotoxicity analysis

The toxicity of copper ion (LD50) has been reported to be in the range of 15 µg/mL of Cu^{2+} [23-25], while $C_{60}(OH)_{20}$ alone at concentrations up to 100 mg/L did not induce toxicity in HT-29 cells after 9 h of incubation [21]. Detailed dose dependence curves representing the toxicity effects of copper and $C_{60}(OH)_{20}$ on HT-29 cell line are presented in Figure 4-1 for our study.
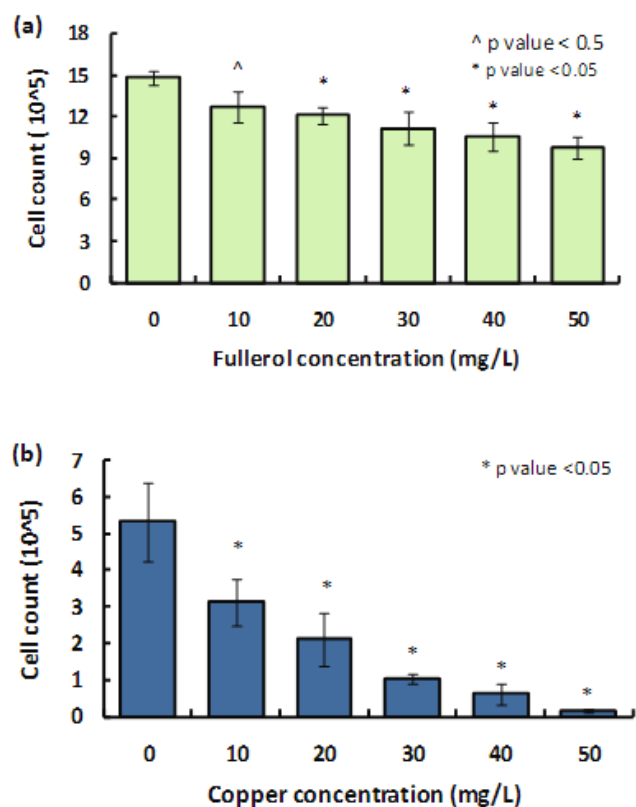
Figure 4-1. Cytotoxicity of fullerols and copper ions on HT-29 cells. (a) Dose-response curve shows cell counts after 33 h of exposure to fullerols. (b) Dose-response curve shows cell counts after 24 h of exposure to copper. The results shown are the means ± standard errors of three experiments. Statistically significant differences between the samples and the controls were determined by the Student t-test (*: $p<0.05$, ^: $p<0.5$).

Consistently, $C_{60}(OH)_{20}$ of 50 mg/L induced a maximal damage of 33.8% after 33 h of incubation with the HT-29 cells (Figure 4-1(a)), while copper nitrate of 10 mg/L and above caused significant toxicity on the HT-29 cells (Figure 4-1(b)). The key lethal doses

(LD10, LD20, and LD50) of copper ions and LD10 and LD20 of $C_{60}(OH)_{20}$ on the HT-29 cells are summarized in Table 4-2 and 4-3.

	LD 10	LD 20	LD 50
Cell count, 10^5	4.79	4.07	2.53
Concentration, mg/L	3.0	6.0	16
Concentration, μM	20	35	85

Table 4-2. Copper lethal doses on HT-29 cells (cell count).

	$LD_{fullerol}10$	$LD_{fullerol}20$
Cell count, 10^5	12.54	11.10
Concentration,mg/L	10	20
Concentration, μM	9.4	18.8

Table 4-3. Fullerols lethal doses on HT-29 cells (cell count).

Figure 4-2 shows optical images (Motic AE31, Martin Microscope Company) of HT-29 cells in the presence of $C_{60}(OH)_{20}$ and copper ions. Specifically, Figures 4-2(b) and (d) show the cells pretreated with 50 mg/L of $C_{60}(OH)_{20}$, while Figures 4-2(c) and

(d)) correspond to the cells exposed for 24 h to additional copper ions of LD50 concentration. No changes in cell density or shape were observed in Figure 4-2(b) compared with 2(a), indicating minimal cell damage caused by the $C_{60}(OH)_{20}$.

In contrast, significant morphological changes can be seen for the cells in figure 4-2(c), where the viable elongated cells turned into round shaped and were detached from the well surfaces due to the loss in cell viability or cell death. Specifically, the wells pretreated with $C_{60}(OH)_{20}$ showed higher numbers of healthy cells (Figure 4-2(d) vs. Figure 4-2(c)), implying a reduction of copper-induced cell damage mediated by the nanoparticles.
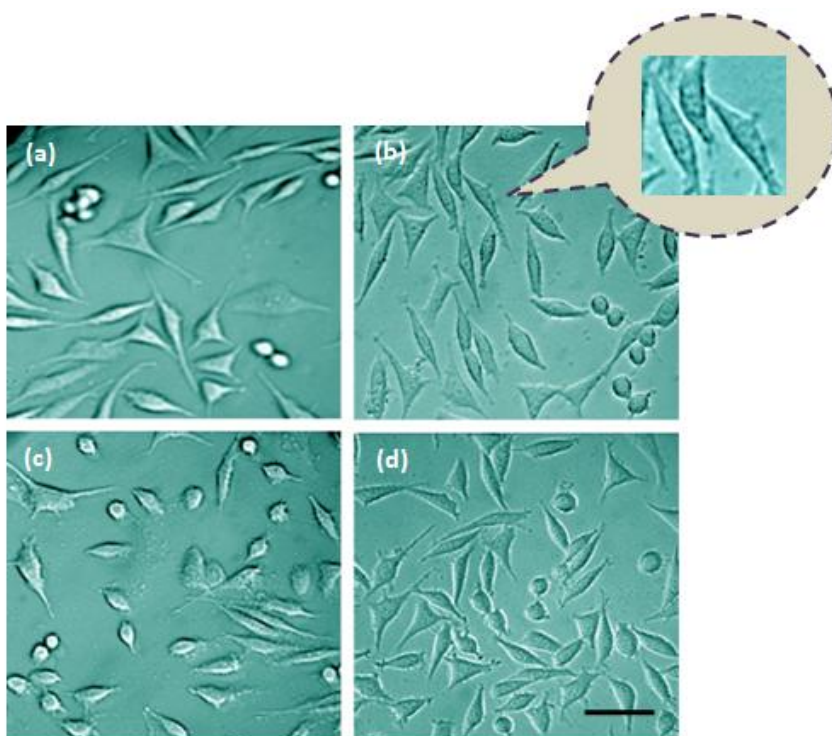
Figure 4-2. Optical images of HT-29 cells exposed to fullerols and copper ions. The cells were incubated in the presence (b and d) and absence (a and c) of 50 mg/L fullerols for 9

h. The cells were washed with PBS thrice and treated with medium containing LD50 of copper (c and d) and medium containing no copper (a and b) for 24 h. The cells in (b) and (d) show more rugged surfaces relative to those in (a) and (c), indicating fullerol adsorption on the cell membranes as exemplified by the inset in (b). All images are of the same scale (scale bar: 50 μm).

The effect of cell damage inhibition by $C_{60}(OH)_{20}$ is quantified in Figure 4-3. Decreased toxic responses were recorded for the cells pre-exposed to 20 mg/L $C_{60}(OH)_{20}$ (right bars, "Medium+Fullerol") relative to the corresponding controls (left bars, "Medium"), by 68.9% and 75.0%, after the cells were washed and then exposed to copper of LD20 and LD50 concentrations (Figure 4-3(a)). This effect can be attributed to the binding of the negatively charged $C_{60}(OH)_{20}$ in the medium to the positive domains of the membrane proteins, or the dipolar inteactions between the hydroxyl moieties of the nanoparticles and the polar head groups of the lipids in the cell membranes [16]. Indeed atomistic and coarse-grained molecular dynamic simulations [31-36] showed that $C_{60}(OH)_{20}$ could adhere onto the lipid bilayers through *van der Waals* as well as dipolar interactions; such membrane adsorbed nanoparticles would then attract copper ions in the extracellular environment to effectively reduce the metal ion concentration. In our experiment, adhesion of fullerols to cell membranes can be inferred from the increased cell surface roughness in Figures 4-2(b) (detail see inset) and 4-2(d), relative to those in Figures 4-2(a) and 4-2(c).
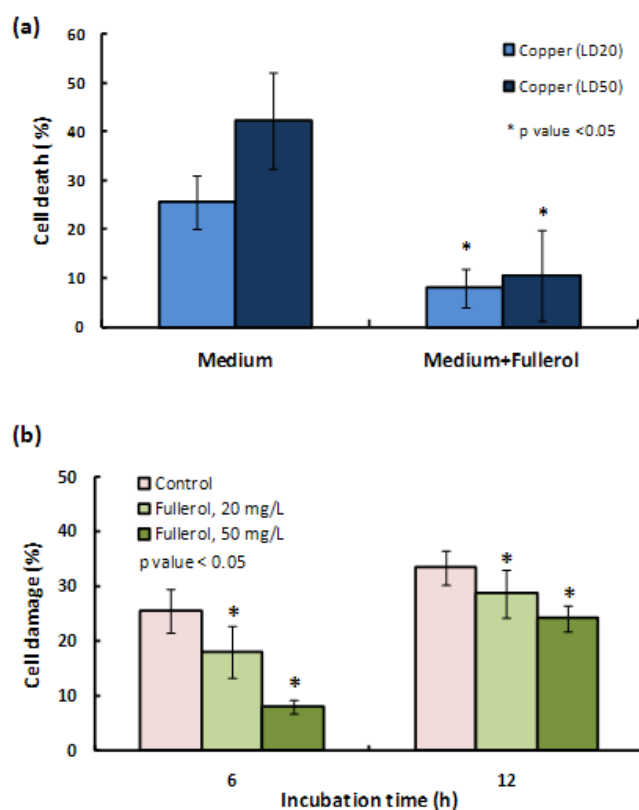
Figure 4-3. Cell damage in the presence of fullerols and copper ions. (a) Cell count: the cells were preexposed to 20 mg/L of fullerols and the washed cells were then treated with copper of LD20 and LD50 concentrations. After 24 h, the cells were washed thrice with PBS and the cell numbers were counted. The controls for calculating cell damage for medium and medium+fullerols (20 mg/L, LD20) samples were the medium and medium+fullerol (LD20) without containing copper ions. The results are the means ± standard errors of three repeats. Statistically significant differences between the band intensities were determined by the Student t-test (*: p<0.05). (b) Relative damage of HT-29 cells pre-exposed to 0 mg/L (control), 20 mg/L, and 50 mg/L fullerols after 6 and 12 h and subsequent exposure to copper of LD50 concentration. The damage was calculated

relative to the controls containing no copper ions. The results are the means ± standard errors of eight repeats.

Detailed data on $C_{60}(OH)_{20}$ binding with copper ions is shown in Figure 4-4 in the supporting information. For example, at a molar ratio of $C_{60}(OH)_{20}$ to copper of 1:10, the zeta potential of the nanoparticles was elevated from -57.9 mV to -17.3 mV upon their mixing with copper. Although the zeta potential measurement was performed in Milli-Q, it is expected that $C_{60}(OH)_{20}$ should also neutralise free copper ions in the cell medium to compensate for the toxicity induced by the metal ions.
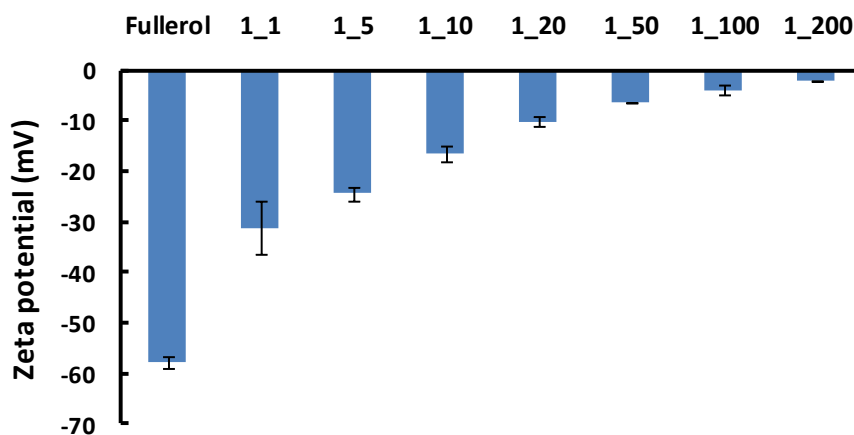
Figure 4-4. Zeta potential of fullerols in the presence of copper. Fullerols of 50 mg/L were mixed with copper of different concentrations in Milli-Q. The molar ratios of fullerol: copper are indicated on the horizontal axis. The results shown are the means ± standard errors of three experiments.

Another plausible mechanism regarding fullerol-suppressed cytotoxicity is the uptake of the nanoparticles by the HT-29 cells, since fullerols have been reported to act as ROS scavengers within cells [79, 212, 213]. Although it is deemed energetically unfavorable for amphiphilic or hydrophilic nanoparticles to directly enter the cell, $C_{60}(OH)_{20}$ can readily bind to the proteins, amino acids, or lipids in the cell medium through hydrogen bonding or electrostatic interaction, or the formation of nanoparticle-protein "corona" [214, 215], and subsequently gain access to the intracellular space. More discussion on fullerol surface modifications by the cell medium is provided in section 4.3.4.

The significant decrease in copper-induced cell damage in the presence of $C_{60}(OH)_{20}$ could -- in principle -- also be induced by the blockage of divalent metal ion channels by the nanoparticles. Because of the specific physiological roles they play, membrane ion channels exhibit unique structures, including the pores that provide the physical pathways for ion movements across the plasma membrane and several charged domains that attract or repel ions. These characteristics make ion channels an easy target for external agents such as natural toxins and synthetic drugs that react with them by establishing electrochemical interactions. The blockage of the K^+ ion channel by single-walled carbon nanotubes has been reported before [216], and such blockage was shown to be dependent on the shape and dimension of the nanotubes. Due to their small size, hydrophilicity, and surface charge, fullerols could physically block the pores of divalent metal-ion transporter DMT1 [217], or offset the ion channel gate sensors by altering the membrane potential through electrostatic interaction or physical adsorption; in each case

the nanoparticles would perturb the exchange of copper and other metal ions across the cell membrane to impact on the metabolic pathways of the cell. However, in view of the fact that fullerols inhibited ROS production by both copper and H_2O_2 in similar trends (Figure 4-5(b)), ion channel blockage by fullerols is deemed as an insignificant factor for the inhibition of copper-induced cytotoxicity.
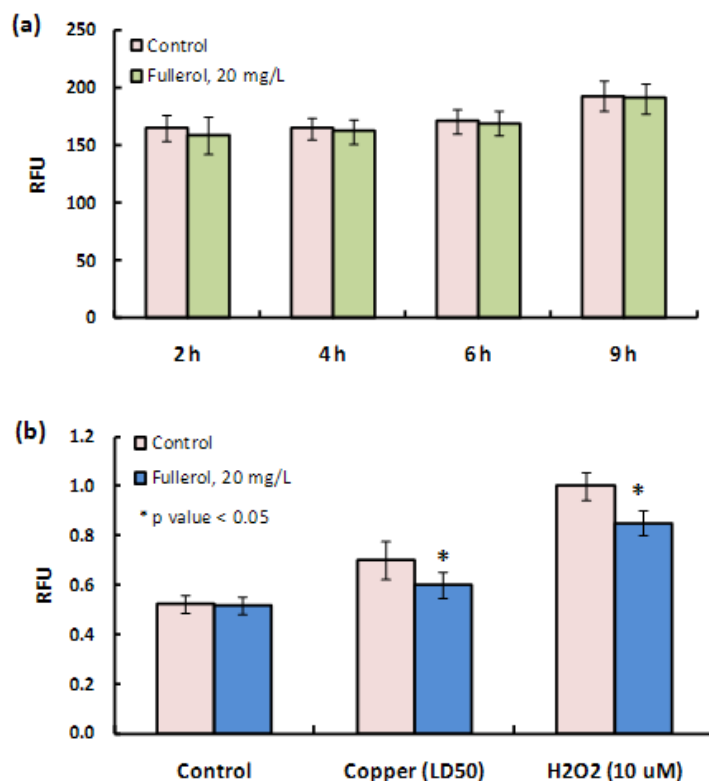
Figure 4-5. Intracellular ROS production after cell exposures to fullerols for 9 h and to copper (LD50) and H_2O_2 (10 µM) for an additional 9 h. The cells were first treated with 1 mM DCFH-DA for 60 min. (a) The cells were incubated with fullerols of 20 mg/L and their fluorescence was monitored up to 9 h. (b) Accumulation of intracellular ROS products in the presence (blue bars) and absence (pink bars) of 20 mg/L fullerols after 9

h. The results are the means ± standard errors of two experiments each carried out in triplet. RFU: relative fluorescence units. Statistically significant differences between the samples and the controls in each condition were determined by the Student t-test (*: $p < 0.05$).

4.3.2 Cell viability and proliferation analysis

To verify the cytoprotective properties of $C_{60}(OH)_{20}$ against copper-induced damage, cell viability and proliferation were assayed for the HT-29 cells. To obtain information on specific cellular changes induced by copper, single point measurements were conducted after 6 and 12 h of incubation. Much longer incubation times were not used since resaurin, the redox indicator of the DHL assay, could be further converted to colourless dihydroresorufin to complicate the fluorescence measurement [218].

To quantify the cytoprotective properties of the $C_{60}(OH)_{20}$, the fluorescence data was analysed and the cell damage was calculated for all samples (Figure 4-3(b)). The presence of the $C_{60}(OH)_{20}$ did not cause significant change on HT-29 cell proliferation up to 24 h. The cell damage was calculated by measuring the fluorescence intensities of the resorudin, which indicated the mitochondrial dehydrogenase activity of the cells. The damages of the cells pre-exposed to 20 mg/L and 50 mg/L of $C_{60}(OH)_{20}$ and then to copper of LD50 concentration were calculated relative to the copper controls.

Specifically, the cells treated with 20 mg/L (light green bars) and 50 mg/L of $C_{60}(OH)_{20}$ (dark green bars) showed reduced damages of 29.6% and 68.5%, 6 h after exposure to copper, and reduced damages of 14.0% and 27.5%, 12 h after exposure to copper (Figure 4-3(b)). These results are in qualitative agreement with the cytotoxicity analysis above (Figure 4-3(a)) and the ROS data discussed below (Figure 4-5(b)).

4.3.3 Intracellular ROS production analysis

One of the major indicators of cell damage is the production and accumulation of ROS products inside of the cell. The presence of unpaired valence shell electron makes ROS extremely reactive, which can result in significant damage to the cell structure, especially damage to the lipids in the cell membrane. As shown in Figure 4-5(a), addition of 20 mg/L $C_{60}(OH)_{20}$ in the cell medium did not affect the accumulation of the ROS products, consistent with previous studies [89, 213]. Figure 4-5(b) shows that pretreating HT-29 cells with 20 mg/L of $C_{60}(OH)_{20}$ significantly decreased the cellular accumulation of ROS production induced by copper and hydrogen peroxide, by 14.3% and 15.0%, respectively. This is in a good agreement with previous reports [79, 212, 213] that water-soluble fullerene derivatives could protect cells from being attacked by ROS. Further incubations led to pronounced cell damage due to the accumulation of the 2',7'-dichlorodihydrofluoresceine dye, suggesting intermediate observation times of 9 h and less are more appropriate for evaluating ROS production.

4.3.4 Analysis of $C_{60}(OH)_{20}$ interaction with HT-29 cells

$C_{60}(OH)_{20}$ suspended in both Milli-Q and PBS absorbed strongly at 253-256 nm (Figure 4-6(a)), while in the cell medium showed two absorbance peaks (Figure 4-6(b)), one contributed by free fullerols at 256 nm, and another by the fullerols surface-modified by the cell medium components such as FBS and amino acids, at 293 nm. The differences in the $C_{60}(OH)_{20}$ absorbance values were then converted to the concentrations of the nanoparticles taken up by the cells or adsorbed onto the cell membranes, as shown in table 4-4. Interestingly, the percent of $C_{60}(OH)_{20}$ taken up by the cells or adsorbed onto the cell membranes in PBS, where the nanoparticles were relatively free of surface modifications due to low salt strength and devoid of biomolecular species, was twice as high as that in the cell medium (3.33-3.64 mg/L vs. 1.78 mg/L). This result indicates that $C_{60}(OH)_{20}$ in PBS could bind to membrane proteins/lipids to initiate the endocytotic pathways, while in cell medium the nanoparticles were largely consumed by the bimolecular species through nonspecific interactions. It is thus conceivable that the extracellular environment, in additional to the host cell itself, also plays an active role in the exchange of ions and toxins across the cell membranes.
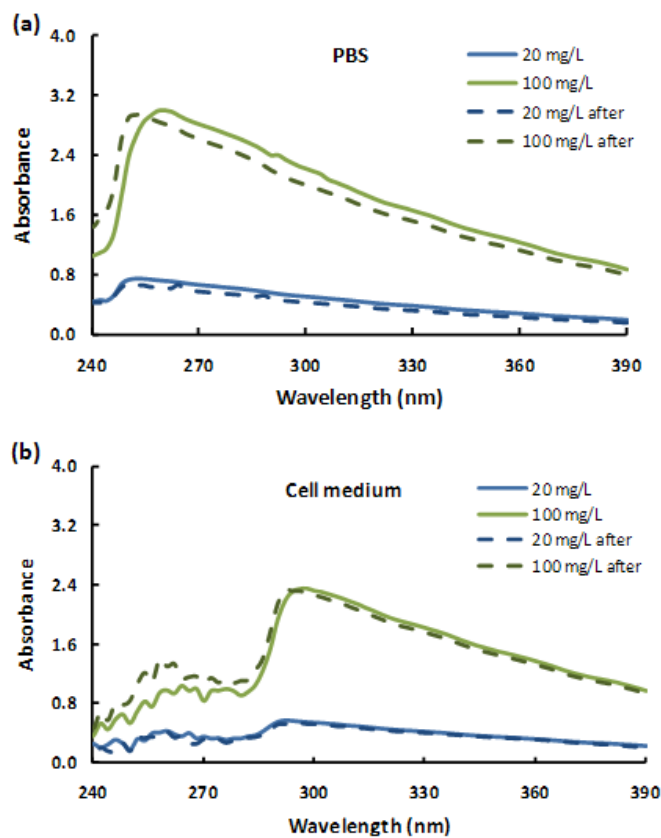
Figure 4-6. Absorbance of fullerols in (a) PBS and (b) the cell medium. The absorbance was read for fullerols in PBS and the medium, with blanks as PBS and the medium, respectively. The legends "after" indicate the absorbance values were read 9 h after the nanoparticles had been incubated with the cells.

Buffer	Medium		PBS	
fullerol concentration (mg/L)	20	100	20	100
absorbance prior to incubation	0.565	2.356	0.736	2.991
absorbance after incubation	0.515	2.314	0.613	2.882
fullerols adsorbed/taken up by cells (%)	8.90	1.78	16.67	3.64
fullerols adsorbed/taken up by cells (mg/L)	1.78	1.78	3.33	3.64

Table 4-4. Fullerol interaction with HT-29 cell membranes.

In summary, we have shown that $C_{60}(OH)_{20}$ can inhibit cell damage and ROS production induced by copper, a major toxin of both biological and environmental relevances. These effects were attributed to the following two mechanisms: binding of the $C_{60}(OH)_{20}$ with the biomolecular species in the cell medium through electrostatic interaction and hydrogen bonding and the subsequent cell uptake of the surface-modified $C_{60}(OH)_{20}$ by the endocytotic pathways, and adsorption of $C_{60}(OH)_{20}$ onto membrane proteins and lipids through electrostatic and dipolar interactions and neutralization of the cationic copper ions in the cell growth medium by the membrane bound nanoparticles. This study is important in view of its practical consideration of toxin uptake post cell exposure to nanoparticles, and is relevant to the potential use of water-soluble fullerene derivatives for the treatment of oxidant-mediated diseases.

CHAPTER FIVE

EXPERIMENTAL AND SIMULATION STUDIES OF REAL-TIME PCR IN THE

PRESENCE OF A FULLERENE DERIVATIVE

With chapters one and two documenting the ecological responses to carbon nanomaterials on the whole organism and molecular level, this chapter aims at evaluating the molecular level response of ecological systems to carbon nanoparticles. Specifically, this chapter examines the amplification of a heat shock transcription factor (HSTF) plant gene by real-time PCR, in the presence of $C_{60}(OH)_{20}$. Molecular dynamics (MD) simulations were performed to extend the understanding of fullerols interaction with the molecular components in the PCR, such as deoxynucleoside triphosphates (dNTPs) and ssDNA.

5.1 Introduction

While nanoparticles possess realistic chances of entering the environment due to their mass production, the impact of fullerenes on ecological systems (e.g., plants and aquatic organisms) is little understood, especially on the molecular level. In this study we examine the amplification of a HSTF gene by real-time PCR, in the presence of

$C_{60}(OH)_{20}$. This system is simple and artificial; however, it offers ample opportunities for elucidating the fundamental mechanisms of nanoparticle-biomolecular interactions.

In eukaryotes HSTF responds and transduces environmental signals to the transcriptional machinery to maintain and protect cell functionality. In addition to reacting to elevated temperature, HSTF also plays critical roles in regulating developmental and stress-dependent gene regulation, and in maintaining cellular homeostasis in response to chemical and physiological stresses [219], and other environmental factors including oxidative stress [220], increased salinity [221] and—though speculative—discharged nanoparticles.

In the following we describe PCR amplification of a HSTF gene, in the presence of fullerol $C_{60}(OH)_{20}$. By altering stoichiometry we conjecture that the binding between the fullerol and Taq DNA polymerase is the major cause for PCR inhibition. Using MD simulations we further examine the interactions between $C_{60}(OH)_{20}$ and both dNTPs and ssDNA, the other major molecular components in PCR reaction. It should be noted that although a specific HSTF gene is used in this study, our conclusions are expected to be applicable to the general case of nanoparticle-nucleic acid interaction. A theoretical study of the binding of $C_{60}(OH)_{20}$ to Taq DNA polymerase will be reported in a future publication.

5.2 Experimental and computational sections

5.2.1 PCR reaction

The PCR primers used in our study were designed from genomic DNA sequence of soybean HSTF gene and synthesized by IDT (Coralville). The gene is localized within the gene-rich region assigned to the Linkage Group A on the soybean genetic molecular map. Physical detection of this gene-rich region was conducted using bacterial artificial chromosome (BAC) library constructed from the ancestral germplasm PI 437654. BAC clone containing HSTF gene was identified and digested with restriction enzyme *Spe*I. A 7kb DNA fragment corresponding to HSTF was isolated and subcloned into the pBlueScriptII plasmid (Figure 5-1). The pBlueScriptII-HSTF was maintained in *Escherica coli* DH5 alpha and used as a template for DNA amplification in PCR in the presence of $C_{60}(OH)_{20}$. For PCR, the primer sequences are HSTF1F 5'-TATTCTTTGTGGGCGTTTAT-3' and HSTF1R 5'-TTTAACTGTTCTCCAAGACA-3'. For real-time PCR, the primer sequences are HSTF2F 5'-TCCGCCAGCTCAATACCTAC-3' and HSTF2R 5'-CAGCTCAGTGCCAATATCCA-3'.
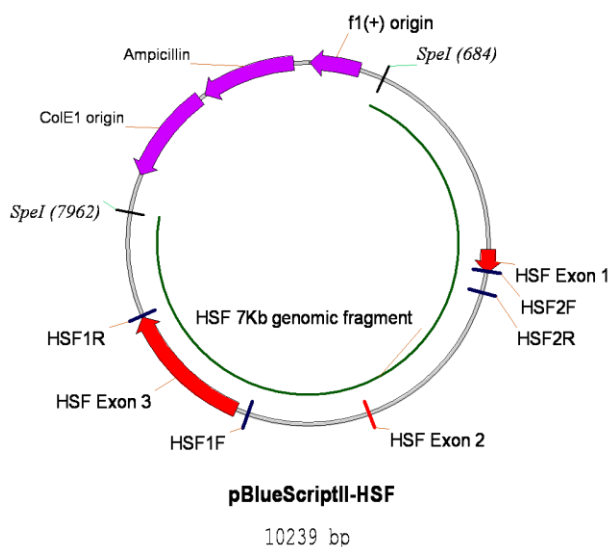
Figure 5-1. PBlueScript II plasmind with HSTF.

Fullerene derivative $C_{60}(OH)_{20}$ (BuckyUSA) was suspended in Milli-Q, filtered and sterilized using Anotop 10 filters (0.2 μm, Whatman). PCR reactions (25 μL) each contained 1 ng pBlueScriptII-HSTF DNA, 10 pmoles primer, 5 nmole dNTPs, 1 unit (1U) AmpliTaq Gold DNA polymerase in $1 \times$ PCR buffer II (Applied Biosystems), 2 mM MgCl$_2$, and 10 μL $C_{60}(OH)_{20}$ of a final concentration of 0.2×10^{-4}, 0.6×10^{-4}, 1.0×10^{-4}, 1.6×10^{-4}, and 4.0×10^{-4} mM, respectively. The experimental scheme is illustrated in the Figure 5-2. PCR was performed using the following protocol: denaturation at 94°C for 5 min, 30 cycles at 94°C for 30 s, 58°C for 30 s and 72°C for 1 min, and extension at 72°C for 10 min. Amplified products were size-fractionated by gel electrophoresis (1% agarose) and visualized by staining with ethidium bromide.

142
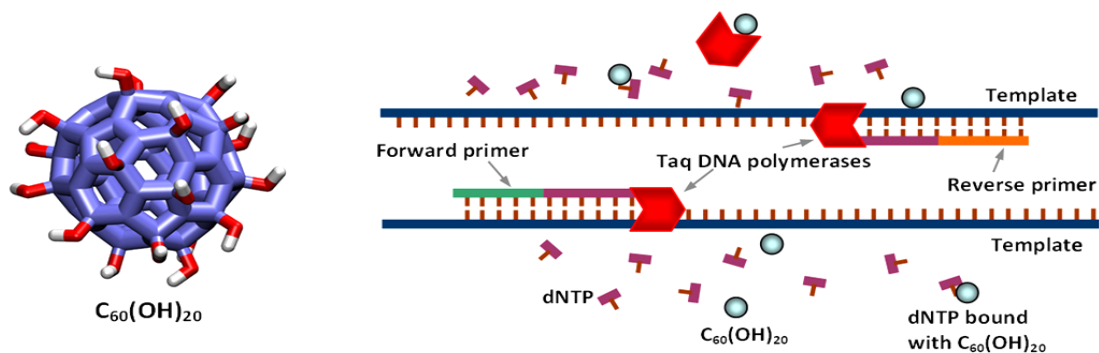
Figure 5-2. Experimental scheme of PCR in the presence of $C_{60}(OH)_{20}$.

5.2.2 Nanosizer measurement

The binding between $C_{60}(OH)_{20}$ and Taq DNA polymerase was probed at room temperature using a nanosizer (Malvern, S90), a dynamic light scattering device which measures the hydrodynamic size distribution for suspended particles and solutes. An upper shift in the peak size was interpreted as an effective binding between $C_{60}(OH)_{20}$ and Taq DNA polymerase. The concentrations of $C_{60}(OH)_{20}$ and Taq DNA polymerase were 4.0×10^{-3} mM and 10U, and the measurement was repeated three times.

5.2.3 Real-time PCR

To provide a dynamic view on HSTF gene amplification in the presence of fullerol, real-time PCR was employed to monitor individual amplification cycles. This experiment was carried out using an iCycler iQ^{TM} Real Time PCR Detection System with iQ SYBR Green Supermix (BioRad). A 25μL volume reaction contained 1 ng pBlueScriptII-HSTF DNA, 10 pmoles each primer and 10 μL $C_{60}(OH)_{20}$ of 0.2×10^{-4} to 4.0×10^{-4} mM. The amplification of HSTF gene was designed as the following: denaturation at 95°C for 2 min, 40 cycles at 95°C for 30 s and 58°C for 30 s, and extension at 72°C for 30 s.

5.2.4. MD simulations

Computational modeling has previously been used to provide atomic-scale insight on the interaction of fullerene and fullerene derivatives with nucleic acids [133, 134]. In the present study, we assessed the possibility of $C_{60}(OH)_{20}$ binding to the dNTPs and ssDNA in the PCR system by using atomistic MD simulations. The simulations were carried out with the GROMACS software package [222, 223], version 3.3.2, employing the GROMOS 53A6 force field [224].

The $C_{60}(OH)_{20}$ model was based on the bare carbon atom (type C) and default hydroxyl group atom types and parameters of the GROMOS 53A6 force field. Non-zero atomic partial charges were assigned only to the hydroxyl groups and the carbon atoms to which the –OH groups were bonded. We used the typical partial charge values for –COH groups [224], with the exception that the carbon atom partial charge was decreased from $0.266e$ to $0.2188e$ in order to impose charge neutrality on the whole molecule.

The dNTP models were based on the existing GROMOS parameters for deoxyribose nucleotides and the triphosphate structure of ATP [224]. The degree of ionization of the dNTPs in the experiments was –4, in contrast to –3 of the hydrogen-terminated GROMOS model for ATP. Thus, the terminating hydrogen in the γ phosphate was removed and the resulting extra negative charge was distributed uniformly over the oxygens in the γ phosphate moiety. The simple point charge (SPC) model was used for water [225].

5.2.4.1. dNTP Simulations

The simulated dNTP-$C_{60}(OH)_{20}$ systems were set up in cubic boxes of side lengths 3.74-3.77 nm, depending on the specific case. Initially, the center of mass (CM) of the dNTP in question was set at the center of the simulation box. The CM of $C_{60}(OH)_{20}$ was set at one corner of the box and the remaining free volume in the system was filled

with water. In order to make the simulated system globally charge-neutral, four randomly chosen water molecules were replaced with Na^+ counterions. For each dNTP-$C_{60}(OH)_{20}$ combination we carried out three independent simulations at room temperature ($T = 298$ K) and a pressure of $p = 1$ bar. To assess the effect of temperature on the intermolecular binding, we further carried out simulations at $T = 345$ K.

Each independent simulation was started with a 100 ps NpT simulation where all dNTP and $C_{60}(OH)_{20}$ atoms were restrained to their initial positions by a harmonic potential with a force constant of 1000 kJmol^{-1}nm^{-2}. The time step length was 2 fs and periodic boundaries were used in all directions. The temperature and pressure were maintained with the Berendsen weak-coupling method [226] with coupling time constants $\tau_T = 0.1$ ps and $\tau_p = 1.0$ ps for temperature and pressure, respectively. All dNTP and $C_{60}(OH)_{20}$ bond lengths were constrained with the LINCS algorithm [227], while the SETTLE algorithm [228] was used for water. For Lennard-Jones interactions we used a twin-range cutoff scheme with cutoff lengths of 0.9 and 1.4 nm. Electrostatic interactions were calculated with the Particle-Mesh Ewald (PME) method [229], with a real-space cutoff of 0.9 nm and a 0.12-nm grid for the long-range interaction part.

The position-restrained simulations were followed by 20 ns unrestrained (equilibrium) NpT simulations. In these simulations temperature was maintained by the Nosé-Hoover algorithm [230, 231] ($\tau_T = 0.5$ ps), and the Parrinello-Rahman algorithm [232] ($\tau_p = 2.0$ ps) was used for pressure coupling. In the case of dCTP at $T = 298$ K, two of the simulations had to be extended to 40 ns, as $C_{60}(OH)_{20}$ and dCTP did not bind early

enough in the first 20 ns for adequate sampling of the binding configurations. This does not imply any weaker binding affinity of dCTP to $C_{60}(OH)_{20}$ as in the case of other dNTPs. Rather, the longer equilibration times were simply a result of the statistical variation of the time required for the molecules in question to diffuse close enough to each other in the simulation box. This was also verified by the similar modes of binding for all the dNTP- $C_{60}(OH)_{20}$ pairs.

The binding of $C_{60}(OH)_{20}$ with the dNTPs was quantified by calculating the radial potentials of mean force (PMFs). As representative cases for dNTPs we considered dATP and dCTP. The PMFs were calculated with the umbrella sampling method [233]. The simulation setups were as described above for the equilibrium simulations. A harmonic biasing potential was imposed on the radial CM-CM separation of the $C_{60}(OH)_{20}$ and dNTP. The force constant used was 1000 kJ $mol^{-1}nm^{-2}$ and the radial distances considered were 0.5-2.0 nm, in increments of 0.1 nm. For each restrained position, the system was equilibrated for 1 ns. This was followed by 20 ns of data sampling. The final PMF profiles were obtained with the weighted histogram analysis (WHAM) method [234]. Errors in the PMF profiles were estimated with the bootstrap method as implemented in the *g_wham* analysis program of GROMACS.

5.2.4.2. ssDNA Simulations

The simulations with $C_{60}(OH)_{20}$ binding to ssDNA followed the simulation protocol (*i.e.,* algorithms and parameters) as outlined above for the dNTP simulations. The ssDNA chain was modeled by a 20-nucleotide-long oligomer of sequence 5'-CGAAACGAGGGTATCGCGCG-3', initially corresponding to the canonical B form. The nucleotides at the ends of the ssDNA chain were hydrogen terminated. The oligonucleotide was first set at the center of a cubic simulation box with a side length of 7.1676 nm. The simulation box was filled with SPC water and 18 randomly chosen water molecules were replaced by Na^+ counter ions for charge neutrality. After a simple conjugate gradient energy minimization the system was simulated for 50 ps at *NVT* conditions. The positions of the nucleotide atoms were restrained with a harmonic potential with a force constant of 20 000 $kJmol^{-1}nm^{-2}$. The *NVT* simulation was followed by a series of five 50 ps *NpT* simulations. The magnitude of the position restraint force was reduced in each successive simulation: 20 000, 10 000, 5000, 2500, and 1000 $kJmol^{-1}nm^{-2}$. After the equilibration, a 5 ns unrestrained *NpT* simulation was run for ssDNA alone, followed by a 40 ns simulation with a single $C_{60}(OH)_{20}$ added to the system.

Unlike in the case of dNTPs, quantifying the binding of $C_{60}(OH)_{20}$ to ssDNA through PMF calculated with umbrella sampling simulations is not computationally feasible. This is because such calculations would need to sufficiently sample the conformational degrees of freedom of the ssDNA oligonucleotide. Thus, for this case we

focus below only on the qualitative aspects of the binding, namely preferential binding sites and hydrogen bonding.

5.3 Results and discussions

5.3.1 Inhibition of PCR

As the concentration of $C_{60}(OH)_{20}$ was increased from 0.2×10^{-4} to 1.0×10^{-4} mM, the amount of amplified dsDNA was reduced accordingly (Figure 5-3(left), lane 7 to lane 5). Specifically, no dsDNA was obtained for $C_{60}(OH)_{20}$ of 1.6×10^{-4} or 4.0×10^{-4} mM (lanes 3 and 4), indicating inhibition of the PCR.

a
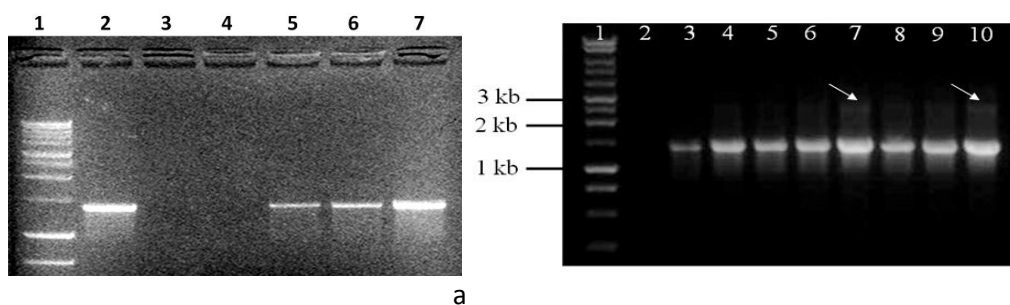
Figure 5-3. (left) PCR products of HSTF amplification. Lane 1: 1 kb DNA ladder. Lane 2: Normal PCR. Lanes 3-7: PCR with 4.0×10^{-4}, 1.6×10^{-4}, 1.0×10^{-4}, 0.6×10^{-4}, and 0.2×10^{-4} mM of $C_{60}(OH)_{20}$, respectively. (right) PCR products of HSTF amplification with additional Taq DNA polymerase. Higher polymerase concentrations yielded stronger amplifications. Lane 1: 1 kb DNA ladder. Lanes 2-4: 4.0×10^{-4} mM of $C_{60}(OH)_{20}$. Lane 2: 1U, Lane 3: 2U, Lane 4: 4U. Amplification was detectable for lanes 3 and 4. Lanes 5-7:

1.0×10^{-4} mM $C_{60}(OH)_{20}$. Lane 5: 1U, Lane 6: 2U, Lane 7: 4U. Lanes 8-10: controls. Lane 8: 1U, Lane 9: 2U, Lane 10: 4U. The arrows in (b) indicate spurious amplification products.

At the highest $C_{60}(OH)_{20}$ concentration of 4.0×10^{-4} mM, the molar ratio of nanoparticles to dNTPs in the reaction was 1:500. This ratio was decreased for lower nanoparticle concentrations. Our PCR experiments indicated that Taq DNA polymerase (1U) was unable to amplify DNA even when most dNTPs were free from binding with the nanoparticles (Figure 5-3(left): lanes 3 and 4, and Figure 5-3(right): lane 2).

This suggests that $C_{60}(OH)_{20}$ bound to Taq DNA polymerase and inhibited its enzymatic activity for DNA replication. Interestingly, amplification process was resumed when the amount of Taq DNA polymerase was increased to 2U (Figure 5-3(right), lane 3). Spurious amplification products (Figure 5-3(right), arrows in lanes 7 and 10) were obtained using Taq DNA polymerase of 4U, with or without $C_{60}(OH)_{20}$ of 1.0×10^{-4} mM, suggesting impaired specificity or increased impurity with excess polymerases.

5.3.2. Binding of Taq DNA polymerase with $C_{60}(OH)_{20}$

As shown in Figure 5-4 the hydrodynamic diameter of the $C_{60}(OH)_{20}$ and Taq polymerase was 1.0 (±0.3) nm and 10.8 (±1.9) nm respectively, while the mixture of

$C_{60}(OH)_{20}$ and Taq DNA polymerase displayed a size distribution at 21.9 ($\pm$10.9) nm, indicating supramolecular assembly between the $C_{60}(OH)_{20}$ and the Taq DNA polymerase.
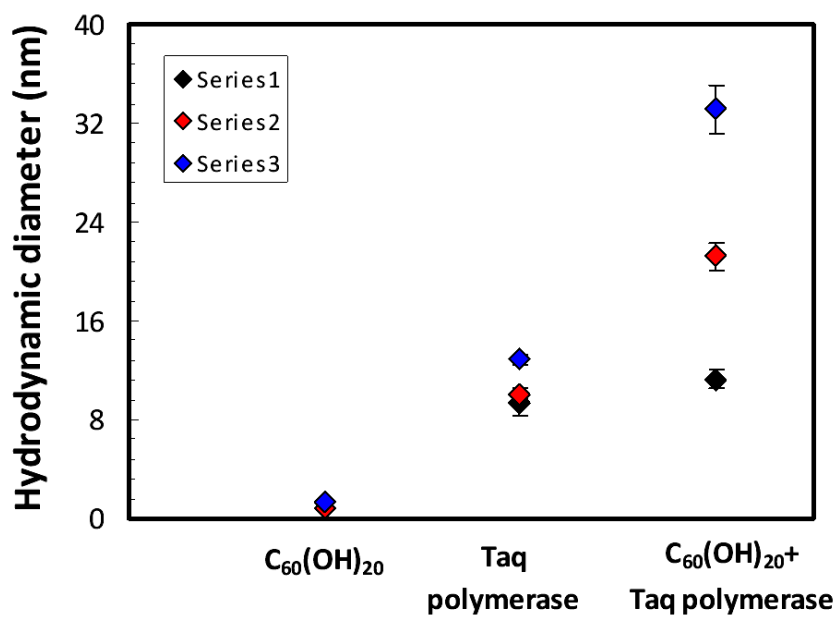
Figure 5-4. Hydrodynamic diameters of $C_{60}(OH)_{20}$ (1.0$\pm$0.3 nm), Taq polymerase (10.8$\pm$1.9 nm), and $C_{60}(OH)_{20}$ mixed with Taq DNA polymerase (21.9$\pm$10.9 nm), measured for three sets of samples shown as blue, red, and green diamonds. $C_{60}(OH)_{20}$: 4.0×10^{-3} mM. Taq DNA polymerase: 10 U.

5.3.3 Inhibition of real-time PCR

The onset of DNA amplification over the threshold was delayed by ~11.5 cycles for $C_{60}(OH)_{20}$ at 1.6×10^{-4} mM as compared with the control (Figure 5-5(a)), possibly due to increased consumption of the PCR reaction, especially DNA polymerase, upon their binding with the $C_{60}(OH)_{20}$. The relative amplification efficiency (Figure 5-5(b)) was calculated via the comparative threshold cycle ($\Delta\Delta Ct$) method [235] using amplification efficiency of the HSTF without $C_{60}(OH)_{20}$ as a reference. No significant amplification above the Ct value was observed for reactions with $C_{60}(OH)_{20}$ of 1.6×10^{-4} mM, and no amplification above the baseline with $C_{60}(OH)_{20}$ of 4.0×10^{-4} mM (Figures 5-5(a) and (b)). The identical melting temperature T_m confirmed specificity of the amplified products (Figure 5-5(b) inset).

All nanoparticle suspensions alone showed negligible absorbance. However, the real-time PCR sample reaction with $C_{60}(OH)_{20}$ of 4.0×10^{-4} mM displayed the highest absorbance peak (Figure 5-5(c)), mainly due to free dNTPs upon PCR inhibition, and little from the primers and the nanoparticles. Due to hypochromicity, dsDNA absorbs 20% less than ssDNA and 30-40% less than dNTPs of the same quantity [236]. As nanoparticle concentration was reduced during PCR, dNTPs were continuously converted to dsDNA with more primers consumed, therefore causing a reduction in absorbance.
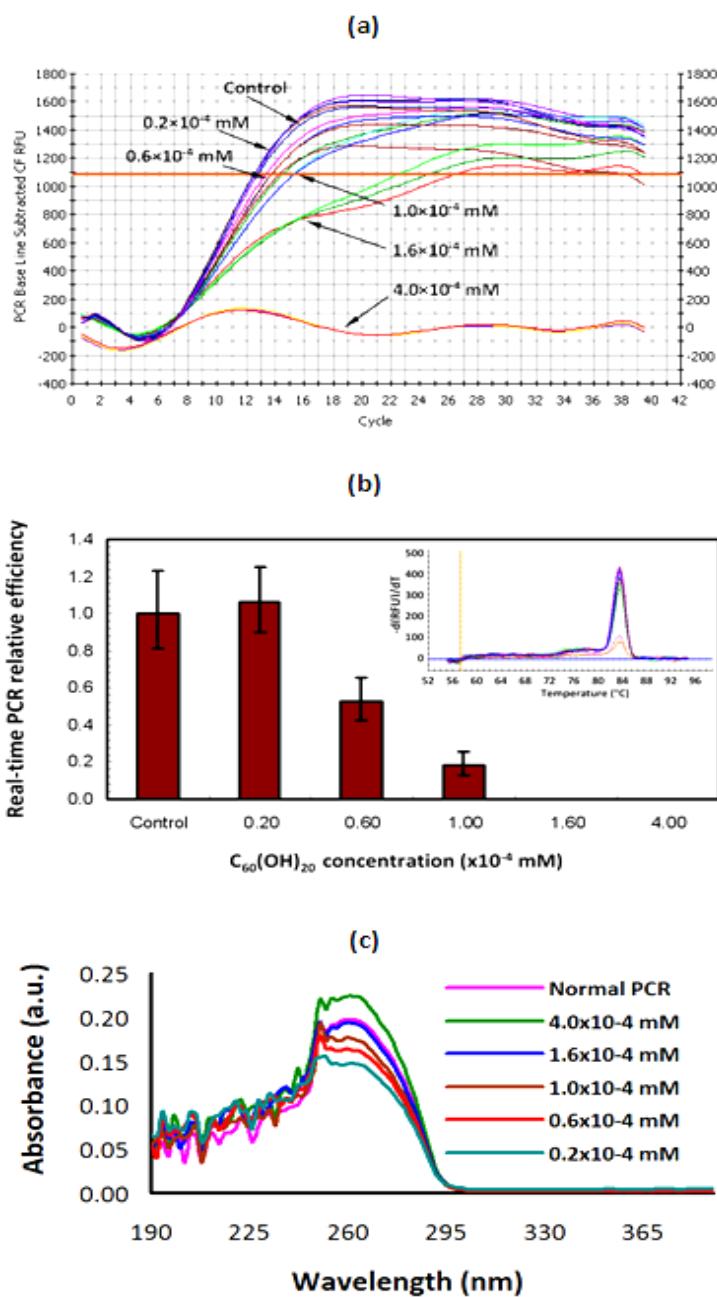
Figure 5-5. Real-time PCR dynamics in the presence of $C_{60}(OH)_{20}$ of different concentrations. Three samples were examined for each condition. The averaged onsets of PCR are Cycle 13.3 (control), Cycle 12.7 (0.2×10^{-4} mM), Cycle 13.7 (0.6×10^{-4} mM), Cycle 15.2 (1.0×10^{-4} mM), and Cycle 24.8 (1.6×10^{-4} mM), respectively. The PCR

process was fully inhibited for $C_{60}(OH)_{20}$ of 4.0×10^{-4} mM. (b) Real-time PCR of HSTF amplification. (Inset) Melting curves for real-time PCR. RFU: relative fluorescence unit. (c) UV absorbance of real-time PCR products in the presence of different $C_{60}(OH)_{20}$ concentrations.

5.3.4 MD simulations of $C_{60}(OH)_{20}$ binding with dNTPs

For all dNTPs, the predominant binding site of $C_{60}(OH)_{20}$ was at the triphosphate side chain. Binding configurations where the number of dNTP-$C_{60}(OH)_{20}$ hydrogen bonds did not show any appreciable drifts were reached after 3-19 ns of simulation time (see Figure 5-6). Analyses of binding geometries were carried out from these times on until the end of the simulation.
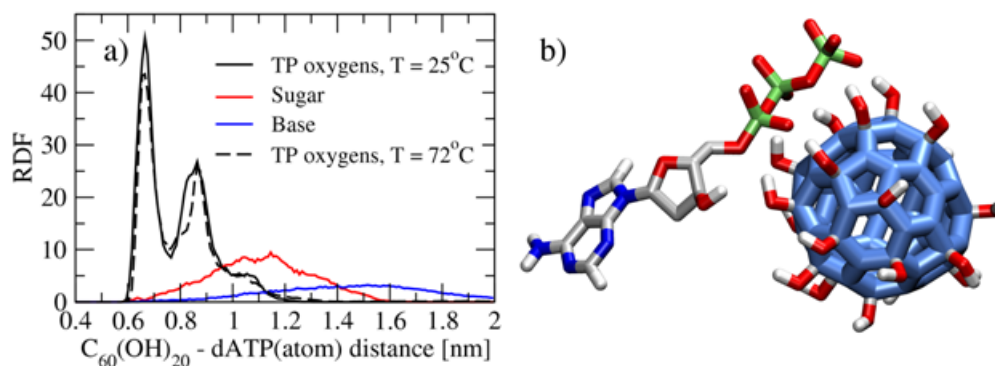
Figure 5-6. Binding between $C_{60}(OH)_{20}$ and dATP. (a) Radial distribution functions (RDFs) between $C_{60}(OH)_{20}$ center of mass and different atoms of dATP in the MD

simulations. (b) Snapshot illustrating a typical binding configuration of a dATP–

$C_{60}(OH)_{20}$ pair.

Hydrogen bonding analysis was based on the standard geometrical criteria for possible donor-hydrogen-acceptor atom triplets [237]. Figure 5-6 (left-hand panel) shows the number of hydrogen bonds formed as a function of time for each dNTP simulation at $T = 298$ K. Deviations of the average numbers of hydrogen bonds, varying from 3.6 ± 0.7 to 4.8 ± 1.0 in the different simulations, were not statistically significant. In agreement with the analysis of the binding configurations above, only 1 - 6% of the dNTP-$C_{60}(OH)_{20}$ hydrogen bonds were formed by the dNTP sugar or base moieties. Figure 5-6 (right-hand panel) further illustrates hydrogen bonding as a function of time in one higher temperature (345 K) simulation for each dNTP. While the averages of the numbers of hydrogen bonds calculated for the bound dNTP-$C_{60}(OH)_{20}$ pairs were similar to the ones at the lower temperature (298 K), it can be seen that in the case of deoxyguanosine triphosphate (dGTP) and deoxythimidine triphosphate (dTTP) there are periods of time when the dNTPs were unbound from $C_{60}(OH)_{20}$.

The dNTP-$C_{60}(OH)_{20}$ binding geometries were quantified by calculating 3D radial distribution functions (RDFs) between the CM of $C_{60}(OH)_{20}$ and atoms in different structural components of the dNTPs (i.e., triphosphate side chain oxygens, sugar and base moieties), see Figure 5-7.

155

The PMF calculations provided the free energy of the system as a function of the CM-CM distance between the $C_{60}(OH)_{20}$ and dNTP (either deoxyadenosine triphosphate (dATP) or deoxycytidine triphosphate (dCTP)). The results show that the $C_{60}(OH)_{20}$-dNTP binding was accompanied by a decrease in free energy by 11 ± 3 kJ/mol for dATP and 14 ± 4 kJ/mol for dCTP (see Figure 5-8).
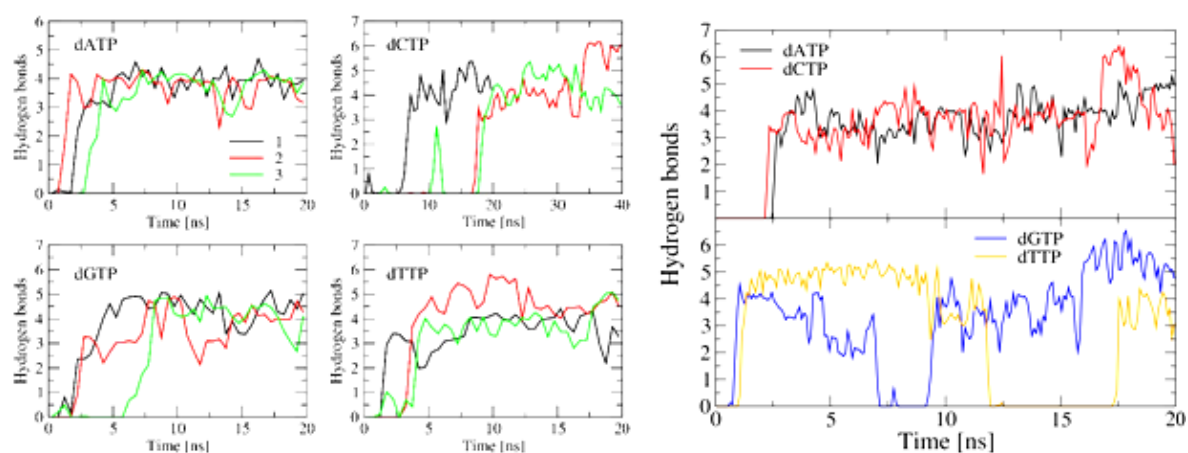
Figure 5-7. Hydrogen bonds formation between $C_{60}(OH)_{20}$ and dNTP. Left: number of $C_{60}(OH)_{20}$-dNTP–hydrogen bonds formed, as a function of time, in the individual simulations at T = 298 K. For clarity, the data are presented as averages over 1 ns blocks. Right: number of dNTP–C60(OH)20 hydrogen bonds in the simulations at T = 345 K. The data are presented as averages over 500 ps blocks. The errors in the average numbers of hydrogen bonds in the different simulations were of the order of ~1.0.
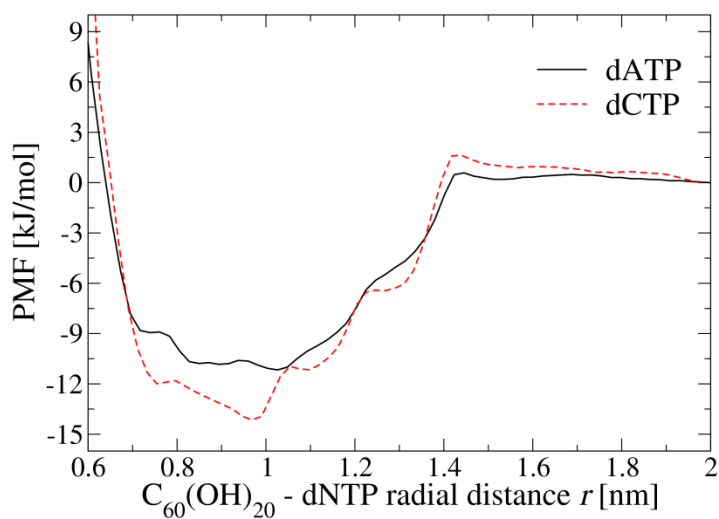
Figure 5-8. Radial potential of mean force (PMF) as a function of $C_{60}(OH)_{20}$-dNTP center of mass separation. The zero level of the PMF curves has been set at $r = 2.0$ nm. For both dATP and dCTP the profiles show the formation of the first hydrogen bonds between the molecules at $r = 1.4$ - 1.5 nm, followed by a clear decrease in free energy at shorter separations. The most favorable binding distances are around $r = 0.9$ - 1.0 nm.

5.3.5 MD simulations of $C_{60}(OH)_{20}$ binding with ssDNA

The equilibrium simulations consisted of a 5 ns run for a ssDNA oligonucleotide alone (see Figure 5-9) and a subsequent 40 ns simulation in the presence of a single $C_{60}(OH)_{20}$.
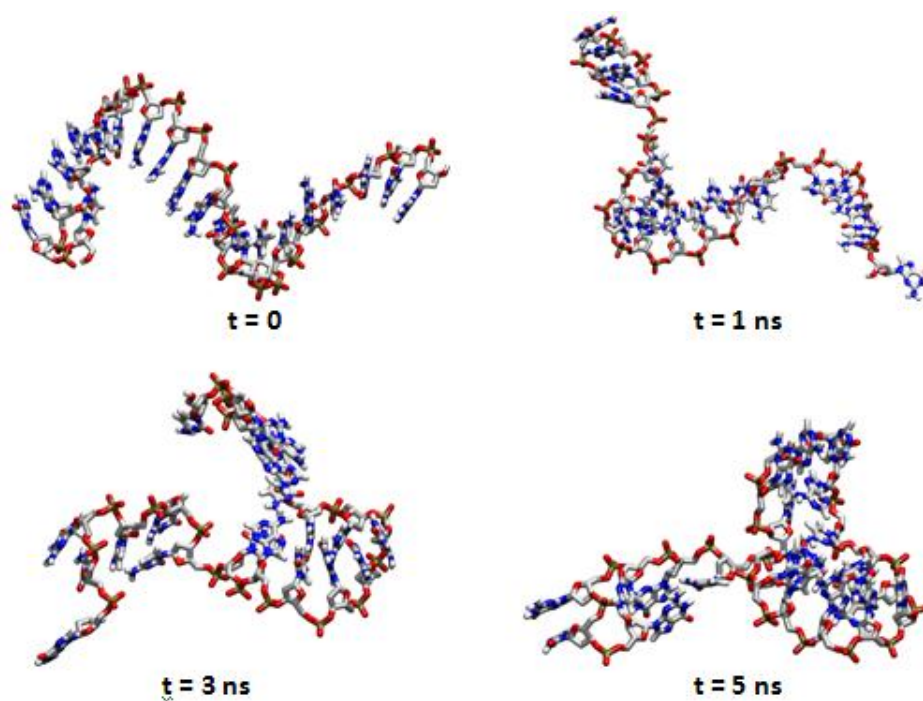
Figure 5-9. Snapshots of the ssDNA oligonucleotide in the 5 ns equilibration simulation in the absence of $C_{60}(OH)_{20}$. The canonical B form (0 ns) is clearly lost already in less than 1 ns. The snapshots at t = 3 ns and t = 5 ns illustrate hydrogen bonding between the bases at different points along the oligonucleotide chain.

In order to assess the stability and changes in the overall molecular conformation, the root mean square deviation (RMSD) value of the ssDNA atoms was monitored throughout the simulations, with the reference structure being the one at the beginning of the simulation in question. The RMSD values showed stable fluctuations around ~0.9 nm and ~0.75 nm in the absence and presence of $C_{60}(OH)_{20}$, respectively. The radius of

gyration of the oligonucleotide was also determined as a function of time, see Figure 5-10.
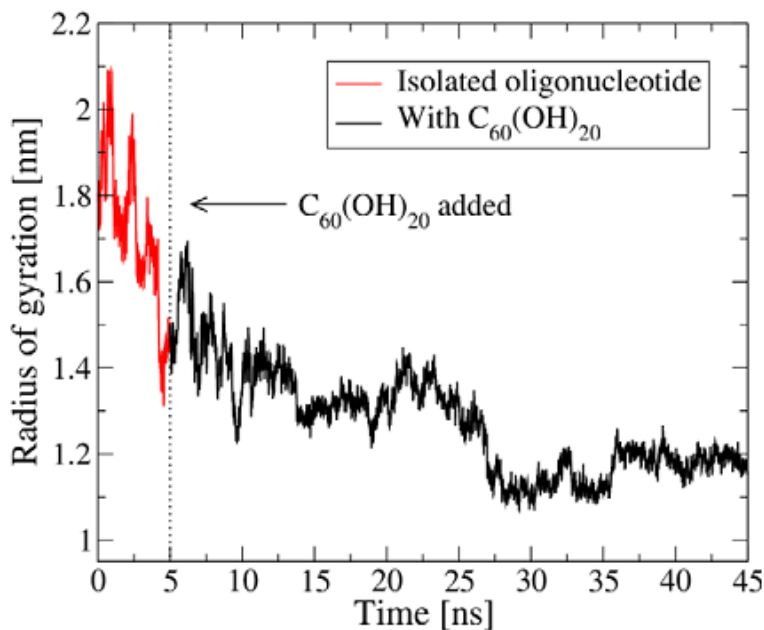
Figure 5-10. Radius of gyration of the ssDNA oligonucleotide. The red line designates the 5 ns equilibration simulation without $C_{60}(OH)_{20}$, and the black line is for the 40 ns simulation with $C_{60}(OH)_{20}$.

Visual inspection of the simulation showed that $C_{60}(OH)_{20}$ was preferentially located close to the oligonucleotide backbone oxygens (see Figure 5-11). This was ascertained by calculating RDFs between the CM of $C_{60}(OH)_{20}$ and different atom groups (backbone oxygen, deoxyribose, bases) in the ssDNA chain.

The binding configuration of the $C_{60}(OH)_{20}$-ssDNA pair was further supported by hydrogen bonding analysis, see Figure 5-12. Hydrogen bonding between $C_{60}(OH)_{20}$ and the deoxyribose or base moieties of ssDNA were not significant, whereas strong interaction with the backbone oxygens persisted from the initial $C_{60}(OH)_{20}$-ssDNA contact (at ~2-3 ns) until the end of the simulation (40 ns).
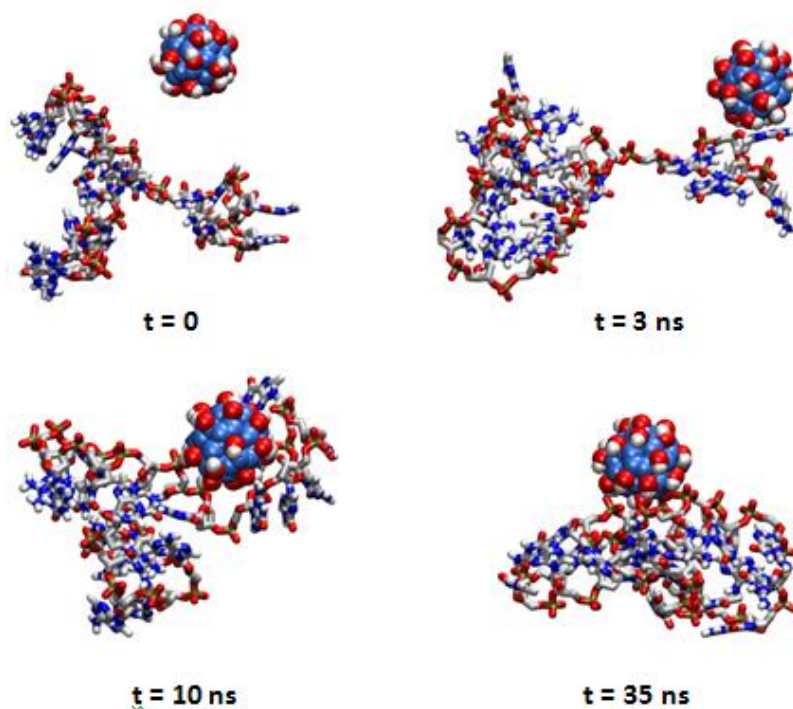
Figure 5-11. Binding of $C_{60}(OH)_{20}$ to ssDNA. After the initial contact with the oligonucleotide (3 ns), $C_{60}(OH)_{20}$ hydrogen bonds to several backbone phosphate groups (10 ns). The conformation of the ssDNA chain is strongly constrained at the end of the simulation by $C_{60}(OH)_{20}$ hydrogen bonding to the phosphate groups at several points along the sugar-phosphate backbone (35 ns; cf. the ssDNA radius of gyration in Figure 5-8).

For pristine fullerenes, stacking of the planar base moieties and subsequent π-π interactions with the fullerene surface could be a possible mode of binding. However, our modeling shows that in the case of $C_{60}(OH)_{20}$ the steric hindrance due to the hydroxyl groups is too unfavorable for such interactions.
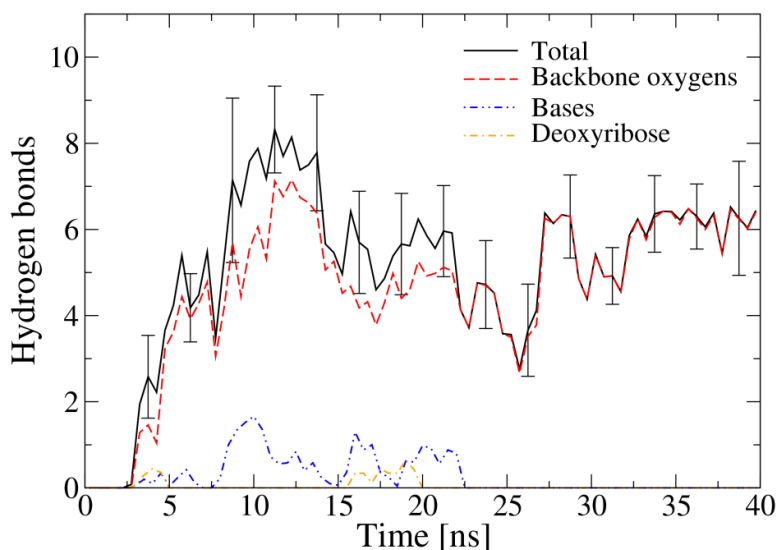
Figure 5-12. Numbers of hydrogen bonds formed between $C_{60}(OH)_{20}$ and different parts of the ssDNA oligonucleotide. The data have been averaged over 500 ps blocks. Typical errors are shown for a few arbitrary blocks of the total number of hydrogen bonds formed. After ~23 ns no hydrogen bonds were formed between $C_{60}(OH)_{20}$ and the deoxyribose or base moieties of the ssDNA.

Based on our experimental study we conclude that the inhibition of DNA amplification was mainly due to the binding of $C_{60}(OH)_{20}$ with Taq DNA polymerase.

The binding of $C_{60}(OH)_{20}$ with free dNTPs, primers, and DNA products also occurred but did not impact on DNA amplification for conventional PCR stoichiometry. Our atomistic MD simulations illustrate a clear tendency for hydrogen-bond-mediated binding between $C_{60}(OH)_{20}$ and the dNTP and ssDNA components of the PCR. Free energy calculations further showed that the binding of $C_{60}(OH)_{20}$ with dNTPs was favorable by 11-14 kJ/mol. Due to the complexity of the problem, detailed MD calculations on the binding modes and free energies of binding between $C_{60}(OH)_{20}$ and Taq DNA polymerase will be reported in a future publication. The results presented here underline the biological and environmental implications of nanoparticles, and are beneficial to the continued development of nanotechnology.

CHAPTER SIX

IN VITRO POLYMERIZATION OF MICROTUBULES WITH A FULLERENE

DERIVATIVE

Chapters three and four were focused on the cellular level interactions between carbon nanomaterials and biological systems. HT-29 human colon carcinoma cells were damaged in the presence of C_{70}-NOM, but did not display any damage in the presence of $C_{60}(OH)_{20}$. To outline the complexity of cell response a double-exposure study was performed, where cells were exposed first to $C_{60}(OH)_{20}$ and then to physiological copper ions. In the presence of $C_{60}(OH)_{20}$ both cell damage and ROS production induced by copper were suppressed, likely through neutralization of the metal ions by the $C_{60}(OH)_{20}$ in the extracellular space, as well as by adsorption and uptake of the nanoparticles which were surface-modified by the biomolecular species in the cell medium. These studies provided new data on the effects of nanoparticles on cell metabolism and could aid the treatment of oxidant-mediated diseases using nanomedicine.

The evident lack of knowledge regarding the interaction between nanoparticles and cell organelles justifies additional molecular level studies. Considering the ubiquitous structural and functional roles of cytoplasmic proteins and the prevalent synthesis of carbon nanoparticles, this chapters aims to examine the polymerization of microtubules (MTs) in the presence of a $C_{60}(OH)_{20}$. Using MT polymerization assay, circular dichroism (CD) spectroscopy, Guanosine-5'-triphosphate (GTP) hydrolysis assay and

isothermal titration calorimetry (ITC), the inhibition of MT polymerization in the presence of low micromolar concentration of $C_{60}(OH)_{20}$ was discovered. MD simulations have provided the insights on how nanoparticles may reshape the assembly of cytoskeletal proteins, a topic of essential importance for revealing cell response to carbon nanoparticles and for the advancement of nanomedicine.

6.1 Introduction

Recent advancement of nanotechnology in imaging, sensing, and medicine and the mass production of nanomaterials presents a crucial need for molecular level research centered on the behaviors of nanomaterials in biological systems [164, 199]. Towards this research direction fullerenes were shown to act as a HIV-1 protease inhibition [136, 137], and facilitate electron transport across a lipid bilayer [203]. In general, the toxicities of fullerenes and their derivatives have been examined *in vitro*, *in vivo*, as well as *in silico*, with consistent conclusions yet to be drawn.

Despite these ongoing research efforts, it is apparent that little is understood regarding the molecular level interaction between nanoparticles and cell organelles. MTs are a major component of the cell cytoskeleton and play essential roles in maintaining cell shape, rigidity, motility, vesicle and organelle transport, cell signaling, and cell division in eukaryotes. Under favorable *in vivo* or *in vitro* conditions MTs can be

polymerized from tubulin heterodimers of alpha and beta subunits into a cylindrical nanostructure of ~25 nm in diameter and up to micrometers long (Figure 6-1). Physically MTs can be viewed as polymers possessing a great persistent length and an exceptionally high bending rigidity to suit their versatile bioactivities. Defined by a dynamic instability which is still not well understood, the MT ends can switch abruptly from persistent slow growth to persistent shortening under solution conditions which support assembly.
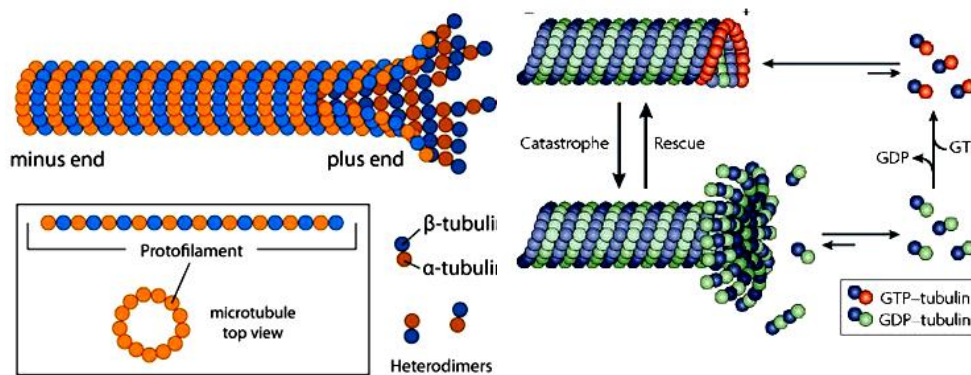
Figure 6-1. MT structure (left) [238] and dynamic (right) [239].

The assembly of MTs has recently been examined with the introduction of nanoparticles. Specifically, Gheshlaghi et al. [240] showed that TiO_2 nanoparticles could alter the MT steady state equilibrium and change tryptophan positions in tubulins to move them towards GTP binding sites. Apopa et al. found [241] that iron nanoparticle-induced ROS production could regulate cell permeability through remodeling of MTs in human microvascular endothelial cells. Using surface enhanced Raman spectroscopy,

Zhou et al. identified [242] a variety of tubulin functional groups including imidazole, sulfur, aromatic rings, amine, and carboxylate which interacted with gold nanoparticles, with the imidazole ring in the histidine acting as the most prominent functional group for the binding.

In view of the ubiquitous structural and functional roles of cytoplasmic proteins and the prevalent synthesis of carbon nanoparticles in research labs and by the industry, this paper examines the *in vitro* polymerization of MTs in the presence of $C_{60}(OH)_{20}$. Specifically, in the following sections we present our study based on the methodologies of fluorescence imaging, CD spectroscopy, ITC, GTP hydrolysis, and docking and atomistic molecular dynamics computer simulations. Our results indicate that $C_{60}(OH)_{20}$ inhibits MT assembly via the formation of multiple hydrogen bonds between the nanoparticle and its neighbouring tublin subunit. The binding between $C_{60}(OH)_{20}$ and the nucleotides, both exchangeable during GTP hydrolysis and immutable in alpha units, is another possible cause for the changes in the tubulin secondary structures and inhibited MT polymerization.

6.2 Experimental and computational sections

6.2.1 MT polymerization

Taxol stabilized fluorescent MTs were polymerized using a Fluorescent Microtubules Biochem Kit (# BK007R, Cytoskeleton). Specifically, MT polymerization reactions (3 µL) were prepared, each consisting of 2.5 µL of unlabeled tubulin (# TL238, Cytoskeleton, 0.045 mM) and 0.5 µL of rhodamine labeled tubulin (# TL331M, Cytoskeleton, 0.11 mM) suspended in the General Tubulin Buffer (or PEM buffer) (80 mM Na-PIPES pH 6.9, 1 mM $MgCl_2$, and 1 mM EGTA; # BST01, Cytoskeleton) to form a stock solution of one dye per three tubulin subunits (MW: 110 kDa). The General Tubulin Buffer also contained 0.03 µL of 100 mM GTP (# BST06, Cytoskeleton) for tubulin assembly. Prior to polymerization, fullerene derivative $C_{60}(OH)_{20}$ (BuckyUSA) was suspended in Milli-Q water (pH6.5) to form a stock concentration of 100 mg/L, filtered, and sterilized using Anotop 10 filters (0.2 µm, Whatman). Approximately 0.5 µL of $C_{60}(OH)_{20}$ (6.6~198 µM) were added to 3 µL of MT polymerization reactions to obtain

final $C_{60}(OH)_{20}$ concentrations of 1~30 mg/L (or 0.94~28.2 µM) respectively and the

mixtures were incubated at 35°C for 20 min. Small aliquots of the polymerized MTs, each added with 1× antifade solution (# BSM02, Cytoskeleton), were examined by fluorescence microscopy (Imager A1, Zeiss) and approximately 200 MTs were measured for each sample condition to establish sufficient statistical distributions. Statistically

significant differences between the samples and the controls were determined by the Student t-test.

6.2.2 Characterization of $C_{60}(OH)_{20}$ suspension

The hydrodynamic size of $C_{60}(OH)_{20}$ was measured at room temperature using a dynamic light scattering device (Malvern, nanosizer S90, range: 0.3 nm-5 μm). Single peaks at ~1.0 nm (polydispersity index: 0.141) and 5.7 nm (polydispersity index: 0.443) were identified for the nanoparticles in Milli-Q water and in the PEM buffer. The stability of the $C_{60}(OH)_{20}$ suspension was further confirmed by its negative zeta potential of -34.3 mV in Milli-Q water and -22.0 mV in the PEM buffer. Such changes in the physicochemistry (size, polydispersity, and charge) of the nanoparticles are attributed to the presence of Na^+ and Mg^{2+} in the PEM buffer.

6.2.3 CD spectroscopy

To probe the conformational change in the tubulin secondary structures due to $C_{60}(OH)_{20}$ binding, CD spectroscopy measurements were performed at room temperature using a Jasco J-810 spectropolarimeter (Easton, MD) with a constant temperature water-

circulating bath over the wavelength range of 200-300 nm. The structural contents of the tubulins were measured using 0.25 mg/mL tubulin solutions in Milli-Q (pH 6.5) loaded into 0.10 mm path length high-transparency quartz cuvettes (Starna Cells, Inc., Atascadero, CA). Milli-Q water was used as the buffer due to the high transparencies of the samples. To prevent possible protein denaturation in the absence of salt, an obervation time of 1 h or less was ensured. The spectrum of each sample was averaged over three scans taken at a speed of 50 nm/min and subtracted by the blanks of Milli-Q. The ellipticity value (θ, in mdeg) provided by the instrument, was converted to standard units of deg·cm^2/dmol (designated as [θ]) using the following equation [θ] = ($\theta \times M_0$)/($10000 \times C_{soln} \times L$) [243, 244], where M_0 is the mean residue molecular weight (118 g/mol), C_{soln} is the tubulin concentration in solution (g/mL), and L is the path length through the buffer (cm).

The molar ellipticities as a function of wavelength that were obtained from the CD scans were deconvoluted using the SP-22X algorithm and analyzed using the SELCON and CONTIN/LL software [245] packages. Such deconvolution yielded the percents of secondary structure components (α-helices and β-sheets) in the protein samples. These programs analyze the ellipticity values at each wavelength and compare them with a library of proteins with known secondary structures. The percents of various secondary structural components are then derived based on the comparisons.

6.2.4 ITC

To provide detailed information on the binding of $C_{60}(OH)_{20}$ with tubulin, ITC measurements were performed on a VP-ITC MicroCalorimeter (MicroCal Inc., Northampton, MA). Tubulins were dialyzed extensively against PEM buffer without GTP to avoid microtubule polymerization, to a final concentration of 0.7 μM. The syringe content was 0.2 mM $C_{60}(OH)_{20}$ dissolved in the last dializant.

A typical titration involved 22 injections of $C_{60}(OH)_{20}$ (14 μL aliquots per shot) into the sample cell at a 4-min interval, each containing 1.46 mL of tubulin. The titration cell was kept at 298 K and stirred continuously at 300 rpm. The heat of diluting $C_{60}(OH)_{20}$ in the buffer alone was subtracted from the titration data when the thermodynamics parameters were calculated. All the data were analyzed to determine binding stoichiometry (N), affinity constant (K), and thermodynamic parameters of the reaction, using Origin 5.0 software.

6.2.5 GTP hydrolysis

To detect the release of inorganic phosphate during the GTP hydrolysis that is associated with MT polymerization, a SensoLyte MG Phosphate Assay Kit (AnaSpec) was used. This kit is based on the quantification of the blue-green complexes formed by

Malachite Green, molybdates, and free orthophosphates, which are released during MT polymerization. The rapid color formation from the reaction was measured on an absorbance microplate reader at 630 nm (µQuant, BioTek Instuments, INC.).

6.2.6 Computational methods

Two computational methods, namely, molecular docking and MD, were used to find out (i) the possible binding sites of $C_{60}(OH)_{20}$ on tubulin alpha-beta dimer, and (ii) how the binding of $C_{60}(OH)_{20}$ affects the structure and dynamics of the tubulin dimer. The molecular structure of the dimer was obtained from protein data bank (PDB ID: 1JFF [246]). The missing residues in the PDB structure were added using MODELLER 9v7 [247] and the complete dimer was energy minimized using a steepest descent algorithm.

6.2.7 Docking simulation

Molecular docking is a computational method used to assess the binding modes and affinities of small molecules (e.g., drugs) on larger molecules such as proteins. Here, docking of $C_{60}(OH)_{20}$ was carried out on tubulin to predict the possible binding sites and binding affinities. One of the most popular docking software packages, AutoDock [248]

(version 4.2), was used. The PDB structure may not represent the actual protein structure, which constantly undergoes conformational changes due to thermal motion. For a more realistic approach, docking can be performed on conformations obtained from MD simulations. Here we performed docking calculations on the conformation at 10 ns of the MD simulation in addition to the PDB structure. Default AutoDock force field parameter [249] were used, setting all bonds rigid except the C-O bonds of $C_{60}(OH)_{20}$, which were made rotatable. Fifty docking runs with 10 trials in each run were performed for both dimer conformations, resulting in a total of 1,000 docked structures.

6.2.8 MD simulation

The binding of $C_{60}(OH)_{20}$ may affect the secondary, tertiary and quaternary structures of tubulin dimers and hence their polymerization into MTs. Since MD simulations are capable of capturing such structural changes, two sets of simulations were carried out to examine this aspect. In the first set (referred to as *set I* in the following) a tubulin dimer was simulated with GTP and guanosine diphosphate (GDP) bound to it as in the PDB crystal structure (PDB ID: 1JFF). In the other set (*set II*), the dimer-GTP-GDP complex was simulated with ten $C_{60}(OH)_{20}$ molecules placed randomly around it. In both sets, the protein complex (with or without $C_{60}(OH)_{20}$ as the case may be) was placed at the center of the simulation box. The size of the box in each case was decided so that the distance from the protein complex (or $C_{60}(OH)_{20}$) to any edge of the box was at least

0.9 nm. The number of water molecules added was approximately 40,000. 36 Na^+ ions were added for charge neutrality. In addition, 122 Na^+ and Cl^- ions were also added such that the salt concentration in the simulation box was about 100 mM. Each of these steps was followed by energy minimization using a steepest descent algorithm, as implemented in GROMACS 4.5 [250].

Four independent simulations were carried out for each set. Each simulation was initiated with a 50 ps long *NVT* thermalization run, followed by a 100 ps long *NPT* simulation, during which the protein/GTP/GDP/$C_{60}(OH)_{20}$ heavy atoms were position restrained. Finally, a 50 ns long unrestrained production run was carried out at $T = 298$ K and $P = 1$ bar.

The simulations were carried out with the GROMACS simulation package, version 4.5 [250]. The Gromos 53A6 force field [251] was used with the SPC model for water [225]. The parameters for GTP and GDP were obtained by augmenting the guanine model of Gromos 53A6 with the triphosphate side chain parameters of ATP in the same force field [251]. For charge states of -4 and -3 for GTP and GDP, respectively, the terminating phosphate group charges were set as in our previous study with dGTP [131]. The model for $C_{60}(OH)_{20}$ was adapted from Ref. [131].

The LINCS algorithm [227] was used to restrain all the bonds and an integration time step of 2 fs was used. Long-range electrostatics was treated with the Particle-Mesh Ewald [229] (PME) method. In all the simulations, the system temperature was maintained at 298 K by using the velocity rescaling algorithm by Bussi et al.[252] The

system pressure was controlled by using the weak coupling algorithm by Berendsen et al. [226] with a coupling time constant $\tau_T = 0.5$ ps in the restrained *NPT* simulations, and the Parrinello-Rahman barostat [232] ($\tau_T = 2.0$ ps) in the unrestrained production runs.

6.3 Results and discussions

6.3.1 Inhibition of tubulin polymerization by $C_{60}(OH)_{20}$

As the concentration of $C_{60}(OH)_{20}$ was increased from 1 to 30 mg/L, the averaged length of polymerized MTs was shortened accordingly (Figure 6-2). Both bimodal and normal single-peak distributions were shifted to the left with the addition of the nanoparticles, indicating inhibition of MT polymerization. Specifically, the presence of highest $C_{60}(OH)_{20}$ concentration of 30 mg/L led to the shift of the single-peak distribution to be centered at 3 μm, indicating that most of the polymerized MTs were shorter than the ones for the control, where two distribution peaks were observed at 5 μm and 20 μm. Also, we observed that the quantity of polymerized MTs per field of view was reduced under the fluorescence microscope with the addition of $C_{60}(OH)_{20}$, and smaller broken segments of MTs were frequently observed (Figure 6-2(B)). To quantify this phenomenon, we further counted the number of polymerized MTs on each coverglass substrate, and the average number of polymerized MTs was obtained for twenty slides of

each sample condition. The MTs shorter than 1 μm were not taken into consideration to eliminate error introduced by the instrument resolution and diffraction limit.
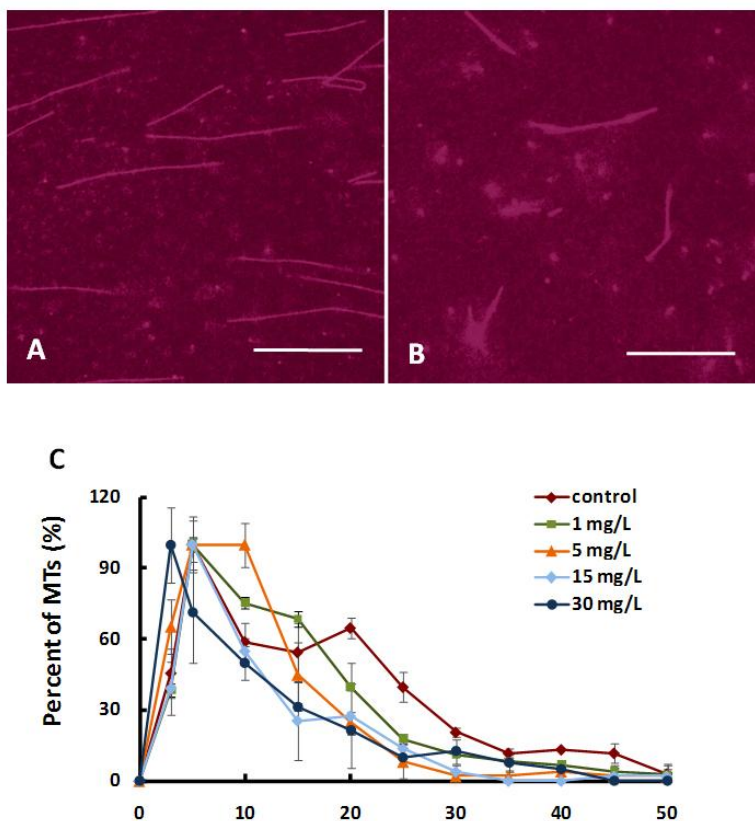
Figure 6-2. MT polymerization in the presence of $C_{60}(OH)_{20}$. (A) Control polymerization of MTs. (B) MT polymerization in the presence of $C_{60}(OH)_{20}$ of 15 mg/L. Scale bars: 20 μm. (C) Length distribution of polymerized MTs (normalized by peak values) vs. $C_{60}(OH)_{20}$ concentration. Approximately 200 MTs were analyzed for each sample condition.

As shown in Figure 6-3, the amount of polymerized MTs was significantly reduced with $C_{60}(OH)_{20}$ concentrations at or above 5 mg/L. Specifically, the presence of the highest $C_{60}(OH)_{20}$ concentration of 30 mg/L led to a 50% decrease in the number of polymerized MTs.
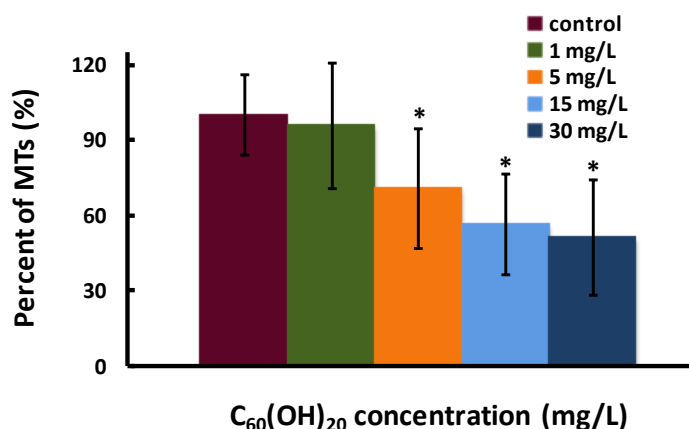
Figure 6-3. Number of polymerized MTs (normalized by the control) vs. $C_{60}(OH)_{20}$ concentration. Statistically significant differences between the samples and the control were determined by the Student t-test (*: $p<0.05$).

Three interactions could have contributed to the hindered MT polymerization. One is that the hydroxyl groups of the nanoparticles could form hydrogen bonding with the electronegative elements on the tubulin surfaces, similar to that described for the interaction between free dNTPs and $C_{60}(OH)_{20}$ in the PCR process [131]; the other is the electrostatic interaction between the negatively charged $C_{60}(OH)_{20}$ in the reaction buffer -

according to the zeta potential measurement - with the abundant amine groups on the protein surfaces. However, since the two carboxyl termini of each tubulin carry a significant electric charge, direct binding between $C_{60}(OH)_{20}$ and assembled MTs is unlikely due to their mutual repulsion, although the hydrogen bonding between the nanoparticles and the Guanosine-5'-diphosphate (GDP) in the MT protofilaments could still take place. Furthermore, due to the steric hindrance of the hydroxyl moieties of the nanoparticles, π-stacking between the sp^2 electrons in the $C_{60}(OH)_{20}$ and the aromatic groups on the tubulin surfaces is not expected to be a contributing factor. In addition to the above two interactions, a third plausible cause for the hindered MT polymerization is that $C_{60}(OH)_{20}$ could be involved in the biochemical process of GTP hydrolysis, through either forming hydrogen bonds with the free nucleotides in the reaction or altering the length and structure of the GTP cap at the growing ends of the MT to impact the polymerization; in either case the conformational changes in the tubulins or in the nucleotides could disrupt the vertical assembly of the tubulins into protofilament or the lateral weak bonds between the tubulins into a sheet that is subsequently curled into a tube.

6.3.2 $C_{60}(OH)_{20}$ binding induced secondary structural changes in tubulin

To delineate the binding mechanisms for tubulin and $C_{60}(OH)_{20}$, CD spectra of the protein were acquired at room temperature. As illustrated in Figure 6-4, addition of

the nanoparticles to the reaction altered the far-UV circular dichroism spectrum of the tubulin, indicating that $C_{60}(OH)_{20}$ indeed bound to the protein to induce a conformational change in the latter. The mathematical method SELCON [244, 245] was used to calculate percents of the secondary structures of the protein, based on the linear dependence between structural fractions and the spectra (see Figure 6-4).
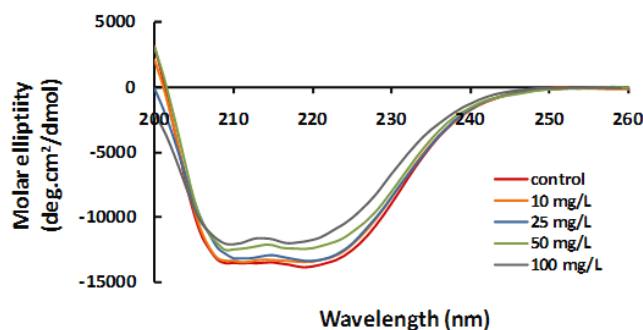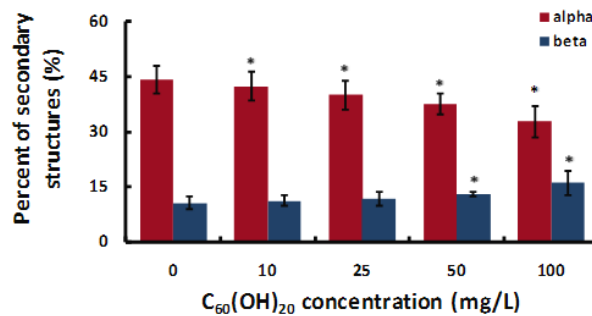
Figure 6-4. (A) Circular dichroism spectra in the presence of $C_{60}(OH)_{20}$. (B) Percent of secondary tubulin structures vs. $C_{60}(OH)_{20}$ concentration. Statistically significant differences between the samples and the control were determined by the Student t-test (*: $p < 0.05$).

As $C_{60}(OH)_{20}$ concentration increased more alpha helices were turned into beta sheets, or denatured further into linear structures since the total percent of alpha and beta sheets was decreased by 6.9% when $C_{60}(OH)_{20}$ concentration was increased from zero to 100 mg/L. The CD spectra of pure proteins incubated under the same conditions were acquired, which showed no significant changes in their secondary structures. This step confirmed that changes in the secondary structures of the tubulin were induced by the binding of the nanoparticle, not by protein denaturation, through the first or second mechanism aforedescribed.

6.3.3 ITC of tubulin- $C_{60}(OH)_{20}$ binding

The inhibition of microtubule polymerization can be attributed to the binding of $C_{60}(OH)_{20}$ with tubulin. Figure 6-5 shows a serial titration analysis of the interaction of $C_{60}(OH)_{20}$ and tubulin. Since ITC measurements require high protein concentrations, the measured parameters are independent of the state of the tubulin. The titration consisted of addition of small aliquots of $C_{60}(OH)_{20}$ per shot per 4 min interval to 0.7 µM tubulin in general tubulin buffer (PEM) without GTP at 298 K. The titration showed monotonic decrease in the exothermic heat of binding with successive injections until saturation.

The upper panel of Figure 6-5 displays raw data in power versus time prior to baseline subtraction.
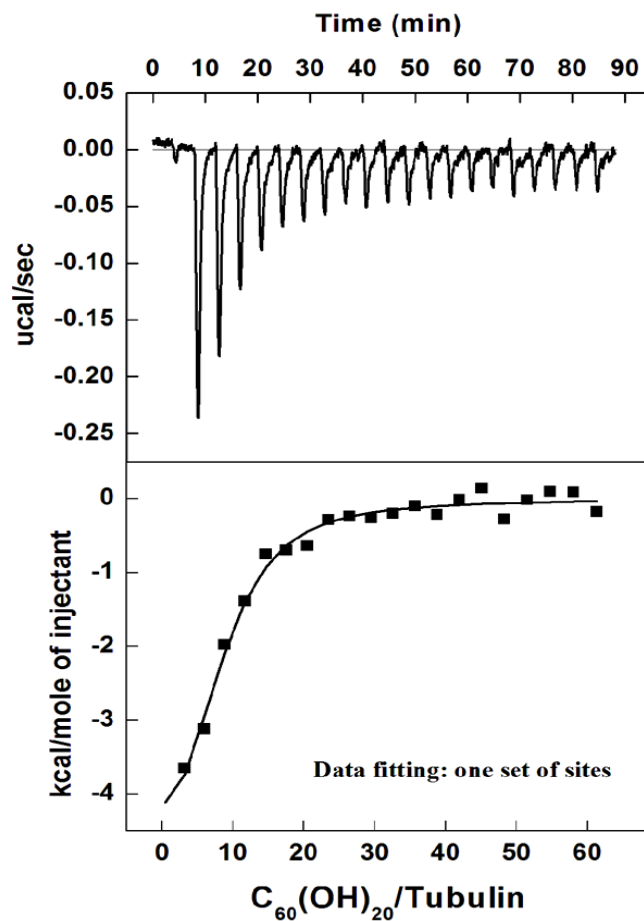
Figure 6-5. Calorimetric titration of tubulins with $C_{60}(OH)_{20}$ at 25°C. The upper panel show raw data, obtained from 22 injections (14 μL each) of $C_{60}(OH)_{20}$. The lower panels show the plot of total energy exchanged (as kcal/mol of injectant) as a function of molar ratio of the $C_{60}(OH)_{20}$ to tubulin. The theoretical curve fitted to the intergraded data yield ΔG = -6.343 kcal/mol and ΔH = -2.648 kcal/mol. On average 9 $C_{60}(OH)_{20}$ molecules were bound to 1 tubulin monomer and the binding constant K was determined as $1.3\pm0.16\times10^6$ M^{-1}.

The area under each injection peak is proportional to the heat produced. The lower panel of Figure 6-5 displays the binding isotherm created by plotting the integrated peaks against the molar ratio of $C_{60}(OH)_{20}$ added to the tubulin. The heat of diluting $C_{60}(OH)_{20}$ in the buffer was taken into account for calculating the thermodynamic parameters. The theoretical curve fitted to the intergraded data yield ΔG = -6.343 kcal/mol and ΔH = -2.648 kcal/mol. On average 9 $C_{60}(OH)_{20}$ molecules were bound to 1 tubulin monomer and the binding constant K was determined as $1.3 \pm 0.16 \times 10^6$ M^{-1}.

6.3.4 Effect of $C_{60}(OH)_{20}$ on GTP hydrolysis

Tubulin is a GTPase that hydrolyzes its bound nucleotide triphosphate [253]. During MT polymerization, both the alpha and beta subunits of a tubulin dimer are bound to a GTP molecule and the tubule elongates from the minus end to the plus end. While the GTP bound to alpha tubulin is stable, the GTP bound to beta tubulin may be hydrolyzed by the protein to GDP and an inorganic phosphate shortly after assembly. A GDP-bound tubulin subunit is prone to depolymerization and will fall off at the tip of an MT or remain integrated if it resides in the middle of the tubule [253]. Once a GTP-bound tubulin is added to the tip of the MT, a new cap is formed to stimulate the growth of the tubule. When hydrolysis catches up to the plus end of the MT, polymerization is switched to shrinkage through the process of catastrophe [254].

As shown in Figure 6-6, the release of inorganic phosphate during GTP hydrolysis was impaired by the presence of $C_{60}(OH)_{20}$ at concentrations of 25 mg/L and above. Interestingly, such inhibition did not increase much for higher nanoparticle concentrations of 50 mg/L and 100 mg/L, by ~5% respectively in comparison with the control. The reduced release of phosphate during MT polymerization is a direct indication of the shrinkage of the GTP cap length at the growing ends of the MT, which would give rise to increased instability in the MT architecture.
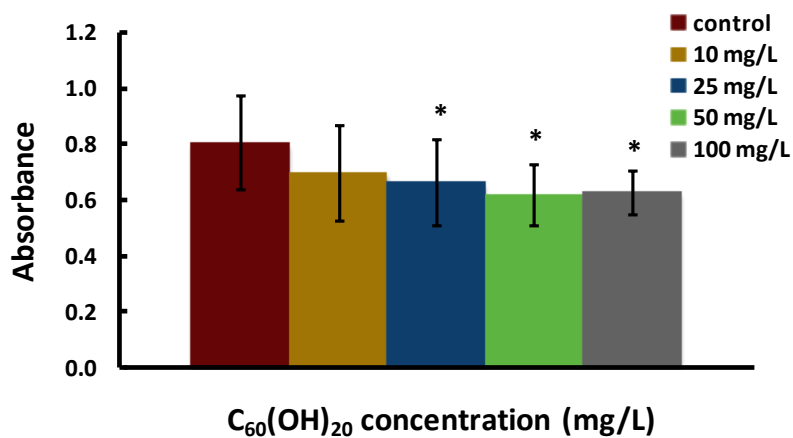
Figure 6-6. GTP hydrolysis (phosphate release) vs. $C_{60}(OH)_{20}$ concentration. Statistically significant differences between the samples and the control were determined by the Student t-test (*: $p < 0.05$).

6.3.5 Binding by docking and MD simulations

The 1,000 conformations from docking were analyzed to identify the most important binding sites of $C_{60}(OH)_{20}$ on tubulin dimer. The conformations were grouped into different clusters based on root-mean-square deviations (RMSDs) of their coordinates. Conformations with their mutual RMSDs within 0.8 nm were considered to be in the same cluster.
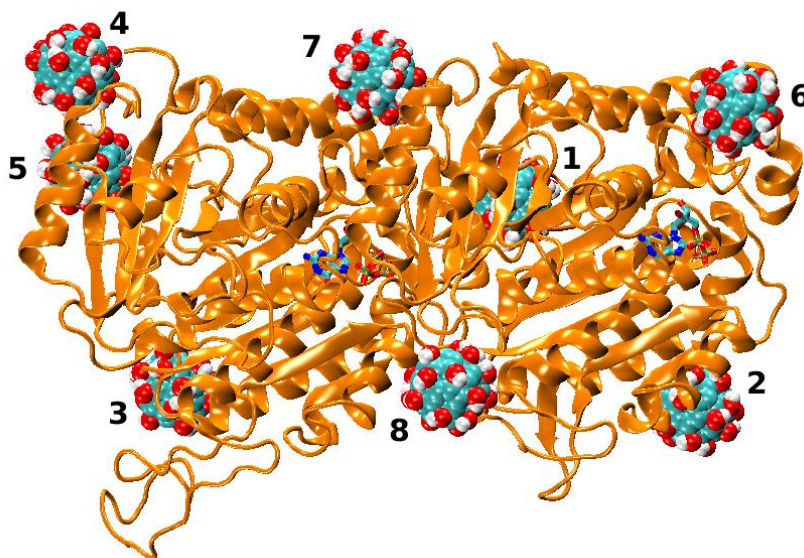
Figure 6-7. Eight binding sites of $C_{60}(OH)_{20}$ on tubulin dimer (alpha subunit on the left side and beta subunit on the right side) identified from docking simulations. No binding was observed near the GTP/GDP binding E-site in the beta subunit

Different conformations in the same cluster thus represent different binding modes at the same binding site. Eight binding sites were identified as the most important ones based on the binding energy, population of the cluster and relevence of the site for polymerization (Figure 6-7).

Table 6-1 summarizes the binding energies and molecular populations of these eight sites. The obtained binding energies range between -6.45 and -2.99 kcal/mol for the eight most prominent sites. These values are in a reasonable agreement with the ITC data analysis based on the single-site binding model (-6.34 kcal/mol).

TABLE 1. Eight Most Important Binding Sites and Their Properties Predicted by Docking Simulations.

Site	Lowest Binding Energy (kcal/mol)	Population	Residues[a] within 0.7 nm of $C_{60}(OH)_{20}$
1	-6.45	85	Asn 102, Glu 411, His 406, *Arg 158, Asp 163, Asn 197, Thr 198, Asp 199, Val 257, Phe 262, Arg 264, His 266*
2	-4.05	60	*Pro 89, Asp 90, Asn 91, Phe 92, Val 93, Phe 94, Leu 114, Ser 117, Asp 120, Val 121, Lys 124, Arg 79*
3	-4.03	91	Phe 49, Asn 50, Phe 53, Arg 123, Asp 127, Cys 129, Leu 130, Phe 135, Tyr 161, Lys 163, Lys 164
4	-3.72	57	Lys 336, Thr 337, Lys 338, Arg 339, Thr 340, Gln 342, Phe 343, Asp 345
5	-3.34	97	Thr 257, Asn 258, Val 260, Pro 261, Tyr 262, Trp 346, Cys 347, Pro 348, Thr 349
6	-2.65	86	*Val 177, Ser 178, Thr 180, Val 181, Val 182, Glu 183, Pro 184, Tyr 185, Arg 390, Glu 393, Gln 394, Phe 395, Phe 404, Lys 176*
7	-3.97	33	Gln 176, Arg 390, His 393, Lys 394, Leu 397, *Leu 333, Gln 336, Asn 337, Glu 345, Trp 346, Ile 347, Pro 348, Asn 349, Asn 350*
8	-2.99	45	*Tyr 36, Asp 39, Ser 40 Asp 41, Leu 42, Gln 43, Ile 358, Pro 359, Arg 369*

[a] Alpha subuint residues in normal and beta subunit residues in italics typeface.

Table 6-1. Eight Most Important Binding Sites and Their Properties Predicted by Docking Simulations.

184

The MD simulations started with 10 $C_{60}(OH)_{20}$ molecules positioned randomly around the tubulin dimer. In all the simulations, it was observed that $C_{60}(OH)_{20}$ binds to different locations around the protein. That is, as in the docking simulations, a single predominent binding site seems to be absent. Instead, $C_{60}(OH)_{20}$ prefers sites with many charged or polar residues. Both of these are consistant with the ITC measurements which showed that up to 9 $C_{60}(OH)_{20}$ molecules bound to each tubulin dimer. Once anchored at these binding sites, $C_{60}(OH)_{20}$ remained bound throughout the simulations. This is illustrated in the plot of minimum distances between 10 $C_{60}(OH)_{20}$ molecules and 1 tubulin (Figure 6-8). Upon binding to the tubulin, $C_{60}(OH)_{20}$ molecules form a number of hydrogen bonds with charged or polar residues.
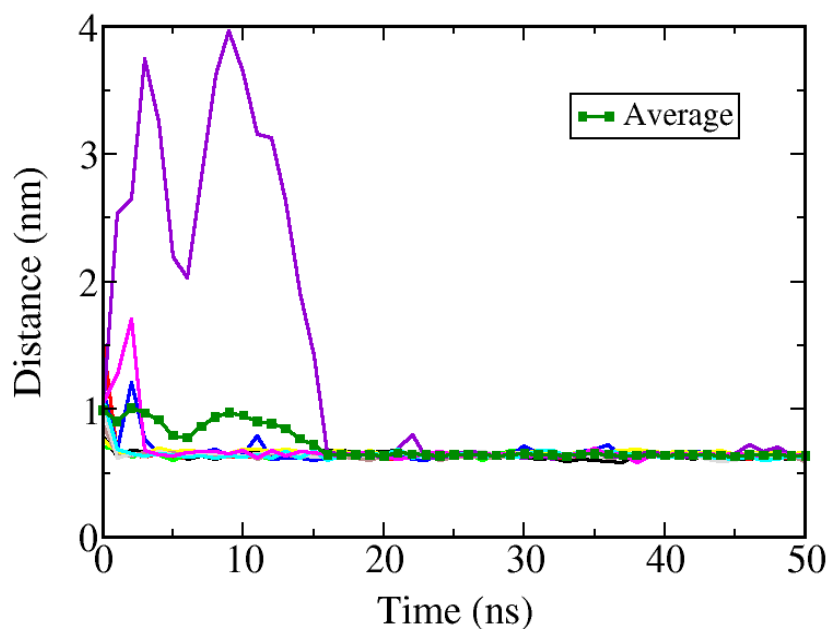
Figure 6-8. The minimum distances between ten $C_{60}(OH)_{20}$ molecules and tubulin in a simulation and their average.

Figure 6-9 shows the number of hydrogen bonds as a function of time for four simulations. On average, each $C_{60}(OH)_{20}$ molecule forms approximately 6 hydrogen bonds with the tubulin.
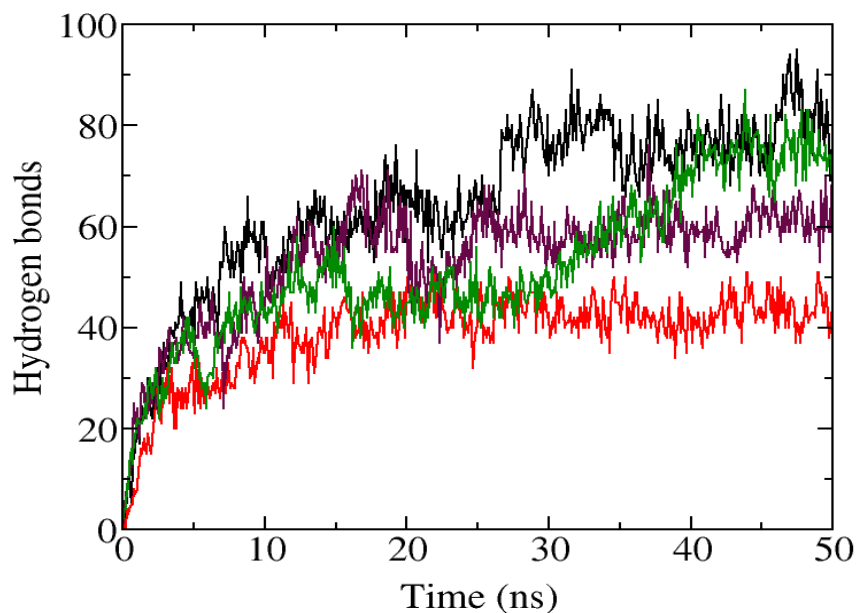
Figure 6-9. The number of hydrogen bonds between ten $C_{60}(OH)_{20}$ molecules and tubulin in four independent simulations.

It was observed in our experiment that the total percent of alpha helices and beta sheets was decreased by 6.9% as $C_{60}(OH)_{20}$ concentration was increased from zero to 100 mg/L (Figure 6-4). To check this, the secondary structure of tubulin was analyzed for two *set I* and *set II* simulations (sets without and with $C_{60}(OH)_{20}$ molecules, respectively)

using the secondary structure assignment algorithm DSSP [255]. First, there was an overall tendancy (for both sets) for a decrease in the number of alpha helix residues and increase in beta sheet residues due to the inherent nature of the Gromos force field [256]. The number of residues forming beta sheets was slightly larger [$(1.9 \pm 1.7)\%$] in *set II* simulations compared to *set I* simulations. Similarly, the number of alpha helix residues was slightly smaller [$(1.8 \pm 1.1)\%$] in *set II* simulations compared to *set I* simulations. Although these observations are consistant with the experimental results, the differences are very small. Futher, between the two sets, there was no noticable difference in the total number of residues forming alpha helix or beta sheets.

The binding of $C_{60}(OH)_{20}$ to tubulin-bound GTP/GDP can affect the GTP hydrolysis or GDP/GTP exchange and thus MT dynamics. It has been shown that $C_{60}(OH)_{20}$ can bind to the triphosphate tail of dNTP, with a binding energy greater than 10 kJ/mol [131]. Since dNTPs and nucleoside triphosphates (NTPs) share the same structures, except that the 2' hydroxyl group is replaced by a hydrogen atom in the former, $C_{60}(OH)_{20}$ should bind to GTP with a similar binding energy. However, $C_{60}(OH)_{20}$ was not found to bind to tubulin-bound GTP/GDP in either MD or docking studies. This is probably due to the size and shape of the GTP/GDP binding site of the tubulin which is not favorable for hosting large spherical molecules like $C_{60}(OH)_{20}$. Conceivably, such steric hindrance could be further reinforced by the prevalent binding of $C_{60}(OH)_{20}$ on the tubulin. Furthermore, the number of GTP molecules in the reaction buffer was two to three orders of magnitude higher than that of $C_{60}(OH)_{20}$ in the

experiment, implying that it was far more likely for $C_{60}(OH)_{20}$ to bind to the free GTP/GDP molecules in the buffer than with the bound nucleotides in the tubulin.

Additional new insight has been obtained from the simulations. First, a tubulin dimer makes a number of contacts with its neighboring dimers when inserted into a MT. If $C_{60}(OH)_{20}$ molecules bind to these contact regions as indicated by docking and MD simulations, they can also prevent the incorporation of the dimer into a MT. The crystal structure of tubulin is obtained from zinc sheets in which the protofilaments are arranged similar to that in a MT, but the protofilaments are antiparallel in zinc sheets [257]. Thus, the longitudinal contacts seen in zinc sheets [246] are the same as that in a MT, but the lateral contacts could be different. Figure 6-10 shows a tubulin dimer with its longitudinal neighbors. The locations of the $C_{60}(OH)_{20}$ molecules that bind at these contact regions in MD simulations are also shown. It is possible that the binding of nanoparticles at these sites could impede MT polymerization.
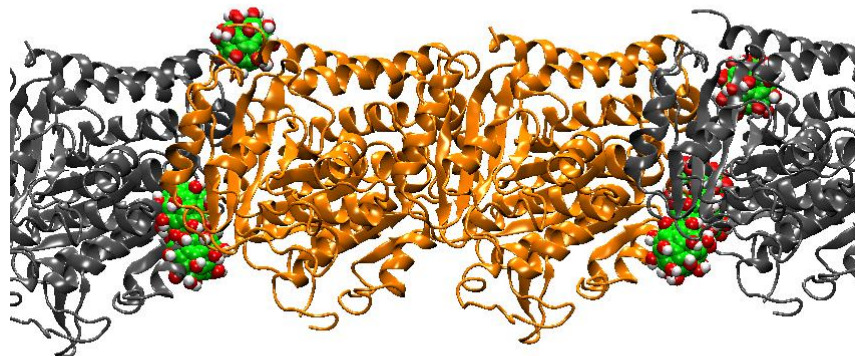
Figure 6-10. The contact between a tubulin dimer (orange) and its longitudinal neighbors (grey) in a protofilament. All the $C_{60}(OH)_{20}$ binding sites at the two longitudinal interfaces predicted by MD are shown.

Second, in MD simulations, $C_{60}(OH)_{20}$ was also seen to bind the M-loop and H5 and H12 helices (Figure 6-11). The interaction between the M-loop in one dimer and helices in neighboring dimer is a major contributor to lateral contacts between tubulin dimers in zinc sheets. Although the lateral contacts in MTs do not necessarily have to be the same as that in zinc sheets, the M-loop is involved in lateral contact in MTs. Thus $C_{60}(OH)_{20}$ could also affect the lateral contacts and thus MT aseembly if bound to these motifs.
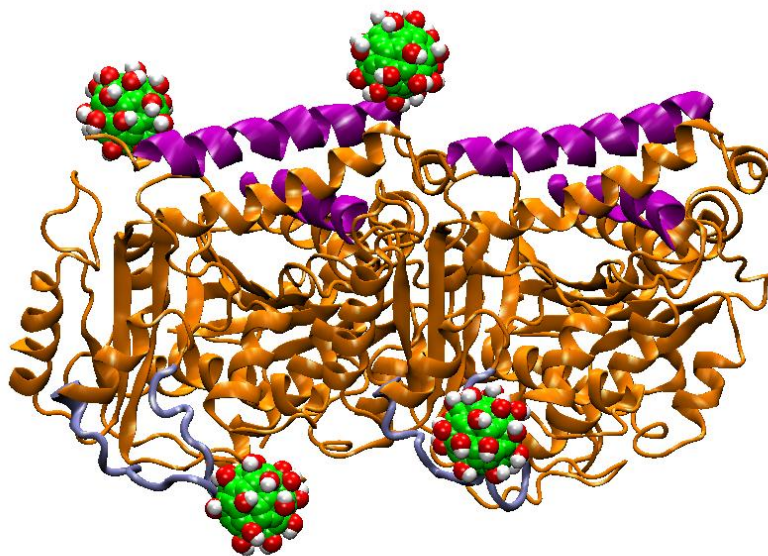
Figure 6-11. The interaction between M-loop of one dimer (blue) and the helices H5 and H12 (purple) in a neighboring dimer contribute most to the inter-dimer lateral contacts in zinc sheets. $C_{60}(OH)_{20}$ was seen to make contacts with these structures in MD simulations.

Our experimental and computer simulation studies have shown that $C_{60}(OH)_{20}$ can inhibit MT polymerization, mainly through the formation of hydrogen bonding between the nanoparticle and the tubulin dimer. The binding of the fullerene derivative has been shown experimentally to alter the secondary structures of the tubulin and impede the release of inorganic phosphate in GTP hydrolysis. Additional simulations have unravelled occupancy of the contacts between adjacent tubulin dimers within a protofilament and between neighboring tubulins by the nanoparticles, which should

conceivably also influence the assembly of tubulins into MTs. Since MTs are important organelles whose structure and dynamics are essential to many functionalities and activities of the cell, this study not only facilitates our understanding of the biological response to engineered nanoparticles on the molecular level, but also aids novel medicinal designs of utilizing the potent antiproliferative activity of $C_{60}(OH)_{20}$ against cancer and cell oxidation [85].

CHAPTER SEVEN

CONCLUSIONS AND FUTURE WORK

7.1 Conclusions

This dissertation is centered on understanding the biological and ecological responses to carbon nanomaterials. The major findings from this research are the following:

- <u>On the whole organism level</u>:   the dynamic uptake, accumulation, and biodistribution of fullerene C_{70} has been observed and quantified in rice plant. Rice plant was selected as the model system because it is a major food crop for over half of the world's population. The mobility of C_{70} was rendered by NOM, a most abundant organic substance in natural river sources and agricultural soil. The stability of C_{70}-NOM resulted from hydrophobic, π stacking, and van der Waals interactions between the nanoparticle and the NOM through self assembly. Importantly, for the first time, we observed transmission of C_{70} through the rice plant progeny, indicating the profound impact of nanoparticle discharge on plant growth and regeneration.

  The uptake and biodistribution of C_{70}-NOM in the rice plant was driven by transpiration in the plant xylem, and was fueled by convection and the

concentration gradient of the nanoparticles from the plant roots to the leaves. In contrast, MWNTs were mostly excluded by the rice plants due to their large hydrodynamic size and hydrophobicity, the two parameters which could not overcome the plant cell wall and waxy root hair for entrance;

- <u>On the cellular level</u>: we have conducted two individual studies to address the cellular level impact of carbon nanoparticles. The first was a biophysical study comparing the uptake of C_{70}-NOM and $C_{60}(OH)_{20}$ − two self assembled and covalent carbon nanostructures of contrasting water solubility and surface chemistry -- by *Allium cepa* plant and HT-29 mammalian cells. The second was a toxicological study on the cytoprotective property of $C_{60}(OH)_{20}$ against toxin copper.

  The findings from the first cellular study are twofold. First, for plant cells, we showed that the plant cell wall, owning to its hydrophobic cellulose content, played a role of filteration against foreign materials. This filtration was effective for retaining the larger and more hydrophobic C_{70}-NOM, but void in guarding against the uptake of the smaller and more hydrophilic $C_{60}(OH)_{20}$. Consequently, driven by its concentration gradient across the extracellular space to the plant cell wall, $C_{60}(OH)_{20}$ accumulated rapidly to exert a mechanical damage to the fluidic plasma membrane and eventually cause cell damage with increased nanoparticle concentration. Second, for mammalian cells, we observed no toxic effect associated with the hydrophilic $C_{60}(OH)_{20}$, but increased damage with increased concentration of C_{70}-NOM.

This differential cytotoxicity between the two types of nanoparticles is understandable. The more hydrophobic C_{70}-NOM possessed a higher affinity for the amphiphilic cell membrane and its partitioning in the cell membrane compromised the cell fluidity and ion exchange to induce damage. In contrast, it was energetically more favorable for $C_{60}(OH)_{20}$ to be excluded by the membrane and, instead, form hydrogen bonding with water and dipolar interaction with the polar lipid head groups in the cell membrane.

For the second cellular study copper was chosen as the model toxin due to its great biological and environmental relevancies. The protection of $C_{60}(OH)_{20}$ against cell damage and ROS production induced by copper was attituted to the two following mechanisms: binding of $C_{60}(OH)_{20}$ with the biomolecular species in the cell medium and subsequent cell uptake of the surface-modified $C_{60}(OH)_{20}$ by the endocytotic pathways, and adsorption of $C_{60}(OH)_{20}$ onto membrane proteins and lipids and neutralization of the copper ions in the cell growth medium by the membrane bound nanoparticles. These two cell level studies are significant in view of guiding the design of nanomedicine and environmentally sustainable nanotechnologies, and are relevant to the potential use of water-soluble fullerene derivatives for the treatment of oxidant-mediated diseases;

- <u>On the molecular level</u>: We have examined the impacts of carbon nanoparticles on DNA amplification and MT polymerization, two major cellular processes. Both experiments were conducted in vitro and were

assisted by MD computer simulations. Specifically, in the presence of a fullerene derivative $C_{60}(OH)_{20}$ at a concentration of 4×10^{-4} mM, the amplification of a plant HSTF gene was completely inhibited. This inhibition was mainly attributed to the physical interaction between the nanoparticle and the Taq DNA polymerase. Atomistic MD simulations showed a clear tendency for hydrogen bonding to occur between $C_{60}(OH)_{20}$ and both the dNTPs and ssDNA components of the polymerase chain reaction.

We demonstrated the inhibition of MT polymerization by $C_{60}(OH)_{20}$ at low micromolar concentrations. The inhibition was mainly attributed to the formation of hydrogen bonding between the nanoparticle and the tubulin heterodimer, the building block of the microtubule, as evidenced by docking and MD simulations. Our circular dichroism spectroscopy measurement indicated changes in the tubulin secondary structures, while our GTP hydrolysis assay showed hindered release of inorganic phosphate by the nanoparticle. Our isothermal titration calorimetry measurement further quantified that $C_{60}(OH)_{20}$ bound to tubulin at a molar ratio of 9:1 and with a binding constant of $1.3\pm0.16\times10^6 \, M^{-1}$, which was substantiated by the binding site and binding energy analysis using docking and MD simulations. Computational simulations further suggested that occupancy by the nanoparticles at the longitudinal contacts between tubulin dimers within a protofilament or at the lateral contacts of the M-loop and H5 and H12 helices of neighboring tubulins could also influence the polymerization process.

7.2 Future work

As a natural extension to my PhD project I propose these following future research topics:

- Firstly, the interactions of nanomaterials with ecological systems need to be better understood. On the whole organism level, the topic "plant-nanoparticle interaction" may be focused on "plant seed-nanoparticle interaction" for the assessment of using nanoparticles as plant fertilizers. Plant seeds contain seed coats which play a vital role in the life cycle of plants by controlling the development of the embryo and determining seed dormancy and germination. Seed coats also play a key role in the protection of embryo from mechanical damage and prevention of drying out. Depending on the plant species, seed coats may vary within the millimeter to centimeter range and should significantly affect the rate of nanoparticle uptake.

- Secondly, on the cellular level, it remains to be seen as how nanomaterials may be surface-modified by cellular enzymes. Motivated by a wide range of potential applications, nanoparticles have been purposefully coated with proteins and other organic molecules and chemical species. These surface coatings are expected to significantly impact the fate of the nanoparticles in living systems, from initial cell adsorption to uptake, translocation, degradation, and eventual discharge of the nanoparticles. In mammalian

systems the storage of nanoparticles typically occurs in endosomes and lysosomes, while in plant cells the storage of nanoparticles usually takes place in vacuoles. How the nanoparticle surface coatings will respond to these acidic environments, and how nanoparticles such as silver and gold may release their ion contents post surface modications by enzymes need to be understood from the perspectives of biophysics, biochemistry, and molecular and cellular toxicology.

- Thirdly, molecular studies on the impact of nanomaterials may consider incorporating different nanoparticles and cellular components. While my PhD research has been focused on the interactions between the negatively charged $C_{60}(OH)_{20}$ with amphiphilic nucleic acids and MTs, additional studies could be done with amine-terminated fullerene derivatives, as well as with other cellular components such as actin filaments, mitochondria, and molecular motors and machines. In addition, it would be beneficial for the purpose of nanomedicine to compare the uptake of nanoparticles by both cell membranes and nuclear membranes.

- Lastly, despite rapid development of nanotechnology and knowledge gained on the interaction of nanomaterials and living systems, little is known about the behaviors of nanoparticles in biological and ecological fluids, which contain a variety of salts, proteins, amino acids, peptides, and lipids. These biomolecular species ought to adsorb onto the nanoparticle surfaces, thus leading to possible alterations to biological responses. Knowledge about the

affinity and conformation of the proteins which are associated with the nanoparticle is expected to shed light on what the cell sees in the nanoparticle, now a nanoparticle-protein corona (NPC). So far a handful studies on this topic have been conducted for the most abundant protein in human bloodstream and cell medium – human serum albumin (HSA), while other functionally important proteins, such as high density lipoprotein (HDL) and low density lipoprotein (LDL) which are responsible for the transport of cholesterols, have not been examined within the context of NPC. Specifically, the aspects of binding affinity, stoichiometry, free energy (entropy and enthalpy), protein conformation, and nanoparticle physicochemistry (surface functional groups, charge, size, and shape) need to be examined. How NPC may interact with cells, tissues, and organisms need to be investigated. In addition to mammalian systems, the use of lipid and protein species from the environment, such as NOM, ubiquitin and actin in plants, may provide great insight for our better understanding of the fate of nanoparticles at large.

APPENDIX

Glossary of terms

Symbol	Quantity
SWNT	single-walled carbon nanotube
MWNT	multi-walled carbon nanotube
DNA	deoxyribonucleic acid
RNA	ribonucleic acid
FITC	fluorescein isothiocyanate
PI	propidium iodide
poly(rU)	RNA polymer polyadenylic-uridylic acid
FRET	fluorescence resonance energy transfer
Rd	Rhodamine
MCF7	human breast adenocarcinoma cells
HIV	human immunodeficiency virus
TEM	transmission electron microscopy
ROS	reactive oxygen species
CCl4	carbon tetrachloride
A549	human alveolar basal epithelial cells
H596	human lung adenosquamous carcinoma cells

MD	molecular dynamics
dsDNA	double stranded DNA
PCR	Polymerase chain reaction
ssDNA	single stranded DNA
PBS	phosphate buffered saline
NOM	natural organic matter
FT	Fourier transform
FTIR	Fourier transform infrared spectroscopy
HT-29	human colonic adenocarcinoma cell lines
PDI	Polydispersity Index
FD	fluorescein diacetate
LDH	lactate dehydrogenase
FBS	fetal bovine serum
LD	lethal dose
Ex	Excitation
Em	Emission
DCFH–DA	2',7'-dichlorofluorescein diacetate
DMT1	divalent metal-ion transporter
RFU	relative fluorescent unit
dNTP	deoxynucleoside triphosphate
HSTF	heat shock transcription factor

CM	center of mass
PMF	potentials of mean force
PMF	Particle-Mesh Ewald method
WHAM	weighted histogram analysis
dCTP	deoxycytidine triphosphate
dATP	deoxyadenosine triphosphate
dGTP	deoxyguanosine triphosphate
dTTP	deoxythimidine triphosphate
RDF	radial distribution function
RMSD	root mean square deviation
MT	microtubule
CD	ciclular dichroism
GTP	guanosine-5'-triphosphate
ITC	isothermal titration calorimetry
MW	molecular weight
GDP	guanosine-5'-diphosphate
PEM	general tubulin buffer
NPC	nanoparticle protein corona

REFERENCES

1. Medina, C., Santos-Martinez, M.J., Radomski, A., Corrigan, O.I., and Radomski, M.W., *Nanoparticles: pharmacological and toxicological significance.* British Journal of Pharmacology, 2007. **150**(5): p. 552-558.

2. Beddow, V. *Research Needs in Leachate Treatment for Remediation of Aquatic Environment*. 2010; Available from: http://www.iwawaterwiki.org/xwiki/bin/view/Articles/tonni2.

3. *Nanotechnology information center: properties, applications, research, and safety quidlines*. Available from: http://www.americanelements.com/nanotech.htm.

4. *Project on emerging nanotechnologies*. 2011; Available from: http://www.nanotechproject.org/inventories/consumer/analysis_draft/.

5. Maynard, A.D., *Nanotechnology: a research strategy for addressing risk* 2006; Available from: http://www.pewtrusts.org/our_work_report_detail.aspx?id=19682.

6. Kroto, H.W., Heath, J.R., O'Brien, S.C., Curl, R.F., and Smalley, R.E., *C60: Buckminsterfullerene.* Nature, 1985. **318**(6042): p. 162-163.

7. Mauter, M.S. and Elimelech, M., *Environmental Applications of Carbon-Based Nanomaterials.* Environmental Science & Technology, 2008. **42**(16): p. 5843-5859.

8. Kroto, H.W., Allaf, A.W., and Balm, S.P., *C60: Buckminsterfullerene.* Chemical Reviews, 1991. **91**(6): p. 1213-1235.

9. Yoon, S.H., Lim, S., Hong, S.-h., Mochida, I., An, B., and Yokogawa, K., *Carbon nano-rod as a structural unit of carbon nanofibers.* Carbon, 2004. **42**(15): p. 3087-3095.

10. Service, R.F., *Carbon Foam Reveals a Fleeting Magnetic Personality.* Science, 2004. **304**(5667): p. 42-42.

11. Sun, Y.P., Zhou, B., Lin, Y., Wang, W., Fernando, K.A.S., Pathak, P., Meziani, M.J., Harruff, B.A., Wang, X., Wang, H., Luo, P.G., Yang, H., Kose, M.E., Chen, B., Veca, L.M., and Xie, S.-Y., *Quantum-Sized Carbon Dots for Bright and Colorful Photoluminescence.* Journal of the American Chemical Society, 2006. **128**(24): p. 7756-7757.

12. Bandow, S., Kokai, F., Takahashi, K., Yudasaka, M., Qin, L.C., and Iijima, S., *Interlayer spacing anomaly of single-wall carbon nanohorn aggregate.* Chemical Physics Letters, 2000. **321**(5-6): p. 514-519.

13. King, M.A., *Detection of dead cells and measurement of cell killing by flow cytometry.* Journal of Immunological Methods, 2000. **243**(1-2): p. 155-166.

14. Schrand, A.M., Huang, H., Carlson, C., Schlager, J.J., Ōsawa, E., Hussain, S.M., and Dai, L., *Are Diamond Nanoparticles Cytotoxic?* The Journal of Physical Chemistry B, 2006. **111**(1): p. 2-7.

15. Lewinski, N., Colvin, V., and Drezek, R., *Cytotoxicity of Nanoparticles.* Small, 2008. **4**(1): p. 26-49.

16. Heller, D.A., Baik, S., Eurell, T.E., and Strano, M.S., *Single-Walled Carbon Nanotube Spectroscopy in Live Cells: Towards Long-Term Labels and Optical Sensors.* Advanced Materials, 2005. **17**(23): p. 2793-2799.

17. Heller, D.A., Jeng, E.S., Yeung, T.-K., Martinez, B.M., Moll, A.E., Gastala, J.B., and Strano, M.S., *Optical Detection of DNA Conformational Polymorphism on Single-Walled Carbon Nanotubes.* Science, 2006. **311**(5760): p. 508-511.

18. Al-Jamal, K.T., Toma, F.M., Yilmazer, A., Ali-Boucetta, H., Nunes, A., Herrero, M.-A., Tian, B., Eddaoudi, A., Al-Jamal, W.T., Bianco, A., Prato, M., and Kostarelo, K., *Enhanced cellular internalization and gene silencing with a series of cationic dendron-multiwalled carbon nanotube:siRNA complexes.* The FASEB Journal, 2010. **24**(11): p. 4354-4365.

19. Singh, R., Pantarotto, D., McCarthy, D., Chaloin, O., Hoebeke, J., Partidos, C.D., Briand, J.-P., Prato, M., Bianco, A., and Kostarelos, K., *Binding and Condensation of Plasmid DNA onto Functionalized Carbon Nanotubes: Toward the Construction of Nanotube-Based Gene Delivery Vectors.* Journal of the American Chemical Society, 2005. **127**(12): p. 4388-4396.

20. Lacerda, L., Bianco, A., Prato, M., and Kostarelos, K., *Carbon nanotube cell translocation and delivery of nucleic acids in vitro and in vivo.* Journal of Materials Chemistry, 2008. **18**(1): p. 17-22.

21. Pantarotto, D., Singh, R., McCarthy, D., Erhardt, M., Briand, J.-P., Prato, M., Kostarelos, K., and Bianco, A., *Functionalized Carbon Nanotubes for Plasmid DNA Gene Delivery.* Angewandte Chemie International Edition, 2004. **43**(39): p. 5242-5246.

22. Pantarotto, D., Partidos, C.D., Graff, R., Hoebeke, J., Briand, J.-P., Prato, M., and Bianco, A., *Synthesis, Structural Characterization, and Immunological Properties of Carbon Nanotubes Functionalized with Peptides.* Journal of the American Chemical Society, 2003. **125**(20): p. 6160-6164.

23. Wu, W., Wieckowski, S., Pastorin, G., Benincasa, M., Klumpp, C., Briand, J.P., Gennaro, R., Prato, M., and Bianco, A., *Targeted delivery of amphotericin B to cells by using functionalized carbon nanotubes.* Angewandte Chemie (International ed. in English), 2005. **44**(39): p. 6358-6362.

24. Ferrari, M., *Cancer nanotechnology: opportunities and challenges.* Nat Rev Cancer, 2005. **5**(3): p. 161-171.

25. Chen, J., Chen, S., Zhao, X., Kuznetsova, L.V., Wong, S.S., and Ojima, I., *Functionalized Single-Walled Carbon Nanotubes as Rationally Designed Vehicles for Tumor-Targeted Drug Delivery.* Journal of the American Chemical Society, 2008. **130**(49): p. 16778-16785.

26. *Tech report: Carbon nanotubes used to more easily detect cancer cells, HIV.* 2011; Available from: http://tech.resuck.com/2011/03/carbon-nanotubes-used-to-more-easily-detect-cancer-cells-hiv/

27. Yang, W., Thordarson, P., Gooding, J. J., Ringer, S. P., and Braet, F., *Carbon nanotubes for biological and biomedical applications.* Nanotechnology, 2007. **18**: p. 412001-412013.

28. Pantarotto, D., Briand, J.-P., Prato, M., and Bianco, A., *Translocation of bioactive peptides across cell membranes by carbon nanotubes.* Chemical Communications, 2004(1): p. 16-17.

29. Kam, N.W.S., Liu, Z., and Dai, H., *Functionalization of Carbon Nanotubes via Cleavable Disulfide Bonds for Efficient Intracellular Delivery of siRNA and Potent Gene Silencing.* Journal of the American Chemical Society, 2005. **127**(36): p. 12492-12493.

30. Lu, Q., Moore, J.M., Huang, G., Mount, A.S., Rao, A.M., Larcom, L.L., and Ke, P.C., *RNA Polymer Translocation with Single-Walled Carbon Nanotubes.* Nano Letters, 2004. **4**(12): p. 2473-2477.

31.   Lin, S., Keskar, G., Wu, Y., Wang, X., Mount, A.S., Klaine, S.J., Moore, J.M., Rao, A.M., and Ke, P.C., *Detection of phospholipid-carbon nanotube translocation using fluorescence energy transfer.* Applied Physics Letters, 2006. **89**(14): p. 143118-143121.

32.   Wu, Y., Hudson, J.S., Lu, Q., Moore, J.M., Mount, A.S., Rao, A.M., Alexov, E., and Ke, P.C., *Coating Single-Walled Carbon Nanotubes with Phospholipids.* The Journal of Physical Chemistry B, 2006. **110**(6): p. 2475-2478.

33.   Kam, N.W.S. and Dai, H., *Carbon Nanotubes as Intracellular Protein Transporters: Generality and Biological Functionality.* Journal of the American Chemical Society, 2005. **127**(16): p. 6021-6026.

34.   Kam, N.W.S., O'Connell, M., Wisdom, J.A., and Dai, H., *Carbon nanotubes as multifunctional biological transporters and near-infrared agents for selective cancer cell destruction.* Proceedings of the National Academy of Sciences of the United States of America, 2005. **102**(33): p. 11600-11605.

35.   Russell-Jones, G., McTavish, K., McEwan, J., Rice, J., and Nowotnik, D., *Vitamin-mediated targeting as a potential mechanism to increase drug uptake by tumours.* Journal of Inorganic Biochemistry, 2004. **98**(10): p. 1625-1633.

36.   Leamon, C.P. and Reddy, J.A., *Folate-targeted chemotherapy.* Advanced Drug Delivery Reviews, 2004. **56**(8): p. 1127-1141.

37.   Cherukuri, P., Bachilo, S.M., Litovsky, S.H., and Weisman, R.B., *Near-Infrared Fluorescence Microscopy of Single-Walled Carbon Nanotubes in Phagocytic Cells.* Journal of the American Chemical Society, 2004. **126**(48): p. 15638-15639.

38.   Jin, H., Heller, D.A., and Strano, M.S., *Single-Particle Tracking of Endocytosis and Exocytosis of Single-Walled Carbon Nanotubes in NIH-3T3 Cells.* Nano Letters, 2008. **8**(6): p. 1577-1585.

39.   Ke, P.C. and Lamm, M.H., *A biophysical perspective of understanding nanoparticles at large.* Physical Chemistry Chemical Physics, 2011. **13**(16): p. 7273-7283.

40.   Johnston, H.J., Hutchison, G.R., Christensen, F.M., Aschberger, K., and Stone, V., *The Biological Mechanisms and Physicochemical Characteristics Responsible for Driving Fullerene Toxicity.* Toxicological Sciences, 2010. **114**(2): p. 162-182.

41.   Holsapple, M.P., Farland, W.H., Landry, T.D., Monteiro-Riviere, N.A., Carter, J.M., Walker, N.J., and Thomas, K.V., *Research Strategies for Safety Evaluation of Nanomaterials, Part II: Toxicological and Safety Evaluation of Nanomaterials, Current Challenges and Data Needs.* Toxicological Sciences, 2005. **88**(1): p. 12-17.

42.   Maynard, A., Baron, P., Foley, M., Schvedova, A., Kisin, E., and Castranova, V., *Exposure to carbon nanotube material: aerosol release during the handling of unrefined single-walled carbon nanotube material.* J. Toxicol. Environ. Health, 2004. **67**: p. 87-107.

43.   Donaldson, K., Aitken, R., Tran, L., Stone, V., Duffin, R., Forrest, G., and Alexander, A., *Carbon Nanotubes: A Review of Their Properties in Relation to Pulmonary Toxicology and Workplace Safety.* Toxicological Sciences, 2006. **92**(1): p. 5-22.

44.   Sager, T. and Castranova, V., *Surface area of particle administered versus mass in determining the pulmonary toxicity of ultrafine and fine carbon black: comparison to ultrafine titanium dioxide.* Particle and Fibre Toxicology, 2009. **6**(1): p. 15-27.

45.   Duffin, R., Tran, C.L., Clouter, A., Brown, D.M., MacNee, W., Stone, V., and Donaldson, K., *The Importance of Surface Area and Specific Reactivity in the Acute Pulmonary*

Inflammatory Response to Particles. Annals of Occupational Hygiene, 2002. **46**(1): p. 242-245.

46. Brown, *Particulate Matter: Properties and Effects upon Health.* Journal of Microscopy, 2000. **197**(2): p. 216-216.

47. Powell, M.C., and Kanarek, M. S., *Nanomaterial health effects - part 1: background and current knowledge.* Wisconsin Medical Journal, 2006. **105**(2): p. 16-20.

48. Donaldson, K., Tran, L., Jimenez, L.A., Duffin, R., Newby, D.E., Mills, N., MacNee, W., and Stone, V., *Combustion-derived nanoparticles: a review of their toxicology following inhalation exposure.* Particle and Fibre Toxicology, 2005. **2**: p. 10-24.

49. Baker, G.L., Gupta, A., Clark, M.L., Valenzuela, B.R., Staska, L.M., Harbo, S.J., Pierce, J.T., and Dill, J.A., *Inhalation Toxicity and Lung Toxicokinetics of C60 Fullerene Nanoparticles and Microparticles*. 2008, Oxford University Press.

50. Fujita, K., Morimoto, Y., Ogami, A., Myojyo, T., Tanaka, I., Shimada, M., Wang, W.-N., Endoh, S., Uchida, K., Nakazato, T., Yamamoto, K., Fukui, H., Horie, M., Yoshida, Y., Iwahashi, H., and Nakanishi, J., *Gene expression profiles in rat lung after inhalation exposure to C60 fullerene particles.* Toxicology, 2009. **258**(1): p. 47-55.

51. Sayes, C.M., Marchione, A.A., Reed, L.K., and Warheit, B.D., *Comparative pulmonary toxicity assessments of C[60] water suspensions in rats : Few differences in fullerene toxicity in vivo in contrast to in vitro profiles*. Nano Letters, 2007. **7**(8): p. 2399-2406.

52. Sayes, C.M., Fortner, J.D., Guo, W., Lyon, D., Boyd, A.M., Ausman, K.D., Tao, Y.J., Sitharaman, B., Wilson, L.J., Hughes, J.B., West, J.L., and Colvin, V.L., *The Differential Cytotoxicity of Water-Soluble Fullerenes.* Nano Letters, 2004. **4**(10): p. 1881-1887.

53. Sayes, C.M., Gobin, A.M., Ausman, K.D., Mendez, J., West, J.L., and Colvin, V.L., *Nano-C60 cytotoxicity is due to lipid peroxidation.* Biomaterials, 2005. **26**(36): p. 7587-7595.

54. Roursgaard, M., Poulsen, S.S., Kepley, C.L., Hammer, M., Nielsen, G.D., and Larsen, S.T., *Polyhydroxylated C60 Fullerene (Fullerenol) Attenuates Neutrophilic Lung Inflammation in Mice.* Basic & Clinical Pharmacology & Toxicology, 2008. **103**(4): p. 386-388.

55. Chen, H.H.C., Yu, C., Ueng, T.H., Chen, S., Chen, B.J., Huang, K.J., and Chiang, L.Y., *Acute and Subacute Toxicity Study of Water-Soluble Polyalkylsulfonated C60 in Rats.* Toxicologic Pathology, 1998. **26**(1): p. 143-151.

56. Valko, M., Rhodes, C.J., Moncol, J., Izakovic, M., and Mazur, M., *Free radicals, metals and antioxidants in oxidative stress-induced cancer.* Chemico-Biological Interactions, 2006. **160**(1): p. 1-40.

57. Girotti, A.W., *Photodynamic lipid peroxidation in biological systems.* Photochemistry and Photobiology, 1990. **51**(4): p. 497-509.

58. Donaldson, K., and Tran, C. L., *Inflammation caused by particles and fibres.* Inhal. toxicol., 2002. **14**: p. 5-27.

59. Warheit, D.B., *What is currently known about the health risks related to carbon nanotube exposures?* Carbon, 2006. **44**(6): p. 1064-1069.

60. Brown, D.M., Wilson, M.R., MacNee, W., Stone, V., and Donaldson, K., *Size-Dependent Proinflammatory Effects of Ultrafine Polystyrene Particles: A Role for Surface Area and Oxidative Stress in the Enhanced Activity of Ultrafines.* Toxicology and Applied Pharmacology, 2001. **175**(3): p. 191-199.

61. Stoeger, T., Reinhard, C., Takenaka, S., Schroeppel, A., Karg, E., Ritter, B., Heyder, J., and Schulz, H., *Instillation of Six Different Ultrafine Carbon Particles Indicates a Surface Area*

Threshold Dose for Acute Lung Inflammation in Mice. Environ Health Perspect, 2005. **114**(3): p. 328-333.

62. Chen, B.X., Wilson, S.R., Das, M., Coughlin, D.J., and Erlanger, B.F., *Antigenicity of fullerenes: antibodies specific for fullerenes and their characteristics.* Proc. Natl. Acad. Sci. U.S.A., 1998. **95**: p. 10809-10819.

63. Erlanger, B.F., Chen, B.-X., Zhu, M., and Brus, L., *Binding of an Anti-Fullerene IgG Monoclonal Antibody to Single Wall Carbon Nanotubes.* Nano Letters, 2001. **1**(9): p. 465-467.

64. Gharbi, N., Pressac, M., Hadchouel, M., Szwarc, H., Wilson, S.R., and Moussa, F., *[60]Fullerene is a Powerful Antioxidant in Vivo with No Acute or Subacute Toxicity.* Nano Letters, 2005. **5**(12): p. 2578-2585.

65. Injac, R., Perse, M., Cerne, M., Potocnik, N., Radic, N., Govedarica, B., Djordjevic, A., Cerar, A., and Strukelj, B., *Protective effects of fullerenol C60(OH)24 against doxorubicin-induced cardiotoxicity and hepatotoxicity in rats with colorectal cancer.* Biomaterials, 2009. **30**(6): p. 1184-1196.

66. Rouse, J.G., Yang, J., Barron, A.R., and Monteiro-Riviere, N.A., *Fullerene-based amino acid nanoparticle interactions with human epidermal keratinocytes.* Toxicology in Vitro, 2006. **20**(8): p. 1313-1320.

67. Nelson, M.A., Domann, F.E., Bowden, G.T., Hooser, S.B., Fernando, Q., and Carter, D.E., *Acute and subchronic exposure of topically applied fullerene extracts on the mouse skin.* Toxicol Ind Health, 1993. **9**: p. 623-630.

68. Huczko, A., Lange, H., and Calko, E., *Short Communication: Fullerenes: Experimental Evidence for a Null Risk of Skin Irritation and Allergy.* Fullerene Science and Technology, 1999. **7**(5): p. 935-939.

69. Lin, S., Reppert, J., Hu, Q., Hudson, J.S., Reid, M.L., Ratnikova, T.A., Rao, A.M., Luo, H., and Ke, P.C., *Uptake, Translocation, and Transmission of Carbon Nanomaterials in Rice Plants.* Small, 2009. **5**(10): p. 1128-1132.

70. Mori, T., Takada, H., Ito, S., Matsubayashi, K., Miwa, N., and Sawaguchi, T., *Preclinical studies on safety of fullerene upon acute oral administration and evaluation for no mutagenesis.* Toxicology, 2006. **225**(1): p. 48-54.

71. Yamago, S., Tokuyama, H., Nakamura, E., Kikuchi, K., Kananishi, S., Sueki, K., Nakahara, H., Enomoto, S., and Ambe, F., *In vivo biological behavior of a water-miscible fullerene: 14C labeling, absorption, distribution, excretion and acute toxicity.* Chemistry & Biology, 1995. **2**(6): p. 385-389.

72. Scrivens, W.A., Tour, J.M., Creek, K.E., and Pirisi, L., *Synthesis of 14C-Labeled C60, Its Suspension in Water, and Its Uptake by Human Keratinocytes.* Journal of the American Chemical Society, 1994. **116**(10): p. 4517-4518.

73. Zakharenko, L.P., Zakharov, I.K., Vasiunina, E.A,, Karamysheva, T.V., Danilenko, A.M., and Nikiforov, A.A., *Determination of the genotoxicity of fullerene C60 and fullerol using the method of somatic mosaics on cells of Drosophila melanogaster wing and SOS-chromotest.* Genetica, 1997. **33**(3): p. 405-409.

74. Moussa, F., Chretie, P., Dubois, P., Chuniaud, L., Dessante, M., Trivin, F., Sizaret, P.Y., Agafonov, V., Céolin, R., Szwarc, H., Greugny, V., Fabre, C., and Rassat, A. , *The influence of C60 powders on cultured human leukocytes.* Fullerenes, Nanotubes and Carbon Nanostructures, 1995. **3**(3): p. 333-42.

75.   Baierl, T., and Seidel, A., *In vitro effects of fullerenes C60 and fullerenes black on immunofunctions of macrophages.* Fullerenes Science and Technology, 1996. **4**: p. 1073-1085.

76.   Oberdörster, E., *Manufactured Nanomaterials (Fullerenes, C60) Induce Oxidative Stress in the Brain of Juvenile Largemouth Bass.* Environ Health Perspect, 2004. **112**(10): p. 1058-1062.

77.   Kamat, J.P., Devasagayam, T.P.A., Priyadarsini, K.I., and Mohan, H., *Reactive oxygen species mediated membrane damage induced by fullerene derivatives and its possible biological implications.* Toxicology, 2000. **155**(1-3): p. 55-61.

78.   Kamat, J.P., Devasagayam, T.P.A., Priyadarsini, K.I., Mohan, H., and Mittal, J.P., *Oxidative damage induced by the fullerene C60 on photosensitization in rat liver microsomes.* Chemico-Biological Interactions, 1998. **114**(3): p. 145-159.

79.   Isakovic, A., Markovic, Z., Todorovic-Markovic, B., Nikolic, N., Vranjes-Djuric, S., Mirkovic, M., Dramicanin, M., Harhaji, L., Raicevic, N., Nikolic, Z., and Trajkovic, V., *Distinct Cytotoxic Mechanisms of Pristine versus Hydroxylated Fullerene.* Toxicological Sciences, 2006. **91**(1): p. 173-183.

80.   Fiorito, S., Serafino, A., Andreola, F., and Bernier, P., *Effects of fullerenes and single-wall carbon nanotubes on murine and human macrophages.* Carbon, 2006. **44**(6): p. 1100-1105.

81.   Porter, A.E., Muller, K., Skepper, J., Midgley, P., and Welland, M., *Uptake of C60 by human monocyte macrophages, its localization and implications for toxicity: Studied by high resolution electron microscopy and electron tomography.* Acta Biomaterialia, 2006. **2**(4): p. 409-419.

82.   Jia, G., Wang, H., Yan, L., Wang, X., Pei, R., Yan, T., Zhao, Y., and Guo, X., *Cytotoxicity of Carbon Nanomaterials: Single-Wall Nanotube, Multi-Wall Nanotube, and Fullerene.* Environmental Science & Technology, 2005. **39**(5): p. 1378-1383.

83.   *Phagocytosis*. Available from: http://en.wikipedia.org/wiki/File:Phagocytosis_ZP.svg.

84.   Chiang, L.Y., Lu, F.-J., and Lin, J.-T., *Free radical scavenging activity of water-soluble fullerenols.* Journal of the Chemical Society, Chemical Communications, 1995(12): p. 1283-1284.

85.   Dugan, L.L., Turetsky, D.M., Du, C., Lobner, D., Wheeler, M., Almli, C.R., Shen, C.K.-F., Luh, T.-Y., Choi, D.W., and Lin, T.-S., *Carboxyfullerenes as neuroprotective agents.* Proceedings of the National Academy of Sciences, 1997. **94**(17): p. 9434-9439.

86.   Dugan, L.L., Lovett, E.G., Quick, K.L., Lotharius, J., Lin, T.T., and O'Malley, K.L., *Fullerene-based antioxidants and neurodegenerative disorders.* Parkinsonism & Related Disorders, 2001. **7**(3): p. 243-246.

87.   Trajkovic, S., Dobric, S., Jacevic, V., Dragojevic-Simic, V., Milovanovic, Z., and Đorđevic, A., *Tissue-protective effects of fullerenol C60(OH)24 and amifostine in irradiated rats.* Colloids and Surfaces B: Biointerfaces, 2007. **58**(1): p. 39-43.

88.   Wang, I.C., Tai, L.A., Lee, D.D., Kanakamma, P.P., Shen, C.K.F., Luh, T.-Y., Cheng, C.H., and Hwang, K.C., *C60 and Water-Soluble Fullerene Derivatives as Antioxidants Against Radical-Initiated Lipid Peroxidation.* Journal of Medicinal Chemistry, 1999. **42**(22): p. 4614-4620.

89.   Yin, J.J., Lao, F., Fu, P.P., Wamer, W.G., Zhao, Y., Wang, P.C., Qiu, Y., Sun, B., Xing, G., Dong, J., Liang, X.-J., and Chen, C., *The scavenging of reactive oxygen species and the*

potential for cell protection by functionalized fullerene materials. Biomaterials, 2009. **30**(4): p. 611-621.

90. Jensen, A.W., Wilson, S.R., and Schuster, D.I., *Biological applications of fullerenes.* Bioorganic & Medicinal Chemistry, 1996. **4**(6): p. 767-779.

91. McEwen, C.N., McKay, R.G., and Larsen, B.S., *C60 as a radical sponge.* Journal of the American Chemical Society, 1992. **114**(11): p. 4412-4414.

92. Boutorine, A.S., Takasugi, M., Hélène, C., Tokuyama, H., Isobe, H., and Nakamura, E., *Fullerene–Oligonucleotide Conjugates: Photoinduced Sequence-Specific DNA Cleavage.* Angewandte Chemie International Edition in English, 1995. **33**(23-24): p. 2462-2465.

93. Dordevich, A.B.G., *Fullerenol - a new nanopharmaceutical?* Arch. Oncol., 2008. **16**(3): p. 42-45.

94. Shvedova, A.A., Castranova, V., Kisin, E.R., Schwegler-Berry, D., Murray, A.R., Gandelsman, V.Z., Maynard, A., and Baron, P., *Exposure to carbon nanotube material: assessment of nanotube cytotoxicity using human keratinocyte cells.* J Toxicol Environ Health A., 2003. **66**(20): p. 1909-26.

95. Manna, S.K., Sarkar, S., Barr, J., Wise, K., Barrera, E.V., Jejelowo, O., Rice-Ficht, A.C., and Ramesh, G.T., *Single-Walled Carbon Nanotube Induces Oxidative Stress and Activates Nuclear Transcription Factor-κB in Human Keratinocytes.* Nano Letters, 2005. **5**(9): p. 1676-1684.

96. Wick, P., Manser, P., Limbach, L.K., Dettlaff-Weglikowska, U., Krumeich, F., Roth, S., Stark, W.J., and Bruinink, A., *The degree and kind of agglomeration affect carbon nanotube cytotoxicity.* Toxicology Letters, 2007. **168**(2): p. 121-131.

97. Tian, F., Cui, D., Schwarz, H., Estrada, G.G., and Kobayashi, H., *Cytotoxicity of single-wall carbon nanotubes on human fibroblasts.* Toxicology in Vitro, 2006. **20**(7): p. 1202-1212.

98. Monteiro-Riviere, N.A. and Inman, A.O., *Challenges for assessing carbon nanomaterial toxicity to the skin.* Carbon, 2006. **44**(6): p. 1070-1078.

99. Ding, L., Stilwell, J., Zhang, T., Elboudwarej, O., Jiang, H., Selegue, J.P., Cooke, P.A., Gray, J.W., and Chen, F.F., *Molecular Characterization of the Cytotoxic Mechanism of Multiwall Carbon Nanotubes and Nano-Onions on Human Skin Fibroblast.* Nano Letters, 2005. **5**(12): p. 2448-2464.

100. Magrez, A., Kasas, S., Salicio, V., Pasquier, N., Seo, J.W., Celio, M., Catsicas, S., Schwaller, B., and Forró, L., *Cellular Toxicity of Carbon-Based Nanomaterials.* Nano Letters, 2006. **6**(6): p. 1121-1125.

101. Flahaut, E., Durrieu, M.C., Remy-Zolghadri, M., Bareille, R., and Baquey, C., *Investigation of the cytotoxicity of CCVD carbon nanotubes towards human umbilical vein endothelial cells.* Carbon, 2006. **44**(6): p. 1093-1099.

102. Sera, N., Tokiwa, H., and Miyata, N., *Mutagenicity of the fullerene C60-generated singlet oxygen dependent formation of lipid peroxides.* Carcinogenesis, 1996. **17**(10): p. 2163-2169.

103. Kotelnikova, R.A., Kotelnikov, A.I., Bogdanov, G.N., Romanova, V.S., Kuleshova, E.F., Parnes, Z.N., and Vol'pin, M.E., *Membranotropic properties of the water soluble amino acid and peptide derivatives of fullerene C60.* FEBS Letters, 1996. **389**(2): p. 111-114.

104. Verma, A., Uzun, O., Hu, Y., Hu, Y., Han, H.-S., Watson, N., Chen, S., Irvine, D.J., and Stellacci, F., *Surface-structure-regulated cell-membrane penetration by monolayer-protected nanoparticles.* Nat Mater, 2008. **7**(7): p. 588-595.

105.   Herbig, M.E., Assi, F., Textor, M., and Merkle, H.P., *The Cell Penetrating Peptides pVEC and W2-pVEC Induce Transformation of Gel Phase Domains in Phospholipid Bilayers without Affecting Their Integrity†.* Biochemistry, 2006. **45**(11): p. 3598-3609.

106.   Takeuchi, T., Kosuge, M., Tadokoro, A., Sugiura, Y., Nishi, M., Kawata, M., Sakai, N., Matile, S., and Futaki, S., *Direct and Rapid Cytosolic Delivery Using Cell-Penetrating Peptides Mediated by Pyrenebutyrate.* ACS Chemical Biology, 2006. **1**(5): p. 299-303.

107.   Yu, J., Patel, S.A., and Dickson, R.M., *In Vitro and Intracellular Production of Peptide-Encapsulated Fluorescent Silver Nanoclusters.* Angewandte Chemie International Edition, 2007. **46**(12): p. 2028-2030.

108.   Kostarelos, K., Lacerda, L., Pastorin, G., Wu, W., WieckowskiSebastien, Luangsivilay, J., Godefroy, S., Pantarotto, D., Briand, J.-P., Muller, S., Prato, M., and Bianco, A., *Cellular uptake of functionalized carbon nanotubes is independent of functional group and cell type.* Nat Nano, 2007. **2**(2): p. 108-113.

109.   Grabinski, C., Hussain, S., Lafdi, K., Braydich-Stolle, L., and Schlager, J., *Effect of particle dimension on biocompatibility of carbon nanomaterials.* Carbon, 2007. **45**(14): p. 2828-2835.

110.   Jin, H., Heller, D.A., Sharma, R., and Strano, M.S., *Size-Dependent Cellular Uptake and Expulsion of Single-Walled Carbon Nanotubes: Single Particle Tracking and a Generic Uptake Model for Nanoparticles.* ACS Nano, 2009. **3**(1): p. 149-158.

111.   Chithrani, B.D., Ghazani, A.A., and Chan, W.C.W., *Determining the Size and Shape Dependence of Gold Nanoparticle Uptake into Mammalian Cells.* Nano Letters, 2006. **6**(4): p. 662-668.

112.   Chithrani, B.D. and Chan, W.C.W., *Elucidating the Mechanism of Cellular Uptake and Removal of Protein-Coated Gold Nanoparticles of Different Sizes and Shapes.* Nano Letters, 2007. **7**(6): p. 1542-1550.

113.   Becker, M.L., Fagan, J.A., Gallant, N.D., Bauer, B.J., Bajpai, V., Hobbie, E.K., Lacerda, S.H., Migler, K.B., and Jakupciak, J.P., *Length-Dependent Uptake of DNA-Wrapped Single-Walled Carbon Nanotubes (Adv. Mater. 7/2007).* Advanced Materials, 2007. **19**(7): p.939-945.

114.   Sato, Y., Yokoyama, A., Shibata, K., Akimoto, Y., Ogino, S., Nodasaka, Y., Kohgo, T., Tamura, K., Akasaka, T., Uo, M., Motomiya, K., Jeyadevan, B., Ishiguro, M., Hatakeyama, R., Watari, F., and Tohji, K., *Influence of length on cytotoxicity of multi-walled carbon nanotubes against human acute monocytic leukemia cell line THP-1 in vitro and subcutaneous tissue of rats in vivo.* Molecular bioSystems, 2005. **1**(2): p. 176-82.

115.   Li, L., Davande, H., Bedrov, D., and Smith, G.D., *A Molecular Dynamics Simulation Study of C60 Fullerenes Inside a Dimyristoylphosphatidylcholine Lipid Bilayer.* The Journal of Physical Chemistry B, 2007. **111**(16): p. 4067-4072.

116.   Bedrov, D., Smith, G.D., Davande, H., and Li, L., *Passive Transport of C60 Fullerenes through a Lipid Membrane: A Molecular Dynamics Simulation Study.* The Journal of Physical Chemistry B, 2008. **112**(7): p. 2078-2084.

117.   Chang, R., and Violi, A., *Insights into the effect of combustion-generated carbon nanoparticles on biological membranes: a computer simulation study.* J. Phys. Chem. B, 2006. **110**(10): p. 5073-5083.

118.   Ginzburg, V.V. and Balijepalli, S., *Modeling the Thermodynamics of the Interaction of Nanoparticles with Cell Membranes.* Nano Letters, 2007. **7**(12): p. 3716-3722.

119.   Li, Y., Chem, X., and Gu, n., *Computational investigation of interaction between nanoparticles and membranes: hydrophobic/hydrophilic effect.* J. Phys. Chem. B, 2008. **112**(51): p. 16647-16663.

120.   Qiao, R., Roberts, A.P., Mount, A.S., Klaine, S.J., and Ke, P.C., *Translocation of C60 and Its Derivatives Across a Lipid Bilayer.* Nano Letters, 2007. **7**(3): p. 614-619.

121.   Wong-Ekkabut, J., Baoukina, S., Triampo, W., Tang, I.M., Tieleman, D.P., and Monticelli, L., *Computer simulation study of fullerene translocation through lipid membranes.* Nat Nano, 2008. **3**(6): p. 363-368.

122.   Wallace, E.J. and Sansom, M.S.P., *Blocking of Carbon Nanotube Based Nanoinjectors by Lipids: A Simulation Study.* Nano Letters, 2008. **8**(9): p. 2751-2756.

123.   Monticelli, L., Salonen, E., Ke, P.C., and Vattulainen, I., *Effects of carbon nanoparticles on lipid membranes: a molecular simulation perspective.* Soft Matter, 2009. **5**(22): p. 4433-4445.

124.   Yamakoshi, Y.N., Yagami, T., Sueyoshi, S., and Miyata, N., *ChemInform Abstract: Acridine Adduct of (60)Fullerene with Enhanced DNA-Cleaving Activity.* ChemInform, 1997. **28**(9): p. 7236-7237.

125.   Pinteala, M., Dascalu, A., and Ungurenasu, C., *Binding fullerenol C60(OH)20 to dsDNA.* International Journal of Nanomedicine, 2009. **4**: p. 193-199.

126.   Bingshe, X., Xuguang, L., Xiaoqin, Y., and Weijun, J., *Studies on the interaction of water-soluble fullerols with BSA anf the Effect of metallic ions.* Mat. Res. Soc. Symp. Proc., 2001. **675**.: p. 741-745.

127.   De Vente, J., Bruyn, P.J.M., and Zaagsma, J., *Fluorescence spectroscopic analysis of the hydrogen bonding properties of catecholamines, resorcinolamines, and related compounds with phosphate and other anionic species in aqueous solution††.* Journal of Pharmacy and Pharmacology, 1981. **33**(1): p. 290-296.

128.   Zhu, L., Chang, D.W., Dai, L., and Hong, Y., *DNA Damage Induced by Multiwalled Carbon Nanotubes in Mouse Embryonic Stem Cells.* Nano Letters, 2007. **7**(12): p. 3592-3597.

129.   Song, G., Yao, L., Huang, C., Xie, X., Tan, X., and Yang, X., *Inhibition of DNA restrictive endonucleases by aqueous nanoparticle suspension of methanophosphonate fullerene derivatives and its mechanisms.* Science in China Series B: Chemistry, 2009. **52**(5): p. 626-631.

130.   Meng, X., Li, B., Chen, Z., Yao, L., Zhao, X., He, M., and Yu, Q., *Inhibition of a thermophilic deoxyribonucleic acid polymerase by fullerene derivatives.* J. Enzyme Inhib Med. Chem., 2007. **22**(3): p. 293-296.

131.   Shang, J., Ratnikova, T. A., Anttalainen, S., Salonen, E., Ke, P. C., Knap, H. T., *Experimental and simulational studies of a real-time polymerase chain reaction in the presence of a fullerene derivative.* Nanotechnology, 2009. **20**(41): p. 415101-415110.

132.   Yang, X.L., Fan, C.H., and Zhu, H.S., *Photo-induced cytotoxicity of malonic acid [C60]fullerene derivatives and its mechanism.* Toxicology in Vitro, 2002. **16**(1): p. 41-46.

133.   Zhao, X., Striolo, A., and Cummings, P.T., *C60 Binds to and Deforms Nucleotides.* Biophysical journal, 2005. **89**(6): p. 3856-3862.

134.   Zhao, X., *Interaction of C60 Derivatives and ssDNA from Simulations.* The Journal of Physical Chemistry C, 2008. **112**(24): p. 8898-8906.

135.   Johnson, R.R., Johnson, A.T.C., and Klein, M.L., *Probing the Structure of DNA–Carbon Nanotube Hybrids with Molecular Dynamics.* Nano Letters, 2007. **8**(1): p. 69-75.

136. Zhu, Z., Schuster, D.I., and Tuckerman, M.E., *Molecular Dynamics Study of the Connection between Flap Closing and Binding of Fullerene-Based Inhibitors of the HIV-1 Protease†.* Biochemistry, 2003. **42**(5): p. 1326-1333.

137. Marcorin, G.L., Da Ros, T., Castellano, S., Stefancich, G., Bonin, I., Miertus, S., and Prato, M., *Design and Synthesis of Novel [60]Fullerene Derivatives as Potential HIV Aspartic Protease Inhibitors.* Organic Letters, 2000. **2**(25): p. 3955-3958.

138. Stedtfeld, R.D., Wick, L., Baushke, S.W., Tourlousse, D., Herzog, A., Xia, Y., Rouillard, J.M., Klappenbach, J., Cole, J.R., Gulari, E., Tiedje, J.M., and Hashsham, S.A., *Influence of Dangling End and Surface Proximal Tail of Targets on Probe-Target Duplex Formation in 16S rRNA Gene-Based Diagnostic Arrays.* Appl. Environ. Microbiol., 2006: p. 380-389.

139. Tokuyama, H., Yamago, S., Nakamura, E., Shiraki, T., and Sugiura, Y., *Photoinduced biochemical activity of fullerene carboxylic acid.* Journal of the American Chemical Society, 1993. **115**(17): p. 7918-7919.

140. Käsermann, F. and Kempf, C., *Buckminsterfullerene and photodynamic inactivation of viruses.* Reviews in Medical Virology, 1998. **8**(3): p. 143-151.

141. Samal, S. and Geckeler, K.E., *DNA-Cleavage by Fullerene-Based Synzymes.* Macromolecular Bioscience, 2001. **1**(8): p. 329-331.

142. Fujiwara, A., Ishii, K., Suematsu, H., Kataura, H., Maniwa, Y., Suzuki, S., and Achiba, Y., *Gas adsorption in the inside and outside of single-walled carbon nanotubes.* Chemical Physics Letters, 2001. **336**(3-4): p. 205-211.

143. Kleinhammes, A., Mao, S. H., Yang, X. J., Tang, X. P., Shimoda, H., Lu, J. P., Zhou, O., and Wu, Y. , *Gas adsorption in single-walled carbon nanotubes studied by NMR.* Phys. Rev. B, 2003. **68**: p. 075418-075424.

144. Varghese, O.K., Kichambre, P.D., Gong, D., Ong, K.G., Dickey, E.C., and Grimes, C.A., *Gas sensing characteristics of multi-wall carbon nanotubes.* Sensors and Actuators B: Chemical, 2001. **81**(1): p. 32-41.

145. Kong, J., Franklin, N.R., Zhou, C., Chapline, M.G., Peng, S., Cho, K., and Dai, H., *Nanotube Molecular Wires as Chemical Sensors.* Science, 2000. **287**(5453): p. 622-625.

146. Li, Y.-H., Ding, J., Luan, Z., Di, Z., Zhu, Y., Xu, C., Wu, D., and Wei, B., *Competitive adsorption of Pb^{2+}, Cu^{2+} and Cd^2+ ions from aqueous solutions by multiwalled carbon nanotubes.* Carbon, 2003. **41**(14): p. 2787-2792.

147. Di, Z.-C., Ding, J., Peng, X.-J., Li, Y.-H., Luan, Z.-K., and Liang, J., *Chromium adsorption by aligned carbon nanotubes supported ceria nanoparticles.* Chemosphere, 2006. **62**(5): p. 861-865.

148. Yan, H., Gong, A., He, H., Zhou, J., Wei, Y., and Lv, L., *Adsorption of microcystins by carbon nanotubes.* Chemosphere, 2006. **62**(1): p. 142-148.

149. Kang, S., Pinault, M., Pfefferle, L.D., and Elimelech, M., *Single-Walled Carbon Nanotubes Exhibit Strong Antimicrobial Activity.* Langmuir, 2007. **23**(17): p. 8670-8673.

150. Brady-Estévez, A.S., Kang, S., and Elimelech, M., *A Single-Walled-Carbon-Nanotube Filter for Removal of Viral and Bacterial Pathogens.* Small, 2008. **4**(4): p. 481-484.

151. Srivastava, A., Srivastava, O.N., Talapatra, S., Vajtai, R., and Ajayan, P.M., *Carbon nanotube filters.* Nat Mater, 2004. **3**(9): p. 610-614.

152. Chen, Z., Zhang, L., Tang, Y., and Jia, Z., *Adsorption of nicotine and tar from the mainstream smoke of cigarettes by oxidized carbon nanotubes.* Applied Surface Science, 2006. **252**(8): p. 2933-2937.

153. Holt, J.K., Park, H.G., Wang, Y., Stadermann, M., Artyukhin, A.B., Grigoropoulos, C.P., Noy, A., and Bakajin, O., *Fast Mass Transport Through Sub-2-Nanometer Carbon Nanotubes.* Science, 2006. **312**(5776): p. 1034-1037.

154. Hinds, B.J., Chopra, N., Rantell, T., Andrews, R., Gavalas, V., and Bachas, L.G., *Aligned Multiwalled Carbon Nanotube Membranes.* Science, 2004. **303**(5654): p. 62-65.

155. MajumderMainak, ChopraNitin, AndrewsRodney, and Hinds, B., *Erratum: Nanoscale hydrodynamics: Enhanced flow in carbon nanotubes.* Nature, 2005. **438**(7070): p. 930-930.

156. Majumder, M., Chopra, N., and Hinds, B.J., *Effect of Tip Functionalization on Transport through Vertically Oriented Carbon Nanotube Membranes.* Journal of the American Chemical Society, 2005. **127**(25): p. 9062-9070.

157. Cai, Y., Jiang, G., Liu, J., and Zhou, Q., *Multiwalled Carbon Nanotubes as a Solid-Phase Extraction Adsorbent for the Determination of Bisphenol A, 4-n-Nonylphenol, and 4-tert-Octylphenol.* Analytical Chemistry, 2003. **75**(10): p. 2517-2521.

158. Cheng, X., Kan, A.T., and Tomson, M.B., *Naphthalene Adsorption and Desorption from Aqueous C60 Fullerene.* Journal of Chemical & Engineering Data, 2004. **49**(3): p. 675-683.

159. Kotani, T., Ueno, M., Kawai, N., and Kitamoto, S., *Development of a new radiation detector utilizing carbon nanotube as anode.* Physica E: Low-dimensional Systems and Nanostructures, 2007. **40**(2): p. 422-424.

160. McGinnis, R.L., McCutcheon, J.R., and Elimelech, M., *A novel ammonia-carbon dioxide osmotic heat engine for power generation.* Journal of Membrane Science, 2007. **305**(1-2): p. 13-19.

161. Elimelech, M., *Nanotechnologies, Hazards and Resource Efficiency: A Three-Tiered Approach to Assessing the Implications of Nanotechnology and Influencing its Development, by Michael Steinfeldt, Arnim von Gleich, Ulrich Petschow, and Rüdiger Haum.* Journal of Industrial Ecology, 2008. **12**(3): p. 493-493.

162. Colvin, V.L., *The potential environmental impact of engineered nanomaterials.* Nat Biotech, 2003. **21**(10): p. 1166-1170.

163. Farré, M., Gajda-Schrantz, K., Kantiani, L., and Barceló, D., *Ecotoxity and analysis of nanomaterials in the aquatic environment.* Analytical and Bioanalytical Chemistry, 2009. **393**(1): p. 81-95.

164. Pu Chun, K. and Rui, Q., *Carbon nanomaterials in biological systems.* Journal of Physics: Condensed Matter, 2007. **19**(37): p. 373101-373126.

165. Hyung, H., Fortner, J.D., Hughes, J.B., and Kim, J.-H., *Natural Organic Matter Stabilizes Carbon Nanotubes in the Aqueous Phase.* Environmental Science & Technology, 2006. **41**(1): p. 179-184.

166. Krysanov, E., Pavlov, D., Demidova, T., and Dgebuadze, Y., *Effect of nanoparticles on aquatic organisms.* Biology Bulletin, 2010. **37**(4): p. 406-412.

167. Lyon, D.Y., Adams, L.K., Falkner, J.C., and Alvarez, P.J.J., *Antibacterial Activity of Fullerene Water Suspensions: Effects of Preparation Method and Particle Size†.* Environmental Science & Technology, 2006. **40**(14): p. 4360-4366.

168. Zhu, Y., Zhao, Q., Li, Y., Cai, X., and Li, W., *The interaction and toxicity of multi-walled carbon nanotubes with Stylonychia mytilus* Journal of nanoscience and nanotechnology, 2006. **6**(5): p. 1357-1364.

169.   Lovern, S., and Klaper, R., *Daphnia magna mortality when exposed to titanium dioxide and fullerene (C60) nanoparticles.* Environmental Toxicology and chemistry, 2006. **25**(4): p. 1132-1137.

170.   Oberdörster, E., Zhu, S., Blickley, T.M., McClellan-Green, P., and Haasch, M.L., *Ecotoxicology of carbon-based engineered nanoparticles: Effects of fullerene (C60) on aquatic organisms.* Carbon, 2006. **44**(6): p. 1112-1120.

171.   Baun, A., Hartmann, N., Grieger, K., and Kusk, K., *Ecotoxicity of engineered nanoparticles to aquatic invertebrates: a brief review and recommendations for future toxicity testing.* Ecotoxicology, 2008. **17**(5): p. 387-395.

172.   Isaacson, C.W., Usenko, C.Y., Tanguay, R.L., and Field, J.A., *Quantification of Fullerenes by LC/ESI-MS and Its Application to in Vivo Toxicity Assays.* Analytical Chemistry, 2007. **79**(23): p. 9091-9097.

173.   Zhu, X., Zhu, L., Li, Y., Duan, Z., Chen, W., and Alvarez, P.J.J., *Developmental toxicity in zebrafish (Danio rerio) embryos after exposure to manufactured nanomaterials: Buckminsterfullerene aggregates (nC60) and fullerol.* Environmental Toxicology and chemistry, 2007. **26**(5): p. 976-979.

174.   Cheng, J., Flahaut, E., and Cheng, S.H., *Effect of carbon nanotubes on developing zebrafish (Danio Rerio) embryos.* Environmental Toxicology and chemistry, 2007. **26**(4): p. 708-716.

175.   Fang, J., Lyon, D.Y., Wiesner, M.R., Dong, J., and Alvarez, *Effect of a Fullerene Water Suspension on Bacterial Phospholipids and Membrane Phase Behavior.* Environmental Science & Technology, 2007. **41**(7): p. 2636-2642.

176.   Roberts, A.P., Mount, A.S., Seda, B., Souther, J., Qiao, R., Lin, S., Ke, P.C., Rao, A.M., and Klaine, S.J., *In vivo Biomodification of Lipid-Coated Carbon Nanotubes by Daphnia magna.* Environmental Science & Technology, 2007. **41**(8): p. 3025-3029.

177.   Kim, K.T., Klaine, S.J., Lin, S., Ke, P.C., and Kim, S.D., *Acute toxicity of a mixture of copper and single-walled carbon nanotubes to Daphnia magna.* Environmental Toxicology and chemistry, 2010. **29**(1): p. 122-126.

178.   Templeton, R.C., Ferguson, P.L., Washburn, K.M., Scrivens, W.A., and Chandler, G.T., *Life-Cycle Effects of Single-Walled Carbon Nanotubes (SWNTs) on an Estuarine Meiobenthic Copepod†.* Environmental Science & Technology, 2006. **40**(23): p. 7387-7393.

179.   Rico, C.M., Majumdar, S., Duarte-Gardea, M., Peralta-Videa, J.R., and Gardea-Torresdey, J.L., *Interaction of Nanoparticles with Edible Plants and Their Possible Implications in the Food Chain.* Journal of Agricultural and Food Chemistry, 2011. **59**(8): p. 3485-3498.

180.   Shen, C.X., Zhang, Q.-F., Li, J., Bi, F.-C., and Yao, N., *Induction of programmed cell death in Arabidopsis and rice by single-wall carbon nanotubes.* Am. J. Bot., 2010: p. 1602-1609.

181.   Khodakovskaya, M., Dervishi, E., Mahmood, M., Xu, Y., Li, Z., Watanabe, F., and Biris, A.S., *Carbon Nanotubes Are Able To Penetrate Plant Seed Coat and Dramatically Affect Seed Germination and Plant Growth.* ACS Nano, 2009. **3**(10): p. 3221-3227.

182.   Wild, E. and Jones, K.C., *Novel Method for the Direct Visualization of in Vivo Nanomaterials and Chemical Interactions in Plants.* Environmental Science & Technology, 2009. **43**(14): p. 5290-5294.

183.   Cañas, J.E., Long, M., Nations, S., Vadan, R., Dai, L., Luo, M., Ambikapathi, R., Lee, E.H., and Olszyk, D., *Effects of functionalized and nonfunctionalized single-walled carbon*

nanotubes on root elongation of select crop species. Environmental Toxicology and chemistry, 2008. **27**(9): p. 1922-1931.

184. Stampoulis, D., Sinha, S.K., and White, J.C., *Assay-Dependent Phytotoxicity of Nanoparticles to Plants.* Environmental Science & Technology, 2009. **43**(24): p. 9473-9479.

185. Serrato-Valenti, G., Gornara, L., Modenesi, P., Piana, M., and Mariotti, M. G., *Structure and Histochemistry of Embryo Envelope Tissues in the Mature Dry Seed and Early Germination of Phacelia tanacetifolia* Annals of Botany, 2000. **85**(5): p. 625-634.

186. Lin, D. and Xing, B., *Phytotoxicity of nanoparticles: Inhibition of seed germination and root growth.* Environmental Pollution, 2007. **150**(2): p. 243-250.

187. Whitby, M. and Quirke, N., *Fluid flow in carbon nanotubes and nanopipes.* Nat Nano, 2007. **2**(2): p. 87-94.

188. Yennawar, N.H., Li, L.-C., Dudzinski, D.M., Tabuchi, A., and Cosgrove, D.J., *Crystal structure and activities of EXPB1 (Zea m 1), a β-expansin and group-1 pollen allergen from maize.* Proceedings of the National Academy of Sciences, 2006. **103**(40): p. 14664-14671.

189. Serag, M.F., Kaji, N., Gaillard, C., Okamoto, Y., Terasaka, K., Jabasini, M., Tokeshi, M., Mizukami, H., Bianco, A., and Baba, Y., *Trafficking and Subcellular Localization of Multiwalled Carbon Nanotubes in Plant Cells.* ACS Nano, 2010. **5**(1): p. 493-499.

190. Liu, Q., Chen, B., Wang, Q., Shi, X., Xiao, Z., Lin, J., and Fang, X., *Carbon Nanotubes as Molecular Transporters for Walled Plant Cells.* Nano Letters, 2009. **9**(3): p. 1007-1010.

191. Chen, R., Ratnikova, T.A., Stone, M.B., Lin, S., Lard, M., Huang, G., Hudson, J.S., and Ke, P.C., *Differential Uptake of Carbon Nanoparticles by Plant and Mammalian Cells.* Small, 2010. **6**(5): p. 612-617.

192. Tan, X.M., and Fugetsu, B. , *Milti-walled carbon nanotubes interact with cultured rice cells:evidence of a self-defense response.* Journal of Biomedical nanotechnology, 2007. **3**: p. 285-288.

193. Tan, X.M., Lin, C., and Fugetsu, B., *Studies on toxicity of multiwalled carbon nanotubes on suspension rice cells.* Carbon, 2009. **47**: p. 3479-3487.

194. Khodakovskaya, M.V., de Silva, K., Nedosekin, D.A., Dervishi, E., Biris, A.S., Shashkov, E.V., Galanzha, E.I., and Zharov, V.P., *Complex genetic, photothermal, and photoacoustic analysis of nanoparticle-plant interactions.* Proceedings of the National Academy of Sciences, 2011. **108**(3): p. 1028-1033.

195. Eklund, P.C., Rao, A.M., Wang, Y., Zhou, P., Wang, K.-A., Holden, J.M., Dresselhaus, M.S., and Dresselhaus, G., *Optical properties of C60- and C70-based solid films.* Thin Solid Films, 1995. **257**(2): p. 211-232.

196. Carpita, N., Sabularse, D., Montezinos, D., and Delmer, D.P., *Determination of the Pore Size of Cell Walls of Living Plant Cells.* Science, 1979. **205**(4411): p. 1144-1147.

197. Smith, H., *The molecular biology of plant cells.* University of california press, Berkley, CA, 1978.

198. van Bavel, C.H.M., Nakayama, F. S., and Ehrler W. L., *Measuring Transpiration Resistance of Leaves.* Plant Physiology, 1965. **40**(3): p. 535–540.

199. Maynard, A.D., Aitken, R.J., Butz, T., Colvin, V., Donaldson, K., Oberdorster, G., Philbert, M.A., Ryan, J., Seaton, A., Stone, V., Tinkle, S.S., Tran, L., Walker, N.J., and Warheit, D.B., *Safe handling of nanotechnology.* Nature, 2006. **444**(7117): p. 267-269.

200. Samaj, J., Baluska, F., Voigt, B., Schlicht, M., Volkmann, D., and Menzel, D., *Endocytosis, Actin Cytoskeleton, and Signaling.* Plant Physiology, 2004. **135**(3): p. 1150-1161.

201. Brett. C., a.W., K., *Physiology and Biochemistry of Plant Cell Walls.* 2nd ed. Chapman and Hall, 1996.

202. Salonen, E., Lin, S., Reid, M.L., Allegood, M., Wang, X., Rao, A.M., Vattulainen, I., and Ke, P.C., *Real-Time Translocation of Fullerene Reveals Cell Contraction.* Small, 2008. **4**(11): p. 1986-1992.

203. Hwang, K.C. and Mauzerall, D., *Photoinduced electron transport across a lipid bilayer mediated by C70.* Nature, 1993. **361**(6408): p. 138-140.

204. Halliwell, B. and Gutteridge, J.M., *Oxygen toxicity, oxygen radicals, transition metals and disease.* Biochem. J., 1984. **219**(1): p. 1-10.

205. Masad, A., Hayes, L., Tabner, B.J., Turnbull, S., Cooper, L.J., Fullwood, N.J., German, M.J., Kametani, F., El-Agnaf, O.M.A., and Allsop, D., *Copper-mediated formation of hydrogen peroxide from the amylin peptide: A novel mechanism for degeneration of islet cells in type-2 diabetes mellitus?* FEBS Letters, 2007. **581**(18): p. 3489-3493.

206. Nel, A.E., Madler, L., Velegol, D., Xia, T., Hoek, E.M.V., Somasundaran, P., Klaessig, F., Castranova, V., and Thompson, M., *Understanding biophysicochemical interactions at the nano-bio interface.* Nat Mater, 2009. **8**(7): p. 543-557.

207. Studer, A.M., Limbach, L.K., Van Duc, L., Krumeich, F., Athanassiou, E.K., Gerber, L.C., Moch, H., and Stark, W.J., *Nanoparticle cytotoxicity depends on intracellular solubility: Comparison of stabilized copper metal and degradable copper oxide nanoparticles.* Toxicology Letters, 2010. **197**(3): p. 169-174.

208. Issa, Y., Brunton, P., Waters, C.M., and Watts, D.C., *Cytotoxicity of metal ions to human oligodendroglial cells and human gingival fibroblasts assessed by mitochondrial dehydrogenase activity.* Dental Materials, 2008. **24**(2): p. 281-287.

209. Wataha, J.C., Hanks, C.T., and Sun, Z., *Effect of cell line on in vitro metal ion cytotoxicity.* Dental Materials, 1994. **10**(3): p. 156-161.

210. Yu, Y.-P., Lei, P., Hu, J., Wu, W.-H., Zhao, Y.-F., and Li, Y.-M., *Copper-induced cytotoxicity: reactive oxygen species or islet amyloid polypeptide oligomer formation.* Chemical Communications, 2010. **46**(37): p. 6909-6911.

211. Klotz, L.-O., Kröncke, K.-D., Buchczyk, D.P., and Sies, H., *Role of Copper, Zinc, Selenium and Tellurium in the Cellular Defense against Oxidative and Nitrosative Stress.* The Journal of Nutrition, 2003. **133**(5): p. 1448S-1451S.

212. Hu, Z., Guan, W., Wang, W., Huang, L., Xing, H., and Zhu, Z., *Protective effect of a novel cystine C60 derivative on hydrogen peroxide-induced apoptosis in rat pheochromocytoma PC12 cells.* Chemico-Biological Interactions, 2007. **167**(2): p. 135-144.

213. Dugan, L.L., Gabrielsen, J.K., Yu, S.P., Lin, T.-S., and Choi, D.W., *Buckminsterfullerenol Free Radical Scavengers Reduce Excitotoxic and Apoptotic Death of Cultured Cortical Neurons.* Neurobiology of Disease, 1996. **3**(2): p. 129-135.

214. Lynch, I., Salvati, A., and Dawson, K.A., *Protein-nanoparticle interactions: What does the cell see?* Nat Nano, 2009. **4**(9): p. 546-547.

215. Cedervall, T., Lynch, I., Lindman, S., Berggård, T., Thulin, E., Nilsson, H., Dawson, K.A., and Linse, S., *Understanding the nanoparticle–protein corona using methods to quantify*

exchange rates and affinities of proteins for nanoparticles. Proceedings of the National Academy of Sciences, 2007. **104**(7): p. 2050-2055.

216. Park, K.H., Chhowalla, M., Iqbal, Z., and Sesti, F., *Single-walled Carbon Nanotubes Are a New Class of Ion Channel Blockers.* Journal of Biological Chemistry, 2003. **278**(50): p. 50212-50216.

217. Andrews, N.C., *The iron transporter DMT1.* The International Journal of Biochemistry & Cell Biology, 1999. **31**(10): p. 991-994.

218. DeBaun, R.M. and de Stevens, G., *On the mechanism of enzyme action. XLIV. Codetermination of resazurin and resorufin in enzymatic dehydrogenation experiments.* Archives of Biochemistry and Biophysics, 1951. **31**(2): p. 300-308.

219. ÅKerfelt, M., Trouillet, D., Mezger, V., and Sistonen, L.E.A., *Heat Shock Factors at a Crossroad between Stress and Development.* Annals of the New York Academy of Sciences, 2007. **1113**(1): p. 15-27.

220. Miller, G. and Mittler, R., *Could Heat Shock Transcription Factors Function as Hydrogen Peroxide Sensors in Plants?* Annals of Botany, 2006. **98**(2): p. 279-288.

221. Ogawa, D., Yamaguchi, K., and Nishiuchi, T., *High-level overexpression of the Arabidopsis HsfA2 gene confers not only increased themotolerance but also salt/osmotic stress tolerance and enhanced callus growth.* Journal of Experimental Botany, 2007. **58**(12): p. 3373-3383.

222. Lindahl, E., Hess, B., and van der Spoel, D., *GROMACS 3.0: a package for molecular simulation and trajectory analysis.* Journal of Molecular Modeling, 2001. **7**(8): p. 306-317.

223. Van Der Spoel, D., Lindahl, E., Hess, B., Groenhof, G., Mark, A.E., and Berendsen, H.J.C., *GROMACS: Fast, flexible, and free.* Journal of Computational Chemistry, 2005. **26**(16): p. 1701-1718.

224. Oostenbrink, C., Villa, A., Mark, A.E., and Van Gunsteren, W.F., *A biomolecular force field based on the free enthalpy of hydration and solvation: The GROMOS force-field parameter sets 53A5 and 53A6.* Journal of Computational Chemistry, 2004. **25**(13): p. 1656-1676.

225. Berendsen, H.J.C., Postma, J.P.M., van Gunsteren, W.F., and Hermans, J., *Interaction models for water in relation to protein hydration.* Intermolecular Forces, 1981: p. 331-342.

226. Berendsen, H.J.C., Postma, J.P.M., van Gunsteren, W.F., DiNola, A., and Haak, J.R., *Molecular dynamics with coupling to an external bath.* The Journal of Chemical Physics, 1984. **81**(8): p. 3684-3690.

227. Hess, B., Bekker, H., Berendsen, H.J.C., and Fraaije, J.G.E.M., *LINCS: A linear constraint solver for molecular simulations.* Journal of Computational Chemistry, 1997. **18**(12): p. 1463-1472.

228. Miyamoto, S. and Kollman, P., *Settle: An analytical version of the SHAKE and RATTLE algorithm for rigid water models.* J. Comput. Chem., 1992. **13**(8): p. 952-962.

229. Essmann, U., Perera, L., Berkowitz, M., Darden, T., Lee, H., and Pedersen, L., *A smooth particle mesh Ewald method.* The Journal of Chemical Physics, 1995. **103**(19): p. 8577-8593.

230.   Nose, S., *A molecular dynamics method for simulations in the canonical ensemble 1 Molecular Physics: An International Journal at the Interface Between Chemistry and Physics.* Mol. Phys., 1984. **52**: p. 255-268.

231.   Hoover, W.G., *Canonical dynamics: Equilibrium phase-space distributions.* Physical Review A, 1985. **31**(3): p. 1695-1697.

232.   Parrinello, M. and Rahman, A., *Polymorphic transitions in single crystals: A new molecular dynamics method.* J. Appl. Phys., 1981. **52**(12): p. 7182-7190.

233.   Torrie, G.M. and Valleau, J.P., *Nonphysical sampling distributions in Monte Carlo free-energy estimation: Umbrella sampling.* Journal of Computational Physics, 1977. **23**(2): p. 187-199.

234.   Kumar, S., Rosenberg, J.M., Bouzida, D., Swendsen, R.H., and Kollman, P.A., *THE weighted histogram analysis method for free-energy calculations on biomolecules. I. The method.* Journal of Computational Chemistry, 1992. **13**(8): p. 1011-1021.

235.   Livak, K.J., ABI Prism 7700 Sequence Detection System. User Bulletin No. 2. PE Applied Biosystems, 1997.

236.   Bloomfield, V.A., Crothers, D. M., and Tinoco, I. , *Nucleic Acids: Structures, Properties, and Functions*, U.S. Books, Editor. 2000.

237.   Luzar, A. and Chandler, D., *Effect of Environment on Hydrogen Bond Dynamics in Liquid Water.* Physical Review Letters, 1996. **76**(6): p. 928-931.

238.   *Microtubules*. Available from: http://manual.blueprint.org/Home/glossary-of-terms/mechano-glossary--m/mechano-glossary-microtubules.

239.   Cheeseman, I.M. and Desai, A., *Molecular architecture of the kinetochore-microtubule interface.* Nat Rev Mol Cell Biol, 2008. **9**(1): p. 33-46.

240.   Gheshlaghi, Z.N., Riazi, G.H., Ahmadian, S., Ghafari, M., and Mahinpour, R., *Toxicity and interaction of titanium dioxide nanoparticles with microtubule protein.* Acta Biochim. Biophys. Sin. , 2008. **40**: p. 777-782.

241.   Apopa, P.L., Qian, Y., Shao, R., Guo, N.L., Schwegler-Berry, D., Pacurari, M., Porter, D., Shi, X., Vallyathan, V., Castranova, V., and Flynn, D.C., *Iron oxide nanoparticles induce human microvascular endothelial cell permeability through reactive oxygen species production and microtubule remodeling.* Particle and Fibre Toxicology, 2009. **6**: p. 1-14.

242.   Zhou, J.C., Wang, X., Xue, M., Xu, Z., Hamasaki, T., Yang, Y., Wang, K., and Dunn, B., *Characterization of gold nanoparticle binding to microtubule filaments.* Materials Science and Engineering: C, 2010. **30**(1): p. 20-26.

243.   Greenfield, N.J., *Using circular dichroism collected as a function of temperature to determine the thermodynamics of protein unfolding and binding interactions.* Nat. Protocols, 2007. **1**(6): p. 2527-2535.

244.   Sreerama, N. and Woody, R.W., *Computation and Analysis of Protein Circular Dichroism Spectra*, in *Methods in Enzymology*, B. Ludwig and L.J. Michael, Editors. 2004, Academic Press. p. 318-351.

245.   Sreerama, N. and Woody, R.W., *Estimation of Protein Secondary Structure from Circular Dichroism Spectra: Comparison of CONTIN, SELCON, and CDSSTR Methods with an Expanded Reference Set.* Analytical Biochemistry, 2000. **287**(2): p. 252-260.

246.   Lowe, J., Li, H., Downing, K. H., and Nogales, E, *Refined Structure of alphabeta-Tubulin at 3.5 A Resolution.* Journal of Molecular Biology, 2001. **313**: p. 1045-1057.

247.   Fiser, A., Do, R. K. G., and Sali, A., *Modeling of Loops in Protein Structures.* Protein Sci., 2000. **9**: p. 1753-1773.

248.   Morris, G.M., Huey, R., Lindstrom, W., Sanner, M.F., Belew, R.K., Goodsell, D.S., and Olson, A.J., *AutoDock4 and AutoDockTools4: Automated docking with selective receptor flexibility.* Journal of Computational Chemistry, 2009. **30**(16): p. 2785-2791.

249.   Huey, R., Morris, G.M., Olson, A.J., and Goodsell, D.S., *A semiempirical free energy force field with charge-based desolvation.* Journal of Computational Chemistry, 2007. **28**(6): p. 1145-1152.

250.   Hess, B., Kutzner, C., van der Spoel, D., and Lindahl, E., *GROMACS 4: Algorithms for Highly Efficient, Load-Balanced, and Scalable Molecular Simulation.* Journal of Chemical Theory and Computation, 2008. **4**(3): p. 435-447.

251.   Oostenbrink, C., Villa, A., Mark, A., and van Gunsteren, W., *A biomolecular force field based on the free enthalpy of hydration and solvation: the GROMOS force-field parameter sets 53A5 and 53A6.* Journal of Computational Chemistry, 2004. **25**(13): p. 1656-1676.

252.   Bussi, G., Donadio, D., and Parrinello, M., *Canonical sampling through velocity rescaling.* J. Chem. Phys., 2007. **126**: p. 014101-014117.

253.   Howard, J. and Hyman, A.A., *Growth, fluctuation and switching at microtubule plus ends.* Nat Rev Mol Cell Biol, 2009. **10**(8): p. 569-574.

254.   Nogales, E. and Wang, H.-W., *Structural intermediates in microtubule assembly and disassembly: how and why?* Cell regulation, 2006. **18**(2): p. 179-184.

255.   Kabsch, W. and Sander, C., *Dictionary of protein secondary structure: Pattern recognition of hydrogen-bonded and geometrical features.* Biopolymers, 1983. **22**(12): p. 2577-2637.

256.   Matthes, D. and de Groot, B.L., *Secondary Structure Propensities in Peptide Folding Simulations: A Systematic Comparison of Molecular Mechanics Interaction Schemes.* Biophysical journal, 2009. **97**(2): p. 599-608.

257.   Crepeau, R.H., McEwen, B., and Edelstein, S.J., *Differences in α and β polypeptide chains of tubulin resolved by electron microscopy with image reconstruction.* Proceedings of the National Academy of Sciences, 1978. **75**(10): p. 5006-5010.